

Thermoelectric Properties of 2D Layered Materials

A Thesis

Submitted for the Degree of

Doctor of Philosophy

by

Sushmita Chandra



**New Chemistry Unit
Jawaharlal Nehru Centre for Advanced Scientific Research
(A Deemed University)
Bangalore - 560 064, India**

July 2022

Dedicated to my parents & sister

DECLARATION

I hereby declare that this thesis entitled “**Thermoelectric Properties of 2D Layered Materials**” is a result of studies carried out by me at the New Chemistry Unit, Jawaharlal Nehru Centre for Advanced Scientific Research, Bangalore, India, under the supervision of **Prof. Kanishka Biswas**. This work has not been submitted elsewhere for the award of any degree or diploma.

In keeping with the general practices of reporting scientific observations, due acknowledgements have been made wherever the work described is based on the findings of other investigators in a collaborative pursuit. Any omission which might have occurred by oversight or error in judgement is regretted.

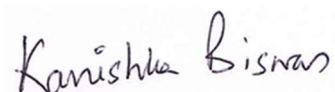
Sushmita Chandra

Bangalore, India
15th July 2022

Sushmita Chandra

CERTIFICATE

I hereby certify that the work described in this thesis titled “**Thermoelectric Properties of 2D Layered Materials**” has been carried out by Ms. Sushmita Chandra at New Chemistry Unit, Jawaharlal Nehru Centre for Advanced Scientific Research, Bangalore, India under my supervision and that it has not been submitted elsewhere for the award of any degree or diploma.



Bangalore, India
15th July 2022

Prof. Kanishka Biswas
(Research Supervisor)

ACKNOWLEDGEMENTS

Completion of my Ph.D. thesis necessitated a lot of guidance and supports from many people. I take this opportunity to mention a few of them. However, my sincere thanks extend to everyone who has played a role in making this dream a reality.

Firstly, my research supervisor, Prof. Kanishka Biswas for constant guidance throughout my Ph.D. career and giving me the freedom to carry out and express my scientific thoughts. His inputs in both scientific and non-scientific problems (for example how to make better presentations and write grant proposals etc.) have led to me become a much well-prepared researcher.

I would like to thank Bharat Ratna Prof. C. N. R. Rao, FRS for his words of encouragements. I also thank him for providing the infrastructure and facilities to carry out my research work.

I would like to thank Prof. Subi Jacob George, NCU chair for all the departmental instrument facilities.

I am extremely grateful to have such beloved lab mates: Dr. Satya, Dr. Manoj, Dr. Ananya, Dr. Subhajit, Dr. Manisha, Dr. Provas, Dr. Tanmoy, Dr. Suresh, Dr. Shidaling, Dr. Kaushik, Dr. Prabir, Dr. Archana, Dr. R. K. Gopal, Dr. Jayita, Dr. Ekashmi, Dr. Subarna, Dr. Abdul, Dr. Anuradha, Dr. Manjunatha, Dr. Moinak, Arka, Paribesh, Krishnendu, Debattam, Riddhimoy, Animesh Bhui, Anustoop, Vaishali, Animesh Das, Subhajit, Aditya, Ivy, Chahat, Anupama, Nupur, Aman, Jatin, Subho, Pavan and Prema for their cheerful company and keeping a healthy competitive spirit in the lab.

I would like to thank Prof. Umesh V. Waghmare, Prof. Ranjan Datta, Prof. Chandrabhas Narayana, Prof. Ajay Soni, Dr. Bobby Joseph, Dr. Koushik Pal, Ms. Raagya Arora, Ms. Koyendrilla Debnath, Dr. Usha Bhat, Ms. Janaky Sunil, and Ms. Divya Rawat for the fruitful scientific collaborations and all the insightful discussions. I have learnt a lot whenever we had meeting or discussion with them. Their discussion on past experiences, valuable inputs about research life and experiments helped me immensely.

I am thankful to all my course instructors: Prof. H. Ila, Prof. A. Sundaresan, Prof. S. C. Peter, Prof. K. Biswas, Prof. S. S. Agasti, Prof. Balasubramanian, Prof. R. Viswanatha, Prof. S. Rajaram, Prof. A. Sundaresan, Prof. M. Eswaramoorthy, Prof. P. Senguttuvan, Prof. S. J. George, Prof. J. Haldar, Prof. U. V. Waghmare, Prof. T. K. Maji, whose courses have been extremely helpful.

Constant assistance and the friendly nature of the technical staff helped me doing my experiments smoothly at JNCASR. I would like to acknowledge Mrs. Usha, Mrs. Selvi, Mr. Vasu, Mr. Anil, Mr. Rahul, Dr. Jay Ghatak, Mr. Mahesh, Mr. Shiva, Mr. Kannan,

Mr. N. Kishore, Mr. M. Gowda, Mr. Dileep, Mr. Srinivas and others for their technical help.

I thank all the staff members associated with Academic, Admin, Purchase, NCU, ICMS, Library, Hostel, Mess, Security, Utility, Gardening, Cleaning, Dhanvantari and other departments.

I would like to thank JNCASR for the research fellowship.

I would like to thank DST for providing the funding support to carry out the pressure-dependent X-ray diffraction studies at Elettra, Trieste, Italy.

I would like to thank my summer students Rajdeep, Abhirup, Vaibhab and Swetha for helping me in the experiments.

I thank all my seniors, juniors and friends in JNCASR, without whom, life at JNC would never be so meaningful: Manisha di, Subhajt da, Madhulika di, Aditya, Koyendrila, Geetika, Aditi, Harshit, Amit, and Navin. I would specially like to thank Albin and Prabir da for their constant guidance, support and motivation.

I would like to acknowledge my childhood, school, college, and university friends: Paramita, Srestha, Sakhshi, Sampreeti, Tamali, and Prerana for all the cheerful memories.

Simple words of thanks are never enough to convey feelings to my parents and sister who have supported me and placed their trust and faith in all activities. Their love, endurance and utmost patience are the backbone of my future. I am grateful to you all for whatever you gave me, and I dedicate my thesis to you.

PREFACE

Recently, two dimensional (2D) layered materials have gained enormous attention among researchers due to their outstanding physical and chemical properties. Unique optical, electronic, and thermal transport properties make this class of compounds as potential candidates for energy conversion. Very recently, metal-based chalcogenides with 2D layered structure are found to show superior thermoelectric performance. My Ph.D. thesis deals with the novel synthesis and structure-property relationships of few 2D layered metal chalcogenides to explore their thermoelectric properties. The thesis is divided into seven parts.

Part 1 presents a brief introduction to the 2D layered metal chalcogenides and their importance in the field of thermoelectrics. Then, I have discussed about the intriguing crystal structure, lattice dynamics, and electronic structure of tin selenide and addressed the key challenges in the way of optimizing the thermoelectric performance of SnSe. I have also discussed about the favourable electronic and phonon transport of a charge density wave (CDW) material, gadolinium tri-telluride (GdTe_3) and why CDW materials are potential candidates for thermoelectrics. Further, I have discussed about the effect of pressure on the electronic transition in topological quantum materials and provided a brief introduction about the crystal and electronic structure of bismuth selenide (BiSe), a weak topological insulator. Lastly, I have described the experimental details including various synthesis, characterizations, and measurement techniques.

Part 2 is divided into 3 chapters. **Chapter 1** deals with the high thermoelectric figure of merit ($zT = 2.1$) in two dimensional (2D) nanoplates of Ge doped SnSe synthesized by a simple hydrothermal route followed by spark plasma sintering (SPS). Ge-doping in SnSe nanoplates significantly enhances the *p*-type carrier concentration which results in high electrical conductivity and power factor. In addition to nanoscale grain boundary and high lattice anharmonicity in SnSe nanoplates, phonon scattering due to Ge precipitates in the SnSe matrix gives rise to an ultralow lattice thermal conductivity (κ_{lat}) of ~ 0.18 W/mK at 873 K in 3 mol% Ge doped SnSe nanoplates. In **Chapter 2**, I have obtained significant enhancement in thermoelectric performance in 2D SnSe nanoplates by introducing magnetic Gd dopants. The *p*-type carrier concentration increases significantly upon 3 mol% Gd addition in SnSe nanoplates due to phase separation of Gd_2Se_3 nanoprecipitates (2-5 nm) and subsequent Sn^{2+} vacancy formation. The presence of magnetic fluctuations induced by small nano-precipitates of Gd_2Se_3 provides additional

scattering of the phonons in SnSe, which reduces the κ_{lat} significantly in $\text{Sn}_{0.97}\text{Gd}_{0.03}\text{Se}$. **Chapter 3** deals with the solution phase synthesis and thermoelectric transport properties of ultrathin (1.2-3 nm thick) few layered *n*-type Bi doped SnSe nanosheets. Bi-doped nanosheets exhibit ultralow κ_{lat} (~ 0.3 W/mK) throughout the temperature range of 300-720 K which can be ascribed to the effective phonon scattering by interface of SnSe layers, nanoscale grain boundaries and point defects.

Part 3 is divided into 2 chapters. In **Chapter 1**, I have reported record high zT of 2.0 in *n*-type polycrystalline $\text{SnSe}_{0.92} + 1$ mol% MoCl_5 resulting from the simultaneous optimization of *n*-type carrier concentration and enhanced phonon scattering due to the formation of modular of layered intergrowth $[(\text{SnSe})_{1.05}]_m(\text{MoSe}_2)_n$ like compounds within the SnSe matrix. These 2D layered modular intergrowth compound resembles the natural nano-heterostructures and their periodicity of 1.2 - 2.6 nm matches the phonon mean free path of SnSe. Thus, the heat carrying phonons were blocked effectively and an ultra-low low κ_{lat} and ultra-high thermoelectric performance were obtained in *n*-type polycrystalline SnSe. **Chapter 2** deals with the high thermoelectric performance of *n*-type $\text{SnSe}_{0.92}$ upon WCl_6 doping. The successful creation of Se vacancy and substitution of W^{6+} at Sn^{2+} and Cl ions at Se^{2-} sites effectively enhance the total *n*-type carrier concentration, thus improving its electrical conductivity. The occurrence of WSe_2 precipitates in the SnSe matrix drastically reduces the lattice thermal conductivity which gives rise to high zT in $\text{SnSe}_{0.92} + 2$ mol% WCl_6 sample.

Part 4 reports the successful stabilization of the high-pressure cubic rock-salt phase of SnSe at ambient conditions by introducing chemical pressure into the lattice upon alloying with 30 mol% AgBiSe_2 . The band gap of the pristine orthorhombic SnSe is 0.90 eV, whereas, when SnSe is alloyed with AgBiSe_2 , band gap closes rapidly near to zero at $x = 0.30$ due to increase in chemical pressure originating from a sharp decrease in unit cell volume. We confirm the stabilization of the cubic structure and its associated changes in electronic structure using first-principles theoretical calculations. Pristine cubic SnSe exhibits topological crystalline insulator (TCI) quantum phase, but the cubic $(\text{SnSe})_{1-x}(\text{AgBiSe}_2)_x$ ($x = 0.33$) possesses semi-metallic electronic structure with overlapping conduction and valence bands. Cubic polycrystalline $(\text{SnSe})_{0.70}(\text{AgBiSe}_2)_{0.30}$ sample shows *n*-type conduction at room temperature while the orthorhombic $(\text{SnSe})_{1-x}(\text{AgBiSe}_2)_x$ ($0.00 \leq x < 0.28$) samples retain its *p*-type character. Thus, by optimizing the electronic structure and the thermoelectric properties of polycrystalline SnSe, a high zT of 1.3 at 823 K has been achieved in $(\text{SnSe})_{0.78}(\text{AgBiSe}_2)_{0.22}$.

Part 5 investigates the origin of low lattice thermal conductivity in GdTe₃, a charge density wave (CDW) material. GdTe₃ possess a quasi-2D layered structure where one corrugated GdTe slab is sandwiched between two Te sheets. From, first-principles theoretical calculations, it was verified that charge transfer take place from the GdTe slab to the adjacent Te sheets and there is a presence of van der Waals (vdW) gap between the two neighbouring Te-sheets. Thus, the structure can be considered as a natural heterostructure of charge and vdW layers. Strong electron-phonon coupling, and Fermi surface nesting play the crucial role behind the CDW transition ($T_{CDW} \sim 380$ K) in GdTe₃. Large anisotropic behaviour was observed both in the electrical and thermal conductivity data of GdTe₃ when measured along parallel and perpendicular to the SPS pressing, which is quite unusual in polycrystalline materials. From the theoretical calculations and Raman spectroscopic analysis, we have confirmed the existence of low-lying optical phonon modes in GdTe₃ which couples with the heat carrying acoustic phonon branches. Thus, the presence of strong electron-phonon coupling and natural heterostructure of charge and vdW layers effectively scatter the phonons which gives rise to low lattice thermal conductivity in GdTe₃.

Part 6 deals with the impact of hydrostatic pressure on the weak topological insulator BiSe, a promising thermoelectric material. We have studied the pressure induced electronic topological transition in BiSe through high pressure synchrotron X-ray diffraction, Raman spectroscopy and first-principles density functional theory calculations. We have observed clear anomalies at ~ 1 and ~ 2.2 GPa in the pressure dependent lattice parameters (a , c , and c/a ratio), cell volume, Raman mode shift and Raman mode linewidth data suggesting the onset of two electronic topological transitions (ETTs) in this system which is further verified by DFT calculations of electronic structure under pressure. The origin of these ETTs is associated with the two different vibrational modes arising from of Bi₂ bilayer and Bi₂Se₃ quintuple layers of BiSe. Detailed electronic band structure calculations also indicate that the emergence of multiple band extrema both in the valence and conduction bands near the vicinity of ETT can improve the thermopower and thermoelectric performance of BiSe.

In **Part 7**, I have summarized the thesis and provided a brief outlook to develop new concepts for improving the thermoelectric properties of layered metal chalcogenides. To summarize, the initial part of the thesis involves the synthesis and enhancement of the thermoelectric performance of p -type nanocrystals and n -type polycrystals off SnSe (**Part 2 and 3**). Then, I have studied the structural attributes of SnSe where I could be able to

successfully stabilize the metastable cubic rock-salt phase of SnSe at ambient conditions with the aid of chemical pressure (**Part 4**). I have also performed an in-depth study to understand the origins of low thermal conductivity in a charge density wave material, GdTe₃ (**Part 4**). Finally, I have studied the pressure dependent electronic topological transitions in a weak topological insulator BiSe (**Part 6**).

TABLE OF CONTENTS

DECLARATION -----	III
CERTIFICATE -----	V
ACKNOWLEDGEMENTS -----	VII
PREFACE -----	IX

Part 1: A Brief Introduction to Thermoelectrics and Layered Metal

Chalcogenides -----	1
Summary-----	3
1.1 Introduction to thermoelectric effect -----	5
1.2 Relevant parameters in thermoelectrics-----	6
1.3 Strategies embraced to improve the efficiency of thermoelectric materials -----	8
1.3.1 Power-factor optimization -----	9
1.3.2 Reduction of thermal conductivity-----	10
1.4 Layered metal chalcogenides and their relevance in the context of thermoelectrics -----	16
1.4.1 Phonon transport in layered materials-----	17
1.4.2 Electronic transport in layered materials-----	19
1.5 Tin selenide (SnSe): An extraordinary thermoelectric material -----	19
1.5.1 Crystal and electronic structures -----	20
1.5.2 Electrical transport properties -----	22
1.5.3 Anharmonicity and ultralow thermal conductivity -----	24
1.5.4 SnSe single crystals -----	25
1.5.5 Polycrystals and nanostructures of SnSe-----	27
1.5.6 Removal of surface oxides in polycrystalline SnSe -----	30
1.6 Gadolinium telluride (GdTe ₃): A charge density wave (CDW) material -----	31
1.6.1 An introduction to CDW -----	32
1.6.2 CDW in the context of thermoelectrics -----	33
1.6.3 Crystal and electronic structures of RTe ₃ (R = rare earth).....	34
1.7 Bismuth selenide (BiSe): A topological quantum material (TQM) -----	35
1.7.1 An introduction to topological quantum materials -----	36
1.7.2 Pressure induced electronic topological transition (ETT) in TQM -----	37
1.7.3 Crystal and electronic structures of BiSe -----	38
1.8 Synthesis and characterization techniques-----	40
1.8.1 Synthesis-----	40
1.8.1.1 Solid state reaction -----	40

1.8.1.2 Solution-phase synthesis -----	43
1.8.2 Characterization techniques-----	44
1.8.2.1 Powder X-ray diffraction (PXRD)-----	44
1.8.2.2 Transmission electron microscopy (TEM) -----	45
1.8.2.3 Scanning transmission electron microscopy (STEM) -----	45
1.8.2.4 Field emission scanning electron microscopy (FESEM)-----	46
1.8.2.5 Energy dispersive X-ray analysis (EDX) -----	46
1.8.2.6 Atomic force microscopy (AFM) -----	47
1.8.2.7 X-ray photoelectron spectroscopy (XPS)-----	47
1.8.2.8 Inductively coupled plasma-atomic emission spectroscopy (ICP-AES) -----	48
1.8.2.9 Optical band gap of solid materials -----	49
1.8.2.10 Raman spectroscopy-----	49
1.8.2.11 Thermogravimetric analysis (TGA) and differential scanning calorimetry (DSC) -----	50
1.9 Physical property measurements -----	50
1.9.1 Electrical transport measurements -----	51
1.9.2 Hall effect -----	52
1.9.3 Thermal transport measurements -----	53
1.9.4 Heat capacity -----	54
1.9.5 Magnetic measurements -----	55
1.9.6 Pressure dependent Raman and XRD measurements -----	56
1.10 Scope of the thesis-----	60
1.11 References -----	65

Part 2: Solution Grown Nanocrystalline SnSe-----75

**Chapter 2.1: Realization of High Thermoelectric Figure of Merit in
Solution Synthesized 2D SnSe Nanoplates via Ge Alloying -----77**

Summary -----	79
2.1.1 Introduction -----	81
2.1.2 Methods -----	82
2.1.3 Results and Discussions-----	85
2.1.4 Conclusion -----	95
2.1.5 References-----	97

**Chapter 2.2: Enhancement of the Thermoelectric Performance of 2D
SnSe Nanoplates through Incorporation of Magnetic Nanoprecipitates --- 101**

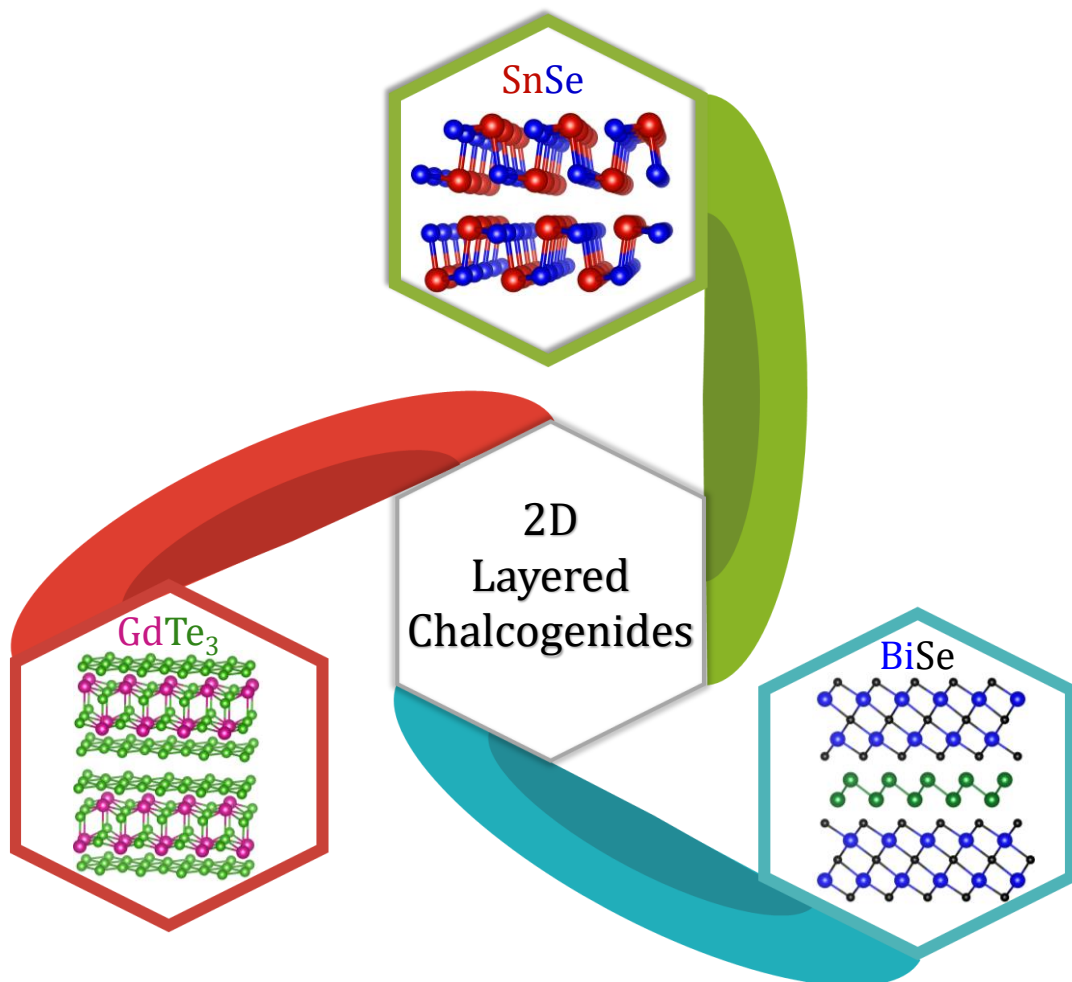
Summary -----	103
2.2.1 Introduction -----	105
2.2.2 Methods -----	106

2.2.3 Results and Discussions-----	108
2.2.4 Conclusion -----	117
2.2.5 References -----	118
Chapter 2.3: <i>n</i>-type Ultrathin Few-layer Nanosheets of Bi-doped SnSe:	
Synthesis and Thermoelectric Properties -----	119
Summary -----	121
2.3.1 Introduction-----	123
2.3.2 Methods -----	124
2.3.3 Results and Discussions-----	128
2.3.4 Conclusion -----	136
2.3.5 References -----	138
Part 3: High Thermoelectric Performance of Polycrystalline <i>n</i>-type SnSe -----	
141	
Chapter 3.1: Modular Nanostructures Facilitate Low Thermal Conductivity and Ultra-high Thermoelectric Performance in <i>n</i>-type SnSe -----	
143	
Summary -----	145
3.1.1 Introduction-----	147
3.1.2 Methods -----	148
3.1.3 Results and Discussions-----	151
3.1.4 Conclusion -----	162
3.1.5 References -----	164
Chapter 3.2: Realization of Excellent Thermoelectric Performance in <i>n</i>-type SnSe via WCl₆ Doping -----	
167	
Summary -----	169
3.2.1 Introduction-----	171
3.2.2 Methods -----	172
3.2.3 Results and Discussions-----	173
3.2.4 Conclusion -----	180
3.2.5 References -----	182
Part 4: Modulation of the Electronic Structure and Thermoelectric Properties of Orthorhombic and Cubic SnSe by AgBiSe₂ Alloying-----	
185	
Summary -----	187
4.1 Introduction -----	189
4.2 Methods-----	190
4.3 Results and Discussions-----	193
4.4 Conclusion -----	207

4.5 References-----	208
Part 5: Low Thermal Conductivity in Charged & van der Waals	
Layered GdTe₃ -----	211
Summary -----	213
5.1 Introduction -----	215
5.2 Methods-----	217
5.3 Results and Discussions -----	220
5.4 Conclusion -----	234
5.5 References-----	236
Part 6: Evidence of Pressure-induced Multiple Electronic Topological	
Transitions in Thermoelectric BiSe -----	241
Summary -----	243
6.1 Introduction -----	245
6.2 Methods-----	248
6.3 Results and Discussions -----	250
6.4 Conclusion -----	263
6.5 References-----	264
Part 7: Summary and Future Outlook -----	
7.1 Summary -----	271
7.2 Future Outlook -----	274
7.3 References-----	278
List of Publications -----	281
Biography -----	283

PART 1

A Brief Introduction to Thermoelectrics and Layered Metal Chalcogenides



A Brief Introduction to Thermoelectrics and Layered Metal Chalcogenides[†]

Summary

Thermoelectric materials can convert waste heat into useful electrical energy and constitute a viable means of efficient energy management. Recently, two dimensional (2D) layered materials have gained enormous attention in the field of thermoelectrics due to their unique electronic and thermal transport properties. Strong in-plane and weak out-of-plane bonding in layered materials cause bonding heterogeneity, and the consequent lattice anharmonicity brings down the lattice thermal conductivity. In addition to this, 2D materials also exhibit some interesting phenomena such as charge density wave (CDW) ground states and pressure-induced electronic topological transitions (ETT). Thus, in a nutshell, layered materials present a common platform for exploring thermoelectrics, and fundamental physical properties. This chapter highlights a brief introduction to (a) thermoelectrics and its recent advances, (b) 2D layered metal chalcogenides of interest for the thesis, (c) charge density wave transitions and its correlation with thermoelectrics, and (d) pressure dependent ETT in layered chalcogenides. The last part of this chapter is focused on a general discussion of synthesis, characterizations, thermoelectric and different physical property measurements of a few novel 2D layered metal chalcogenides.

[†]A part of this chapter is published in **S. Chandra**, M. Samanta, K. Biswas, High-Performance Thermoelectric Energy Conversion Based on Lead-Free Group IV–VI Metal Chalcogenides. In *Inorganic Thermoelectric Materials: From Fundamental Concepts to Materials Design*; A. V. Powell, Eds.; Royal Society of Chemistry, 2021; pp 157–215 (Book Chapter); **S. Chandra**, P. Dutta, and K. Biswas, *ACS Nano*, 2022, 16, 7-14 (Invited Perspective).

1.1. Introduction to thermoelectric effect

Thermoelectric (TE) materials, by virtue of a unique combination of electrical and thermal properties, can convert thermal gradients into electrical energy or vice versa and are posited to play a significant role in the future energy management.¹⁻⁵ Given the current global energy crisis and the dwindling non-renewable resources, capturing and converting the otherwise wasted heat back into useful electrical power will have a huge impact.

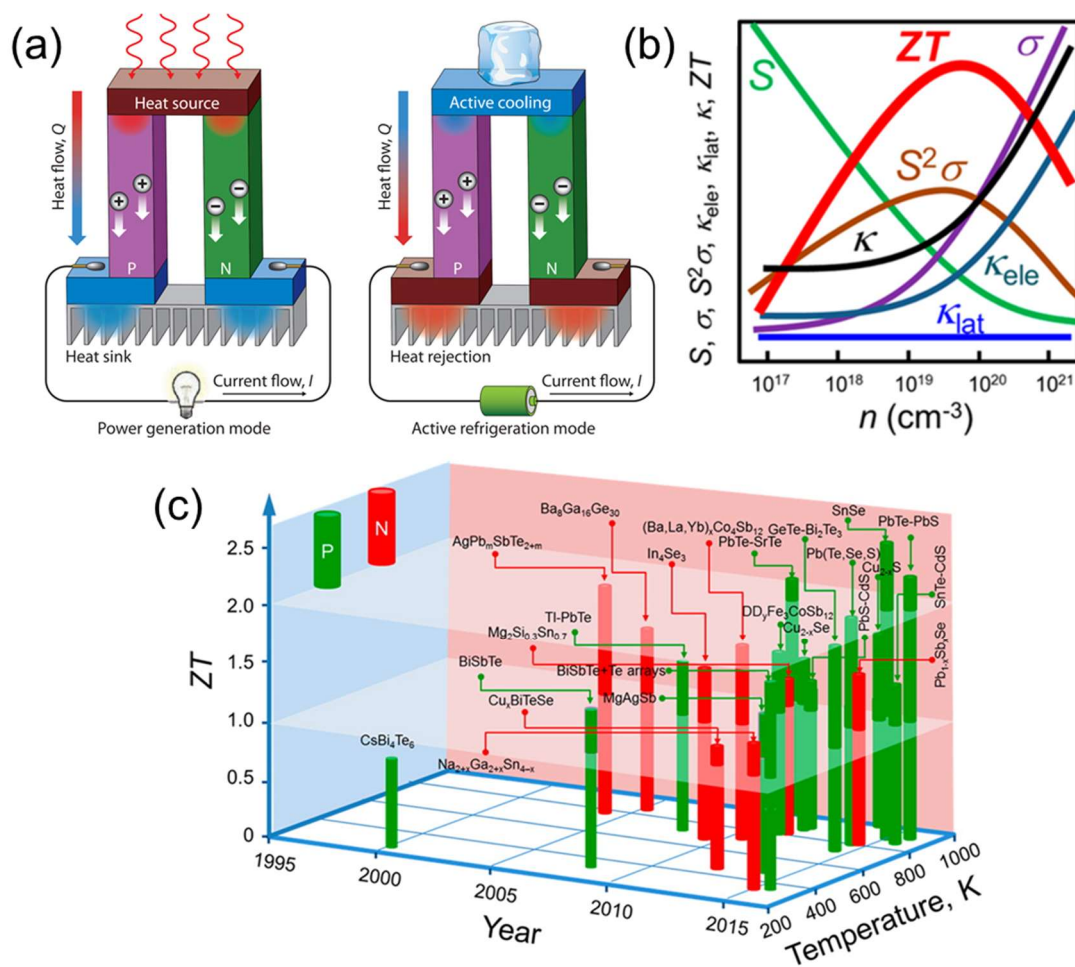


Figure 1.1. (a) Schematic illustrations of a thermoelectric (TE) module for active power generation-Seebeck effect (left) and refrigeration-Peltier effect (right). (b) Schematic diagram showing the dependence of zT and its parameters (electrical conductivity σ , Seebeck coefficient S , power factor $S^2\sigma$, electronic thermal conductivity κ_{ele} , lattice thermal conductivity κ_{lat} and total thermal conductivity, κ_{total}) on carrier concentration n . (c) TE figure-of-merit (zT) as a function of temperature and year illustrating important milestones.¹ (b) and (c) are reproduced with permission from ref. 1 © 2016 American Chemical Society.

In general, a thermoelectric module consists of both p -type and n -type semiconductors connected through metallic conducting pad.⁶⁻⁸ When a temperature gradient (ΔT) is applied to a TE couple consisting of n -type and p -type elements, the mobile charge carriers (electrons in n -type and holes in p -type) at the hot end diffuse to the cold end, producing a potential difference (ΔV). This effect known as Seebeck effect, where $S = \Delta V/\Delta T$ is defined as the Seebeck coefficient, forms the basis of TE power generation. (Figure 1.1a). Conversely, when a potential difference is applied to a TE couple, carriers bring heat from one side to the other so that one side gets cooler while the other gets hotter, an effect known as the Peltier effect (Figure 1.1a) which forms the basis of TE refrigeration.

1.2. Relevant parameters in thermoelectrics

The thermoelectric conversion efficiency for a material requires both high zT values and a large temperature difference across the thermoelectric materials, as given by the following relation:³

$$\eta_{TE} = \eta_c \frac{(\sqrt{1 + zT} - 1)}{(\sqrt{1 + zT} + \frac{T_c}{T_H})} \quad (1.1)$$

where η_c , T_H and T_C are Carnot Efficiency, the temperatures of the hot and cold ends and zT , the dimensionless figure of merit is expressed as:

$$zT = \frac{\sigma S^2}{\kappa_{total}} T \quad (1.2)$$

where σ , S , κ_{total} and T are the electrical conductivity, Seebeck coefficient, thermal conductivity and absolute temperature, respectively.²⁻⁴

To maximize the thermoelectric figure of merit (zT) of a material, high electrical conductivity, a large Seebeck coefficient and a low thermal conductivity are needed. The quantity σS^2 is defined as power factor and is the key to achieve high thermoelectric performance. A large power factor means the generation of large voltage and a high current. For high σS^2 , a material is needed to have high electrical conductivity (σ) and large Seebeck coefficient (S). For metals or degenerate semiconductors (parabolic band, energy-independent scattering approximation),³ the Seebeck coefficient is proportional to

the effective mass (m^*) and temperature, and inversely proportional to the charge carrier concentration (n_H), as seen in equation 1.3.

$$S = \frac{8\pi^2 k_B^2}{3eh^2} m^* T \left(\frac{\pi}{3n_H}\right)^{\frac{2}{3}} \quad (1.3)$$

where k_B is the Boltzmann constant, h is the Planck constant, and e is the electron charge. Thus, a large Seebeck coefficient indicates a large effective mass which is equivalent to a large density-of-states (DOS) or flat bands at the Fermi level. High electrical conductivity requires a large mobility (μ) and a large carrier (electrons or holes) concentration (n_H), as seen in equation 1.4.

$$\sigma = ne\mu \quad (1.4)$$

where mobility, μ can be defined by the following expression:

$$\mu = \frac{e\tau}{m^*} \quad (1.5)$$

where τ is the relaxation time and m^* is the carrier effective mass.¹

On the other hand, thermal conductivity (κ_{total}) has two parts: the lattice or phonon contribution (κ_{lat}) and the electronic contribution (κ_{ele}).

$$\kappa_{total} = \kappa_{ele} + \kappa_{lat} \quad (1.6)$$

κ_{ele} is proportional to the electrical conductivity through the Wiedemann–Franz law.

$$\kappa_{ele} = L\sigma T \quad (1.7)$$

where L is the Lorenz Number. For free electrons, it is $2.45 \times 10^{-8} \text{ W } \Omega \text{ K}^{-2}$. The Lorenz number varies with the material's carrier concentration and can be reduced by as much as 20% from the free-electron value for the materials with low-carrier-concentration.^{1,3} From equation 1.7, it is clear that increasing electrical conductivity is detrimental to realize high zT because of simultaneous enhancement in electrical and thermal conductivity.

Since κ_{ele} is proportional to σ via Wiedemann–Franz law (equation 1.7), the only way to achieve low thermal conductivity (κ_{total}) is to manipulate κ_{lat} . According to the kinetic theory of ‘phonon gas’, the lattice thermal conductivity of a solid material can be described as^{1,9,10}

$$\kappa_{lat} = \frac{1}{3} C_V \vartheta l \quad (1.8)$$

where C_V is the specific heat capacity at constant volume, l is phonon mean free path

(MFP, defined as the average distance travelled by phonons between successive scatterings), and ϑ is the average velocity of sound. Unlike C_V and l , the velocity of sound (ϑ) is material-dependent and varies very little with changes with temperature, morphology, or doping. At high temperatures ($T \gg \Theta_D$, Debye temperature), since the energy carried by each atom in bulk materials approaches to $3k_B T$, specific heat reaches the Dulong–Petit limit ($3k_B$ per atom), resulting in the difficulty for manipulating the specific heat of thermoelectric materials. Thus, above Debye temperature (Θ_D), κ_{lat} primarily depends on phonon mean free path, l . Phonon mean free path is determined by rate of a) phonon-phonon scattering and (b) scattering with grain-boundaries or static impurities. In case of semiconductors when carrier concentration is lesser than 10^{19} cm^{-3} , κ_{lat} usually dominates the κ_{total} . Moreover, acoustic phonons usually dominate κ_{lat} over optical phonons because of their higher group velocities, $\vartheta_i = \frac{\partial \omega}{\partial k}$ (here ‘ i ’ refers to polarization of acoustic phonons *i.e.*, longitudinal acoustic (LA) or transverse acoustic (TA1, TA2)). Since phonon mean free path of any material is limited by inter atomic distance, minimum the lattice thermal conductivity, κ_{min} cannot be reduced lower than that of the amorphous limit, as defined by Cahill:^{11,12}

$$\kappa_{min} = \frac{1}{2} \left(\frac{\pi}{6}\right)^{\frac{1}{3}} k_B V^{-\frac{2}{3}} (2\vartheta_t + \vartheta_l) \quad (1.9)$$

where V is average volume per atom, k_B is the Boltzmann constant, ϑ_t and ϑ_l are the transverse and longitudinal sound velocities.

1.3. Strategies embraced to improve the efficiency of thermoelectric materials

Thermoelectric have always been a materials design problem relating complicated tuning of structure-property relationships in inorganic solids through principles of solid-state chemistry. An ideal thermoelectric material should have high electrical conductivity similar to metals, large Seebeck coefficient as in semiconductors and ultra-low thermal conductivity like glasses. It is always challenging for the chemists to design a single TE material that meets all the above criteria; moreover, the high interdependence of all the above properties poses an inherent limit to the maximum zT that can be attained in a given material (Figure 1.1b) Therefore, to design a high-performance TE material, these quantities must be optimized. The major obstacle lies in the optimization of all of these

parameters together in a single material due to their strong interdependence.^{2,3} However, in the last few years, numerous efforts have been devoted to decoupling and synergizing individual TE parameters. Figure 1.1c shows the evolution of zT over the past two decades and it clearly shows that state-of-the-art TE materials are found among heavy metal chalcogenides, especially those based on Bi and Pb such as Bi_2Te_3 , PbTe , and PbSe .¹

Two approaches are employed to boost zT viz. enhancement of power factor (σS^2) and reduction of thermal conductivity. In the following section, I will summarize the most recent approaches of designing high-performance TE materials.

1.3.1. Power-factor optimization

Power factor (σS^2) is a purely electronic property, governed by materials' electronic structure and scattering mechanism.

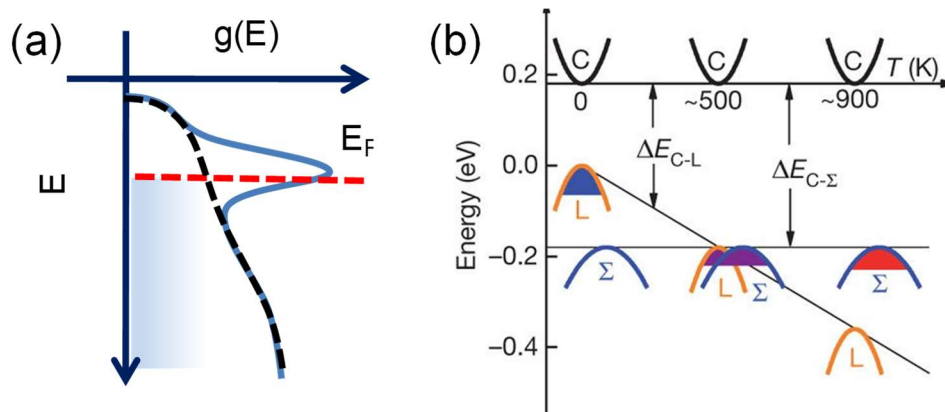


Figure 1.2. (a) Schematic diagram of resonance level in the valence band. The dotted black line represents the density of state (DOS) of the valence band of pristine sample. For example, Tl -doped PbTe shows asymmetric distortion of DOS (blue line) near Fermi level.¹³ (b) Relative energy of the valence bands in $\text{PbTe}_{0.85}\text{Se}_{0.15}$. At 500 K the two valence bands converge, resulting in contributions from both the L and Σ bands in the transport properties.¹⁸ (b) is reproduced with permission from ref. 18 © 2011 Nature Publishing Group.

Strategies to enhance power factor include: (a) engineering of carrier-concentration (n_H) through chemical doping, (b) enhancement of the effective carrier mass and Seebeck coefficient via distortion of the density of states near Fermi level by resonance impurity levels (Figure 1.2a),^{13–17} or the convergence of multiple valence/conduction band extrema (Figure 1.2b),^{18–22} and (c) enhancement of carrier mobility (μ) by modulation-doping.^{1,23}

1.3.2. Reduction of thermal conductivity

As discussed earlier in equation 1.8, lattice thermal conductivity of bulk materials is provided by $\kappa_{lat} = \frac{1}{3} C_V v_g^2 \tau$.¹⁰ Thus, to minimize the κ_{lat} , one has to engineer materials which decrease the specific heat (C_V), the group velocity (v_g), and the phonon relaxation time (τ).

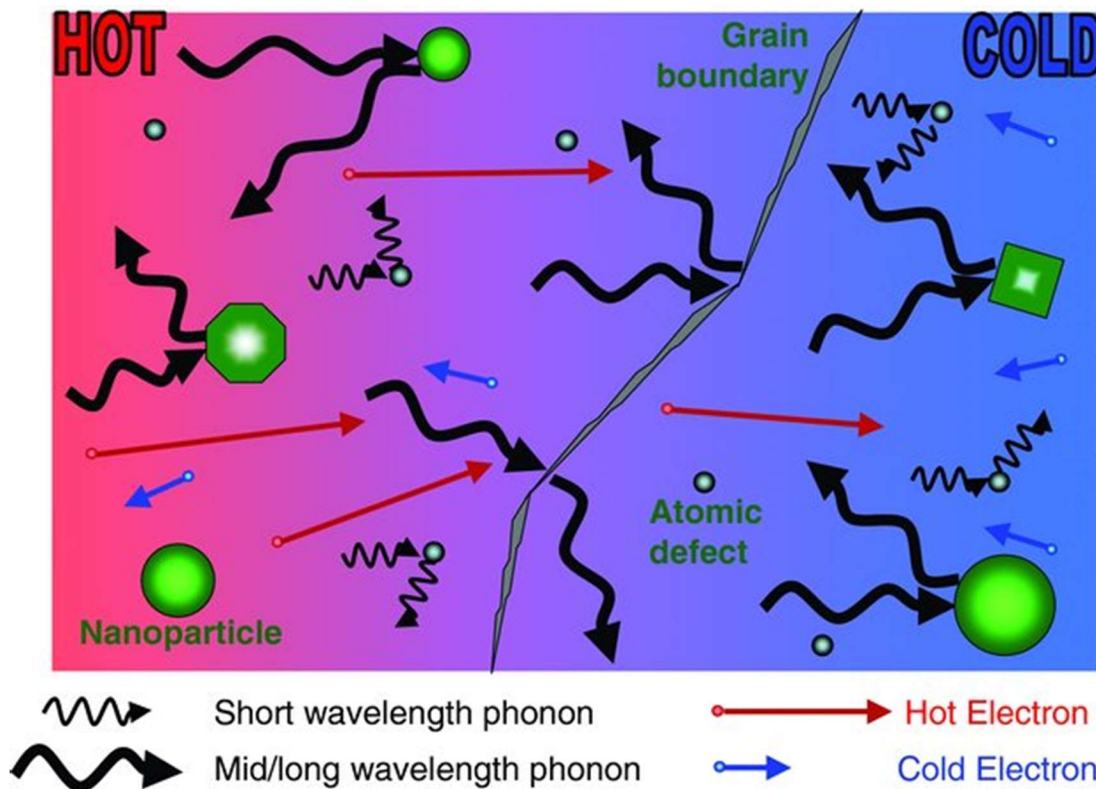


Figure 1.3. Schematic illustration of phonon-scattering by atomic defects (short wavelength phonons), nanoparticles (mid-long wavelength phonons) and grain boundaries (long wavelength phonons) in a solid (lower panel).²⁴ Reproduced with permission from ref. 24 © 2010 John Wiley and Sons.

Typically in thermoelectrics, the phonon relaxation time is the most focused variable to tweak and achieve desirable κ_{lat} via extrinsically introducing 0D point defects, 1D dislocations or 2D grain boundaries or fine precipitates (Figure 1.3).^{9,24} Each of these defects enhances the phonon-scattering process and decreases the relaxation time (τ) and thereby decreasing the κ_{lat} . Each of the aforementioned processes has their own frequency (ω) dependence. For example, the 0D point defects scatters the high frequency phonons ($\tau_{PD} \sim \omega^{-4}$); 1D dislocation scatters the mid frequency phonons (τ_{DC}

$\sim \omega^{-3}$ for dislocation cores and $\tau_{DS} \sim \omega^{-1}$ for dislocation strains); 2D interface scattering originating from grain boundaries or precipitates are effective for the low frequency phonons ($\tau_{inter} \sim \omega^0$). The Umklapp (U) process, which is ubiquitous has a relaxation time, $\tau_U \sim \omega^{-2}$, thus being effective in scattering the phonons of all frequencies. Callaway devised a phenomenological model considering all the contributions arising from the microstructural effects on phonon scattering at various length scales. The model which is given as:^{9,24,25}

$$\kappa_{lat} = \frac{k_B}{2\pi^2 v_g} \left(\frac{k_B T}{\hbar} \right)^3 \int_0^{\theta_D/T} \tau_C(x) \frac{x^4 e^x}{(e^x - 1)^2} dx \quad (1.10)$$

acts as a guide to quantitatively access the contributions arising from each microstructural effect. Here, k_B corresponds to Boltzmann's constant; \hbar , T and τ_C denote reduced Planck's constant, absolute temperature and total relaxation time respectively. τ_C corresponds to the individual relaxation time via the relation $\tau_C^{-1} = \tau_U^{-1} + \tau_{PD}^{-1} + \tau_{DS}^{-1} + \tau_{DC}^{-1} + \tau_{inter}^{-1} + \dots$, where τ_U , τ_{PD} , τ_{DS} , τ_{DC} and τ_{inter} corresponds to relaxation times arising from the contributions of Umklapp scattering, point defects, dislocation strain, dislocation cores and interface scattering respectively.

Apart from the extrinsic approaches to reduce the thermal conductivity, rational unearthing of materials with intrinsically low lattice thermal conductivity is an intriguing and efficient prospect.¹⁰ Since electrons and phonons propagate within the same sublattice, suppressing the phonon transport also handicaps the electron mobility. Thus materials with innate κ_{lat} offer an independent control to achieve high TE performances without having to compromise on the electrical mobility which is beneficial in maintaining high power factor.¹⁰ In this section, we have touched upon several techniques to reduce the κ_{lat} of the materials using extrinsic approaches such as alloying and nano-structuring as well as the intrinsic approaches.

Phonon-phonon scattering

There are two types of phonon-phonon scattering process - normal process (N process), and Umklapp process. While N-processes don't directly contribute to thermal resistance, U-processes hinder thermal transport. The effectiveness of U-processes in inhibiting heat transfer depends on (i) the scattering cross-section or frequency of collisions, and (ii) the amount of momentum loss during each collision. Since the U-process depends on the phonons density, it becomes more dominant as the temperature

is increased, and the phonon mean free path corresponding to U-process is inversely proportional to temperature, $\sim 1/T$ ($T \gg \Theta_D$). For ideal crystal, U-scattering is the dominant process for thermal resistivity at high temperatures.

Point defects

Introduction of lattice imperfections (point defects) in the host lattice (doping or alloying) is a well-known strategy of decreasing the κ_{lat} via scattering of short-wavelength phonons.^{26,27} According to the thermal conductivity model developed by Callaway²⁸ and Klemens,²⁹ reduction of κ_{lat} can be attributed to the combined effect of mass contrast and strain field fluctuations.

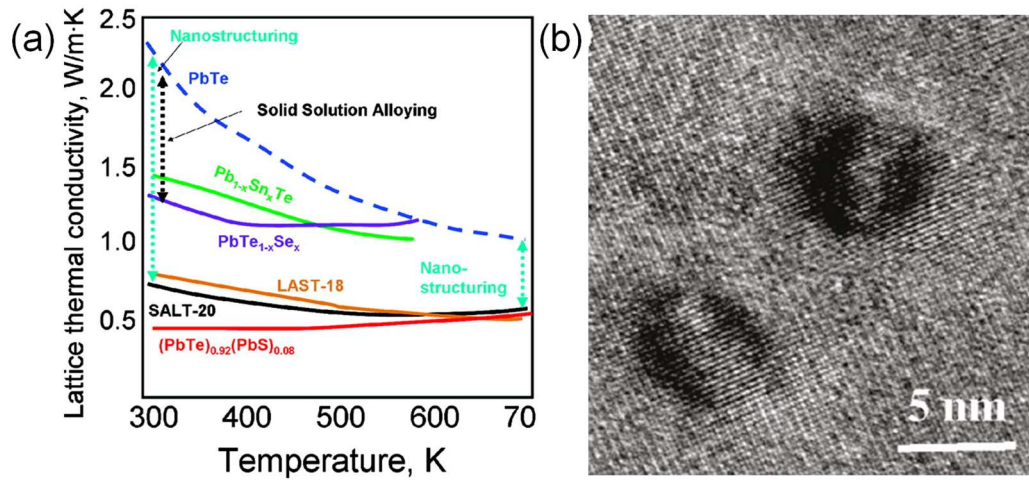


Figure 1.4. (a) Lattice thermal conductivity (κ_{lat}) as a function of temperature for various PbTe-based alloys and nanostructured samples. (b) High resolution transmission electron microscopy of a LAST-18 sample.³⁰ Reproduced with permission from ref. 30 © 2010 American Chemical Society.

The degree of κ_{lat} reduction can be evaluated by the following expression of scattering parameter (Γ):

$$\Gamma = x(1-x) \left[\left(\frac{\Delta M}{M} \right)^2 + \varepsilon \left(\frac{\Delta a}{xa} \right)^2 \right] \quad (1.11)$$

where ε is a phenomenological parameter related to the material's Grüneisen parameter γ , M and a are the molar mass and lattice constant of the alloy, ΔM and Δa are the differences in mass and lattice constant between the two constituents. From equation 1.11, one can conclude that to maximize Γ and achieve the lowest κ_{lat} , it is necessary to have (i) a high doping fraction x , (ii) a large mass difference between the dopant and the

host element (ΔM) creating disorder in the lattice, and (iii) a significant lattice mismatch (Δa) between the disordered phase and the host phase. Thus, solid solutions of $\text{PbTe}_{1-x}\text{Se}_x$ has lower κ_{lat} as compared to that of pure PbTe (Figure 1.4a).³⁰ Although most of the notable binary alloying is governed by enthalpy of the system, Kanatzidis and his co-workers argued that ternary alloying of $(\text{PbTe})_{1-x-y}(\text{PbSe})_x(\text{PbS})_y$ is driven by the configurational entropy.³¹ A low κ_{lat} of $0.5 \text{ W m}^{-1} \text{ K}^{-1}$ have been achieved in $(\text{PbTe})_{1-2x}(\text{PbSe})_x(\text{PbS})_x$ system owing to strong point defect scattering.

Nanostructuring

An innovative way to inhibit the transport of phonons having mid and longer wavelength is via introducing nano-scaled defects into the matrix.^{24,32} An effective scattering of mid and low frequency phonons would be possible only if the nano-scaled defects are distributed uniformly and are of similar size to these phonons, typically upto to dozens of nanometres. Quite a few approaches have been undertaken to achieve nanoscale in homogeneity viz. external addition of guest phase via chemical of mechanical mixing,³³ and *in-situ* precipitation of second phase via kinetically or thermodynamically driven processes.^{24,34,35} *In-situ* approach is the widely used due to even dispersion of the nano-precipitates which are also favourable for charge transport. Spinodal decomposition,³⁶ and nucleation and growth,³⁷ matrix encapsulation^{38,39} are the most common approaches for producing *in-situ* nanostructures in bulk matrix.

Since the well-known TE materials such as PbTe, SnTe and GeTe have a wide array of phonons with mean free paths of 1-100 nm, nanostructuring is proved to be effective pathway to reduce the κ_{lat} of these compounds. Replacing Pb in PbTe with two aliovalent atoms (*i.e.*, Ag and Sb) to form $\text{AgPb}_m\text{SbTe}_{m+2}$ (LAST-m) shows a substantial decrease in the κ_{lat} (Figure 1.4). Particularly LAST-18 shows a significant reduction in the κ_{lat} ($0.5 \text{ W m}^{-1} \text{ K}^{-1}$ at 700 K) as compared to PbTe. It has been argued that the very low κ_{lat} of the LAST system was attributed to the spontaneous formation of nanostructured second phases in the PbTe matrix (Figure 1.4b).³⁰

Meso-scale grain boundaries

So far, I have discussed about κ_{lat} reduction by scattering of low- and medium-mean free path phonons, which carry $\sim 75\%$ of the transported heat. To further reduce κ_{lat} it is necessary to scatter phonons with long mean free path ($\sim 0.1\text{-}1 \mu\text{m}$) (Figure 1.3). Necessary approaches involve the formation of crystal defects at submicrometer length

scale (mesoscale, grain size $\sim 0.1\text{-}3\ \mu\text{m}$), which can be engineered into materials through careful powder processing.

Rowe *et al.* have investigated the thermal conductivities of SiGe alloys with different grain sizes and compared them with that of their single crystals.⁴⁰ They showed that grains with relatively small sizes ($<5\ \mu\text{m}$) could scatter phonons strongly ($\sim 20\%$ reduction of thermal conductivity with respect to the single crystal). This work highlights the importance of mesoscale grains in impeding the phonon transport of bulk materials and points to further research to better understand mesoscale effects.

All-scale hierarchical architectures

When point defects, nanostructuring, and meso-structuring are all combined into a single thermoelectric material, it is termed as all-scale hierarchical architectures (Figure 1.5).

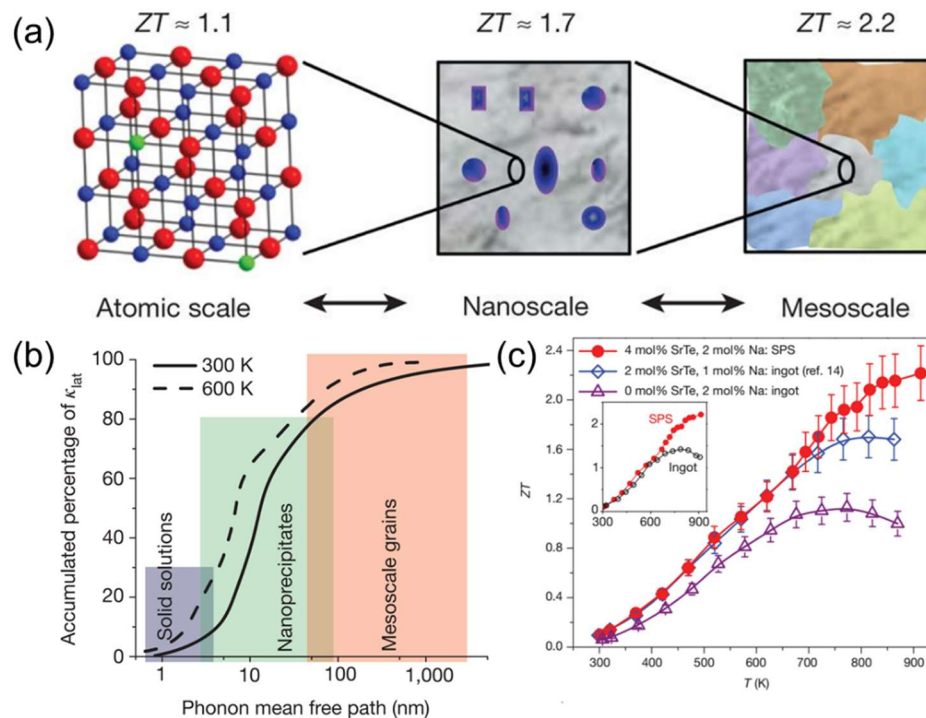


Figure 1.5. (a) Maximum achievable ZT ($\sim zT$) values for the respective length scales: the atomic scale (alloy scattering: red, Te; blue, Pb; green, dopant) the nanoscale (PbTe matrix, grey; SrTe nanocrystals, blue) to the mesoscale (grain-boundary scattering). (b) Contributions of phonons with different mean free paths to the cumulative κ_{lat} value for PbTe. (c) Temperature dependent thermoelectric figure-of-merit ZT ($\sim zT$) for the all-scale hierarchical architecture PbTe system.⁴² Reproduced with permission from ref. 42 © 2012 Nature Publishing Group.

Thermal conductivity in crystalline materials can be significantly decreased by defects present at different length scales with a broad range of wavelengths and mean free paths. Theoretical calculations suggest that, in PbTe, over 50% of the κ_{lat} value comes from the contribution by phonons with MFP less than 1 nm, which can be scattered significantly by atomic-scale point defects. The remaining contribution to κ_{lat} is almost equally divided between phonon modes with MFP of 1–10 nm and phonon modes with MFP 10–1000 nm (Figure 1.5) which can be notably impeded by nanoscale precipitates and mesoscale grains, respectively.^{41,42} Biswas and co-workers have demonstrated the substantial suppression of lattice thermal conductivity at high temperature in the PbTe-SrTe system that led to a record high zT of ~ 2.2 at 915 K in spark plasma sintered samples.⁴² This is the result of introducing phonon scattering at all-length scales in a hierarchical fashion from atomic scale doping and endotaxial nanostructuring to mesoscale grain boundary engineering.

Modular materials with intrinsic low lattice thermal conductivity

Modular inorganic materials like layered intergrowth (*e.g.* $\text{Pb}_m\text{Bi}_{2n}\text{Te}_{3n+m}$, $\text{Sn}_m\text{Bi}_{2n}\text{Te}_{3n+m}$, *etc.*)^{43–45} and misfit (*e.g.* SnS_2/SnS , LaS/TaSe_2 , *etc.*)^{46–50} compounds have emerged as one of the interesting candidates in the field of thermoelectrics (Figure 1.6).

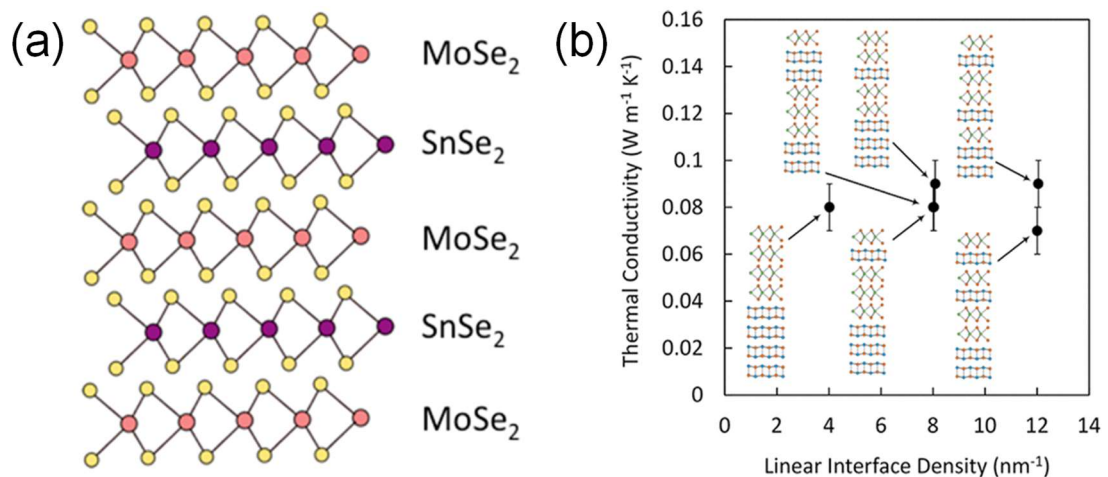


Figure 1.6. (a) Schematic representation of misfit $\text{SnSe}_2(\text{MoSe}_2)_{1.32}$ structure.⁴⁶ (b) Cross-plane thermal conductivity of $[(\text{SnSe})_{1.05}]_m(\text{MoSe}_2)_n$ ($m, n = 1, 2, 3 \dots$) measured with time domain thermal reflectance (TDTR) method.⁴⁷ (a) is reproduced with permission from ref. 46 © 2016 American Chemical Society. (b) is reproduced with permission from ref. 47 © 2016 American Chemical Society.

These materials are considered as natural heterostructures which show low lattice thermal conductivity due to inherent phonon scattering at the interfaces when stabilized in the form of nanosheets or/and embedded in bulk thermoelectric matrix.^{39,44,45} It is worth mentioning here that in recent times Rosseinsky and co-workers have shown the presence of chemical bond contrast and structural mismatch in a modular inorganic compound can result in low κ_{lat} and glass like thermal transport behaviour.⁵¹

The above strategies for reducing the lattice thermal conductivity give emphasis to the reduction of the phonon relaxation time through the enhancement of phonon scattering. Besides these conventional approaches, solids with complex crystal structures, part-crystalline part-liquid state rattling modes,⁵²⁻⁵⁴ superionic substructures with liquid-like cation disordering,^{55,56} resonant bonding,⁵⁷ lattice anharmonicity due to lone pair^{58,59} and anisotropic layered crystal structure,⁶⁰ has drawn huge attention of the thermoelectric community. Ultralow thermal conductivity in these materials arises either from low sound velocity or from low specific heat.

1.4. Layered metal chalcogenides and their relevance in the context of thermoelectrics

Dimensionality of the material plays a crucial role in determining its electronic and phonon transport properties.⁶¹⁻⁶⁴ With the developments of various material synthesis techniques it is now possible to prepare various low dimensional materials like quantum dots (zero dimensional), nanowire (one dimensional) and thin films/nanosheets (two dimensional). However, robust and reliable measurement of all the thermoelectric properties and practical use of low dimensional materials are still the challenges in thermoelectrics. On the other hand, many bulk materials have various low dimensional features embedded in their crystal structure because of the chemical bonding environment of the constituent atoms. For example, chemical bonding for the constituent atoms in many materials extend only in-plane direction and the chemical bonding in the out-of-plane direction is van der Waals (vdW) type (such as Bi_2Te_3 , SnSe etc.)⁶⁵⁻⁷⁰ or have weak electrostatic interactions (such as charged layered materials like BiCuSeO , $\text{Bi}_2\text{O}_2\text{Se}$ etc.).⁷¹⁻⁷⁴ Similarly, many layered materials have one dimensional chain like bonding environment for its constituent atoms like In_4Se_3 ⁷⁵ and TlSe .⁷⁶ The presence of such low dimensional chemical bonding environment strongly modulates the electronic and

phonon transport properties in bulk materials, a prime example of which is the phonon transport in single crystal SnSe,⁶⁸ which exhibits strong covalent bonding within the layer (2D-connectivity) and weak the van der Waals type interaction between the layers. Another example of such case is the single crystal In₄Se₃,⁷⁵ which has one dimensional atomic chains resulting in Peierls distortion. As a matter of fact, 2D layered materials have been established as potential candidates for thermal energy management and TE energy generation due presence of favorable electrical and phonon transport properties, which can be seen from their significantly large figure of merit.^{77–81} These 2D-layered metal chalcogenides have always aced the field of thermoelectrics because of their high-performance, facilitated by their unusual phonon and electronic transport properties.

1.4.1. Phonon transport in layered materials

Materials with intrinsically low κ_{lat} and understanding the correlation between lattice dynamics and chemical bonding in those materials would enable us to manipulate various intrinsic parameters in order to control phonon transport through bulk medium. As lattice thermal conductivity holds direct proportional to the square of phonon group velocity (v_g), slight change in the sound velocity will have high impact on the phonon transport. Phonon group velocity, which is intrinsic property of each material, is directly proportional to the square root of (f/m) where f and m signify force-constant and mass of the compound of interest, respectively.¹⁰ Materials with weak chemical bonding and heavy constituent elements are ideal for achieving low v_g . Layered materials generally have very weak bonding along stacking direction, which eventually result in low phonon group velocity such in those materials, such as in Bi₂Te₃ ($v_g \sim 1750$ m/S)⁸² and SnSe ($v_g \sim 1420$ m/S)⁶⁰, limiting the lattice thermal conductivity. Further weak interlayer bonding in layered materials also results in soft optical phonons which strongly couple with heat carrying acoustic phonons, such as in natural van der Waals heterostructure, reflecting in their extremely low κ_{lat} . Lattice anharmonicity, renders κ_{lat} to a temperature-dependent finite quantity, plays an important role in manipulating the phonon transport in crystalline solids.⁸³ Strong lattice anharmonicity amplifies phonon–phonon Umklapp scatterings which cause significant reduction in κ_{lat} . Lattice anharmonicity, a measure of deviation of real crystal from ideal harmonic behavior, is quantified by the Grüneisen parameter, defined by¹⁰

$$\gamma(\omega) = - d \ln(\omega) / d \ln(V) \quad (1.12)$$

for a given frequency (ω) of the phonon where V is volume of the system. Relation of κ_{lat} with Grüneisen parameter can be seen from the Slack's model:⁸⁴

$$\kappa_{lat} = B(\bar{M} \theta_D^3 \delta) / \gamma^2 T \quad (1.13)$$

considering that the heat transport is governed by acoustic phonons and three-phonon Umklapp scattering is the dominant scattering mechanism. In the Slack's model of κ_{lat} , B is a numerical coefficient and \bar{M} is the average mass of the basis atoms. The average volume per atom is denoted by δ^3 and θ_D is the acoustic Debye temperature. In general, the materials with complex crystal structure and bonding heterogeneity possess strong lattice anharmonicity. Bonding heterogeneity and consequent lattice anharmonicity are common to most of the layered materials because of their strong in-plane covalent bonding while having weak van der Waals bonding for the out-of-plane direction.

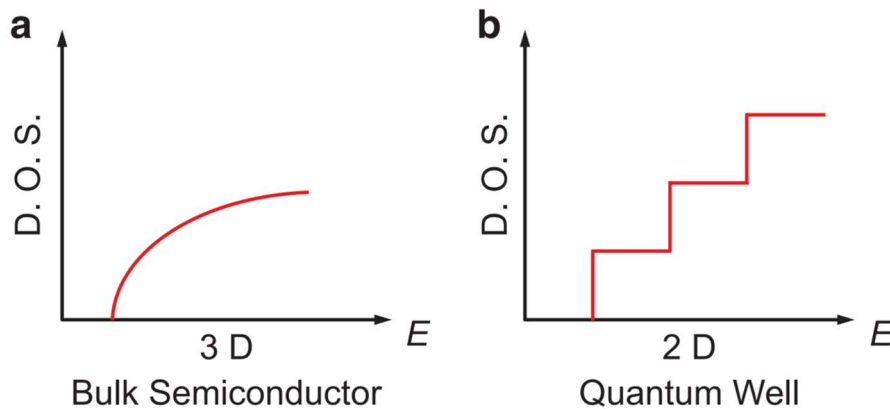


Figure 1.7. Schematic diagram of electronic density of states (DOS) for (a) 3D bulk semiconductor and (b) 2D quantum well.⁷⁷ Reproduced with permission from ref. 77 © 2016 Nature Publishing Group.

For example, SnSe shows average Grüneisen parameter of ~ 3.13 , which is much higher than that of PbTe ($\gamma \sim 1.65$) or PbSe ($\gamma \sim 1.69$),⁶⁰ explaining occurrence of ultra-low κ_{lat} in SnSe. Further, presence of resonant bonding in some of the layered compounds (e.g., Bi₂Te₃, SnSe) with distorted rock-salt-based structures produce soft optical phonons.^{57,60} These compounds unable to form six two-center-two-electron (2c–2e) octahedral bonds due to fewer valence electrons available per atom. However, coordination can be satisfied by forming long-range resonance bonds which result in highly polarizable bonds as well as soft phonons, enhancing anharmonic optical-acoustic scattering. Also, Slack's formula describes the general material's feature to

realize low κ_{lat} which are the presence heavy atomic mass, weak inter-atomic bonding, complex crystal structure and high anharmonicity, and the layered materials with heavy constituent elements possess all these features, in general. As a result of these favorable materials traits, plenty of layered chalcogenides/oxy-chalcogenides exhibit low-lattice thermal conductivity.

1.4.2. Electronic transport in layered materials

Layered materials host atomically thin layers bound by weak vdWs interaction, which can be considered as quasi 2D materials and hence free charge carriers within each layer can experience quantum confinement, like 2D.⁷⁷⁻⁸⁰ Consequently, electronic-DOS of these quasi-2D layered materials exhibits strong anisotropy, deviating from a 3D-bulk material. For instance, DOS in the basal plane can rise sharply, in contrast to smooth change in DOS of 3D materials (Figure 1.7).⁷⁷ If Fermi level of quasi-2D layered materials is tuned within rapidly varying DOS, it can result a large asymmetry between hot carriers ($E > E_F$) and cold ($E < E_F$) carriers, hence more effective transportation of entropy per charge, facilitating higher Seebeck coefficient with minimal effect on electrical conductivity.⁷⁹ Further, tunability of the position of the E_F is easily accessible in 2D-layered materials, than that in bulk materials by intercalating ions or applying an external electric field which can effectively assist in enhancing the thermopower of the system. Moreover, anisotropic crystal structure of layered materials can individually engineer the phonon-transport and electronic-transport by the changing the sizes of dimensionality close to wavelengths of the phonons and/or electrons.⁷⁷⁻⁷⁹

Among various layered materials, I have extensively studied the structural, electronic and thermoelectric properties of three 2D metal chalcogenides namely, (i) tin selenide (SnSe), (ii) gadolinium telluride (GdTe₃), and (iii) bismuth selenide (BiSe) in my Ph.D. thesis. In the following section, I will provide a brief overview of crystal and electronic structure of these compounds and their relevance in the field of thermoelectrics.

1.5. Tin selenide (SnSe): An extraordinary thermoelectric material

The group of tin chalcogenides encompasses a variety of potential thermoelectric materials for example, SnTe, SnSe, SnSe₂ and SnS. This class of metal chalcogenide

could emerge as a potential alternative for the commercially-available bismuth and lead based analogues due to their superior thermoelectric properties arising from the presence of resonant bonding, non-trivial topology and favorable crystal structure.⁸⁵⁻⁸⁷ Among them, recently, SnSe has created sensation as an outstanding thermoelectric material for the mid-temperature range, both as *p*-type^{67,68} and *n*-type^{69,70} thermoelectric material and hence SnSe is being considered as potential alternative to PbTe.⁸⁸

As **part 2, part 3, and part 4** of my thesis deals with the thermoelectric properties of nanocrystalline and polycrystalline SnSe, in this section, I have discussed about the structure-property relationship and recent advances of SnSe in the field of thermoelectrics.

1.5.1. Crystal and electronic structures

At ambient temperature and pressure, SnSe crystallizes in a layered orthorhombic structure (space group *Pnma*). The structure consists of SnSe double layers where Sn and Se atoms are arranged in a criss-cross fashion along the crystallographic *b*-axis (Figure 1.8a).⁶⁸ Within the two-atom thick Sn-Se slabs, there are strong covalent interactions between tin and selenium atoms within the crystallographic *bc* plane, whereas along the *a*-direction Sn and Se are weakly bonded. The structure contains distorted SnSe₇ polyhedra comprising four long, and three short, Sn–Se bonds. The 5s lone pair of Sn²⁺ is sterically located in between these bonds in such a way that results in anharmonicity and anisotropy in the crystal structure (Figure 1.8a).⁶⁸ SnSe possesses a high Grüneisen parameter ($\gamma \sim 3.13$) along the crystallographic *a*-direction (Figure 1.9a)⁶⁸ resulting from the confined movement of the lateral phonons in the layered geometry. This induces a strong lattice anharmonicity in SnSe,⁶⁰ contributing to its low lattice thermal conductivity, $\kappa_{lat} = 0.48 \text{ W m}^{-1} \text{ K}^{-1}$ (Figure 1.8b).⁶⁸ At $\sim 800 \text{ K}$, the lower symmetry *Pnma* structure undergoes a shear or displacive phase transition to the higher symmetry *Cmcm* phase. The volume of the *Pnma* phase is 2.5% higher than that of the *Cmcm* phase. Consequently, during the crystal growth of SnSe, the silica ampoules break easily, and samples can get damaged.

SnSe is a narrow bandgap semiconductor with a highly complex electronic structure. The electronic band structure of SnSe comprises six degenerate valence bands (Figure 1.9b).⁶⁷ The valence band maximum (VBM) in SnSe lies along the Γ -Z direction and the

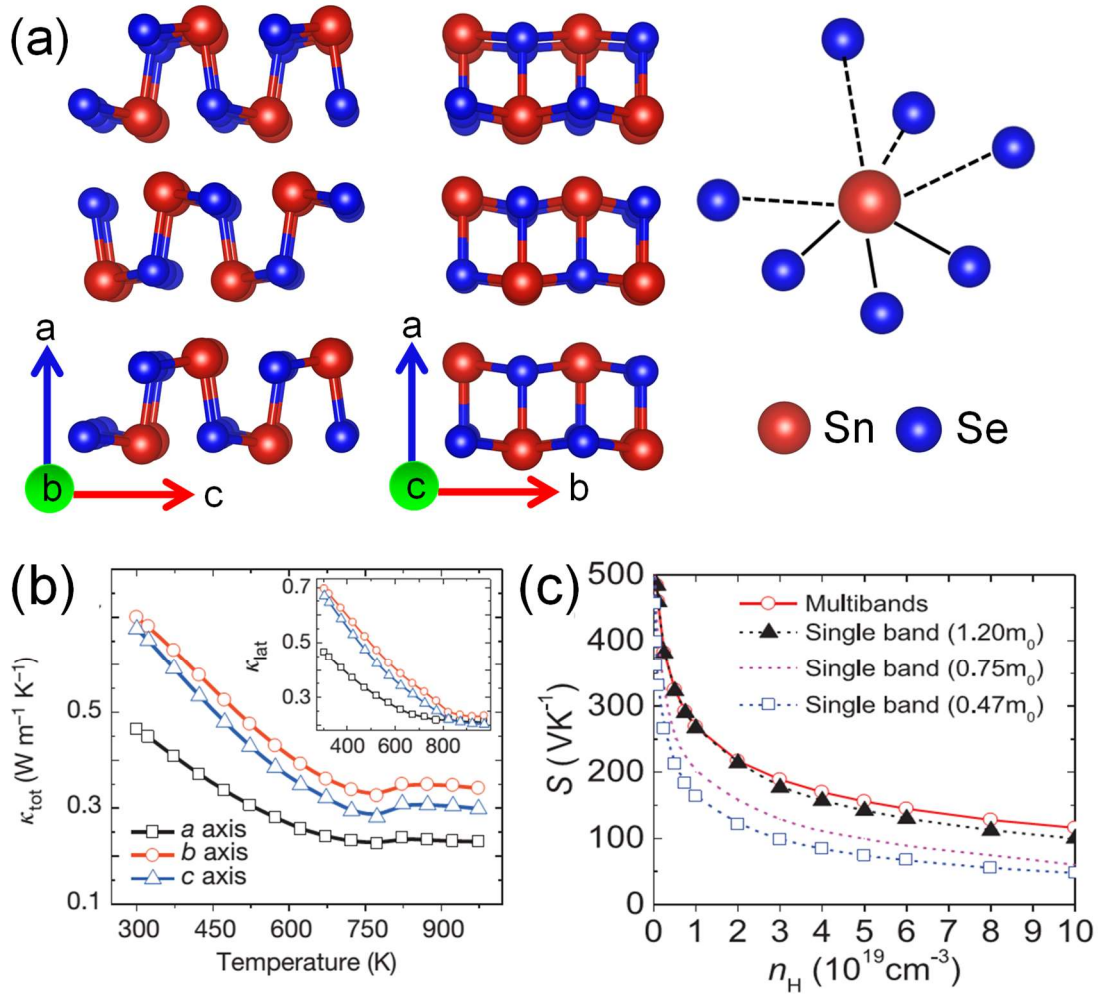


Figure 1.8. (a) Crystal structure of layered SnSe viewed along the crystallographic *b* and *c* directions. The structure consists of SnSe₇ polyhedra containing three short, and four long, Sn-Se bonds. (b) Temperature dependent total and lattice thermal conductivities of SnSe single crystals along different crystallographic directions.⁶⁸ (c) Pisarenko plot for hole-doped SnSe single crystals at 300 K. When calculations are performed based on a single-band model, significant deviations were observed from the experimental results.⁶⁷ (b) is reproduced with the permission from ref. 68 © 2014 Springer Nature. (c) is reproduced with the permission from ref. 67 © 2016 American Association for the Advancement of Science.

second VBM is offset by 0.06 eV from the highest energy band in the same direction.

This small energy offset can be easily achieved by tuning the Fermi level in SnSe by optimizing the hole carrier concentration to $n_H \sim 4 \times 10^{19} \text{ cm}^{-3}$. Moreover, the energy difference ($\Delta E = 0.13 \text{ eV}$) between the first and the third band edges is also very low. Furthermore, even with the hole carrier concentration of $n_H \sim 5 \times 10^{20} \text{ cm}^{-3}$, the

contributions from the 4th, 5th and 6th valence bands of SnSe can be easily achieved due to the shift in the Fermi level. Owing to the highly anisotropic 2D layered structure of SnSe, the effective mass is higher along the out-of-plane k_x direction (a axis) in comparison to the in-plane k_y and k_z directions (b and c axes respectively)⁶⁷ as shown by the DFT calculations. The effective mass of the carriers at the first valence band maximum along the Γ - Z direction are $m_{k_x}^* = 0.76 m_0$, $m_{k_y}^* = 0.33 m_0$, and $m_{k_z}^* = 0.14 m_0$. Due to the accessibility of multiple valence band and conduction band extrema as suggested by the complex electronic band structure, SnSe single crystals possess correspondingly high Seebeck coefficients (Figure 1.8c)⁸⁸. The improvement in the power factor originates from the additional contributions of the conductivity weighted Seebeck coefficient. Furthermore, the multiple Fermi-surface pocket electron/hole states are easily accessible in SnSe through carrier concentration enhancement, which leads to an enhanced Seebeck coefficient and power factor in an eco-friendly Pb-free 2D layered chalcogenide.⁶⁸

1.5.2. Electrical transport properties

p -type single crystals of pristine SnSe possess a low carrier concentration of $n_H \approx 10^{17} \text{ cm}^{-3}$ at room temperature, which can be tuned through hole doping. The poor carrier concentration of SnSe, results in a low electrical conductivity at ambient temperature and similar $\sigma(T)$ behaviour is observed along each of the crystallographic directions. An upturn in the electrical conductivity at ca. 525 K may be attributed to the thermal excitation of minority carriers in the pristine SnSe single crystals.⁶⁸ With Na doping in SnSe, the room temperature electrical conductivity can be improved from 12 S cm^{-1} to 1500 S cm^{-1} , due to an increase in carrier concentration ($n_H \sim 10^{19} \text{ cm}^{-3}$).⁶⁷ It should also be mentioned that with the heavy hole doping in SnSe single crystals, the semiconducting transport changes to metallic type behaviour. The Seebeck coefficient for the un-doped SnSe single crystals also shows a directionally independent, highly isotropic behaviour. The decrease of the Seebeck coefficients above 525 K is expected from the electrical conductivity behaviour and it occurs due to the presence of bipolar conduction, which can be attributed to the narrowing of the bandgap (E_g) during the phase transition from $Pnma$ ($E_g = 0.61 \text{ eV}$) to $Cmcm$ ($E_g = 0.39 \text{ eV}$).

On hole doping, the Fermi level can be tuned to access the heavy hole valence bands

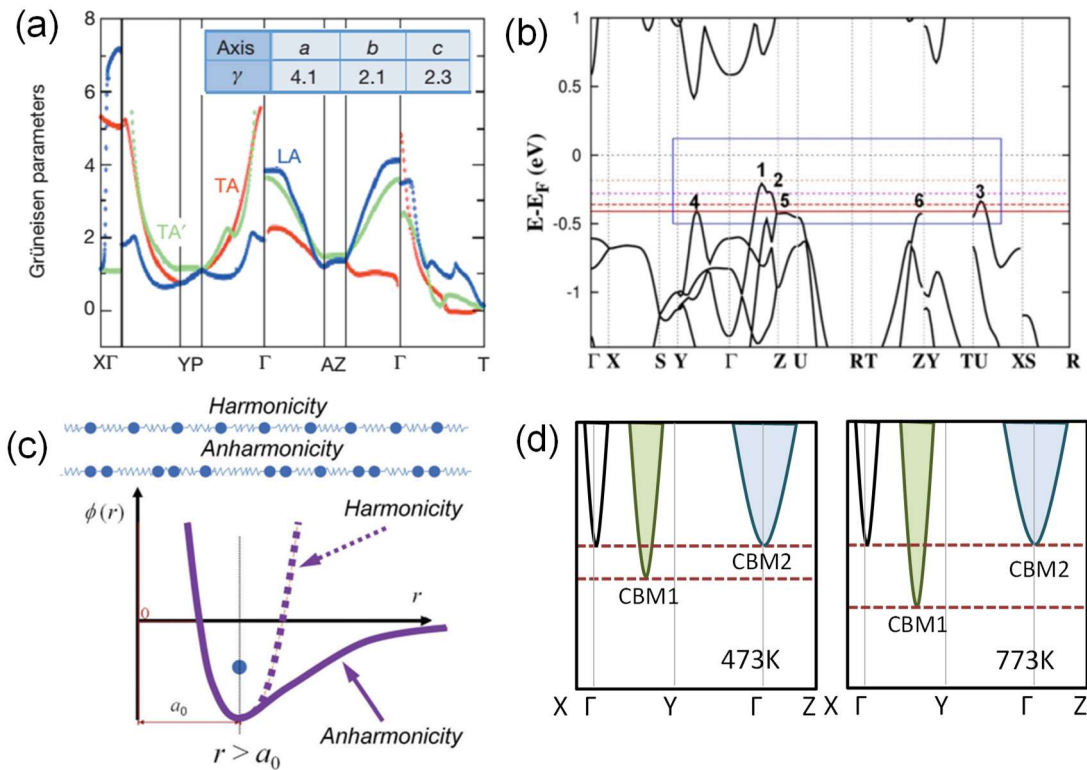


Figure 1.9. (a) Grüneisen parameters of SnSe single crystals along the a , b and c crystallographic directions (TA, TA' and LA denotes transverse-acoustic and longitudinal-acoustic phonon scattering branches respectively).⁶⁸ (b) Electronic band structure of hole-doped SnSe single crystals. The red dotted lines represent the Fermi levels for different carrier concentrations.⁶⁷ (c) Schematic representations of harmonicity and anharmonicity where $\phi(r)$, a_0 and r are the potential energy, lattice parameter and distance between two adjacent atoms, respectively.⁸⁸ (d) Electronic band structures of Br-doped n-type SnSe at 473 and 773 K.⁶⁹ (a) is reproduced with the permission from ref. 68 © 2014 Springer Nature. (b) is reproduced with the permission from ref. 67 © 2016 American Association for the Advancement of Science. Figure (c) is reproduced with the permission from ref. 88 © 2016 Royal Society of Chemistry. (d) is reproduced with the permission from ref. 69 © 2018 American Association for the Advancement of Science.

in SnSe and, due to the contribution of the multiple valence bands (Figure 1.8c), there is a substantial enhancement in the Seebeck coefficient. In a similar fashion, single crystals of pristine SnSe exhibit a low power factor at room temperature owing to the poor electrical conductivity. However, with the incorporation of p -type dopants, the power factor increases significantly to $S^2\sigma = 40 \mu\text{W cm}^{-1} \text{K}^{-2}$ at 300 K, along the crystallographic b -direction.⁶⁷ The key reason for the high Seebeck coefficient and

power factor is the near degeneracy of the valence bands in SnSe at room temperature. The multi-valley transport mechanism in hole-doped SnSe is supported by Hall measurements and validated by DFT calculations.⁶⁷ Thus, the high power factor attained by the hole-doped SnSe single crystals exceeds the thermoelectric performance of the hierarchically-architected *p*-type PbTe–SrTe⁴² framework making it a prospective candidate for the future energy management applications.

1.5.3. Anharmonicity and ultralow thermal conductivity

Single crystals of SnSe exhibit very low total thermal conductivities of $\kappa_{total} = 0.46$, 0.70 and 0.68 W m⁻¹ K⁻¹ along the crystallographic *a*, *b* and *c* directions, respectively (Figure 1.8b).⁶⁸ Apart from the anisotropic 2D layered structure, the stereochemically-active 5s² lone pair of Sn²⁺ plays an active role in introducing a high degree of anharmonicity and strong phonon scattering into the crystal structure of SnSe (Figure 1.8a). Although, all real materials exhibit anharmonic bonding, generally those with significantly high anharmonicity gives rise to low thermal conductivity. In a typical potential well, the energy of an atom is directly proportional to its displacement from the equilibrium position and the proportionality constant is termed the spring constant of the material and is a measure of stiffness in the system. In an anharmonic case, the spring constant changes with the movement of the atom from its equilibrium position. This has significant consequences when two phonons collide with each other (Figure 1.9c),⁸⁸ as the first phonon alters the spring constant of the second phonon, thereby changing the elastic properties of the system. Thus, high anharmonicity results in improved phonon–phonon scattering in SnSe and consequently decreases its lattice thermal conductivity. In a typical crystal structure, the Grüneisen parameter (γ) reflects the extent of anharmonicity in the material. Single crystals of SnSe possess a high Grüneisen parameter of $\gamma \sim 3.13$, along the crystallographic *a*-axis, a value which is quite large in comparison to that of PbTe ($\gamma = 1.45$) or AgSbTe₂ ($\gamma = 2.05$) based systems. The origin of the anomalous Grüneisen parameter in SnSe lies in the existence of dynamic resonance bonding states due to the presence of the stereochemically active 5s² lone pair of Sn in SnSe₇ polyhedra.^{68,88} Thus, the soft malleable coordination environment of Sn and Se atoms gives rise to anharmonicity and an ultra-low lattice thermal conductivity in SnSe.

1.5.4. SnSe single crystals

In 2014, the extraordinarily high figure of merit of $zT = 2.6$ at 923 K along the b -direction (Figure 1.10a) in SnSe single crystals, created a sensation in the thermoelectric community.⁶⁸ However the electrical conductivity lies in the lower range due to the relatively low carrier concentration ($n_H \sim 10^{17} \text{ cm}^{-3}$).⁶⁸ By doping Na and Ag atoms into single crystals of SnSe, multiple valence bands become accessible due to the lowering of Fermi level. The flattening of valence band edges, and enlargement of the number of carrier pockets take place concurrently.⁸⁹ Because of the existence of multiple valence bands, hole doped SnSe possesses a relatively high Seebeck coefficient,⁶⁷ consistent with a detailed investigation of the Pisarenko plots. At the same time, Na doping can increase the mass defect and size defect scattering of phonons giving rise to a reduced lattice thermal conductivity and yielding a high figure of merit over an extended temperature range in the hole-doped SnSe single crystals.⁸⁹ Zhao *et al.* reported significant changes in the p -type SnSe single crystals upon Te alloying.⁹⁰ Incorporation of Te atoms improves the carrier mobility through the synergistic modulation of crystal and band structures, thus increasing the Seebeck coefficient by multiple valence band activation. Tellurium also facilitates the formation of Sn vacancies which boosts the hole carrier concentration of the system. In addition, it plays a crucial role in reducing the lattice thermal conductivity by increasing the amplitude of local displacements of Sn atoms within the crystal structure. This which gives rise to a remarkably high figure of merit, $zT = 2.1$ at 793 K, along the crystallographic b -direction in single crystals of $\text{Na}_{0.02}\text{Sn}_{0.98}\text{Se}_{0.98}\text{Te}_{0.02}$ (Figure 1.10a). Another interesting approach to enhance the thermoelectric performance of SnSe single crystals has recently been discovered by Zhao *et al.*, by utilizing the concept of SnSe₂-induced defect engineering (Figure 1.10b).⁹¹ Extrinsic SnSe₂ induces Sn vacancies in the SnSe single crystals, thus increasing the hole carrier concentration of the system and improving the Seebeck coefficient by activating multiple valence bands near E_F . In addition, the SnSe₂ microdomains effectively take part in phonon scattering that reduces the lattice thermal conductivity of the system. Due to the synergistic modulation of both the electrical and phonon transport properties, a high average figure of merit, $(zT)_{\text{avg}} > 1.7$, could be achieved in single crystals of SnSe-2%SnSe₂.

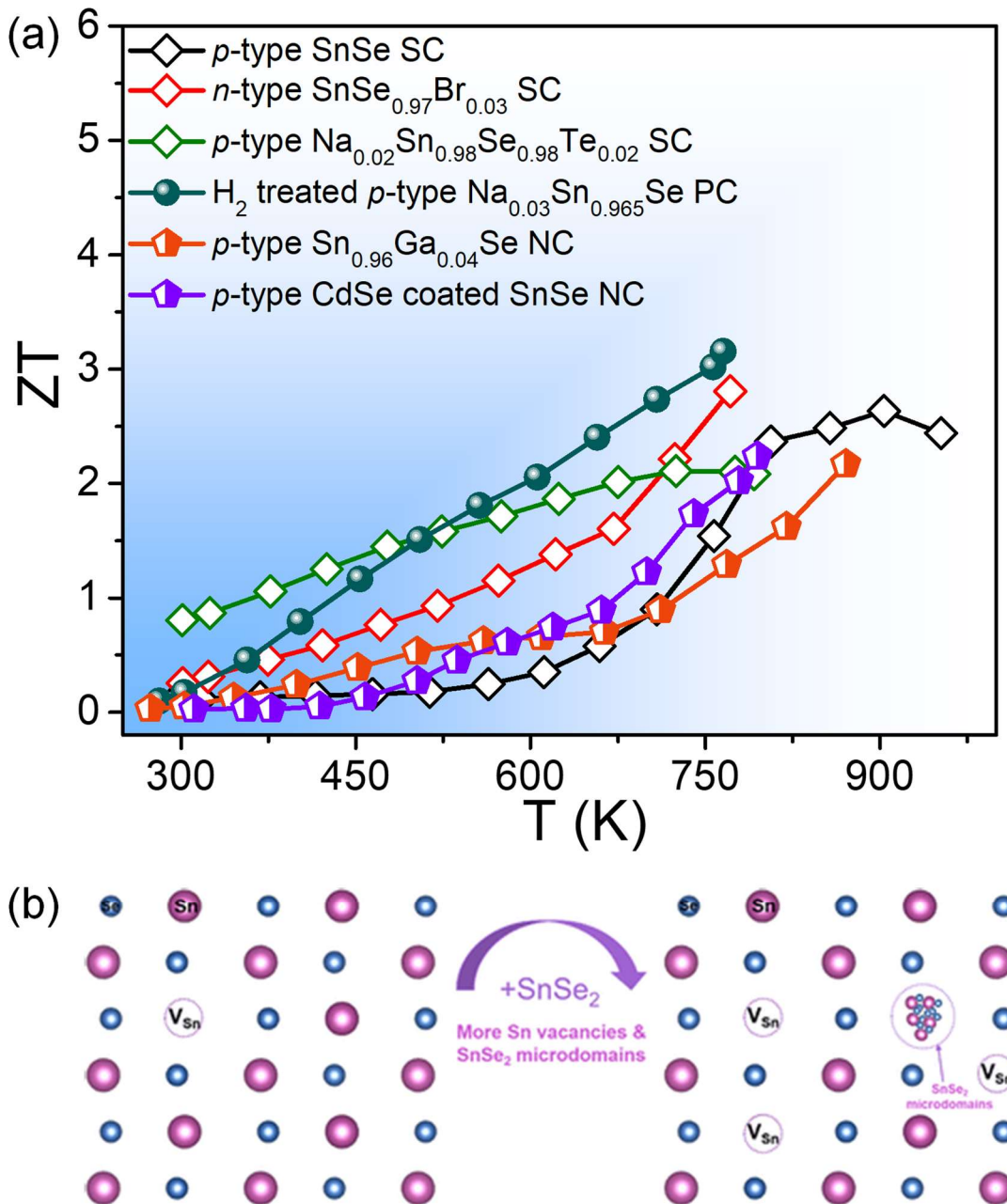


Figure 1.10. (a) Comparative study of thermoelectric figure of merit of various SnSe samples (where SC, PC and NC denote single crystals, polycrystals and nanocrystals respectively).^{68,69,90,92–94} (b) Schematic representation of the presence of extrinsic SnSe_2 microdomains in SnSe single crystals.⁹¹ (b) is reproduced with the permission from ref. 91 © 2020 American Chemical Society.

Single crystals of SnSe are intrinsically p -type in nature, but in recent years research into its n -type analogues has also produced promising results. In 2016, Duong *et al.* reported n -type thermoelectric behaviour in Bi-substituted single crystals of SnSe for

the first time.⁷⁰ Increasing the *n*-type carrier concentration to $n_H = 2.1 \times 10^{19} \text{ cm}^{-3}$, a figure of merit of $zT = 2.2$ could be achieved at 733 K, along the crystallographic *b*-direction in $\text{Sn}_{0.94}\text{Bi}_{0.06}\text{Se}$ single crystals. Zhao *et al.* reported the 3D charge and 2D phonon-transport in the Br-doped *n*-type single crystals of SnSe with an exceptionally high out-of-plane figure of merit, $zT = 2.8$ at 773 K⁶⁹ (Figure 1.10a). The low lattice thermal conductivity along the *a*-direction is generally associated with strong interlayer phonon scattering. Furthermore, this 2D phonon transport, when accompanied by 3D electronic transport gives rise to a substantially higher electrical conductivity in the same direction, resulting from the overlapping of the interlayer charge density. Also, a continuous structural phase transition from *Pnma* to *Cmcm* imparts higher symmetry in Br-doped SnSe followed by conduction band divergence (Figure 1.9d), which reduces the average inertial band mass as well as increasing the carrier mobility. These two factors simultaneously give rise to such an ultrahigh figure of merit in *n*-type Br-doped SnSe single crystals.

1.5.5. Polycrystals and nanostructures of SnSe

The eco-friendly layered chalcogenide, SnSe has been one of the key areas of research in thermoelectrics over recent years, due to the unique structural and bonding characteristics. However, there are still some major drawbacks to the material, such as fragility and a difficult synthesis procedure, which make SnSe single crystals unsuitable for commercialization. It implies the necessity for research on poly/nanocrystalline SnSe, as a suitable alternative to single crystals. Numerous research works have been performed on *p*- and *n*-type poly/nanocrystalline SnSe. Polycrystalline, hole-doped (Na, K, Ag)^{95–98} SnSe has shown a maximum figure of merit of $zT = 1$ at high temperatures (parallel, || to the SPS pressing direction) due to the activation of multiple valence bands by tuning the carrier concentration near the Fermi level. Potassium doping also facilitates coherent nanostructure formation that scatters phonons effectively.⁹⁶ Therefore, in SnSe polycrystals, Na doping tends to augment the electrical transport while K-doping can be selected to reduce the lattice thermal conductivity.⁹⁷ Similar to SnSe single crystals, PbSe alloying in polycrystalline SnSe along with Na co-doping gives rise to a remarkably high figure of merit of $zT = 1.2$ at 773 K.⁹⁹ Na-Ag co-doping in SnSe improves the carrier concentration with valence band convergence, which synergistically increases both the electrical conductivity and Seebeck coefficient in

SnSe polycrystals.¹⁰⁰ Moreover, the presence of Ag₈SnSe₆ nanostructures brings about *ca.* 20% decrease in lattice thermal conductivity and results in a figure of merit of $zT = 1.33$ at 773 K in Ag₈SnSe₆ nanostructured and 1 mol% Na doped SnSe, when measured in the direction parallel to SPS pressing.

Applying similar strategies, an ultralow lattice thermal conductivity of $0.11 \text{ W m}^{-1} \text{ K}^{-1}$ and correspondingly high figure of merit, $zT = 1.67$ at 823 K, were attained for polycrystalline Ag_{0.01}Sn_{0.99}Se_{0.85}S_{0.15}.¹⁰¹ Kanatzidis *et al.* has reported a peak $zT = 1.14$ at 723 K in a 1:1 alloy of SnSe-AgSbSe₂ that crystallizes in a cation-disordered cubic rocksalt-type lattice.¹⁰² AgSnSbSe₃ exhibits an intrinsically low lattice thermal conductivity of $0.47 \text{ W m}^{-1} \text{ K}^{-1}$ at 673 K, mainly due to the presence of a high degree of cation disorder and low-frequency optical phonon modes. Te-substitution on the Se sublattice promotes valence band convergence due to the enhancement in carrier concentration and decreases lattice thermal conductivity to $0.32 \text{ W m}^{-1} \text{ K}^{-1}$ at 723 K, due to increased phonon scattering resulting from the randomly distributed cations and anions, lattice dislocations, and point defects. Combining the results of all these effects, a high-power factor of $9.54 \mu\text{W cm}^{-1} \text{ K}^{-2}$ and a moderately high figure of merit, $zT = 1.14$ at 723 K have been achieved in polycrystalline AgSnSbSe_{1.5}Te_{1.5}.

Experimentally, it has been generally found that nanocrystalline SnSe synthesized by low temperature solvothermal routes possesses a much lower lattice thermal conductivity. The possible reasons include the presence of a greater extent of nano-scale precipitates and mesoscale grain-boundaries that contribute to significant phonon scattering.^{103–105} Phase-separated nanocrystalline Sn_{0.99}Pb_{0.01}Se is one of the well-established examples, that has $zT = 1.7$ at 873 K.¹⁰³ Incorporation of Zn in the same crystal structure enhances the carrier concentration, thereby improving the electrical transport properties.¹⁰⁶ Thus co-doping of Zn and Pb in this system is expected to synergistically optimize the electrical as well as thermal properties of nanocrystalline SnSe. This was realized when a high figure of merit, $zT = 2.2$ was reported at 873K in the Sn_{0.98}Pb_{0.01}Zn_{0.01}Se sample. Similarly, $zT = 2.1$ was achieved by Tang *et al.* in SnSe nanocrystals by synergistically optimizing both the thermal and electrical transport properties through the introduction of Sn vacancies.¹⁰⁴ Very recently, in a study by Ibáñez and co-workers have embraced a simple and cost-effective solution-based synthesis of CdSe coated SnSe nanostructures for high performance thermoelectric

applications.⁹⁴ Incorporation of CdSe nanoparticles inhibits the grain growth of SnSe during consolidation which results in high density of nanoscale grain boundaries. It also creates multiscale defects such as planar defects, point defects, nanoprecipitates, and dislocations in the system (Figure 1.11a-c).

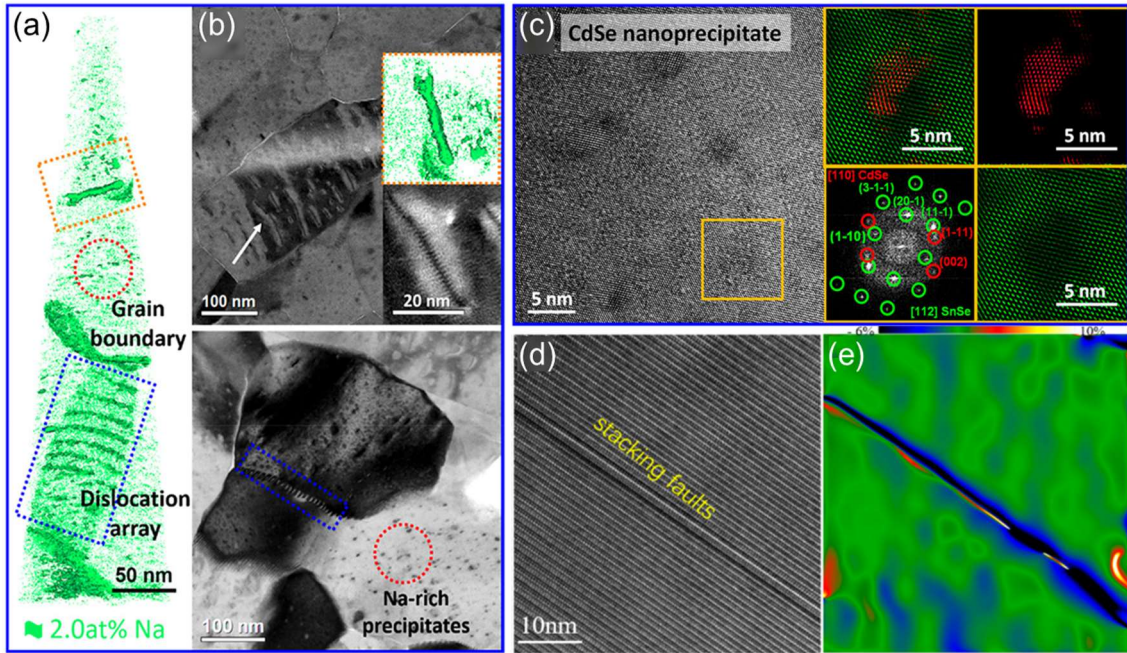


Figure 1.11. (a) APT characterization and (b) TEM images of SnSe-3%CdSe nanocomposites. The areas highlighted with red, blue, and orange boxes represent the 3D distribution of Na, dislocation arrays and grain boundaries (GB), respectively. (c) HRTEM image showing the distribution of CdSe nanoparticles (NP) in SnSe matrix. The power spectrum analysis has been carried out on the region highlighted in yellow which shows the phase filtered images of CdSe NP (red) and the SnSe matrix (green) along with the corresponding ED pattern.⁹⁴ (d) Low magnification TEM image of $\text{Sn}_{0.96}\text{Ga}_{0.04}\text{Se}$ nanocrystals showing the presence stacking faults. (e) The strain mapping corresponding to the stacking faults.⁹³ (a)-(c) are reproduced with permission from ref. 94. © 2022, American Chemical Society. Figure (d)-(e) are reproduced with permission from ref. 93. © 2021, American Chemical Society.

Due to the presence of large number of multiscale defects, an ultra-low κ_{lat} of $0.14 \text{ W m}^{-1} \text{ K}^{-1}$ has been achieved in SnSe-3%CdSe nanocomposite owing to enhanced phonon scattering. In addition, the grain boundaries also act as an energy barrier for holes which boosts the Seebeck coefficient through carrier-energy filtering effects. Thus, due to the synergistic effect of improved Seebeck-coefficient and decreased lattice thermal

conductivity, a significantly high zT of ~ 2.2 at 786 K has been obtained in surface-engineered nanocrystalline SnSe-3%CdSe⁹⁴ (Figure 1.10a). Recently, Lou *et al.* have adopted an innovative approach to modulate the κ_{lat} in nanocrystalline SnSe by introducing lattice strain upon Ga doping.⁹³ To understand the mechanism behind this lattice strain, they have extensively studied the microstructural analysis of Ga doped SnSe via transmission electron microscopy (TEM). Several lattice dislocations, stacking faults and nanoprecipitates of GaSe have been observed in the matrix of SnSe as evident from Figure 1.11d-e. All these defects effectively reduce the phonon relaxation time and hence decrease the κ_{lat} to $0.17 \text{ W m}^{-1} \text{ K}^{-1}$ at 873 K. Furthermore, Ga creates a resonance level and induces band-convergence promoting the Seebeck coefficient and power factor. Consequently, a peak zT of ~ 2.2 at 873 K (Figure 1.10a) has been achieved in solution-processed nanocrystalline SnSe and the corresponding thermoelectric energy conversion efficiency is calculated to be 12.4%.⁹³ In a similar study by Shi *et al.* have also shown that incorporation of InSe_y nanoprecipitates in solvothermally fabricated nanocrystalline SnSe reduced the κ_{lat} to $0.24 \text{ W m}^{-1} \text{ K}^{-1}$ which leads to a high zT of 1.7 ± 0.2 at 823 K.¹⁰⁷

Upon doping with BiCl₃,¹⁰⁸ ReCl₂,¹⁰⁹ Br,¹¹⁰ or Sb¹¹¹ nano/polycrystalline SnSe displays favourable n -type thermoelectric features. Ren *et al.* have shown a moderate figure of merit ($zT = 1$ at $\sim 773 \text{ K}$) along the direction perpendicular to the SPS pressing, in iodine and sulfur co-doped n -type polycrystalline material.¹¹² Jiang *et al.* have reported high $zT = 1.22$ in NbCl₅-doped n -type SnSe_{0.95} polycrystals.¹¹³

1.5.6. Removal of surface oxides in polycrystalline SnSe

Numerous chemical and synthetic approaches have been applied in the case of nano/polycrystalline SnSe materials in an effort to modify their thermoelectric properties. Unfortunately, the figure of merit does not reach that of the single crystals of SnSe. Nanocrystalline and polycrystalline SnSe samples are very susceptible to surface oxidation. The charge carriers are involved in interfacial and surface scattering, leading to a reduced carrier mobility, poor electrical conductivity and higher thermal conductivity. Thus the figure of merit of pristine SnSe polycrystals remains below unity even at high temperatures.¹⁰⁵ Lee *et al.* demonstrated removal of tin oxide impurities, by heating the samples under a continuous flow of a 4% H₂/Ar gas mixture at 613 K.¹¹⁴ After the reduction treatment, the polycrystalline SnSe samples showed a significantly

lower lattice thermal conductivity of $\kappa_{lat} = 0.11 \text{ W m}^{-1} \text{ K}^{-1}$. This value is lower even than that of SnSe single crystals, and leads to $zT = 2.5$ for 1.5% Na-doped and 5% PbSe alloyed polycrystalline SnSe at 773 K, measured along the direction parallel to the SPS pressing.¹¹⁴ In a similar fashion, Zhou *et al.* have also reported an ultralow κ_{lat} ($\sim 0.07 \text{ W m}^{-1} \text{ K}^{-1}$ at 783 K) and astonishingly high zT of ~ 3.1 at 783 K in highly purified, tin oxides (SnO_x) removed and spark plasma sintered (SPS) polycrystalline $\text{Na}_{0.03}\text{Sn}_{0.965}\text{Se}$ (Figure 1.10a).⁹² These experimental observations have shed light on the physical and chemical properties of SnSe, which will continue to motivate researchers in the exploration of 2D thermoelectric materials.

1.6. Gadolinium telluride (GdTe_3): A charge density wave (CDW) material

vdW materials having 2D layered crystal structure are actively studied for novel twistrionic or spintronic applications.¹¹⁵ This class of compounds are found to exhibit low lattice thermal conductivity due to the presence of bonding heterogeneity and strong lattice anharmonicity. Recently, it has been shown that the strong electron-phonon coupling (EPC) can effectively reduce the lattice thermal conductivity of a material when the carrier concentration is above 10^{19} cm^{-3} .¹¹⁶ In addition to this, ultralow κ_{lat} has been observed in disordered thin films of 2D layered WSe_2 .¹¹⁷ Realizing the idea of layered disordered crystal structure, as well as strong electron phonon coupling, charge density wave (CDW) materials can be a good candidate for low lattice thermal conductivity as they have layered structure where strong EPC breaks the translation symmetry of the lattice and induces lattice distortion into the system. Among several CDW materials, rare earth tellurides with general formula RTe_3 (R = rare earth element and Te = tellurium) have gained enormous attention in the field of chemistry and condensed matter physics due their structural diversity,¹¹⁸ exotic magnetic properties¹¹⁹ and pressure induced superconductivity.¹²⁰ However, thermoelectric properties of RTe_3 systems have not been studied yet.

As a part of my thesis (**part 5**) deals with the origin of low lattice thermal conductivity and thermoelectric properties of a CDW material, GdTe_3 , in this section, I have given a general introduction to CDW and its correlation with thermoelectrics and provided a brief discussion on the crystal and electronic structure of RTe_3 .

1.6.1. An introduction to CDW

The phrase charge density wave (CDW) was first used by Fröhlich but originates from Peierls description of a fundamental instability in a one-dimensional (1D) chain of atoms equally spaced by a lattice constant, a .^{121,122} Figure 1.12a shows the free electron band of such a 1D chain with one electron per atomic site.

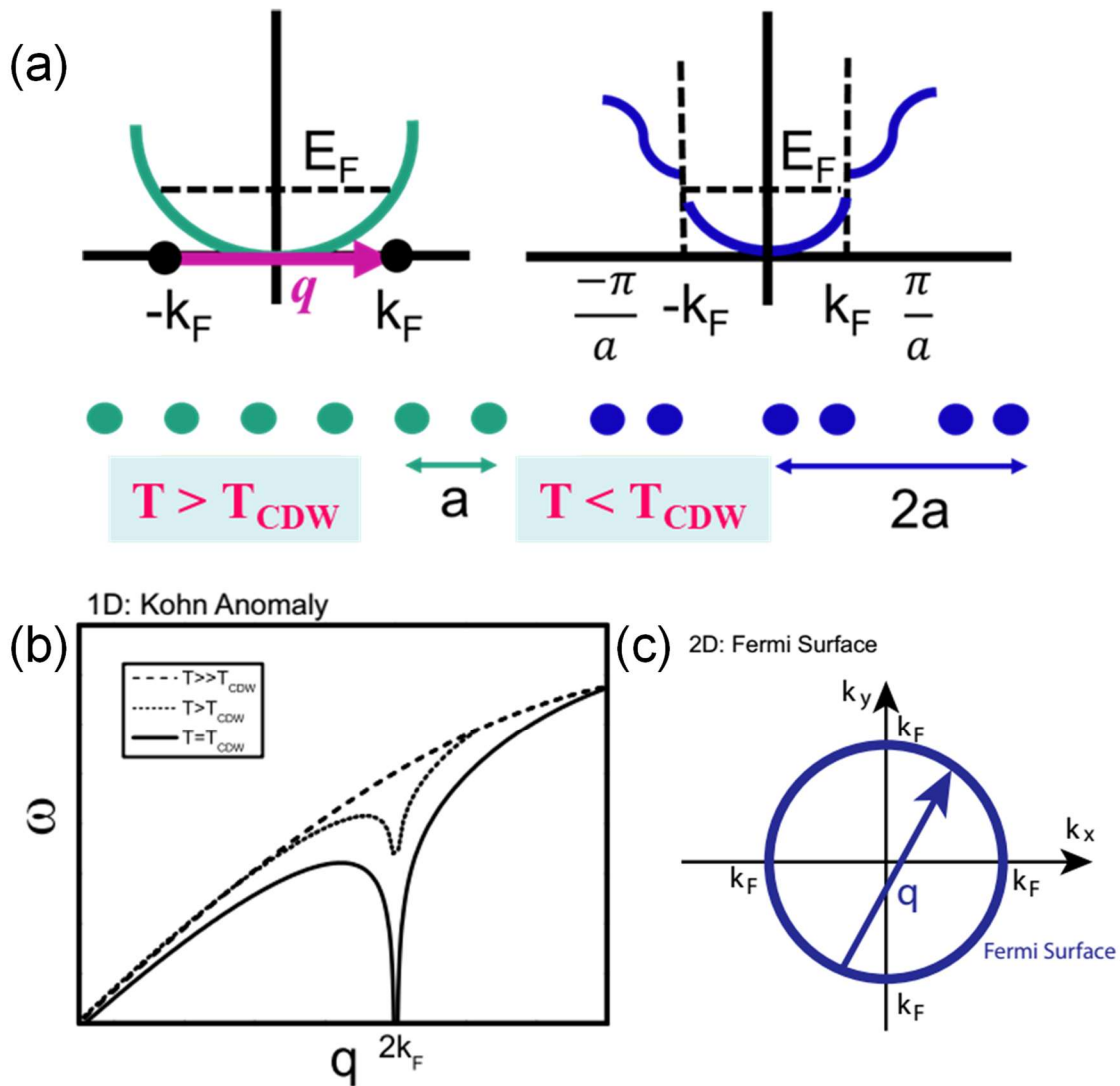


Figure 1.12. (a) The plot of the one-dimensional free electron band structure for a chain of atoms with separation " a " and one electron per atom site before and after the CDW transition. The location of the Fermi energy is indicated with the nesting vector q . (b) Kohn anomaly in the acoustic phonon branch as a function of temperature, which results from Fermi surface nesting. (c) The Fermi contour of a 2D free electron system.¹²³ (b) and (c) are reproduced with permission from ref. 123 © 2015 National Academy of Sciences.

The Fermi points are at $k_F = \pm\pi/2a$ and are connected by the nesting vector $q = 2k_F$. In 1930 Peierls asserted that this system is unstable, showing an electronic disturbance with the wave vector $2k_F$, changing the periodicity of the chain, and opening up a gap at the zone boundary ($k = \pi/2a$) of the new unit cell containing two atoms (Figure 1.12a). The conjecture was that the gain in electronic energy would always overwhelm the cost of restructuring the atoms. Consequently, in the Peierls model there would be a transition from the metallic high-temperature state to the insulating-dimerized ground state at a critical temperature T_{CDW} . Kohn pointed out that there is an image of the Fermi surface in the vibrational spectrum, because the zero energy electronic excitations at $2k_F$ will effectively screen any lattice motion with this wave vector.¹²³ Figure 1.12b shows the phonon dispersion for this 1D chain at different temperatures. Below T_{CDW} the phonon energy at $q = 2k_F$ becomes imaginary, meaning there is a new lattice structure. Above T_{CDW} there is a sharp dip (Kohn anomaly) in the phonon dispersion but no static restructuring. Thus, CDWs would exist in an ideal 1D chain of atoms, lowering the energy of the system and driving a reconstruction of the lattice which results in a simultaneous softening of coherent lattice vibrations (phonon softening). CDW is a Fermi-surface driven phenomenon.¹²⁴ The extension of this concept to reduced dimensional systems has led to the concept of Fermi surface nesting (FSN), dictated by the wave vector (q) and the corresponding lattice distortion. Figure 1.12c displays the free-electron Fermi contour in 2D connected by wave vector (q) resulting in the effective screening of phonons which induces Kohn anomalies at q_{CDW} .¹²³

1.6.2. CDW in the context of thermoelectrics

Till date, most of the CDW materials are explored in the context of superconductivity,^{115,125} whereas they are rarely studied in the field of thermoelectrics. It is well-known that in the vicinity of CDW formation, the electron–phonon coupling breaks the translational symmetry of the lattices and creates a structural perturbation which gives rise to reduced lattice thermal conductivity in these CDW materials making them a suitable candidate for thermoelectric applications.

For example, recently, exceptional thermoelectric properties have been observed in In_4Se_3 due to the presence of Peierls distortion. In_4Se_3 crystallizes in layered orthorhombic structure and comprises of anionic $[\text{In}_3\text{Se}_3]^-$ layers stacked along the crystallographic a -direction and extended along the b - c plane forming a two

dimensional sheet.¹²⁶ In^+ cations sit between the $[\text{In}_3\text{Se}_3]^-$ layers weakly connecting the anionic layers along the crystallographic a -direction. The two-dimensional sheet also features five membered In-Se rings, which comprises three zigzags In/Se chains running along the crystallographic c -direction. These quasi-one-dimensional In/Se chains are believed to undergoes Peierls distortion due to the inherent instability of a periodic arrangement. This distortion in atomic arrangement further leads to the appearance of a charge density wave (CDW) due to fluctuations in electron density, and consequently, a strong electron-phonon coupling builds up in the system.¹²⁷ This strong electron-phonon coupling causes a rapid increase in phonon scattering and a consequent ultralow thermal conductivity. As a result, high $zT \sim 1.48$ was achieved at 705 K in the b - c plane in Se deficient $\text{In}_4\text{Se}_{3.8}$ single crystals.⁷⁵ Interestingly, another CDW material, TiSe_2 , also shows minimum thermal conductivity of $1.5 \text{ W m}^{-1}\cdot\text{K}^{-1}$ at 300 K which in turn resulted in a moderately high zT value of 0.14.¹²⁸ Thus, the inherent strong anharmonicity due to the layered structure, manifestation of quantum effects in transport properties and discretized electronic density of states makes these CDW materials an attractive playground to enhanced thermoelectric performance.

1.6.3. Crystal and electronic structures of RTe_3 ($\text{R} = \text{rare earth}$)

In the undistorted phase, RTe_3 crystallizes in a quasi-2D layered orthorhombic structure with the space group $Cmcm$ (No. 63).¹¹⁵ The structure is formed by double Te square-net sheets (perpendicular to the c axis), separated by double-corrugated RTe slabs, as illustrated in Figure 1.13a. Thus, it can be mechanically exfoliated into flakes due to the weak vdW binding between two neighbouring Te sheets, and its cleaved surface is parallel to the ab plane. RTe_3 consists of a 3D and a 2D BZ in the reciprocal space, as shown in Figure 1.13b.¹²⁵ The 3D BZ is produced by the stacking of puckered GdTe slabs, and the 2D BZ is built based on Te square-net sheets. The 3D BZ is reduced by half and rotated by 45° from the 2D one. The in-plane p_x and p_y orbitals of Te atoms from square nets dominate electronic states near E_F . Three electrons are donated per R ion in RTe_3 , two of these denoted electrons fill the Te $5p$ bands of the RTe slabs, while one electron transfers to the Te square-net sheets. This results in the RTe slabs being insulating and the Te square-net sheets being conductive for these $5p$ bands which are half filled. As a whole 3D crystal, the charge density from the underlying RTe layers indeed impinges upon Te square-net planes, serving as a commensurate potential that

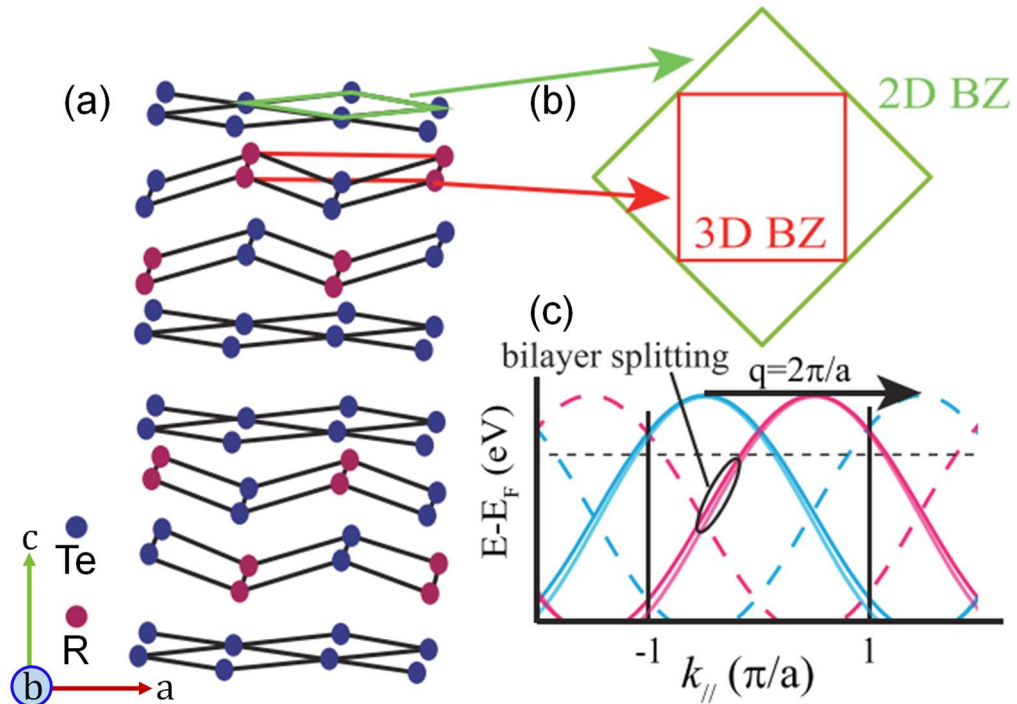


Figure 1.13. (a) Crystal structure of $R\text{Te}_3$ viewed along b -axis. (b) Sketch of 3D BZ and 2D BZ, which result from the 3D unit cell and the Te square-net sheet, respectively. (c) A schematic to visualize the dispersion for folded band and bilayer splitting.¹²⁵ Reproduced with permission from ref. 125 © 2020 American Physical Society.

scatters the electrons therein, as sketched in Figure 1.13c, suggesting a sizable coupling between the Te square-net and the R-Te magnetic slab.¹²⁵ Thus, motivated by these exotic structural features, we have done a detailed study on the thermoelectric properties of GdTe_3 .

1.7. Bismuth selenide (BiSe): A topological quantum material (TQM)

Layered binary bismuth and antimony chalcogenides (tetradymite compounds) such as Bi_2Se_3 , Bi_2Te_3 and Sb_2Te_3 are the widely studied compounds as 3D strong topological insulators (TIs) because of several enviable properties.^{66,129–131} Recently, BiSe which belongs to the same homologous series $(\text{Bi})_m(\text{Bi}_2\text{Se}_3)_n$ ¹³² as that of Bi_2Se_3 , have emerged as a weak topological insulators¹³³ and a promising n -type thermoelectric material.¹³⁴

As a part of my thesis (**part 6**) deals with the application of hydrostatic pressure on an intriguing topological quantum material (TQM), BiSe, which is a weak topological insulator, in this section, I have provided a general introduction to TQMs, pressure

induced electronic topological transitions in TQMs, and discussed about the crystal and electronic structure of BiSe.

1.7.1. An introduction to topological quantum materials

Topological quantum materials (*e.g.*, topological insulators [TI], topological crystalline insulators [TCI] and topological semimetals), characterized by their nontrivial electronic surface states, have created a sensation in designing new thermoelectric materials.^{66,86,135–138} Many TQM such as Bi₂Te₃ (TI), Bi₂Se₃ (TI), SnTe (TCI) have been established as potential thermoelectric materials. Underlying reason for TQM being a source of potential candidates for thermoelectrics is ascribed to the fact that both TQM and TE materials demand similar material features such as the presence of heavy constituent elements, narrow band gap and strong spin-orbit coupling. The robust surface states with linearly dispersed Dirac cones lead to high mobility across the surface of topological materials. Fascinating electronic transport properties of TQM originates from the presence of metallic surface states, which offers high carrier mobility and makes them potential candidates for TE applications also. Interestingly, band inversion in TQM generates many local extrema in the valence or conduction bands during the electronic topological transition, resulting in large DOS and asymmetry near the Fermi level which additionally helps to improve σ and S values. Moreover, TQM with heavy constituent elements have soft vibrational (phonon) modes and consequently have low κ_{lat} which is one of the key requirements to achieve high TE performance. Further, topologically nontrivial boundary states also help to improve the thermoelectric performance of a material compared to the trivial phase because boundary states act as conducting channels for carriers with minimal backscattering effect.

In general, topological insulators (TIs) behave as the normal insulator/semiconductor in bulk with time-reversal symmetry (TRS) protected non-trivial metallic surface states.¹³⁹ Topological insulators can be distinguished from a trivial insulator by introducing novel Z_2 topological index which is classified as Hamiltonian for time-reversal invariant (T).¹⁴⁰ The value of topological invariant (ν) should be equal to zero and one for existing even and an odd number of Dirac cones in the BZ, respectively for both the 2D and 3D topological insulators. 3D topological insulators can be classified into strong and weak topological insulators depending on

the nature of the surface states. The 3D weak topological insulator can be created by stacking 2D TI which is identical to the layered Quantum Hall (QH) states. Weak topological insulator (WTI) and strong topological insulator (STI) both are characterized by four Z_2 indexes ($\nu_0, \nu_1, \nu_2, \nu_3$). STI has a nontrivial ν_0 which implies the presence of an odd number of Dirac cones in the surface states. For WTI, ν_0 is 0 and $\nu_1, \nu_2, \nu_3 \neq 0$ and thus it possesses an even number of Dirac cones in the surface states.¹⁴¹ Recently, BiSe emerges as weak topological insulator which has been verified by experimentally.¹³³

1.7.2. Pressure induced electronic topological transition (ETT) in TQM

Electronic topological transition (ETT) is mainly caused by the drastic changes in the topology of electronic Fermi surface.^{142,143} It is also called Lifshitz transition.¹⁴² Thermodynamically, ETT is a second order isostructural transition without volume collapse and with no change in its Wyckoff positions.

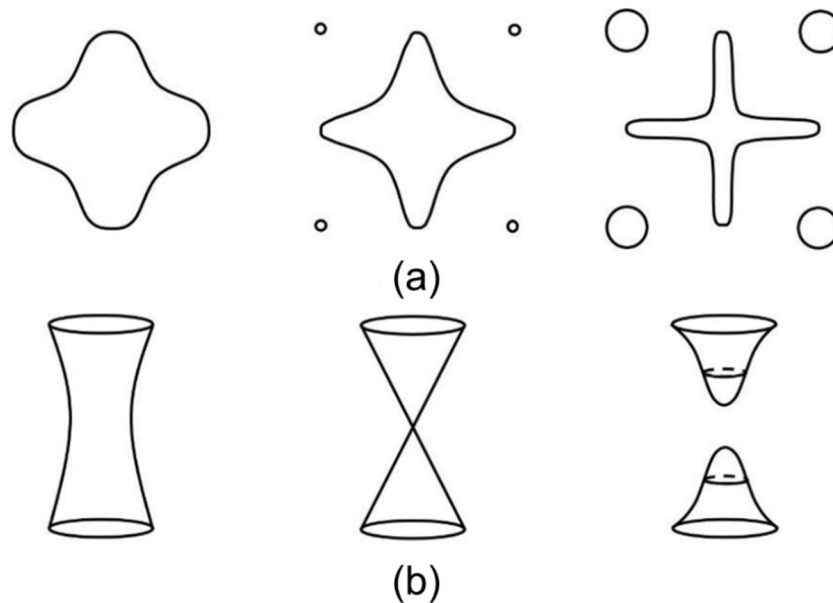


Figure 1.14. Schematic diagram of the typical ETT. (a) The appearance of new voids and (b) Fermi surface neck disruption.¹⁴³ Reproduced with permission from ref. 143 © 1994 Elsevier.

The application of hydrostatic pressure varies the unit cell volume and consequently electron density of states, Fermi surfaces size and its shape. The external perturbations

like pressure, chemical doping, temperature, *etc.*, in metals or degenerate semiconductors, may lead to the crossing of van Hove singularity (band extremum in the density of states) through the Fermi level and strong redistribution of electrons occurs near the Fermi surface.¹⁴³ Hence, Fermi surface can undergo different types of topological transition (changes) like appearance and disappearance of voids, formation and disruption of a neck, depending on the type of critical point passing through the Fermi surface.¹⁴³

The schematic representation of the appearance of voids and disruption of Fermi surface neck are shown in Figure 1.14.¹⁴³ Due to ETT, electrons near the Fermi surface show some peculiar kinetic and thermodynamic characteristics.¹⁴⁴ Since transport properties strongly depend on the density of states near Fermi level; it can show significant changes during ETT. Recently, it was experimentally shown that the tetradymite semiconducting compounds A_2B_3 ($A = \text{Bi, Sb}$, and $B = \text{Se, Te, S}$) exhibit pressure induced ETT around 3–5 GPa.^{145,146} The transverse-optical (E_{2g}) phonon mode of Zn metal shows the occurrence of an ETT at ~ 10 GPa through electron-phonon coupling anomalies via changes in Raman linewidth.¹⁴⁷ In this thesis, ETT has been explored in BiSe through anomalies in lattice parameters and Raman linewidths along with DFT calculations and has been discussed in **part 6**.

1.7.3. Crystal and electronic structures of BiSe

BiSe possesses a layered crystal structure consisting of a bismuth bilayer (Bi_2) sandwiched between two Bi_2Se_3 quintuple [Se-Bi-Se-Bi-Se] layers (Figure 1.15a): essentially a natural heterostructure.¹³⁴ The hallmark of this structure is that it consists of quantum spin hall insulators (*i.e.*, the bismuth bilayer) coupled weakly through 3D topological insulators (*i.e.*, Bi_2Se_3 quintuple layers).¹³³ BiSe belongs to the (0;001) class of Z_2 weak TIs, where the band inversion takes place at Γ and A points in the Brillouin Zone to which both the Bi_2 layer and Bi_2Se_3 quintuple layers (QLs) contribute. The electronic structure of BiSe, (calculated without spin-orbit coupling) reveals a metallic character with a localized (Figure 1.15b) flat conduction band (CB) along the Γ - A line just above the Fermi level (E_F). The unoccupied conduction band constitutes primarily σ -bonded p_x and p_y orbitals of Bi in the bismuth bilayer and is narrowly dispersed along Γ - A , indicating its confinement to the Bi bilayer. The orbital projected electronic

structure reveals that the contributions to the valence band and conduction band around the Fermi level are mainly from the Bi bilayer and Bi_2Se_3 quintuple layers (QLs), respectively, except along the Γ -A line where this is reversed, indicating an inverted band structure and the possibility of a topologically nontrivial phase in BiSe.

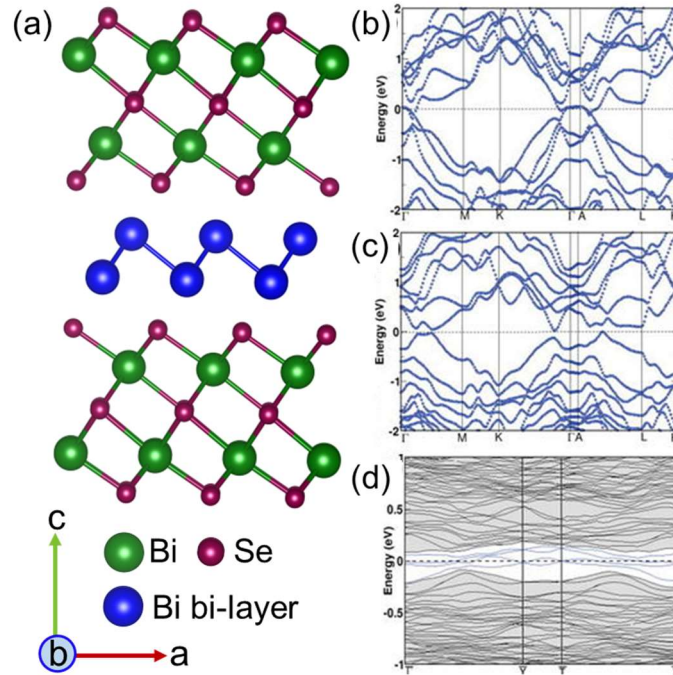


Figure 1.15. (a) Crystal structures of BiSe.¹³⁴ (b) Electronic structure of BiSe calculated without the spin-orbit interaction reveals a metallic state. (c) Spin-orbit interaction opens up a bandgap throughout the Brillouin zone (BZ), making BiSe a small (42 meV) indirect bandgap semiconductor. (d) Electronic structure of the (100) surface of BiSe reveals the even number of Dirac cones (highlighted with blue colors) at $\bar{\Gamma}$ and \bar{V} points in the surface BZ; here, grey shaded regions represent the bands arising from the bulk.¹³³ Figure (a) is reproduced with permission from ref. 134 ©2018 American Chemical Society. (b)-(d) are reproduced with permission from ref. 133 © 2017 American Institute of Physics.

With inclusion of spin-orbit coupling in determination of the electronic structure, the doubly degenerate flat bands open up a gap along Γ -A (Figure 1.15c) and elsewhere in the Brillouin Zone (smallest indirect gap being 42 meV). As BiSe is centrosymmetric and invariant under time reversal, the topological Z_2 invariant of its electronic structure effectively determines its topological nature. The Z_2 invariants of BiSe are (0:001), and hence it belongs to the class of weak topological insulators.¹³³ Moreover, from the

surface electronic structure calculation on the (100) surface of BiSe, it was revealed that the surface states cross only at \bar{Y} and \bar{T} points in the Brillouin zone (Figure 1.15d), giving rise to an even number of Dirac points and remain gapped elsewhere which is the characteristic feature of a WTI. Thus, the intriguing crystal and electronic structure of BiSe motivates the researchers to study its fundamental properties.

1.8. Synthesis and characterization techniques

In this part, I have provided a detailed discussion on different synthesis methods and general principle of characterization techniques used in my thesis work. Specific details are also discussed in each chapter separately.

1.8.1. Synthesis

The successful utilization of TE devices depends critically on the synthesis techniques which has been discussed in detail in the following section.

1.8.1.1. Solid state reaction

Solid-state reaction is a common synthesis method to obtain polycrystalline and single crystalline material from solid reagents. Factors that affect solid-state reaction are chemical and morphological properties of the reagents including the reactivity, surface area, and free energy change with the solid-state reaction, and other reaction conditions, such as the temperature, pressure, and the environment of the reaction. The advantage of solid-state reaction method includes the simplicity and large-scale production.

(A) Seal-tube melting reaction: Metal chalcogenides are known to be synthesized by sealed-tube reactions in vacuum (10^{-3} - 10^{-5} Torr) at high-temperature. In high temperature vacuum sealed tube melting reaction, appropriate quantities of starting materials (mostly in their elemental form) are heated above the melting point of the desired product in absence of air, followed by cooling of the subsequent reaction mixture at a specific cooling speed depending upon material's nature (congruent/incongruent). Products of the reactions are generally thermodynamically stable polycrystalline or single-crystalline ingots.

(B) Ball milling: It is a mechanical technique widely used to grind powders into fine particles and blend materials. During the ball milling process, the collision between

the tiny rigid balls in a concealed container will generate localized high pressure. Generally, ball milling equipment consists of a hollow cylindrical shell rotating around its axis, which is partially filled with balls made of stainless steel, ceramic, tungsten carbide or rubber. It relies on the energy released from impact and attrition between the balls (grinding or milling medium) and the powder. Advantages of this technique include cost-effectiveness, reliability, ease of operation, reproducible results due to energy and speed control, applicability in wet and dry conditions on a wide range of materials (*e.g.*, cellulose, chemicals, fibres, polymers, hydroxyapatite, metal oxides, pigments, catalysts). The method is highly useful to reduce the particle size of a material less than or equal to 10 microns. I have used a planetary Ball Mill (FRITSCH PULVERISETTE 7, Germany) and stainless-steel containers to prepare the meal chalcogenide samples during my Ph.D. experiments.

(C) Spark plasma sintering: The Spark plasma sintering (SPS) is a newly developed technique for the syntheses and processing of thermoelectric materials employing ON-OFF pulse DC voltage/ current (Figure 1.16).^{148,149} This is considered an energy-saving sintering technology due to its short processing time and small number of processing steps. The SPS process is based on the electrical spark discharge phenomenon. Application of high energy, low voltage spark pulse (spark discharge) momentarily produces a local high-temperature state (several to ten thousand degrees) in the gap between the particles of a material *via* Joule heating (Figure 1.16c-d). This results in vaporization and melting of the powder particles' surfaces and the formation of constricted shapes or "necks" around the contact area between the particles. These constricted shapes gradually develop, and plastic transformation progresses during sintering, resulting in a sintered material with density of $\geq 95\%$. By application of voltage and current repeatedly with this ON-OFF, the discharge point and the Joule heating point (locally high-temperature generation field) move throughout the sample, resulting in less power consumption and efficient sintering. Since only the surface temperature of the particles rises rapidly by self-heating, particle growth of the starting powder materials is controlled. Therefore, a precision sintered compact is manufactured in a shorter time. At the same time, bulk fabrication of particles with an amorphous structure and crystalline nanostructure formation are now possible without changing their characteristics. Vaporization, melting, and sintering are completed in

short periods of approximately 5-20 minutes, including temperature rise and holding times.

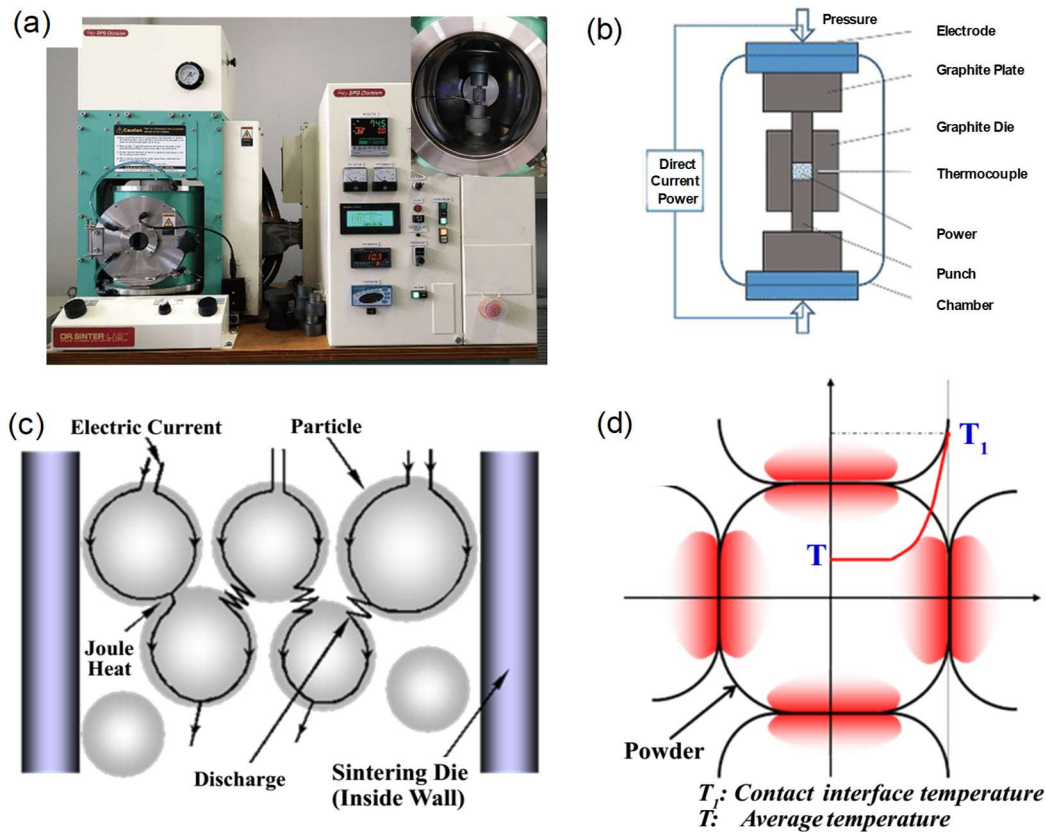


Figure 1.16. (a) Photograph of SPS-211Lx instrument. The inset image shows sintering chamber. (b) Schematic illustration of a spark plasma sintering equipment. (c) Possible electric current path through powder particles inside the die. (d) The temperature image on powder particles surface. Contact surface temperature (T_1) differs significantly from average temperature (T).¹⁴⁹ (c)-(d) are reproduced with permission from ref. 149 © 2013 OMICS International.

In order to prepare high performance thermoelectric materials, spark plasma sintering (SPS) of the melt grown ingots in SPS-211Lx, Fuji Electronic Industrial Co., Ltd (Figure 1.16a). The SPS process and geometrical configuration of the punches, mould and powder are illustrated in Figure 1.16. Powders to be consolidated, are placed in a die and heated by applying the electric current. The melt grown ingots were first ground into fine powders using a mortar and pestle to reduce the grains size in an inert glove box. This powder was then pressed into cylindrical shape by SPS method (SPS-211Lx, Fuji Electronic Industrial Co., Ltd.) at specific temperature and pressure

under vacuum (Figure 1.16a). I have obtained highly dense ($\geq 95\%$ of theoretical density) disk-shaped pellets with ~ 10 mm diameter and ~ 10 mm thickness which were further used for transport property measurements.

1.8.1.2. Solution-phase synthesis

Innovative LMC nanomaterials synthesized on a large scale with controlled morphology, size, composition, and structure lie at the heart of their practical applications. To achieve this, conventional solid-state strategies are often unsatisfactory. On the other hand, soft-chemical solution phase synthesis has been witnessed to be very powerful for obtaining desired LMC functional nanomaterials. In this process, the employed solutions and/or surfactants can be rationally selected based on the target LMCs, and the nucleation and growth process of the products can be easily controlled by adjusting the thermodynamic and kinetic parameters of the reaction. Additionally, liquid-based synthetic routes do not involve the use of drastic conditions (*e.g.*, high temperatures, high pressures) and yield products in large amounts. Most commonly used liquid-based methods are solvothermal method and Schlenk line (also vacuum gas manifold) techniques which are often used to synthesize high-quality LMCs.

(A) Solvothermal method: The solvothermal method involves heating the reactants and solvent in a closed vessel, called autoclave. An autoclave is usually constructed from thick stainless steel to withstand the high pressures and is fitted with safety valves; it may be lined with nonreactive materials such as teflon. The pressure generated in the vessel due to the solvent vapours elevates the boiling point of the solvent. Typically, solvothermal methods make use of various organic solvents such as ethanol, toluene, long chain organic molecule (oleic acid, octadecene, oleylamine, ethylene glycol) and water. This method has been widely used to synthesize zeolites, inorganic open-framework structures, and other solid materials. In the past few years, solvothermal synthesis has emerged to become the chosen method to synthesize nanocrystals of inorganic materials. By employing a metal salt, elemental Te/Se/S and a reducing agent, it is possible to produce metal chalcogenide nanocrystals. Control over size is generally rendered by the slow release of chalcogenide ions.

(B) Schlenk techniques: The Schlenk line (also known as vacuum gas manifold) techniques are very useful to work with air sensitive compounds. It consists of a duplex

of glass tubes with several ports connected side-by-side, which together is called a manifold. One manifold is connected to a source of purified inert gas (Ar, N₂), while the other is connected to a vacuum pump. The inert gas line is vented through an oil bubbler. A liquid nitrogen or dry ice/acetone cold trap generally use in the connector line of pump and manifold to prevent the contamination of the vacuum pump oil from solvent vapours and gaseous reaction products. Special stopcocks or teflon taps allow vacuum or inert gas to be selected without the need for placing the sample on a separate line.

For my Ph.D. work, I have used both the vacuum sealed melting routes and soft chemical solution phase synthesis.

1.8.2. Characterization techniques

I have used the following characterization techniques for my thesis work.

1.8.2.1. Powder X-ray diffraction (PXRD)

Powder X-ray diffraction is the most commonly used technique in solid state inorganic chemistry and has many uses from analysis and assessing phase purity to determine the structure. In this thesis, lab source X-ray have been used for structural characterization. In the laboratory, X-rays are generated in a cathode tube. In this technique, a tungsten filament was heated to produce electrons and electron beam was then accelerated towards an anode by applying a voltage (~ 30 - 40 kV). When electrons have sufficient energy to dislodge inner shell electrons of the target material, characteristic X-ray spectra are produced. These spectra consist of several components, the most common being K_α and K_β. K_α consists, in part, of K_{α1} and K_{α2}. K_{α1} has a slightly shorter wavelength and twice intensity than K_{α2}. The specific wavelengths are characteristic of the target material (Cu, Fe, Mo, Cr). Cu is the most common target material use for laboratory X-ray. To produce monochromatic X-rays, it is required filtering out K_β radiation by foils or crystal monochromators. For Cu radiation, a sheet of Ni foil is a very effective filter, but it is difficult to remove K_{α2} from K_{α1} because of close wavelength. The filtering process in laboratory X-ray leads to a reduction in intensity and hence it is difficult to detect low-intensity peaks in laboratory X-ray diffraction. In addition, it is difficult to distinguish peak splitting when peaks appear closely. X-ray diffraction obeys Bragg's law, which states that

constructive interference would occur if the path difference between the X-rays scattered from parallel planes were an integer number of the wavelength of radiation. If the planes of atoms, separated by a distance d , make an angle θ with the incident beam, then the path difference would be $2d \sin\theta$. So, for constructive interference, the Braggs law must be satisfied:

$$n\lambda = 2d \sin\theta, n = 1, 2, 3\dots \quad (1.14)$$

where, λ = wavelength of the X-ray radiation.

In this thesis, room-temperature PXRD experiments on the samples are carried out using Bruker D8 diffractometer and Rigaku SmartLab SE.

1.8.2.2. Transmission electron microscopy (TEM)

TEM is one of the important tools in material science for characterization of the microscopic structure of materials. A TEM image represents a two-dimensional projection of a three-dimensional object. TEM operates on the same basic principles as the light microscope, however, uses electrons as “light source” that makes it possible to get a resolution of about thousand times better than a visible light microscope. Instead of glass lenses focusing the light on the light microscope, the TEM uses electromagnetic lenses to focus the electrons into a very thin beam. The electron beam then travels through the specimen you want to study. When the electron beam passes through an ultra-thin specimen, it gets absorbed or diffracted through the specimen. Some of the electrons are scattered and disappear from the beam depending on the density of the material present on the focused region. A “shadow image” is formed by the interaction of the electrons transmitted through the specimen focused onto a fluorescent screen or a photographic film or by a sensor such as a charge-coupled device (CCD). TEM study allows to focus electron beam to any part of specimen and electron diffraction data from a different area of the specimen can give us more details about the accurate local structure of the sample.

The details of TEM instrument used during the experiments are provided in the respective chapters.

1.8.2.3. Scanning transmission electron microscopy (STEM)

Scanning transmission electron microscope (STEM) is a special kind of transmission electron microscope, where the electron beam is focused to a fine spot

(with the typical spot size of ~ 0.05 - 0.2 nm) and then scanned over the sample in such way that at each point, sample illuminated with the beam is parallel to the optical axis. The sample preparation technique is similar to that of TEM and STEM imaging was carried out using FEITECNAI G2 20 STWIN TEM operating at 200 KV.

1.8.2.4. Field emission scanning electron microscopy (FESEM)

A FESEM is used to visualize topographic details of the sample surface. Similar to TEM, FESEM microscope also uses electrons as a light source. Electrons are ejected from a field emission source and accelerated in a high electrical field gradient. These electrons (termed as primary electrons) produce a narrow scan beam within the high vacuum column, which bombards the sample material. The incident electrons cause emission of electrons from the sample due to elastic and inelastic scattering. The angle and velocity of these secondary electrons produced by inelastic collision of accelerated electrons with sample atoms relate to the surface structure of the object. High-energy electrons those are produced by an elastic collision of a primary electrons with atom's nucleus of the sample are termed as backscattered electrons (BSE). Larger atoms (with a high atomic number, Z) have a higher chance of producing elastic collisions because of their greater cross-sectional area. Thus, a "brighter" BSE intensity correlates with higher average Z in the sample, and "dark" areas have lower average Z . BSE images are very helpful for obtaining high-resolution compositional maps of a sample.

In my Ph.D. work, I have performed both normal and BSE mode FESEM experiments using NOVA NANO SEM 600 (FEI, Germany) operated at 15 kV to study surface morphology and phase homogeneity. For BSE imaging, I have used a finely polished sample in the back-scattering mode to produce a BSE image of the surface. Specific details of the FESEM instruments were also provided in the respective chapters.

1.8.2.5. Energy dispersive X-ray analysis (EDX)

EDX is an analytical technique used for elemental composition analysis of the sample. EDX makes use of the X-ray spectrum emitted by a solid sample bombarded with a focused beam of electrons. For EDX analysis, an X-ray detector is generally integrated with FESEM instrument. Its characterization capabilities are due in large part to the fundamental principle that each element has a unique atomic structure allowing a unique set of peaks on its electromagnetic emission spectrum. In my Ph.D.,

FESEM images in back scattered electron (BSE) mode and normal mode were taken using ZEISS Gemini attached to JEOL (JEM2100PLUS) FESEM instrument.

1.8.2.6. Atomic force microscopy (AFM)

AFM is a method to see a surface morphology as well as surface roughness in its full, three-dimensional glory of nano to micrometer sized materials. AFM provides important information regarding the height profile of the sample. Typically, AFM consists of a cantilever with a sharp tip whose radius is in the order of nanometers. In proximity of a sample surface, forces between the tip and the sample lead to a deflection of the cantilever according to the Hooke's law and this deflection is measured using a laser spot reflected from the top surface of the cantilever into an array of photodiodes.

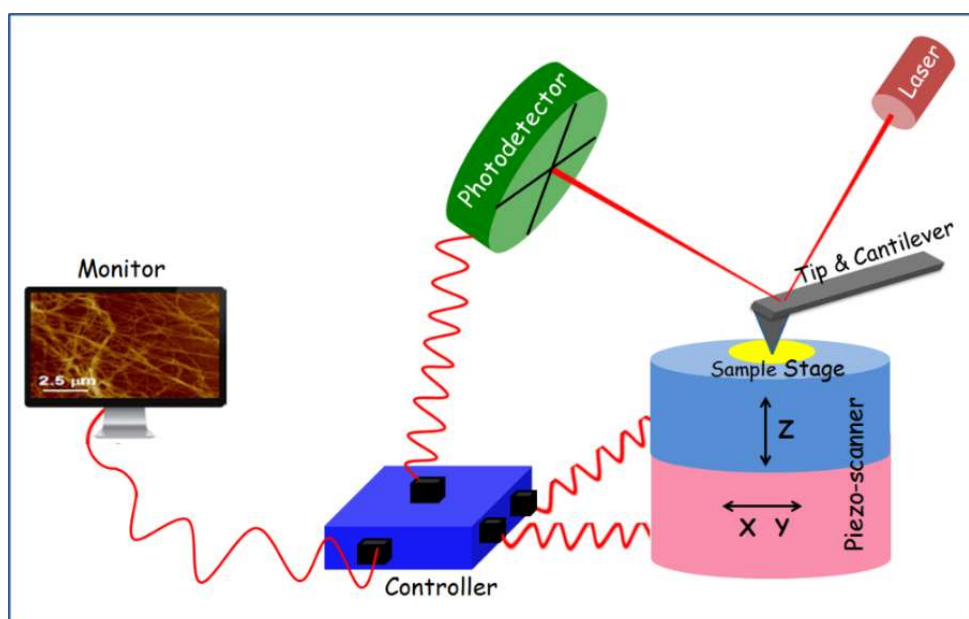


Figure 1.17. Simplified schematic representation of an atomic force microscope (AFM) showing the main components and working principles of the instrument.

1.8.2.7. X-ray photoelectron spectroscopy (XPS)

In static mode, the cantilever is dragged across the surface of the sample and the contours of the surface are directly measured using the The AFM can be operated in various modes, depending on the application and the primary imaging modes including static (also called contact) mode and dynamic (noncontact or tapping) mode. deflection of the cantilever. In the dynamic mode, the cantilever is externally oscillated at or close

to its fundamental resonance frequency or in a harmonic. The oscillation amplitude, phase and resonance frequency are modified by tip sample interaction forces. These changes in oscillation with respect to the external reference oscillation provide information about the sample's characteristics. The major advantage of AFM over other microscopic technique is the fact that AFM provides a three-dimensional surface profile instead of a two-dimensional projection of the sample. The working principle of a typical AFM is described in Figure 1.17. In my thesis work we have used Bruker Innova Microscope in tapping mode with 10 nm diameter containing antimony doped Silicon tip.

XPS is a surface analysis technique, which measures surface composition, chemical and electronic state of the present elements in a material. This technique is based on Einstein's photoelectric effect. When an X-Ray beam directs to the sample surface, the energy of the X-Ray photon is absorbed completely by core electrons of the atoms presents at the surface. XPS spectra are obtained by irradiating a material with a beam of X-rays while simultaneously measuring the kinetic energy ($E_{kinetic}$) and the number of core electrons of atoms that escape from the top 0-10 nm of the material being analyzed. A typical XPS spectrum is a plot of the number of electrons detected vs the binding energy of the detected electrons ($E_{binding}$), as obtained from Einstein relationship ($E_{photon} = E_{binding} + E_{kinetic} + \nu$, where ν is threshold frequency). Each element produces a characteristic set of XPS peaks at characteristic $E_{binding}$ values that directly identify each element presents in or on the surface of the material being analyzed. Since core electrons are close to nucleus and have binding energies characteristic of the certain chemical environment, XPS allows determining the atomic compositions of a sample or chemical state of certain elements. From the binding energy and intensity of a photoelectron peak, the elemental identity, chemical state, and quantity of a detected element can be determined. The details of XPS instruments used during the experiments were provided in the respective chapters.

1.8.2.8. Inductively coupled plasma-atomic emission spectroscopy (ICP-AES)

ICP-AES is an analytical technique used to determine the accurate elemental composition of the sample. Through the use of the Inductively Coupled Plasma, an ICP-AES produces excited ions and atoms (by ionization in an intense electromagnetic

field) that emit detectable amounts of light at characteristic wavelengths, with intensities proportional to the concentration of the ion. As indicated by the name, the spectra is measured and analyzed by atomic emission spectrometer (AES) using concentration-intensity correlations which are similar to the Beer-Lambert Law. ICP-AES measurements were done in Perkin-Elmer Optima 7000DV instrument. Samples were prepared by dissolved powdered samples in aqua regia ($\text{HNO}_3:\text{HCl} = 1:3$) followed by dilution with Millipore water.

1.8.2.9. Optical band gap of solid materials

In my thesis work, the diffuse reflectance method has been used for the determination of band gap of the solid powdered materials. Diffuse reflectance is an excellent sampling tool for powdered crystalline materials. When light shines onto a powder sample, two types of reflections can occur. Some of the light undergoes specular reflection at the powder surface. Diffuse reflection happens when radiation penetrates into the sample and then emerges at all the angles after suffering multiple reflections and refractions by sample particles. A diffuse reflection accessory is designed to minimize the specular component. To estimate optical energy difference between the valence band and conduction band, optical diffuse reflectance measurements have been done with finely ground powder at room temperature using FT-IR Bruker IFS 66V/S spectrometer and Perkin-Elmer Lambda 900, UV/Vis/NIR spectrometer. Absorption (α/A) data were estimated from reflectance data using Kubelka–Munk equation:

$$\alpha/A = (1-R)^2 / (2R) \quad (1.15)$$

where R is the reflectance, α and A are the absorption and scattering coefficients, respectively. The energy band gaps were derived from α/A vs E (eV) plots.

1.8.2.10. Raman spectroscopy

Raman spectroscopy is one of the vibrational spectroscopic techniques used to provide information on molecular vibrations and crystal structures. This technique is based on inelastic scattering of monochromatic light. A change in the molecular polarizability with respect to the vibronic coordinate is required for a molecule to exhibit Raman effect. Normally, a laser source Nd-YAG with a fixed wavelength of 532 nm, an Argon ion laser source at 514 nm or He-Ne laser at 633 nm is used as light source. The laser light interacts with molecular vibrations, phonons or other excitations

in the system, resulting in the energy of the laser photons being shifted up or down. The shift in energy gives information about the vibrational modes in the system. Low temperature Raman spectroscopic measurements were carried out on pellet shaped samples using Horiba Jobin-Yvon LabRAM HR evolution Raman spectrometer with 1800 gr/mm and Peltier cooled CCD detector.

1.8.2.11. Thermogravimetric analysis (TGA) and differential scanning calorimetry (DSC)

Thermogravimetric analysis or thermal gravimetric analysis (TGA) is a method of thermal analysis in which the mass of a sample is measured over time as the temperature changes. This measurement provides information about physical phenomena, such as phase transitions, absorption, adsorption and desorption; as well as chemical phenomena including chemisorptions, thermal decomposition, and solid-gas reactions. TGA experiments were carried out using a PerkinElmer TGA8000 instrument. The temperature range has been given in the relevant chapter.

DSC is a thermo-analytical technique in which the difference in the amount of heat required to increase the temperature of a sample and reference is measured as a function of temperature. Both the sample and reference are maintained at nearly the same temperature throughout the experiment. The basic principle underlying this technique is that when the sample undergoes any physical transformation such as phase transition, melting *etc*, amount of heat flow required to maintain both at the same temperature will be different. When the amount of heat required for the sample is lesser than the reference, the process is termed as exothermic. Endothermic process requires a higher amount of heat flow to maintain the temperature. By observing the difference in heat flow between the sample and reference, differential scanning calorimeters are able to measure the amount of heat absorbed or released during such transitions. DSC data were collected using a TA DSC Q2000 in N₂ atmosphere. The temperature range has been given in the relevant chapter.

1.9. Physical property measurements

In this part, I have discussed about the different measurements used in my thesis work. Specific measurements are discussed in each chapter separately.

1.9.1. Electrical transport measurements

The power factor ($S^2\sigma$) depends on the product of the Seebeck coefficient and the electrical conductivity. The Seebeck coefficient is the ratio of a resulting electric field gradient to an applied temperature gradient. In a typical measurement, the temperature is varied around a constant average temperature and the slope of the voltage (V) vs. temperature difference (ΔT) curve gives the Seebeck coefficient (the slope method) or just $\Delta V/\Delta T$ is measured (single point measurement). Either a specific temperature difference is stabilized before each measurement (steady-state), which takes longer, or measurements are conducted continuously while the temperature difference is varied slowly (quasi-steady-state). Little difference was found between steady-state and quasi-steady-state measurements when good thermal and electrical contact is ensured. The employed temperature difference should be kept small, but too small will lead to decreased accuracy. Usually, 4 - 20 K (or 2 - 10 K) is appropriate for the full temperature span.

In the present thesis, temperature dependent Seebeck coefficient measurement has been done using the most popular commercial instruments ULVAC ZEM 3 RIKO using off-axis 4-point geometry under low-pressure helium (He) atmosphere (Figure 1.18a). In the off-axis, 4-point geometry, the thermocouples, and voltage leads are pressed against the sides of the sample (Figure 1.18b).

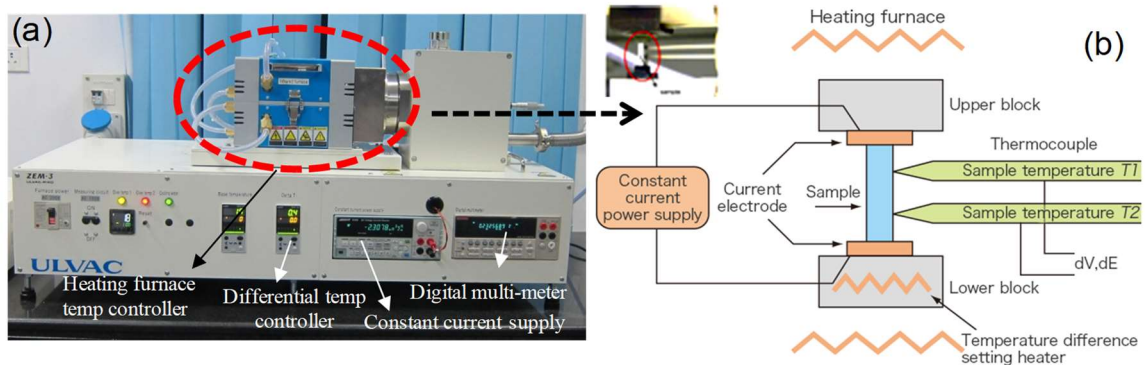


Figure 1.18. (a) Photograph of sample-chamber in ULVAC-ZEM3 apparatus. (b) Schematic of ULVAC-ZEM 3 four-probe measurement system.

The instrument uses slope method to extract the Seebeck coefficient from steady-state measurements. In the slope method, the measured raw data is corrected for constant

offset voltages by using the slope of several $(\Delta T, V)$ points for extracting the Seebeck coefficient. The typical sample for measurement has a rectangular shape with the dimensions of $\sim 2 \text{ mm} \times 2 \text{ mm} \times 8 \text{ mm}$ and ΔT values 5, 10, 15 K have been used in the measurement. The error in the measurement is $\sim 5\%$. In a typical measurement, the sample is set in a vertical position between the upper and lower electrode blocks in the heating furnace. For temperature dependent measurement, the sample was first heated to a specified temperature using an infrared (IR) furnace. Thereafter a temperature gradient across the sample was created by heating the lower part of it by a heater. Seebeck coefficient is measured by measuring the upper and lower temperatures T_1 and T_2 with the thermocouples pressed against the side of the sample, followed by measurement of voltage (ΔV) between the same wires on one side of the thermocouple.

The electrical conductivity, σ is measured using the four-probe method. Temperature dependent σ has been measured concurrently during Seebeck measurement in ULVAC ZEM 3 RIKO. For the measurement, a constant current I is applied to both ends of the sample to measure the voltage V between the thermocouples. By knowing resistance of sample, R ($R = V/I$), we can calculate σ from resistivity (ρ) of the sample using following equations:

$$\rho = R \times \frac{A}{l} \quad (1.16)$$

$$\sigma = \frac{1}{\rho} \quad (1.17)$$

where A is sample cross section and l is the distance between probes.

1.9.2. Hall effect

The Hall effect describes the behaviour of the free carriers in a semiconductor when applying an electric as well as a magnetic field along the perpendicular direction.¹⁵⁰ Thus, measurement of the Hall voltage is used to determine the type of charge carrier present in the system, the free carrier density and the carrier mobility. When a current-carrying semiconductor is kept in a magnetic field, the charge carriers of the semiconductor experience a force in a direction perpendicular to both the magnetic field and the current. At equilibrium, a voltage appears at the semiconductor edges. The ratio of the induced voltage (V) to the product of the current density (I/t , where I is applied current and t is sample thickness) and the applied magnetic field (B) is defined as Hall coefficient (R_H) as shown in the following equations:

$$R_H = \frac{Vt}{IB} \quad (1.18)$$

$$n_H = \frac{1}{R_H e} \quad (1.19)$$

where, e is the charge of an electron (1.602×10^{-19} C) and n_H is charge carrier density. In this thesis, Hall measurement has been done in an inhouse equipment developed by Excel instrument. We have used a four-contact Hall-bar geometry and a varying magnetic field up for the measurements.

1.9.3. Thermal transport measurements

The flash diffusivity method most frequently is used for the determination of thermal conductivity (κ) of material. Non-contact, non-destructive, easy sample preparation, applicability for a wide range of diffusivity values with excellent accuracy and reproducibility makes this method more advantageous than direct method. In the flash diffusivity method, the thermal conductivity is calculated as $\kappa = DC_p\rho$, where D is thermal diffusivity, ρ is density, and C_p is the constant pressure heat capacity. In this method, the sample is mounted on a carrier system, which is located in a furnace.

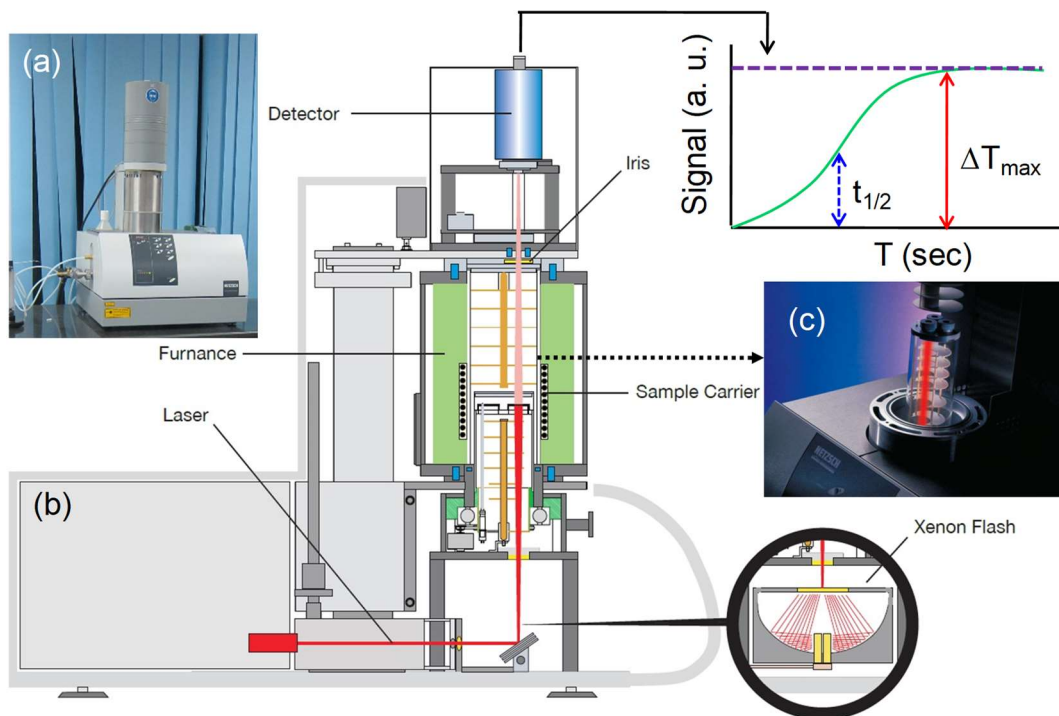


Figure 1.19. (a) Photograph of NETZSCH LFA-457 instrument. (b) and (c) Schematic of LFA-457 diffusivity measurement apparatus.

After the sample reaches a predetermined temperature, a short heat pulse from a pulsed laser is applied to one side of a thin sample, resulting in homogeneous heating. The relative temperature increase on the rear face of the sample is then measured as a function of time by an IR detector. The temperature will rise to a maximum, after which it will decay. The time for the temperature to increase to half-maximum, $t_{1/2}$, is used to calculate the thermal diffusivity using the following equation:

$$D = 0.1388 \times \frac{l^2}{t_{1/2}} \quad (1.20)$$

where D is thermal diffusivity in cm^2/s , l is the thickness.¹⁵¹

In this thesis, temperature dependent thermal transport measurement has been done using the most popular NETZSCH LFA-457 instrument in N_2 atmosphere (Figure 1.19). Coins with ~ 10 mm diameter and ~ 2 mm thickness were used for all the measurements. The samples were coated with a thin layer of graphite ($\sim 5 \mu\text{m}$) in order to enhance the absorption of laser energy and emission of IR radiation to the detector. It also increases the signal to noise ratio. The error for the κ_{total} measurement is $\sim 5\%$. The samples were placed inside SiC sample holder to mount on carrier system (Figure 1.19c). A Nd-Glass pulsed laser source of wavelength 1054 nm has been used for all the measurement. To measure the increased temperature on the rear face of the sample a liquid N_2 cooled InSb IR detector has been used. The ρ was determined using the dimensions and mass of the sample and C_p , was derived indirectly using a standard sample (pyroceram). The thermal diffusivity data were analyzed using a Cowan model with pulse correction to account for heat losses on the sample faces.¹⁵²

1.9.4. Heat capacity

The low temperature (2-300 K) heat capacity at constant pressure was measured using Physical Property Measurement System (PPMS), Quantum Design (DynaCool) over the temperature range 1.9-300 K by utilizing the following principle:

$$C_p = \left(\frac{dQ}{dT}\right)_p \quad (1.21)$$

Quantum Design Heat Capacity option controls the heat added to and removed from a sample while monitoring the resulting change in temperature. During a measurement, a known amount of heat is applied at constant power for a fixed time, and then this heating period is followed by a cooling period of the same duration. A platform heater and plat-

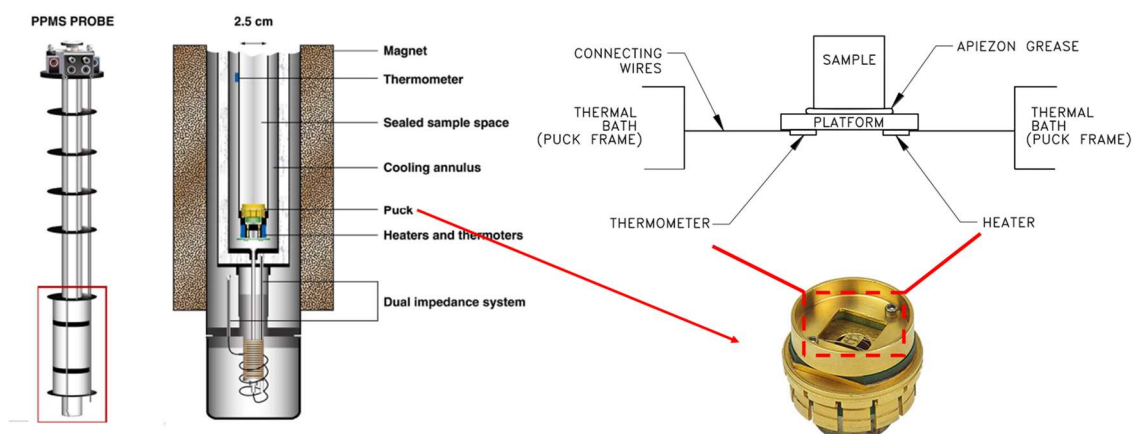


Figure 1.20. Left. Detailed view of the sample chamber of PPMS probe. Right. Heat capacity puck along with the schematic diagram of the sample stage.¹⁵³ (adapted from ref. 153)

form thermometers are attached to the bottom side of the sample platform (see Figure 1.20).

1.9.5. Magnetic measurements

The dc magnetic measurements were performed with the help of a commercial Quantum Design Superconducting Quantum Interference Device (SQUID) magnetometer and in a vibrating sample magnetometer from Cryogenic Ltd., U.K. in the temperature range 1.8-300 K and magnetic field range 0-150 kOe. In the case of dc measurements, magnetization data were recorded as a function of temperature, field and time in different protocols. In general, three standard protocols namely (i) zero field cooled heating (ZFCH), (ii) field cooling (FC) and (iii) field cooled heating (FCH) were used for thermal variation of dc magnetization measurements. In ZFCH, the sample was cooled from room temperature to 5 K in absence of any magnetic field and subsequent heating data were collected in presence of magnetic field. On the other hand, in the case of FC and FCH protocols, the data were recorded during cooling and heating respectively in presence of magnetic field. Isothermal magnetization measurements as a function of applied field at different constant temperatures were performed in a thermally demagnetized state. Thermally demagnetized state is obtained by cooling the sample from paramagnetic region to the lowest temperature (typically well below the transition temperature) and then heat it back to the respective temperature of measurements in zero magnetic field.

1.9.6. Pressure dependent Raman and XRD measurements

In this thesis, we have used pressure dependent Raman scattering and synchrotron XRD measurements for probing the structural and isostructural electronic transitions in TQMs.

(A) Pressure dependent Raman experiment: The main idea of generating high pressure is based on the simple definition of pressure (P):

$$P = F/A \quad (1.22)$$

where F is the force applied perpendicular to an area A . From equation 1.22, there are two critical factors (F and A) influencing the high-pressure generation.

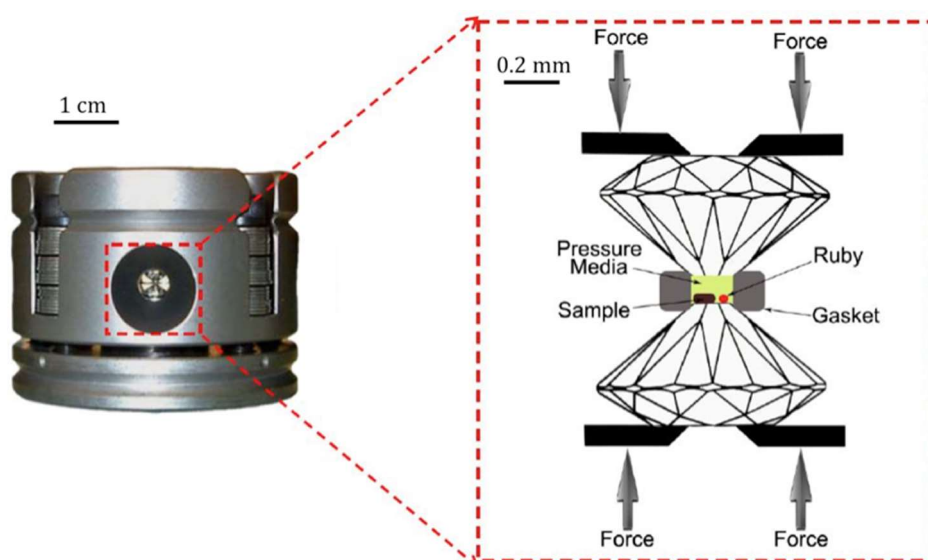


Figure 1.21. The schematic and working principle of the DAC.

A large force applied to a small area through an opposed anvil device will generate high pressure, and this is a commonly used strategy. For instance, the typical force of a few kN applied on a square micrometer area will result in a pressure in the order of GPa. Therefore, anvils with smaller faces are required for achieving high pressures. This is the basic reason for using small size diamond tips in diamond anvil cell for high pressure generation, and this device revolutionized the high-pressure science.^{154,155} The working principle of DAC is shown in Figure 1.21. Diamonds are used in the DAC because of their hardness and transparent nature to a wide frequency range of the electromagnetic spectrum (X-ray, visible light, γ ray, and most of the infrared and ultraviolet region).

Therefore, DAC can be used to study a wide range of materials' properties under high pressure at *in-situ* conditions. The DAC is composed of two opposed diamond anvils, and it creates high pressure by trapping the sample between polished culets of two diamonds inside metal gaskets. Due to this specific configuration, a small force is enough to create extremely large pressures in the sample chamber.

The gasket present in between the two diamond anvils has an important purpose. (i) It acts as the chamber which confines the sample, the pressure transmitting medium (PTM) and pressure calibrant. (ii) It extrudes around the diamonds on compression and acts as a supporting ring for the diamond culets. Hence the gaskets are protecting the diamonds from touching each other. Usually, the gaskets are commonly made of a hard material like hardened stainless steel, tungsten, rhenium, inconel, and copper-beryllium alloy. A mixture of methanol and ethanol in the ratio of 4:1 or silicone oil are commonly used as a PTM which maintain the hydrostaticity up to 10.5 GPa at room temperature.¹⁵⁶

A reliable and accurate pressure gauge is essential for all high-pressure experiments. The Ruby fluorescence method is the widely used pressure calibration technique¹⁵⁷ in the DAC. Ruby is Al_2O_3 doped with Cr^{3+} and it does not undergo any phase transition under pressure at room temperature conditions. The fluorescence signal of the Ruby is very strong and appear at ~ 694.2 nm and ~ 692.7 nm respectively. These lines originate from the lifting of the degeneracy of the d-orbitals of the Cr^{3+} ion by the octahedral coordination of the oxygen atoms due to crystal field theory proposed for this geometry. Under pressure, the position of these peaks shifts to a longer wavelength. Pressure can be determined from the wavelength of the first peak using the following formula:¹⁵⁸

$$P(\text{GPa}) = \frac{1904}{B} \left[1 + \frac{\Delta\lambda}{\lambda_0} \right]^B - 1 \quad 1.23$$

where, $\Delta\lambda = \lambda_p - \lambda_0$ is the difference between the wavelength at a pressure P and ambient pressure, and B is empirically determined coefficients. $B = 7.665$ and 5 for quasi-hydrostatic and non-hydrostatic conditions respectively. Using Ruby pressure calibration method, the precision of the pressure can be achieved to the order of ± 0.03 GPa. The precision of the pressure measurement depends on the degree of crystallinity, size, shape, and importantly annealing of the Ruby crystals to remove the residual strains when the Ruby particles are made into spheres using ball milling. Ruby can be well detected even from a very small (~ 10 μm diameter) sphere because of the large strength

of its signal. This is helpful in safely placing the Ruby in the gasket hole without altering the measurement. In this thesis, we have used a Mao-Bell type DAC (fabricated in house), and Ruby fluorescence method for the high-pressure Raman experiments. These experiments have been performed in collaboration with Prof. Chandrabhas Narayana from JNCASR, India.

(B) Pressure dependent synchrotron XRD: The schematic outline of the beamline is shown in Figure 1.22.

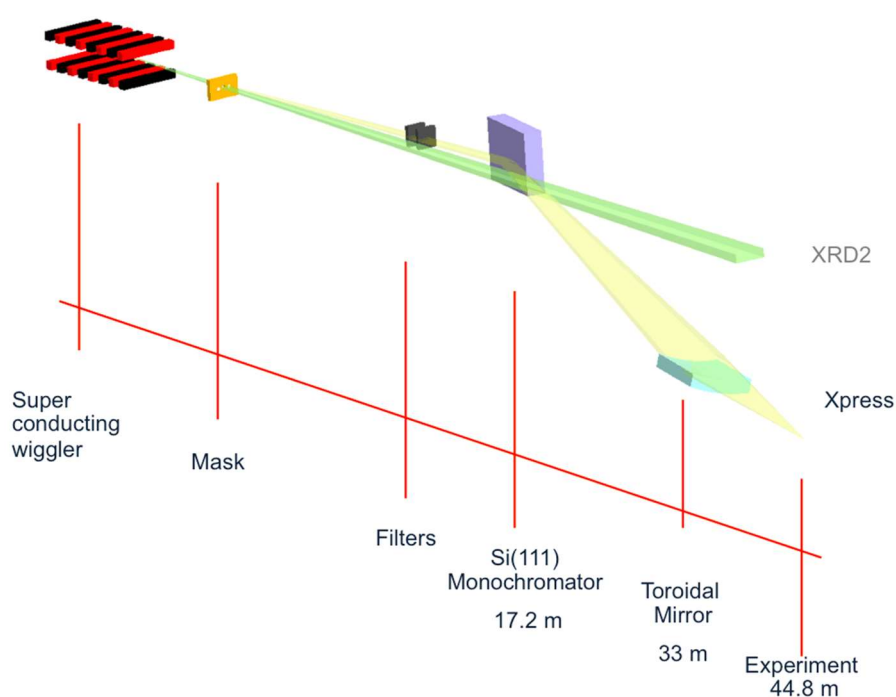


Figure 1.22. Schematic of the Xpress beamline. Here, XRD2 beamline (next to Xpress beamline) is sharing the superconducting wiggler (SCW). Adapted from the website: www.elettra.trieste.it/lightsources/elettra/elettra-beamlines/xpress/info-beamline

A photograph of the end station of the Xpress beamline together with a schematic diagram explaining the main components are shown in Figure 1.23. The Xpress beamline provides a high photon flux at a fixed energy of 25 keV which is ideal for high pressure powder experiments using DAC. A multipole superconducting wiggler (SCW) is the source of the beamline. Liquid nitrogen cooled Si(111) single crystal hosted in the splitter chamber intercepts the X-ray beam from the SCW. The monochromator directs the X-ray beam to the focusing mirror at a fixed energy of 25 keV. The focusing mirror is Pt coated to achieve 80% reflectivity at 25 keV and is a 1.4 m long torus, kept at 2.9

mrad grazing angle. Finely focused beam from this mirror is further optimized by collimators (200 - 20 μm in diameter pin holes) which gives an intense and well-defined monochromatic beam with minimum divergence for the diffraction experiments. An image plate detector MAR345 is used to record the XRD patterns of the samples under pressure from inside DAC. Further, this MAR345 detector is placed in a special stage which allows the controllable linear movement along the beam direction at two fixed vertical positions. A Ruby fluorescence microscope is connected side by side to the pinhole stage which helps to estimate the accurate measurements of the sample's pressure (Figure 1.23). Xpress beamline has a friendly graphical user interface permitting an easy setting-up of the beamline as well as data collection parameters.

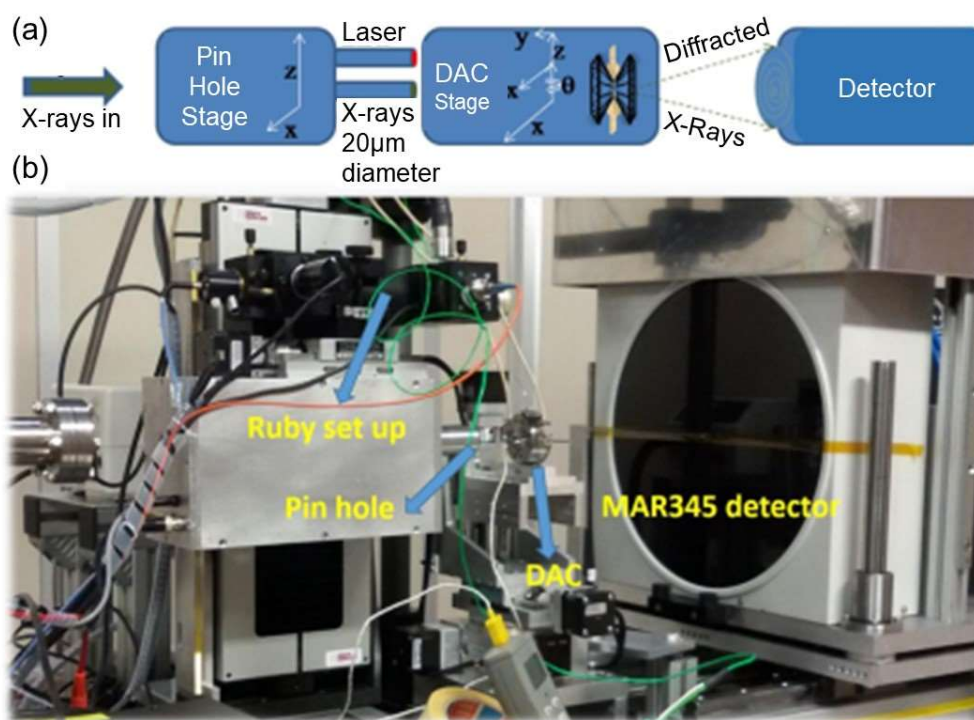


Figure 1.23. (a) Block diagram of the synchrotron high pressure XRD set up at Xpress beamline and (b). Photograph of the Xpress beamline set up. Adapted from the website: www.elettra.trieste.it/lightsources/elettra/elettra-beamlines/xpress/info-beamline

A membrane DAC, silicone oil as PTM and Ruby fluorescence method were used for the high-pressure synchrotron XRD experiments. These experiments have been performed in collaboration with Dr. Bobby Joseph at Xpress beamline in Elettra, Trieste, Italy.

1.10. Scope of the thesis

Two-dimensional layered metal chalcogenides have emerged as one of the most important classes of materials with a rich structural diversity and plethora of diverse transport properties. In my Ph.D. work, I have synthesized and investigated detailed structure-property relationships of a few novel 2D layered metal chalcogenides and studied their fundamental physical properties and applicability in thermoelectric research. Apart from the present introductory part (**part 1**), my thesis consists of six parts (**part 2-7**), where **part 2** and **part 3** is sub-divided into three and two chapters respectively, and **part 7** provides a summarized future outlook.

Thermoelectric materials constitute a viable means of efficient energy management in near future, by converting the untapped heat into electrical energy. PbTe and its derivatives from IV-VI metal chalcogenides family have been established as champion thermoelectric materials for mid-temperature power generation.^{13,18,42} However, it is the toxicity of lead which prevents mass market applications for TE power-generation. Recently, 2D layered tin selenide (SnSe) has attracted immense interest in thermoelectrics due to its ultralow lattice thermal conductivity and high-power factor. To date, majority of the thermoelectric studies of SnSe are based on single crystals. However, an expensive and time-consuming high temperature synthesis procedure of SnSe single crystals, and its poor mechanical stability make it unfavourable for scaling up synthesis, commercialization and practical applications which necessitates the research on nanocrystalline SnSe that can be produced in large quantities by simple and low temperature solution phase synthesis. Till date, the outstanding thermoelectric performance has only been reported for single crystals whereas, the polycrystalline or nanocrystalline analogues exhibit relatively poorer thermoelectric figure of merit due to its poor electrical conductivity. Thus, in **part 2** of my thesis, I have optimized the synthesis and thermoelectric properties of SnSe nanocrystals by adopting various doping strategies. First, I have discussed about the high thermoelectric figure of merit ($zT = 2.1$) in two dimensional (2D) nanoplates of Ge doped SnSe synthesized by a simple hydrothermal route followed by spark plasma sintering (SPS). Ge-doping in SnSe nanoplates significantly enhances the *p*-type carrier concentration which results in high electrical conductivity and power factor. In addition to nanoscale grain boundary and high

lattice anharmonicity in SnSe nanoplates, phonon scattering due to Ge precipitates in the SnSe matrix gives rise to an ultralow lattice thermal conductivity (κ_{lat}) of $\sim 0.18 \text{ W m}^{-1} \text{ K}^{-1}$ at 873 K in 3 mol% Ge doped SnSe nanoplates. Next, I have also obtained significant enhancement in thermoelectric performance in 2D SnSe nanoplates by introducing magnetic Gd dopants. The *p*-type carrier concentration increases significantly upon 3 mol% Gd addition in SnSe nanoplates due to phase separation of Gd_2Se_3 nanoprecipitates (2-5 nm) and subsequent Sn^{2+} vacancy formation. The presence of magnetic fluctuations induced by small nano-precipitates of Gd_2Se_3 provides additional scattering of the phonons in SnSe, which reduces the κ_{lat} significantly in $\text{Sn}_{0.97}\text{Gd}_{0.03}\text{Se}$. This is the first experimental report of magnetic rare earth doping in SnSe nanoplates in the area of thermoelectrics. Finally, I have also reported the solution phase synthesis and thermoelectric transport properties of ultrathin (1.2-3 nm thick) few layered *n*-type Bi doped SnSe nanosheets. Bi-doped nanosheets exhibit ultralow κ_{lat} ($\sim 0.3 \text{ W m}^{-1} \text{ K}^{-1}$) throughout the temperature range of 300-720 K which can be ascribed to the effective phonon scattering by interface of SnSe layers, nanoscale grain boundaries and point defects.

Till date, a plethora of research has been carried out to modulate the thermoelectric performance of *p*-type nanocrystalline/polycrystalline SnSe. However, in most of the cases, reported SnSe materials are *p*-type while thermoelectric applications demand both *p*-type and *n*-type materials. So, in **part-3** of my thesis, I have tried to optimize the thermoelectric properties of *n*-type polycrystalline SnSe by doping with MoCl_5 and WCl_6 . I have reported record high zT of 2.0 polycrystalline $\text{SnSe}_{0.92} + 1 \text{ mol}\% \text{ MoCl}_5$ resulting from the simultaneous optimization of *n*-type carrier concentration and enhanced phonon scattering due to the formation of modular of layered intergrowth $[(\text{SnSe})_{1.05}]_m(\text{MoSe}_2)_n$ like compounds within the SnSe matrix. These 2D layered modular intergrowth compound resembles the natural nano-heterostructures and their periodicity of 1.2 - 2.6 nm matches the phonon mean free path of SnSe. Thus, the heat carrying phonons were blocked effectively and an ultra-low κ_{lat} and ultra-high thermoelectric performance were obtained in *n*-type polycrystalline SnSe. By following the similar strategy, I have also obtained high thermoelectric performance of *n*-type $\text{SnSe}_{0.92}$ upon WCl_6 doping. The successful creation of Se vacancy and substitution of W^{6+} at Sn^{2+} and Cl^- ions at Se^{2-} sites effectively enhance the total *n*-type carrier concentration, thus improving its electrical

conductivity. The occurrence of WSe_2 precipitates in the SnSe matrix drastically reduces the lattice thermal conductivity which gives rise to high zT in $\text{SnSe}_{0.92} + 2 \text{ mol\% WCl}_6$ sample.

It is well-known that SnSe undergoes a displacive phase transition from low symmetric $Pnma$ phase to high symmetric $Cmcm$ phase at $\sim 800 \text{ K}$. This phase transition at elevated temperature results in extended defects and enhancement in the lattice strain which degrades the mechanical properties of SnSe and limits its long-term power generation applications at high temperature. Furthermore, it has been reported that the metastable cubic phase can only be stabilized at very high pressure or by inducing strain. So, in **part 4**, I have reported the successful stabilization of the high-pressure cubic rock-salt phase of SnSe at ambient conditions by introducing chemical pressure into the lattice upon alloying with 30 mol% AgBiSe_2 . The band gap of the pristine orthorhombic SnSe is 0.90 eV, whereas, when SnSe is alloyed with AgBiSe_2 , band gap closes rapidly near to zero at $x = 0.30$ due to increase in chemical pressure originating from a sharp decrease in unit cell volume. We confirm the stabilization of the cubic structure and its associated changes in electronic structure using first-principles theoretical calculations. Pristine cubic SnSe exhibits topological crystalline insulator (TCI) quantum phase, but the cubic $(\text{SnSe})_{1-x}(\text{AgBiSe}_2)_x$ ($x = 0.33$) possesses semi-metallic electronic structure with overlapping conduction and valence bands. Cubic polycrystalline $(\text{SnSe})_{0.70}(\text{AgBiSe}_2)_{0.30}$ sample shows n -type conduction at room temperature while the orthorhombic $(\text{SnSe})_{1-x}(\text{AgBiSe}_2)_x$ ($0.00 \leq x < 0.28$) samples retain its p -type character. Thus, by optimizing the electronic structure and the thermoelectric properties of polycrystalline SnSe, I have achieved a high zT of 1.3 at 823 K in $(\text{SnSe})_{0.78}(\text{AgBiSe}_2)_{0.22}$.

A charge density wave is a static modulation of conduction electrons and is a Fermi-surface driven phenomenon usually accompanied by a periodic distortion of the lattice. It is well-known that in the vicinity of CDW formation, the electron–phonon coupling breaks the translational symmetry of the lattices and creates a structural perturbation which gives rise to reduced lattice thermal conductivity in these CDW materials making them a suitable candidate for thermoelectric applications. In **part 5**, I have investigated the origin of low lattice thermal conductivity in GdTe_3 , a CDW material. GdTe_3 possess a quasi-2D layered structure where one corrugated GdTe slab is sandwiched between two Te sheets. From, first-principles theoretical calculations, it was verified that charge

transfer take place from the GdTe slab to the adjacent Te sheets and there is a presence of van der Waals gap between the two neighbouring Te-sheets. Thus, the structure can be considered as a natural heterostructure of charge and vdW layers. Strong electron-phonon coupling, and Fermi surface nesting play the crucial role behind the CDW transition ($T_{CDW} \sim 380$ K) in GdTe₃. Large anisotropic behaviour was observed both in the electrical and thermal conductivity data of GdTe₃ when measured along parallel and perpendicular to the SPS pressing, which is quite unusual in polycrystalline materials. From the theoretical calculations and Raman spectroscopic analysis, we have confirmed the existence of low-lying optical phonon modes in GdTe₃ which couples with the heat carrying acoustic phonon branches. Thus, the presence of strong electron-phonon coupling and natural heterostructure of charge and vdW layers effectively scatter the phonons which gives rise to low lattice thermal conductivity in GdTe₃.

Topological quantum materials (*e.g.*, topological insulators, topological crystalline insulators and topological semimetals), characterized by their nontrivial electronic surface states, have created a sensation in designing new TE materials. Recently, it was experimentally shown that hydrostatic pressure plays an important role to modify the structural, electronic and physical properties of TQMs and one such interesting phenomenon is electronic topological transition (ETT). ETT is mainly caused by the drastic changes in the topology of electronic Fermi surface associated with a change in unit cell volume and elasticity of the material. In **part 6** of my thesis, I have reported pressure induced ETT in a weak topological insulator BiSe for the very first time. We have performed a detailed pressure dependent powder X-ray diffraction (PXRD) and Raman spectroscopic analysis of BiSe and inferred that the room temperature trigonal ($P\bar{3}m1$) phase is stable up to ~ 7 GPa. Interestingly, we have observed two distinct slope changes around ~ 1 and ~ 2.2 GPa in the pressure-dependent lattice parameters, volume, Raman mode shift, and Raman mode linewidth data which suggests the onset of two electronic topological transitions (ETT) in this material. A change in the topology of the Fermi surface also verified from the first-principles theoretical calculations. Finally, DFT calculations have revealed that with further increasing the pressure, BiSe undergoes a semiconductor to semimetal transition at ~ 6 GPa. The origin of these ETTs is associated with the two different vibrational modes arising from of Bi₂ bilayer and Bi₂Se₃ quintuple layers of BiSe. Detailed electronic band structure calculations also indicate that the

emergence of multiple band extrema both in the valence and conduction bands as a function pressure can improve the thermopower and thermoelectric performance of BiSe near the vicinity of ETT.

In **part 7**, I have summarized all the chapters and provided a brief outlook into the future direction in optimizing the thermoelectric performance of layered materials.

1.11. References

- (1) Tan, G.; Zhao, L. D.; Kanatzidis, M. G. *Chem. Rev.* **2016**, *116*, 12123–12149.
- (2) Zeier, W. G.; Zevalkink, A.; Gibbs, Z. M.; Hautier, G.; Kanatzidis, M. G.; Snyder, G. J. *Angew. Chem. Int. Ed.* **2016**, *55*, 6826–6841.
- (3) Sootsman, J. R.; Chung, D. Y.; Kanatzidis, M. G. *Angew. Chem. Int. Ed.* **2009**, *48*, 8616–8639.
- (4) Snyder, G. J.; Toberer, E. S. *Nat. Mater.* **2008**, *7*, 105–114.
- (5) Samanta, M.; Dutta, M.; Biswas, K. Thermoelectric Energy Conversion. In *Advances in the Chemistry and Physics of Materials*; George, S. J., Narayana, C., Rao, C. N. R., Eds.; World Scientific, 2019; pp 350–375.
- (6) Snyder, G. J.; Ursell, T. S. *Phys. Rev. Lett.* **2003**, *91*, 148301.
- (7) Liu, W.; Jie, Q.; Kim, H. S.; Ren, Z. *Acta Mater.* **2015**, *87*, 357–376.
- (8) Kim, H. S.; Liu, W.; Chen, G.; Chu, C.-W.; Ren, Z. *Proc. Natl. Acad. Sci.* **2015**, *112*, 8205–8210.
- (9) Chen, Z.; Zhang, X.; Pei, Y. *Adv. Mater.* **2018**, *30*, 1705617.
- (10) Jana, M. K.; Biswas, K. *ACS Energy Lett.* **2018**, *3*, 1315–1324.
- (11) Cahill, D. G.; Watson, S. K.; Pohl, R. O. *Phys. Rev. B* **1992**, *46*, 6131–6140.
- (12) Agne, M. T.; Hanus, R.; Snyder, G. J. *Energy Environ. Sci.* **2018**, *11*, 609–616.
- (13) Heremans, J. P.; Jovovic, V.; Toberer, E. S.; Saramat, A.; Kurosaki, K.; Charoenphakdee, A.; Yamanaka, S.; Snyder, G. J. *Science* **2008**, *321*, 554–557.
- (14) Jaworski, C. M.; Kulbachinskii, V.; Heremans, J. P. *Phys. Rev. B* **2009**, *80*, 233201.
- (15) Wu, L.; Li, X.; Wang, S.; Zhang, T.; Yang, J.; Zhang, W.; Chen, L.; Yang, J. *NPG Asia Mater.* **2017**, *9*, e343.
- (16) Zhang, Q.; Liao, B.; Lan, Y.; Lukas, K.; Liu, W.; Esfarjani, K.; Opeil, C.; Broido, D.; Chen, G.; Ren, Z. *Proc. Natl. Acad. Sci.* **2013**, *110*, 13261–13266.
- (17) Heremans, J. P.; Wiendlocha, B.; Chamoire, A. M. *Energy Environ. Sci.* **2012**, *5*, 5510–5530.
- (18) Pei, Y.; Shi, X.; LaLonde, A.; Wang, H.; Chen, L.; Snyder, G. J. *Nature* **2011**, *473*, 66–69.
- (19) Zheng, Z.; Su, X.; Deng, R.; Stoumpos, C.; Xie, H.; Liu, W.; Yan, Y.; Hao, S.; Uher, C.; Wolverton, C.; Kanatzidis, M. G.; Tang, X. *J. Am. Chem. Soc.* **2018**, *140*,

- 2673–2686.
- (20) Banik, A.; Shenoy, U. S.; Saha, S.; Waghmare, U. V.; Biswas, K. *J. Am. Chem. Soc.* **2016**, *138*, 13068–13075.
- (21) Banik, A.; Shenoy, U. S.; Anand, S.; Waghmare, U. V.; Biswas, K. *Chem. Mater.* **2015**, *27*, 581–587.
- (22) Nshimiyimana, E.; Hao, S.; Su, X.; Zhang, C.; Liu, W.; Yan, Y.; Uher, C.; Wolverton, C.; Kanatzidis, M. G.; Tang, X. *J. Mater. Chem. A* **2020**, *8*, 1193–1204.
- (23) Berry, T.; Fu, C.; Auffermann, G.; Fecher, G. H.; Schnelle, W.; Serrano-Sanchez, F.; Yue, Y.; Liang, H.; Felser, C. *Chem. Mater.* **2017**, *29*, 7042–7048.
- (24) Vineis, C. J.; Shakouri, A.; Majumdar, A.; Kanatzidis, M. G. *Adv. Mater.* **2010**, *22*, 3970–3980.
- (25) Callaway, J.; von Baeyer, H. *Phys. Rev.* **1960**, *120*, 1149–1154.
- (26) Xiao, Y.; Wang, D.; Qin, B.; Wang, J.; Wang, G.; Zhao, L.-D. *J. Am. Chem. Soc.* **2018**, *140*, 13097–13102.
- (27) Samanta, M.; Biswas, K. *J. Am. Chem. Soc.* **2017**, *139*, 9382–9391.
- (28) Callaway, J. *Phys. Rev.* **1960**, *120*, 1149–1154.
- (29) Klemens, P. G. *Phys. Rev.* **1960**, *119*, 507–509.
- (30) Kanatzidis, M. G. *Chem. Mater.* **2010**, *22*, 648–659.
- (31) Korkosz, R. J.; Chasapis, T. C.; Lo, S.; Doak, J. W.; Kim, Y. J.; Wu, C.-I.; Hatzikraniotis, E.; Hogan, T. P.; Seidman, D. N.; Wolverton, C.; Dravid, V. P.; Kanatzidis, M. G. *J. Am. Chem. Soc.* **2014**, *136*, 3225–3237.
- (32) Roychowdhury, S.; Ghosh, T.; Arora, R.; Samanta, M.; Xie, L.; Singh, N. K.; Soni, A.; He, J.; Waghmare, U. V.; Biswas, K. *Science* **2021**, *371*, 722–727.
- (33) Min, Y.; Roh, J. W.; Yang, H.; Park, M.; Kim, S. Il; Hwang, S.; Lee, S. M.; Lee, K. H.; Jeong, U. *Adv. Mater.* **2013**, *25*, 1425–1429.
- (34) Biswas, K.; He, J.; Zhang, Q.; Wang, G.; Uher, C.; Dravid, V. P.; Kanatzidis, M. G. *Nat. Chem.* **2011**, *3*, 160–166.
- (35) Kuei Fang Hsu, Sim Loo, Fu Guo, Wei Chen, Jeffrey S. Dyck, Ctirad Uher, Tim Hogan, E. K. P. and M. G. K. *Science* **2004**, *303*, 818–821.
- (36) Androulakis, J.; Lin, C.-H.; Kong, H.-J.; Uher, C.; Wu, C.-I.; Hogan, T.; Cook, B. A.; Caillat, T.; Paraskevopoulos, K. M.; Kanatzidis, M. G. *J. Am. Chem. Soc.* **2007**, *129*, 9780–9788.

- (37) Ke, X.; Chen, C.; Yang, J.; Wu, L.; Zhou, J.; Li, Q.; Zhu, Y.; Kent, P. R. C. *Phys. Rev. Lett.* **2009**, *103*, 145502.
- (38) Sootsman, J. R.; Pcionek, R. J.; Kong, H.; Uher, C.; Kanatzidis, M. G. *Chem. Mater.* **2006**, *18*, 4993–4995.
- (39) Banik, A.; Vishal, B.; Perumal, S.; Datta, R.; Biswas, K. *Energy Environ. Sci.* **2016**, *9*, 2011–2019.
- (40) Rowe, D. M.; Shukla, V. S.; Savvides, N. *Nature* **1981**, *290*, 765–766.
- (41) Zhao, L. D.; Wu, H. J.; Hao, S. Q.; Wu, C. I.; Zhou, X. Y.; Biswas, K.; He, J. Q.; Hogan, T. P.; Uher, C.; Wolverton, C.; Dravid, V. P.; Kanatzidis, M. G. *Energy Environ. Sci.* **2013**, *6*, 3346–3355.
- (42) Biswas, K.; He, J.; Blum, I. D.; Wu, C.-I.; Hogan, T. P.; Seidman, D. N.; Dravid, V. P.; Kanatzidis, M. G. *Nature* **2012**, *489*, 414–418.
- (43) Kanatzidis, M. G. *Acc. Chem. Res.* **2005**, *38*, 359–368.
- (44) Banik, A.; Biswas, K. *Angew. Chem. Int. Ed.* **2017**, *129*, 14753–14758.
- (45) Chatterjee, A.; Biswas, K. *Angew. Chem. Int. Ed.* **2015**, *127*, 5715–5719.
- (46) Hadland, E.; Jang, H.; Falmbigl, M.; Fischer, R.; Medlin, D. L.; Cahill, D. G.; Johnson, D. C. *Chem. Mater.* **2019**, *31*, 5699–5705.
- (47) Gunning, N. S.; Feser, J.; Beekman, M.; Cahill, D. G.; Johnson, D. C. *J. Am. Chem. Soc.* **2015**, *137*, 8803–8809.
- (48) Radovsky, G.; Popovitz-Biro, R.; Stroppa, D. G.; Houben, L.; Tenne, R. *Acc. Chem. Res.* **2014**, *47*, 406–416.
- (49) Sreedhara, M. B.; Hettler, S.; Kaplan-Ashiri, I.; Rechav, K.; Feldman, Y.; Enyashin, A.; Houben, L.; Arenal, R.; Tenne, R. *Proc. Natl. Acad. Sci.* **2021**, *118*, e2109945118
- (50) Hettler, S.; Sreedhara, M. B.; Serra, M.; Sinha, S. S.; Popovitz-Biro, R.; Pinkas, I.; Enyashin, A. N.; Tenne, R.; Arenal, R. *ACS Nano* **2020**, *14*, 5445–5458.
- (51) Gibson, Q. D.; Zhao, T.; Daniels, L. M.; Walker, H. C.; Daou, R.; Hébert, S.; Zanella, M.; Dyer, M. S.; Claridge, J. B.; Slater, B.; Gaultois, M. W.; Corà, F.; Alaria, J.; Rosseinsky, M. J. *Science* **2021**, *373*, 1017–1022.
- (52) Qiu, W.; Xi, L.; Wei, P.; Ke, X.; Yang, J.; Zhang, W. *Proc. Natl. Acad. Sci.* **2014**, *111*, 15031–15035.
- (53) Snyder, G. J.; Christensen, M.; Nishibori, E.; Caillat, T.; Iversen, B. B. *Nat. Mater.*

- 2004, 3, 458–463.
- (54) Jana, M. K.; Pal, K.; Waghmare, U. V.; Biswas, K. *Angew. Chem. Int. Ed.* **2016**, 55, 7792–7796.
- (55) Li, B.; Wang, H.; Kawakita, Y.; Zhang, Q.; Feyngenson, M.; Yu, H. L.; Wu, D.; Ohara, K.; Kikuchi, T.; Shibata, K.; Yamada, T.; Ning, X. K.; Chen, Y.; He, J. Q.; Vaknin, D.; Wu, R. Q.; Nakajima, K.; Kanatzidis, M. G. *Nat. Mater.* **2018**, 17, 226–230.
- (56) Liu, H.; Shi, X.; Xu, F.; Zhang, L.; Zhang, W.; Chen, L.; Li, Q.; Uher, C.; Day, T.; Snyder, G. J. *Nat. Mater.* **2012**, 11, 422–425.
- (57) Lee, S.; Esfarjani, K.; Luo, T.; Zhou, J.; Tian, Z.; Chen, G. *Nat. Commun.* **2014**, 5, 3525.
- (58) Nielsen, M. D.; Ozolins, V.; Heremans, J. P. *Energy Environ. Sci.* **2013**, 6, 570–578.
- (59) Skoug, E. J.; Morelli, D. T. *Phys. Rev. Lett.* **2011**, 107, 235901.
- (60) Xiao, Y.; Chang, C.; Pei, Y.; Wu, D.; Peng, K.; Zhou, X.; Gong, S.; He, J.; Zhang, Y.; Zeng, Z.; Zhao, L.-D. *Phys. Rev. B* **2016**, 94, 125203.
- (61) Mas-Ballesté, R.; Gómez-Navarro, C.; Gómez-Herrero, J.; Zamora, F. *Nanoscale* **2011**, 3, 20–30.
- (62) Rao, C. N. R.; Ramakrishna Matte, H. S. S.; Maitra, U. *Angew. Chem. Int. Ed.* **2013**, 52, 13162–13185.
- (63) Zhang, H. *ACS Nano* **2015**, 9, 9451–9469.
- (64) Sun, Y.; Gao, S.; Xie, Y. *Chem. Soc. Rev.* **2014**, 43, 530–546.
- (65) Yim, W. M.; Rosi, F. D. *Solid State Electron.* **1972**, 15, 1121–1140.
- (66) Heremans, J. P.; Cava, R. J.; Samarth, N. *Nat. Rev. Mater.* **2017**, 2, 17049.
- (67) Zhao, L.-D.; Tan, G.; Hao, S.; He, J.; Pei, Y.; Chi, H.; Wang, H.; Gong, S.; Xu, H.; Dravid, V. P.; Uher, C.; Snyder, G. J.; Wolverton, C.; Kanatzidis, M. G. *Science* **2016**, 351, 141–144.
- (68) Zhao, L.-D.; Lo, S.-H.; Zhang, Y.; Sun, H.; Tan, G.; Uher, C.; Wolverton, C.; Dravid, V. P.; Kanatzidis, M. G. *Nature* **2014**, 508, 373–377.
- (69) Chang, C.; Wu, M.; He, D.; Pei, Y.; Wu, C.-F.; Wu, X.; Yu, H.; Zhu, F.; Wang, K.; Chen, Y.; Huang, L.; Li, J.-F.; He, J.; Zhao, L.-D. *Science* **2018**, 360, 778–783.
- (70) Duong, A. T.; Nguyen, V. Q.; Duvjir, G.; Duong, V. T.; Kwon, S.; Song, J. Y.;

- Lee, J. K.; Lee, J. E.; Park, S.; Min, T.; Lee, J.; Kim, J.; Cho, S. *Nat. Commun.* **2016**, *7*, 13713.
- (71) Wang, C.; Ding, G.; Wu, X.; Wei, S.; Gao, G. *New J. Phys.* **2018**, *20*, 123014.
- (72) Kumar, S.; Schwingenschlogl, U. *Phys. Chem. Chem. Phys.* **2016**, *18*, 19158–19164.
- (73) Zhao, L.-D.; He, J.; Berardan, D.; Lin, Y.; Li, J.-F.; Nan, C.; Dragoe, N. *Energy Environ. Sci.* **2014**, *7*, 2900–2924.
- (74) Ghosh, T.; Samanta, M.; Vasdev, A.; Dolui, K.; Ghatak, J.; Das, T.; Sheet, G.; Biswas, K. *Nano Lett.* **2019**, *19*, 5703–5709.
- (75) Rhyee, J.-S.; Lee, K. H.; Lee, S. M.; Cho, E.; Kim, S. Il; Lee, E.; Kwon, Y. S.; Shim, J. H.; Kotliar, G. *Nature* **2009**, *459*, 965–968.
- (76) Dutta, M.; Matteppanavar, S.; Prasad, M. V. D.; Pandey, J.; Warankar, A.; Mandal, P.; Soni, A.; Waghmare, U. V.; Biswas, K. *J. Am. Chem. Soc.* **2019**, *141*, 20293–20299.
- (77) Mao, J.; Liu, Z.; Ren, Z. *npj Quantum Mater.* **2016**, *1*, 16028.
- (78) Zhou, Y.; Zhao, L. D. *Adv. Mater.* **2017**, *29*, 1702676.
- (79) Wu, J.; Chen, Y.; Wu, J.; Hippalgaonkar, K. *Adv. Electron. Mater.* **2018**, *4*, 1800248.
- (80) Dresselhaus, M. S.; Chen, G.; Tang, M. Y.; Yang, R.; Lee, H.; Wang, D.; Ren, Z.; Fleurial, J. P.; Gogna, P. *Adv. Mater.* **2007**, *19*, 1043–1053.
- (81) Samanta, M.; Ghosh, T.; Chandra, S.; Biswas, K. *J. Mater. Chem. A* **2020**, *8*, 12226–12261.
- (82) Bessas, D.; Sergueev, I.; Wille, H. C.; Peron, J.; Ebling, D.; Hermann, R. P. *Phys. Rev. B* **2012**, *86*, 224301.
- (83) Heremans, J. P. *Nat. Phys.* **2015**, *11*, 990–991.
- (84) Slack, G. A. *J. Phys. Chem. Solids* **1973**, *34*, 321–335.
- (85) Li, S.; Li, X.; Ren, Z.; Zhang, Q. *J. Mater. Chem. A* **2018**, *6*, 2432–2448.
- (86) Banik, A.; Roychowdhury, S.; Biswas, K. *Chem. Commun.* **2018**, *54*, 6573–6590.
- (87) Chandra, S.; Samanta, M.; Biswas, K. High-Performance Thermoelectric Energy Conversion Based on Lead-Free Group IV–VI Metal Chalcogenides. In *Inorganic Thermoelectric Materials: From Fundamental Concepts to Materials Design*; Powell, A. V., Eds.; Royal Society of Chemistry, 2021; pp 157–215.

- (88) Zhao, L. D.; Chang, C.; Tan, G.; Kanatzidis, M. G. *Energy Environ. Sci.* **2016**, *9*, 3044–3060.
- (89) Peng, K.; Lu, X.; Zhan, H.; Hui, S.; Tang, X.; Wang, G.; Dai, J.; Uher, C.; Wang, G.; Zhou, X. *Energy Environ. Sci.* **2016**, *9*, 454–460.
- (90) Qin, B.; Wang, D.; He, W.; Zhang, Y.; Wu, H.; Pennycook, S. J.; Zhao, L. D. *J. Am. Chem. Soc.* **2019**, *141*, 1141–1149.
- (91) Qin, B.; Zhang, Y.; Wang, D.; Zhao, Q.; Gu, B.; Wu, H.; Zhang, H.; Ye, B.; Pennycook, S. J.; Zhao, L. D. *J. Am. Chem. Soc.* **2020**, *142*, 5901–5909.
- (92) Zhou, C.; Lee, Y. K.; Yu, Y.; Byun, S.; Luo, Z.; Lee, H.; Ge, B.; Lee, Y.-L.; Chen, X.; Lee, J. Y.; Cojocaru-Mirédin, O.; Chang, H.; Im, J.; Cho, S.; Wuttig, M.; Dravid, V. P.; Kanatzidis, M. G.; Chung, I. *Nat. Mater.* **2021**, *20*, 1378–1384.
- (93) Lou, X.; Li, S.; Chen, X.; Zhang, Q.; Deng, H.; Zhang, J.; Li, D.; Zhang, X.; Zhang, Y.; Zeng, H.; Tang, G. *ACS Nano* **2021**, *15*, 8204–8215.
- (94) Liu, Y.; Calcabrini, M.; Yu, Y.; Lee, S.; Chang, C.; David, J.; Ghosh, T.; Spadaro, M. C.; Xie, C.; Cojocaru-Mirédin, O.; Arbiol, J.; Ibáñez, M. *ACS Nano* **2022**, *16*, 78–88.
- (95) Wei, T. R.; Tan, G.; Zhang, X.; Wu, C. F.; Li, J. F.; Dravid, V. P.; Snyder, G. J.; Kanatzidis, M. G. *J. Am. Chem. Soc.* **2016**, *138*, 8875–8882.
- (96) Chen, Y. X.; Ge, Z. H.; Yin, M.; Feng, D.; Huang, X. Q.; Zhao, W.; He, J. *Adv. Funct. Mater.* **2016**, *26*, 6836–6845.
- (97) Ge, Z. H.; Song, D.; Chong, X.; Zheng, F.; Jin, L.; Qian, X.; Zheng, L.; Dunin-Borkowski, R. E.; Qin, P.; Feng, J.; Zhao, L. D. *J. Am. Chem. Soc.* **2017**, *139*, 9714–9720.
- (98) Chen, C. L.; Wang, H.; Chen, Y. Y.; Day, T.; Snyder, G. J. *J. Mater. Chem. A* **2014**, *2*, 11171–11176.
- (99) Lee, Y. K.; Ahn, K.; Cha, J.; Zhou, C.; Kim, H. S.; Choi, G.; Chae, S. I.; Park, J. H.; Cho, S. P.; Park, S. H.; Sung, Y. E.; Lee, W. B.; Hyeon, T.; Chung, I. *J. Am. Chem. Soc.* **2017**, *139*, 10887–10896.
- (100) Luo, Y.; Cai, S.; Hua, X.; Chen, H.; Liang, Q.; Du, C.; Zheng, Y.; Shen, J.; Xu, J.; Wolverton, C.; Dravid, V. P.; Yan, Q.; Kanatzidis, M. G. *Adv. Energy Mater.* **2019**, *9*, 1803072.
- (101) Lin, C. C.; Lydia, R.; Yun, J. H.; Lee, H. S.; Rhyee, J. S. *Chem. Mater.* **2017**, *29*,

5344–5352.

- (102) Luo, Y.; Hao, S.; Cai, S.; Slade, T. J.; Luo, Z. zhen; Dravid, V. P.; Wolverton, C.; Yan, Q.; Kanatzidis, M. G. *J. Am. Chem. Soc.* **2020**, *142*, 15187–15198.
- (103) Tang, G.; Wei, W.; Zhang, J.; Li, Y.; Wang, X.; Xu, G.; Chang, C.; Wang, Z.; Du, Y.; Zhao, L. D. *J. Am. Chem. Soc.* **2016**, *138*, 13647–13654.
- (104) Wei, W.; Chang, C.; Yang, T.; Liu, J.; Tang, H.; Zhang, J.; Li, Y.; Xu, F.; Zhang, Z.; Li, J.-F.; Tang, G. *J. Am. Chem. Soc.* **2018**, *140*, 499–505.
- (105) Chandra, S.; Dutta, P.; Biswas, K. *ACS Nano* **2022**, *16*, 7–14.
- (106) Liu, J.; Wang, P.; Wang, M.; Xu, R.; Zhang, J.; Liu, J.; Li, D.; Liang, N.; Du, Y.; Chen, G.; Tang, G. *Nano Energy* **2018**, *53*, 683–689.
- (107) Shi, X.; Wu, A.; Liu, W.; Moshwan, R.; Wang, Y.; Chen, Z.-G.; Zou, J. *ACS Nano* **2018**, *12*, 11417–11425.
- (108) Wang, X.; Xu, J.; Liu, G.; Fu, Y.; Liu, Z.; Tan, X.; Shao, H.; Jiang, H.; Tan, T.; Jiang, J. *Appl. Phys. Lett.* **2016**, *108*, 083902.
- (109) Ge, Z.; Qiu, Y.; Chen, Y.; Chong, X.; Feng, J.; Liu, Z.; He, J. *Adv. Funct. Mater.* **2019**, *29*, 1902893.
- (110) Li, S.; Wang, Y.; Chen, C.; Li, X.; Xue, W.; Wang, X.; Zhang, Z.; Cao, F.; Sui, J.; Liu, X.; Zhang, Q. *Adv. Sci.* **2018**, *5*, 1800598.
- (111) Shi, X.-L.; Zheng, K.; Liu, W.-D.; Wang, Y.; Yang, Y.-Z.; Chen, Z.-G.; Zou, J. *Adv. Energy Mater.* **2018**, *8*, 1800775.
- (112) Zhang, Q.; Chere, E. K.; Sun, J.; Cao, F.; Dahal, K.; Chen, S.; Chen, G.; Ren, Z. *Adv. Energy Mater.* **2015**, *5*, 1500360.
- (113) Cai, J.; Zhang, Y.; Yin, Y.; Tan, X.; Duan, S.; Liu, G.; Hu, H.; Xiao, Y.; Ge, Z.; Jiang, J. *J. Mater. Chem. C* **2020**, *8*, 13244–13252.
- (114) Lee, Y. K.; Luo, Z.; Cho, S. P.; Kanatzidis, M. G.; Chung, I. *Joule* **2019**, *3*, 719–731.
- (115) Lei, S.; Lin, J.; Jia, Y.; Gray, M.; Topp, A.; Farahi, G.; Klemen, S.; Gao, T.; Rodolakis, F.; McChesney, J. L.; Ast, C. R.; Yazdani, A.; Burch, K. S.; Wu, S.; Ong, N. P.; Schoop, L. M. *Sci. Adv.* **2020**, *6*, eaay6407.
- (116) Shi, X.; Pei, Y.; Snyder, G. J.; Chen, L. *Energy Environ. Sci.* **2011**, *4*, 4086.
- (117) Costescu, R. M.; Cahill, D. G.; Fabreguette, F. H.; Sechrist, Z. A.; George, S. M. *Science* **2004**, *303*, 989–990.

-
- (118) Malliakas, C.; Billinge, S. J. L.; Kim, H. J.; Kanatzidis, M. G. *J. Am. Chem. Soc.* **2005**, *127*, 6510–6511.
- (119) Ru, N.; Chu, J.-H.; Fisher, I. R. *Phys. Rev. B* **2008**, *78*, 012410.
- (120) Zocco, D. A.; Hamlin, J. J.; Grube, K.; Chu, J.-H.; Kuo, H.-H.; Fisher, I. R.; Maple, M. B. *Phys. Rev. B* **2015**, *91*, 205114.
- (121) Gruner, G. *Density Waves in Solids* CRC Press, 1994.
- (122) Peierls, R. E. *Quantum Theory of Solids*; Oxford University Press, 2001.
- (123) Zhu, X.; Cao, Y.; Zhang, J.; Plummer, E. W.; Guo, J. *Proc. Natl. Acad. Sci.* **2015**, *112*, 2367–2371.
- (124) Kohn, W. *Phys. Rev. Lett.* **1959**, *2*, 393–394.
- (125) Liu, J. S.; Huan, S. C.; Liu, Z. H.; Liu, W. L.; Liu, Z. T.; Lu, X. L.; Huang, Z.; Jiang, Z. C.; Wang, X.; Yu, N.; Zou, Z. Q.; Guo, Y. F.; Shen, D. W. *Phys. Rev. Mater.* **2020**, *4*, 114005.
- (126) Hogg, J. H. C.; Sutherland, H. H.; Williams, D. J. *Acta Cryst.* **1973**, *29*, 1590–1593.
- (127) Pouget, J.-P. *C. R. Phys.* **2016**, *17*, 332–356.
- (128) Bhatt, R.; Bhattacharya, S.; Basu, R.; Ahmad, S.; Chauhan, A. K.; Okram, G. S.; Bhatt, P.; Roy, M.; Navaneethan, M.; Hayakawa, Y.; Debnath, A. K.; Singh, A.; Aswal, D. K.; Gupta, S. K. *ACS Appl. Mater. Interfaces* **2014**, *6*, 18619–18625.
- (129) Kim, D.; Cho, S.; Butch, N. P.; Syers, P.; Kirshenbaum, K.; Adam, S.; Paglione, J.; Fuhrer, M. S. *Nat. Phys.* **2012**, *8*, 459–463.
- (130) Chen, Y. L.; Analytis, J. G.; Chu, J.-H.; Liu, Z. K.; Mo, S.-K.; Qi, X. L.; Zhang, H. J.; Lu, D. H.; Dai, X.; Fang, Z.; Zhang, S. C.; Fisher, I. R.; Hussain, Z.; Shen, Z.-X. *Science* **2009**, *325*, 178–181.
- (131) Zhang, H.; Liu, C. X.; Qi, X. L.; Dai, X.; Fang, Z.; Zhang, S. C. *Nat. Phys.* **2009**, *5*, 438–442.
- (132) Lind, H.; Lidin, S.; Häussermann, U. *Phys. Rev. B* **2005**, *72*, 184101.
- (133) Majhi, K.; Pal, K.; Lohani, H.; Banerjee, A.; Mishra, P.; Yadav, A. K.; Ganesan, R.; Sekhar, B. R.; Waghmare, U. V.; Anil Kumar, P. S. *Appl. Phys. Lett.* **2017**, *110*, 162102.
- (134) Samanta, M.; Pal, K.; Pal, P.; Waghmare, U. V.; Biswas, K. *J. Am. Chem. Soc.* **2018**, *140*, 5866–5872.

- (135) Gooth, J.; Schierning, G.; Felser, C.; Nielsch, K. *MRS Bull.* **2018**, *43*, 187–192.
- (136) Xu, N.; Xu, Y.; Zhu, J. *npj Quantum Mater.* **2017**, *2*, 51.
- (137) Roychowdhury, S.; Samanta, M.; Banik, A.; Biswas, K. *J. Solid State Chem.* **2019**, *275*, 103–123.
- (138) MÜchler, L.; Zhang, H.; Chadov, S.; Yan, B.; Casper, F.; Kübler, J.; Zhang, S. C.; Felser, C. *Angew. Chem. Int. Ed.* **2012**, *51*, 7221–7225.
- (139) Moore, J. E. *Nature* **2010**, *464*, 194–198.
- (140) Hasan, M. Z.; Kane, C. L. *Rev. Mod. Phys.* **2010**, *82*, 3045–3067.
- (141) Ringel, Z.; Kraus, Y. E.; Stern, A. *Phys. Rev. B* **2012**, *86*, 045102.
- (142) Lifshitz, I. M. *Sov. Phys. JETP.* **1960**, *11*, 1130–1135.
- (143) Blanter, Y. M.; Kaganov, M. I.; Pantsulaya, A. V.; Varlamov, A. A. *Phys. Rep.* **1994**, *245*, 159–257.
- (144) Polvani, D. A.; Meng, J. F.; Chandra Shekar, N. V.; Sharp, J.; Badding, J. V. *Chem. Mater.* **2001**, *13*, 2068–2071.
- (145) Manjón, F. J.; Vilaplana, R.; Gomis, O.; Pérez-González, E.; Santamaría-Pérez, D.; Marín-Borrás, V.; Segura, A.; González, J.; Rodríguez-Hernández, P.; Muñoz, A.; Drasar, C.; Kucek, V.; Muñoz-Sanjose, V. *Phys. Status Solidi B* **2013**, *250*, 669–676.
- (146) Vilaplana, R.; Santamaría-Pérez, D.; Gomis, O.; Manjón, F. J.; González, J.; Segura, A.; Muñoz, A.; Rodríguez-Hernández, P.; Pérez-González, E.; Marín-Borrás, V.; Muñoz-Sanjose, V.; Drasar, C.; Kucek, V. *Phys. Rev. B* **2011**, *84*, 184110.
- (147) Olijnyk, H.; Jephcoat, A. P.; Novikov, D. L.; Christensen, N. E. *Phys. Rev. B* **2000**, *62*, 5508–5512.
- (148) Munir, Z. A.; Anselmi-Tamburini, U.; Ohyanagi, M. *J. Mater. Sci.* **2006**, *41*, 763–777.
- (149) Xie, G. *J. Powder Metall. Min.* **2013**, *2*, e109.
- (150) Hall, E. H. *Am. J. Math.* **1879**, *2*, 287–292.
- (151) Parker, W. J.; Jenkins, R. J.; Butler, C. P.; Abbott, G. L. *J. Appl. Phys.* **1961**, *32*, 1679–1684.
- (152) Cowan, R. D. *J. Appl. Phys.* **1963**, *34*, 926–927.
- (153) Physical Property Measurement System - Heat Capacity Option - User's Manual

(Quantum Design), **1999**.

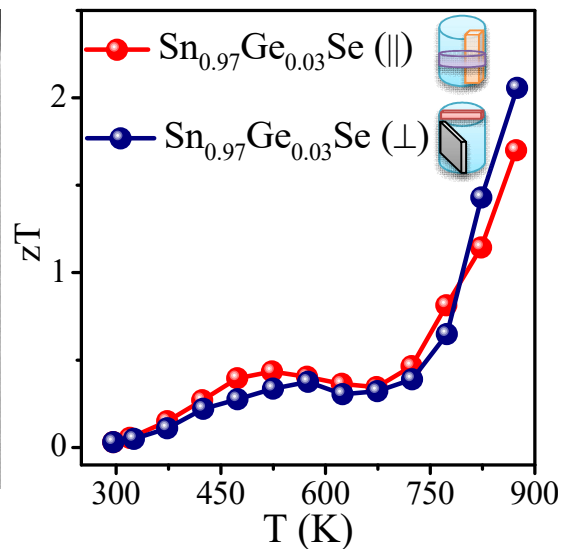
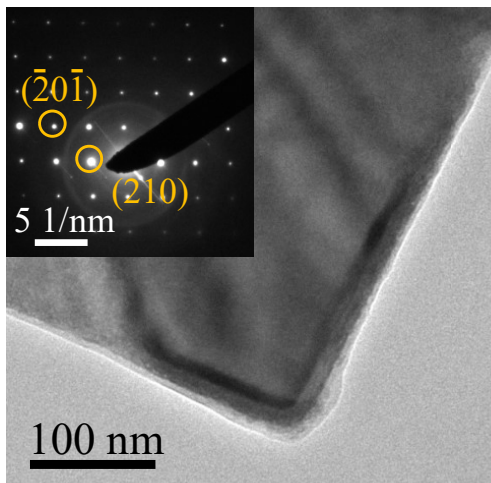
- (154) Weir, C. E.; Lippincott, E. R.; Van Valkenburg, A.; Bunting, E. N. *J. Res. Natl. Bur. Stand.* **1959**, *63A*, 55.
- (155) Bassett, W. A. *High Press. Res.* **2009**, *29*, 163–186.
- (156) Klotz, S.; Chervin, J.-C.; Munsch, P.; Le Marchand, G. *J. Phys. D. Appl. Phys.* **2009**, *42*, 075413.
- (157) Barnett, J. D.; Block, S.; Piermarini, G. J. *Rev. Sci. Instrum.* **1973**, *44*, 1–9.
- (158) Mao, H. K.; Bell, P. M.; Shaner, J. W.; Steinberg, D. J. *J. Appl. Phys.* **1978**, *49*, 3276–3283.

PART 2

Solution Grown Nanocrystalline SnSe

Chapter 2.1

Realization of High Thermoelectric Figure of Merit in Solution Synthesized 2D SnSe Nanoplates via Ge Alloying



Realization of High Thermoelectric Figure of Merit in Solution Synthesized 2D SnSe Nanoplates via Ge Alloying[†]

Summary

Recently, single crystals of layered SnSe have created a paramount importance in thermoelectrics owing to their ultralow lattice thermal conductivity and high thermoelectric figure of merit (zT). However, nanocrystalline or polycrystalline SnSe offers a wide range of thermoelectric applications for the ease of its synthesis and machinability. Here, we have demonstrated high zT of 2.1 at 873 K in two dimensional (2D) nanoplates of Ge doped SnSe synthesized by a simple hydrothermal route followed by spark plasma sintering (SPS). Anisotropic measurements also show a high zT of ~ 1.8 at 873 K parallel to the SPS pressing direction. 3 mol% Ge-doping in SnSe nanoplates significantly enhances the p-type carrier concentration which results in high electrical conductivity and power factor of $\sim 5.10 \mu\text{W}/\text{cmK}^2$ at 873 K. In addition to nanoscale grain boundary and high lattice anharmonicity in SnSe nanoplates, phonon scattering due to Ge precipitates in the SnSe matrix gives rise to the ultralow lattice thermal conductivity of $\sim 0.18 \text{ W}/\text{mK}$ at 873 K.

[†]S. Chandra, and K. Biswas. *J. Am. Chem. Soc.*, 2019, *141*, 6141–6145.

2.1.1. Introduction

Two dimensional layered metal chalcogenides have recently gained momentous attention in the field of thermoelectrics owing to their anisotropic crystal structure and low thermal conductivity.¹⁻⁵ Among the 2D layered materials, the IV-VI semiconductors are contemplated as the most promising thermoelectric materials, for instance SnSe, which sparked a huge interest among the scientists due to its fascinating thermoelectric properties arising from its ultralow thermal conductivity, chemical stability, earth-abundance, and low toxicity.⁶⁻¹¹ Single crystals of SnSe have lately shown an outstanding zT of ~ 2.6 at 923 K along crystallographic b -direction.⁶ However, polycrystalline or nanocrystalline SnSe is a preferred choice for thermoelectric applications due to the ease of its production and processability.¹² But polycrystalline samples generally show lower carrier mobility as compared to that of the single crystals, thus effectively reduce the zT values.¹²⁻¹⁷ Important reports are present which corroborate polycrystalline or nanocrystalline SnSe with various doping such alkali metal ions, Pb, Sb, Cu, Cl and I showing reasonably high zT .¹⁸⁻²³ However, in comparison with single crystals of SnSe, there are still scopes to improve the thermoelectric properties of polycrystalline SnSe by controlling the synthesis process and balancing the nanostructuring to optimize both the electronic and thermal transport properties.

Incidentally, GeSe adopts identical layered orthorhombic structure as SnSe at ambient conditions and showed promises in thermoelectrics.²⁴⁻²⁶ Thus, GeSe may form a solid solution with SnSe and can decrease the thermal conductivity. Moreover, Ge being more electronegative than Sn, can form an impurity dopant level slightly below the conduction band formed mainly by Sn, thus can effectively decrease the band gap of SnSe which may also optimize the electronic transport properties. Although, there are few earlier reports on the Ge doping in polycrystalline SnSe synthesized by high temperature solid state reaction, but the zT remains very low ~ 0.7 at around 850 K.²⁷⁻²⁹ Thus, we thought to explore the effect of Ge doping on the thermoelectric properties of 2D SnSe nanoplates synthesized by low temperature solution route.

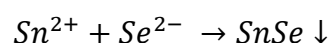
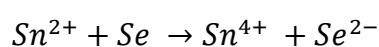
In this chapter, I present high thermoelectric figure of merit (zT) of 2.1 at 873 K in Ge doped 2D SnSe nanoplates synthesized by a facile low temperature hydrothermal synthesis followed by spark plasma sintering (SPS). Ge doping increases the carrier

concentration which leads to enhanced electrical conductivity and power factor in $\text{Sn}_{1-x}\text{Ge}_x\text{Se}$. Upon 3 mol% Ge doping in SnSe, the system deviates from solid solution and Ge starts precipitating in the SnSe matrix. $\text{Sn}_{0.97}\text{Ge}_{0.03}\text{Se}$ sample exhibits ultralow thermal conductivity of ~ 0.18 W/mK at 873 K due to synergistic phonon scattering by point defects, nano precipitates, nanoscale grains and inherent lattice anharmonicity. As SnSe possess an anisotropic structure, we have measured thermoelectric properties in both the parallel and perpendicular directions to the SPS pressing axis, which show a high zT of ~ 1.8 at 873 K parallel to the SPS pressing direction in $\text{Sn}_{0.97}\text{Ge}_{0.03}\text{Se}$.

2.1.2. Methods

Reagents. Tin (II) chloride dihydrate ($\text{SnCl}_2 \cdot 2\text{H}_2\text{O}$, 98%, Sigma Aldrich), selenium powder (Se, 99.99%, Alfa Aesar), germanium (IV) iodide (GeI_4 , 99%, Sigma Aldrich) and sodium hydroxide pellets (NaOH, 98% Sigma Aldrich) were used for the synthesis.

Synthesis. $\text{Sn}_{1-x}\text{Ge}_x\text{Se}$ ($x = 1-3$ mol%) nanoplates were synthesized using simple hydrothermal route. First a mixture of $\text{SnCl}_2 \cdot 2\text{H}_2\text{O}$ (2 mmol) and GeI_4 (x mmol%) were dissolved in deionized water. The solution was then sonicated at room temperature for 10 min, followed by addition of NaOH (30 mmol) and sonication for another 10 min unless a clear solution was obtained. The mixture was then transferred to a Teflon-lined stainless-steel autoclave of 25 ml capacity and Se powder (1 mmol) was added to it that results in a black solution. The autoclaves were then sealed tightly and heated to 130 °C for 36 h. After cooling to room temperature, the black precipitate was collected and thoroughly washed with absolute ethanol and deionized water for several times. Finally, the product was vacuum dried at 60 °C for 6 h and collected as powder. During the synthesis, NaOH acts as a solubilizing agent. Slight excess of Sn^{2+} should always be present in the reaction mixture (molar ratio of Sn^{2+} and Se must be higher than two) as Sn^{2+} itself acts as a reductant and precipitant.^{16,30}



The yield of the reaction was $\sim 95\%$ and the product was scaled up to 10 gm for the thermoelectric measurements. The nanoplates were dispersed in ethanol for further characterizations.

Powder X-ray diffraction (PXRD) patterns of the samples were collected using $\text{CuK}\alpha$ ($\lambda=1.5406 \text{ \AA}$) radiation on a Bruker D8 diffractometer at room temperature.

Field emission scanning electron microscopy (FESEM) experiments were performed using NOVANO SEM 600 (FEI, Germany) operated at 15 kV. EDAX compositional analysis was performed during FESEM imaging.

Back-scattered electron microscopy (BSE) imaging was performed during FESEM using ZEISS Gemini SEM – Field Emission Scanning Electron Microscope operated at 500V.

Atomic force microscopy (AFM) was performed on a Bruker Innova Microscope in tapping mode with 10 nm diameter containing antimony doped Silicon tip.

Transmission electron microscopy (TEM) images of the as synthesized materials were taken using a JEOL (JEM3010) TEM instrument (300 kV accelerating voltage) fitted with a Gatan CCD camera and also with a FEI TECNAI G2 20 STWIN TEM instrument (operating at 200 kV). A suspension of the nanosheets was prepared in cyclohexane solution and it was then drop casted in a holey carbon coated Cu grid for TEM imaging.

Scanning transmission electron microscopy (STEM) imaging was carried out using FEITECNAI G² 20 STWIN TEM operating at 200 KV. The sample preparation was same as that of TEM. EDAX compositional analysis and color mapping were performed during STEM imaging. Background was subtracted (using multi-polynomial model) during the data processing for EDAX color mapping (with 500 eV minimum region of interest width). Errors in the determination in compositions of nanosheets in EDAX measurements is nearly 5%.

X-ray photoelectron spectroscopy (XPS) measurement was performed with $\text{MgK}\alpha$ (1253.6 eV) X-ray source with a relative composition detection better than 0.1% on an Omicron Nano-technology spectrometer.

Band gap measurements. To estimate the optical band gap, diffuse reflectance measurements were carried out in the range of $\lambda = 250$ to 800 nm by using a Perkin-Elmer Lambda 900 UV/Vis/near-IR spectrometer in reflectance mode. Absorption (α/λ) data were calculated from reflectance data by using the Kubelka–Munk equation: $\alpha/\lambda = (1-R)^2/(2R)$, in which R is the reflectance, α and λ are the absorption and scattering coefficients respectively. The energy band gaps were derived from α/λ vs. E (eV) plots.

Inductively coupled plasma atomic emission spectroscopy (ICP-AES). The exact composition of the as synthesized nanosheets was calculated based on ICP-AES data. ICP-AES measurements were carried out using Perkin-Elmer Optima 7000DV instrument. ICP-AES measurement were carried out by dissolving the powder nanosheets in aquaregia ($\text{HNO}_3:\text{HCl} = 1:3$) followed by diluting with millipore water. Sn standard (1000 mg/L, Sigma-Aldrich), Se standard (1000 mg/L, Sigma-Aldrich) and Bi standard (1000 mg/L, Sigma-Aldrich) were used to determine the compositions in ICP. In the present measurement, error bar lies below 1.5 %.

Spark plasma sintering (SPS) was done using a SPS211-LX (Dr. Sinter Lab) instrument. The powdered nanoplates were sintered to prepare a rectangular column (8 mm \times 8 mm \times 8 mm) and coin (2 mm \times 10 mm) using graphite dies at 50 MPa pressure and 450 °C temperature for 10 minutes. From the rectangular column, a rectangular bar (2 mm \times 2 mm \times 8 mm) was made using a typical cutter-polisher. The density of the SPS processed samples were found to be about ~ 95 % of theoretical density.

For further comparison, powdered samples had been compacted using Inductively heated uniaxial hot press in argon atmosphere at 45 MPa pressure and 500 °C temperature.

Electrical transport properties. Electrical conductivity (σ) and Seebeck coefficients (S) were measured simultaneously from the rectangular bar under helium atmosphere from room temperature to 873 K using a ULVAC-RIKO ZEM-3 instrument system. σ and S were measured in both the parallel and perpendicular to the pressing directions.

Hall measurement. Room temperature carrier concentrations were determined from Hall coefficient measurements with the equipment developed by Excel Instrument, India. Four-contact Hall-bar geometry was used for the measurement. The applied magnetic

field was 0.57 Tesla. Room temperature carrier concentration, n , was measured using the formula $n = I/eR_H$, where e is the electronic charge, R_H is hall coefficient.

Thermal transport properties. The thermal diffusivity (D) of the coin-shaped samples have been measured by laser flash diffusivity technique using NETZSCH LFA 457 instrument in 300–873 K range. Total thermal conductivity (κ) was calculated using the formula $\kappa = DC_p\rho$, where D is the thermal diffusivity, C_p is specific heat, and ρ is density of the sample. Temperature dependent heat capacity, C_p was derived using standard sample (pyroceram). Further, the electronic thermal conductivities, κ_{ele} were estimated using Wiedemann-Franz Law, $\kappa_{ele} = L\sigma T$, where L is the Lorenz number which is estimated by fitting reduced chemical potential derived from temperature-dependent Seebeck coefficient using single parabolic band conduction and dominant acoustic phonon scattering of carriers.

2.1.3. Results and Discussions

The powder X-ray diffraction (PXRD) patterns of as synthesized $\text{Sn}_{1-x}\text{Ge}_x\text{Se}$ ($x = 0-3$ mol%) were indexed with orthorhombic SnSe ($Pnma$).^{6,7} However, an additional low intense peak appears in case of 3 mol% Ge doped SnSe near the $(011)_{\text{SnSe}}$ peak which can be attributed as Ge second phase (Figure 2.1.1). Thus, the solid solution limit exceeds after 2 mol% of Ge doping in SnSe and traces of Ge starts precipitating out into the matrix. The peaks for $\text{Sn}_{1-x}\text{Ge}_x\text{Se}$ are slightly right shifted than that of the pristine sample which is in good agreement with the smaller atomic radius of Ge (211 pm) in comparison to Sn (225 pm).

The optical band gap of SnSe (1.01 eV) decreases slightly after Ge incorporation (Figure 2.1.2). Ge being more electronegative than Sn creates an impurity acceptor level slightly below the conduction band formed mainly by Sn, which reduces the band gap of the $\text{Sn}_{1-x}\text{Ge}_x\text{Se}$ nanoplates.

The morphology of the as synthesized $\text{Sn}_{0.97}\text{Ge}_{0.03}\text{Se}$ samples resembles to that of the 2D nanoplates which is evident from TEM (Figure 2.1.3a) and FESEM (Figure 2.1.3c) images. The lateral dimension of the nanoplates ranges from 0.5 - 1.0 μm . The single crystalline nature of the nanoplate is verified by the HRTEM image (Figure 2.1.3b). The

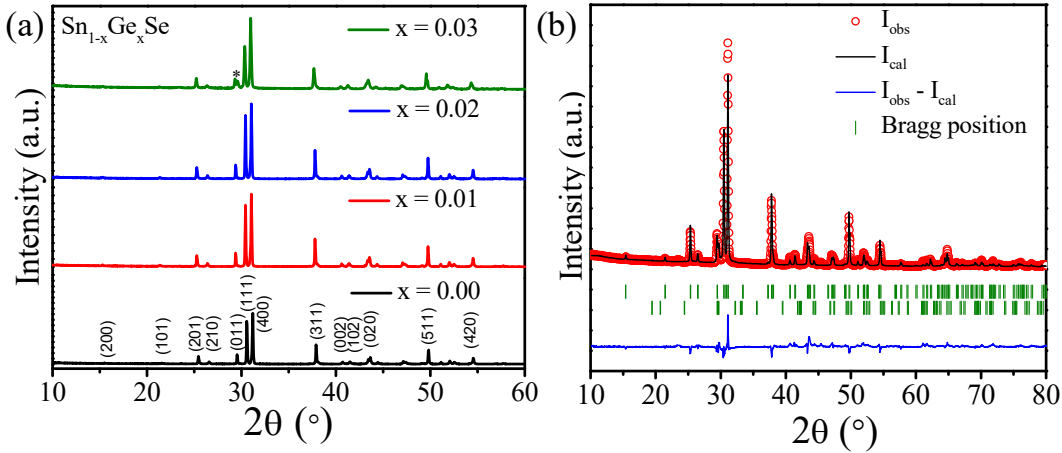


Figure 2.1.1. (a) PXRD patterns of as-synthesized Ge doped SnSe nanoplates. The additional peak (denoted by *) that appears near the (011)_{SnSe} peak indicates the trace of Ge precipitates in SnSe matrix. (b) Rietveld refinement of room-temperature PXRD data of as-synthesized Sn_{0.97}Ge_{0.03}Se sample using Fullprof. We have included Ge second phase during refinement.

lattice spacing between two apparent planes was estimated to be 3.07 Å which indicates that the (011) set of planes are exposed in Sn_{0.97}Ge_{0.03}Se nanoplates. In addition, selected area electron diffraction (SAED) of a single Sn_{0.97}Ge_{0.03}Se nanoplate shows a spot pattern

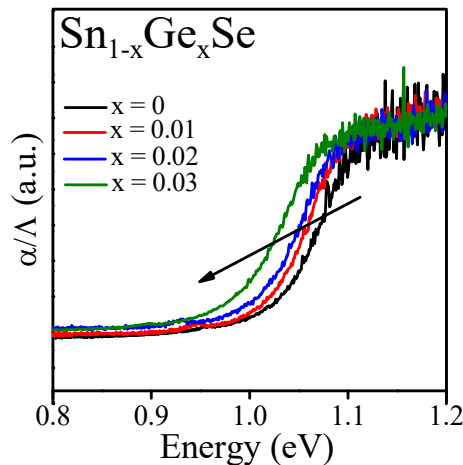


Figure 2.1.2. Electronic absorption spectra of Sn_{1-x}Ge_xSe nanoplates.

for (0kl) set of reflections (see inset of Figure 2.1.3a) confirming the single crystalline nature. The thickness of the as synthesized sample was determined by atomic force microscopy (AFM) (Figure 2.1.3d) which indicates the formation of 7 to 14 nm thick 2D nanoplates.

The elemental compositions of $\text{Sn}_{1-x}\text{Ge}_x\text{Se}$ nanoplates were determined from two independent experiments: energy-dispersive analysis of X-rays (EDAX) and inductively coupled plasma atomic emission spectroscopy (ICP-AES). Actual compositions determined by these two techniques are in well agreement with that of the nominal compositions (Table 2.1.1).

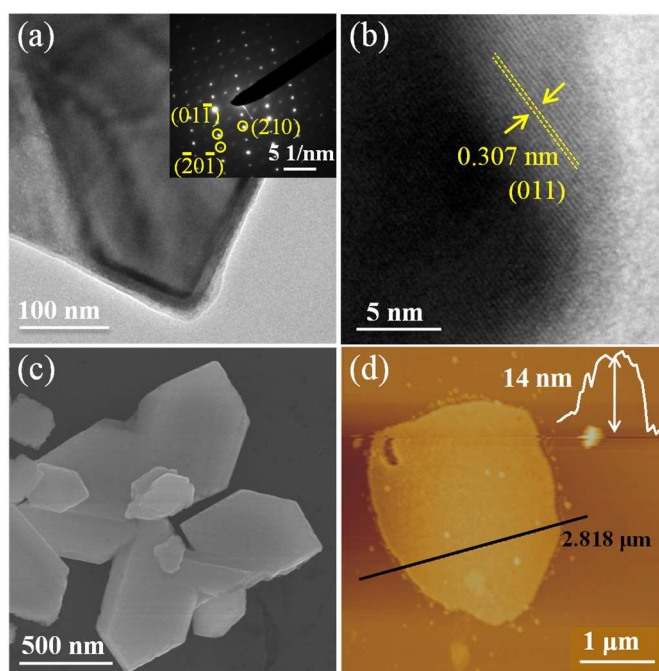


Figure 2.1.3. (a) TEM image of $\text{Sn}_{0.97}\text{Ge}_{0.03}\text{Se}$ nanoplates. SAED pattern of the same nanoplate is shown in the inset. (b) HRTEM and (c) FESEM image of $\text{Sn}_{0.97}\text{Ge}_{0.03}\text{Se}$ nanoplates. (d) AFM images of as-synthesized $\text{Sn}_{0.97}\text{Ge}_{0.03}\text{Se}$ nanoplates. The height profile acquired from the AFM micrographs indicate the thickness of the nanoplates lies in the range of 7–14 nm. The lateral dimension ranges from 0.5–3 μm .

Table 2.1.1. Analysis of sample compositions from ICP-AES and EDAX.

Nominal Composition	Composition obtained from ICP-AES	Composition obtained from EDAX
SnSe	$\text{SnSe}_{1.05}$	$\text{SnSe}_{1.1}$
$\text{Sn}_{0.99}\text{Ge}_{0.01}\text{Se}$	$\text{Sn}_{0.987}\text{Ge}_{0.014}\text{Se}_{1.03}$	-
$\text{Sn}_{0.98}\text{Ge}_{0.02}\text{Se}$	$\text{Sn}_{0.980}\text{Ge}_{0.026}\text{Se}$	-
$\text{Sn}_{0.97}\text{Ge}_{0.03}\text{Se}$	$\text{Sn}_{0.969}\text{Ge}_{0.036}\text{Se}_{1.1}$	$\text{Sn}_{0.959}\text{Ge}_{0.039}\text{Se}_{1.4}$

EDAX elemental color mapping was performed during scanning transmission electron microscopy (STEM) imaging which shows the presence of Sn, Se and Ge in $\text{Sn}_{0.97}\text{Ge}_{0.03}\text{Se}$ nanoplates (Figure 2.1.4).

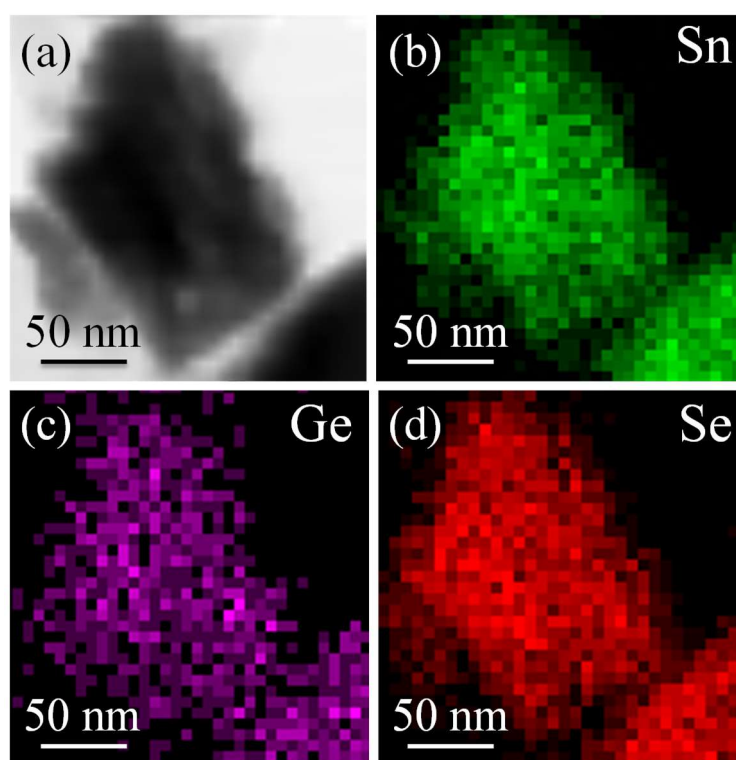


Figure 2.1.4. (a) STEM image of $\text{Sn}_{0.97}\text{Ge}_{0.03}\text{Se}$ nanoplates and EDAX color mapping for (b) Sn, (c) Ge, and (d) Se.

To understand the microstructure compositions in $\text{Sn}_{0.97}\text{Ge}_{0.03}\text{Se}$ SPS'ed and hot-pressed samples, back-scattered electron imaging (BSE) was performed during FESEM (Figure 2.1.5), which shows the presence of the dark contrast Ge precipitates of $\sim 2\text{--}10\ \mu\text{m}$ size embedded in lighter contrast SnSe matrix. Furthermore, EDAX line scanning on a precipitate along with the matrix (Figure 2.1.5a, denoted by a white line) was performed, which clearly indicates that the matrix is SnSe, whereas the precipitate is Ge rich (Figure 2.1.5b).

X-ray photoelectron spectroscopy (XPS) was performed on $\text{Sn}_{0.99}\text{Ge}_{0.01}\text{Se}$ which confirms the presence of Sn, Ge and Se in as synthesized nanoplates (Figure 2.1.6). The Sn 3d spin-orbit doublet peaks appeared at 489.1 eV and 499.3 eV with splitting of 10.2 eV, which can be assigned to Sn 3d_{5/2} and Sn 3d_{3/2}, respectively. We could be able to

deconvolute the broad peak of selenium as Se 3d_{5/2} and Se 3d_{3/2} at 53.3 eV and 55.7 eV respectively. Presence of Ge 3d_{5/2} and Ge 2p_{3/2} peaks at 32.1 eV and 1219.5 eV can be attributed to Ge (II) states in Sn_{0.99}Ge_{0.01}Se.^{27–29}

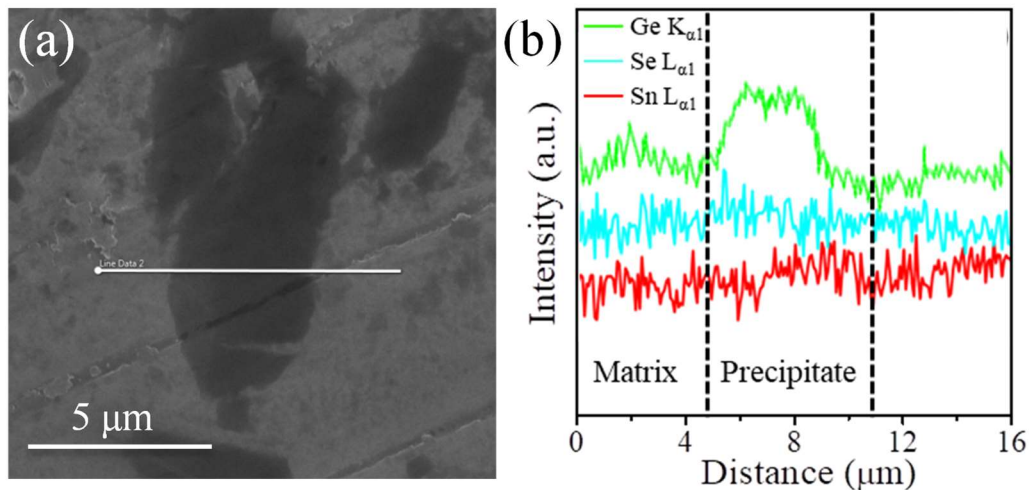


Figure 2.1.5. (a) Backscattered FESEM image from SPS processed Sn_{0.97}Ge_{0.03}Se, which shows the presence of precipitates of relatively dark contrast and large size. (b) EDAX line scan along the precipitate (highlighted in image a).

SnSe exhibits anisotropy in different crystallographic directions, thereby the thermoelectric measurements are done both in \parallel (parallel) & \perp (perpendicular) to the pressing direction of SPS. A schematic illustration of the anisotropic measurement is given in Figure 2.1.7.

We have measured the thermoelectric properties (\parallel & \perp direction) of the SPS'ed samples of Sn_{1-x}Ge_xSe ($x = 0-3$ mol%) in the temperature range of 300 – 873 K. In each case, thermoelectric properties are higher in the perpendicular direction as compared to parallel direction to the SPS which is a typical behavior of SnSe.^{13,19} Figure 2.1.8a and 2.1.8b represent the variation of σ with temperature measured along the parallel and perpendicular to the pressing direction respectively. The dependence of electrical conductivity for all the samples follows a similar trend which can be described as follows. First, semiconducting transport behavior exhibits from 300 to 500 K due to the thermal excitation of minority carriers; then a metallic behavior is noticed up to 675 K; then the σ increases significantly with increasing temperature further to 873 K, which can be

attributed to the structural phase transition from $Pnma$ to $Cmcm$ at ~ 800 K, which has a similar trend to the previous SnSe samples.^{13,22} Typically, the σ values for the Sn_{0.97}Ge_{0.03}Se (for the \perp direction) was measured to be 13.8 Scm^{-1} at 295 K, which increases to 67.9 Scm^{-1} with the increase in temperature. Ge doping in SnSe increases the p -type carrier concentration (Table 2.1.2).

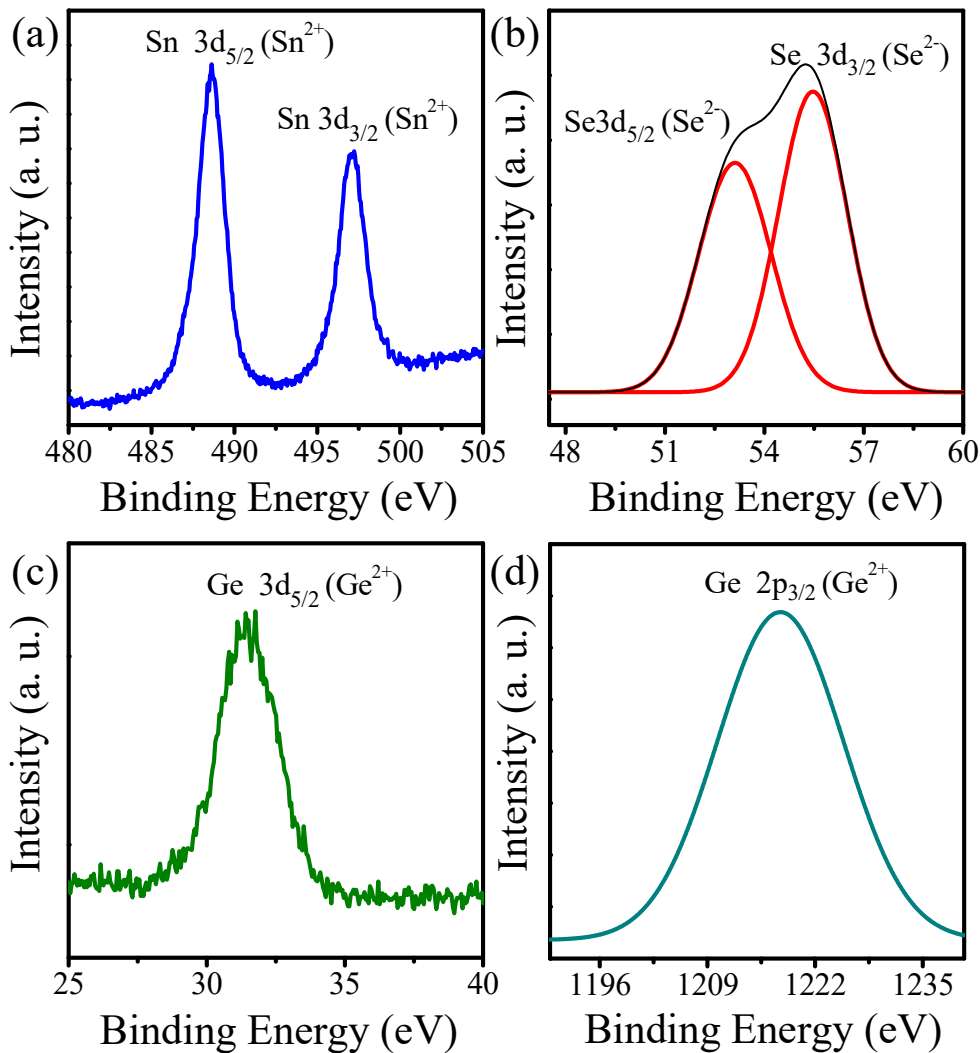


Figure 2.1.6. High-resolution XPS of (a) Sn 3d, (b) Se 3d, (c) Ge 3d and (d) 2p orbital in Sn_{0.99}Ge_{0.01}Se nanoplates. The binding energy of the elements confirms that Sn, Se and Ge are in +2, -2 and +2 oxidation states respectively.

For 3 mol% Ge doped SnSe, carrier concentration ($4.2 \times 10^{19} \text{ cm}^{-3}$) is increased by two orders of magnitude than the pristine sample ($3.9 \times 10^{17} \text{ cm}^{-3}$). With increasing the Ge

concentration in $\text{Sn}_{1-x}\text{Ge}_x\text{Se}$, Ge started precipitating out in SnSe matrix when the solid solution limit exceeds, which creates Sn^{2+} vacancies and thereby enhances the overall p -type carrier concentration. Thus, the improved carrier concentration in $\text{Sn}_{0.97}\text{Ge}_{0.03}\text{Se}$ gives rise to enhanced electrical conductivity compared to the pristine SnSe.

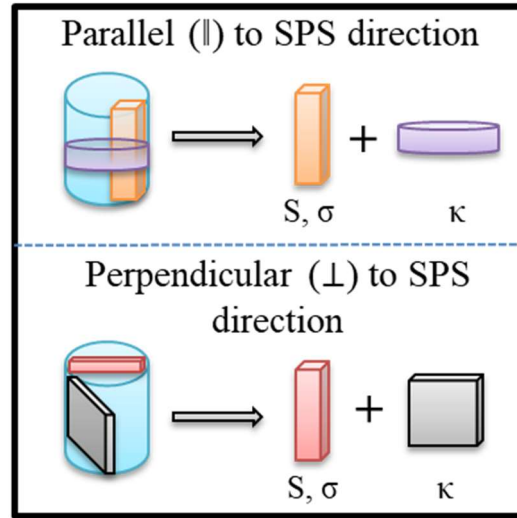


Figure 2.1.7. A schematic illustration to understand the anisotropic transport properties of SnSe.

Figures 2.1.8c and 2.1.8d show the temperature dependence of Seebeck coefficient for the $\text{Sn}_{1-x}\text{Ge}_x\text{Se}$ ($x = 0-3$ mol%) samples measured in the parallel and perpendicular directions, respectively. The $\text{Sn}_{1-x}\text{Ge}_x\text{Se}$ samples exhibit lower S values than the pristine sample, which is consistent with the enhanced carrier concentrations as confirmed by Hall measurements.

Table 2.1.2. Room temperature carrier concentrations of $\text{Sn}_{1-x}\text{Ge}_x\text{Se}$ samples.

Composition	Carrier Concentration (n) cm^{-3}
SnSe	3.9×10^{17}
$\text{Sn}_{0.99}\text{Ge}_{0.01}\text{Se}$	6.7×10^{18}
$\text{Sn}_{0.98}\text{Ge}_{0.02}\text{Se}$	9.0×10^{18}
$\text{Sn}_{0.97}\text{Ge}_{0.03}\text{Se}$	4.2×10^{19}

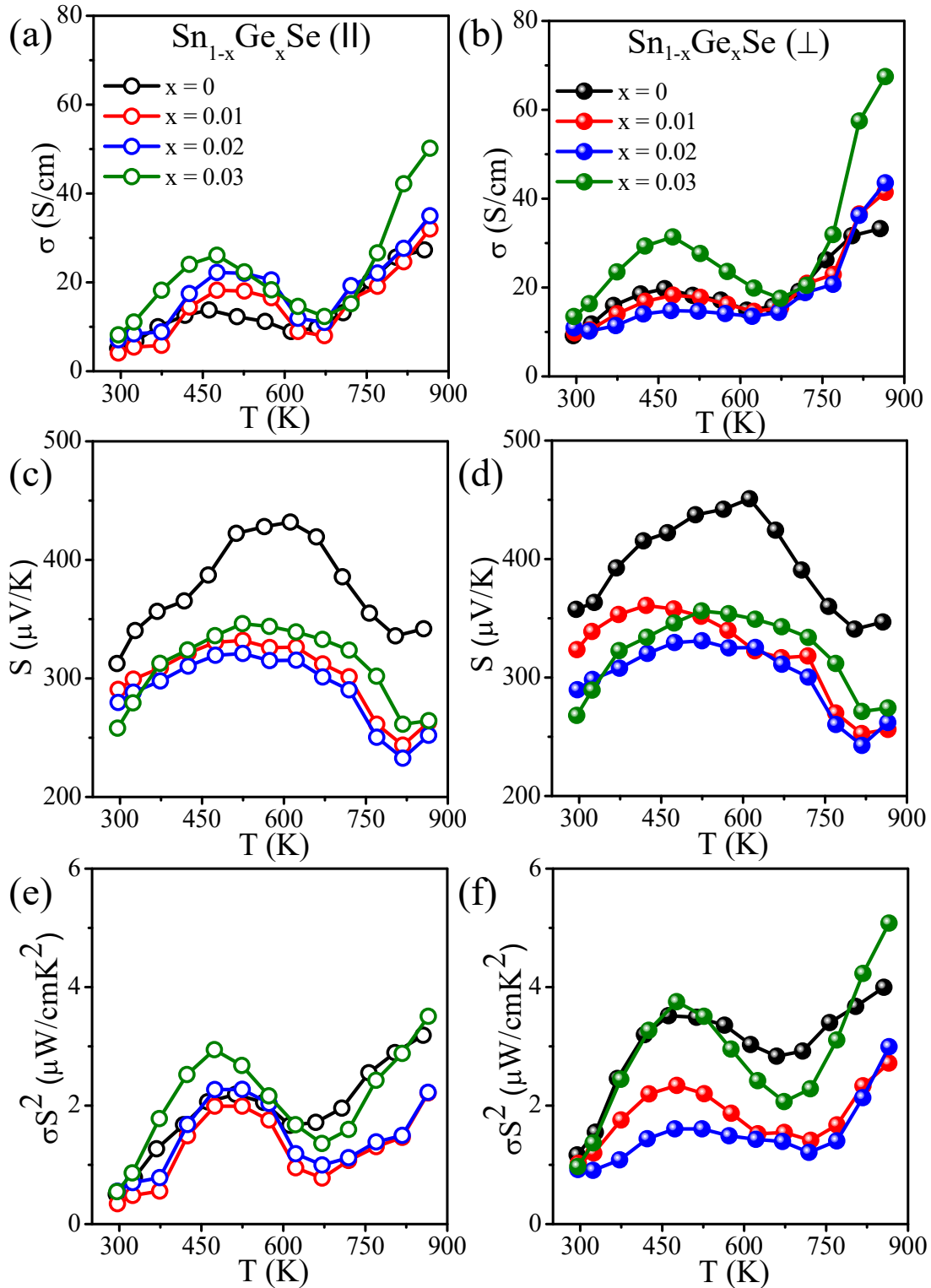


Figure 2.1.8. Temperature dependent (a), (b) electrical conductivity, (c), (d) Seebeck coefficient, and (e), (f) power factor of $\text{Sn}_{1-x}\text{Ge}_x\text{Se}$ measured parallel (open symbols) and perpendicular (solid symbols) to the SPS pressing direction respectively.

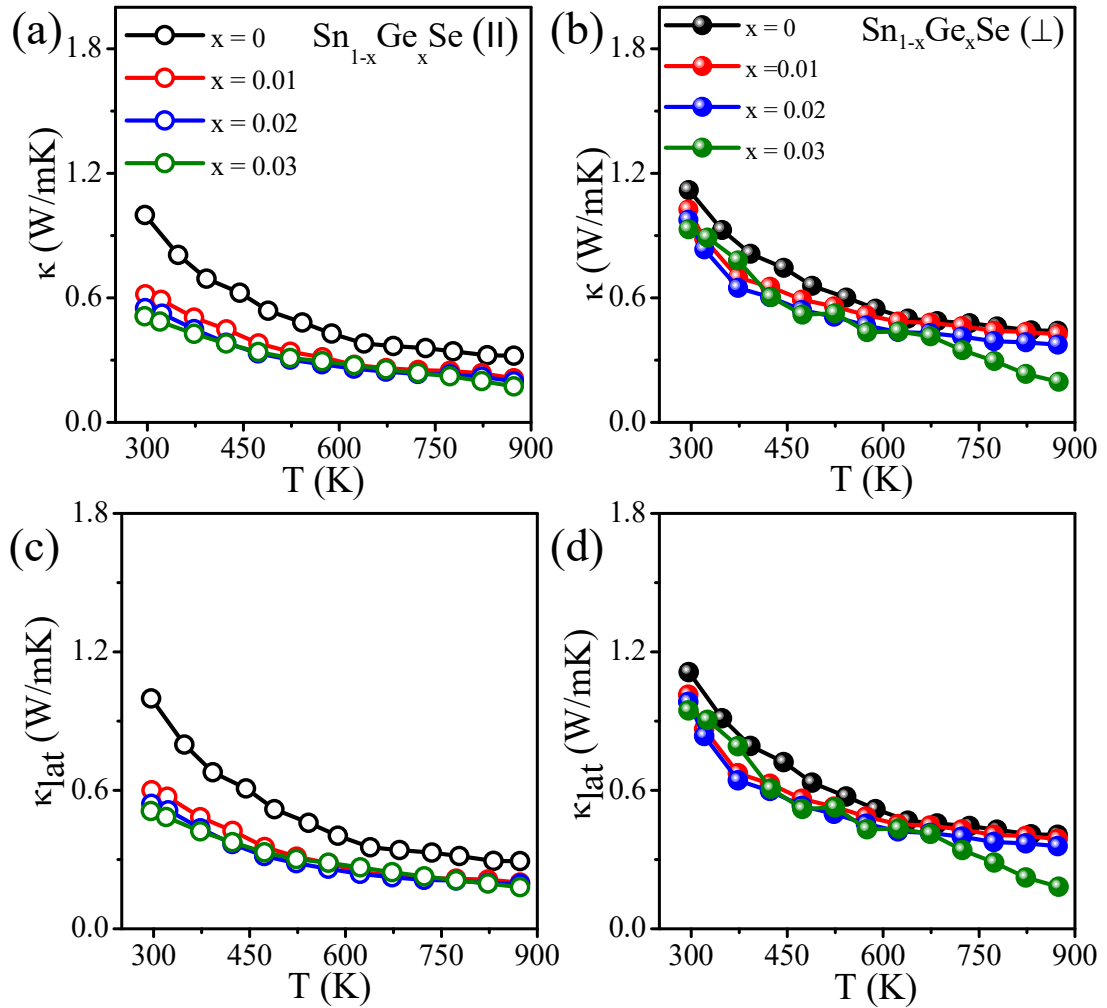


Figure 2.1.9. Temperature dependent (a), (b) total thermal conductivity, and (c), (d) lattice thermal conductivity of $\text{Sn}_{1-x}\text{Ge}_x\text{Se}$ measured parallel (open symbols) and perpendicular (solid symbols) to the SPS pressing direction respectively.

Initially, with increase in temperature, Seebeck coefficient increases and reaches to a maximum value in the temperature range of 550-650 K which is typical for solution processed SnSe samples.^{13,22} The peak in the temperature dependent Seebeck coefficient indicates the bipolar conduction.^{13,22} The increase in Seebeck coefficient after 800 K indicates the structural phase transition.^{13,22} The power factor of the $\text{Sn}_{1-x}\text{Ge}_x\text{Se}$ samples is given in Figures 2.1.8e and 2.1.8f. Remarkable high value of power factor ($\sim 5.10 \mu\text{W}/\text{cmK}^2$) is obtained for 3 mol% Ge doped polycrystalline SnSe at 873 K along perpendicular to SPS pressing direction.

Figures 2.1.9a and 2.1.9b show the temperature dependent κ measured parallel and

perpendicular to the SPS directions, respectively. The negligible difference between κ (Figures 2.1.9c and 2.1.9d) and κ_{lat} clearly indicates that the thermal transport is mainly dominated by phonons. In addition to the significant lattice anharmonicity in SnSe, the presence of solid solution point defects and Ge precipitates scatter the phonons in the Sn_{0.97}Ge_{0.03}Se samples, thereby effectively reduces the lattice thermal conductivity. For Sn_{0.97}Ge_{0.03}Se sample, κ_{lat} of ~ 0.18 W/mK is observed at 873 K for measurement perpendicular to the SPS direction.

Table 2.1.3. A comprehensive summary of κ_{lat} of various high performance SnSe samples. Here, solvothermal is abbreviated as ST, hydrothermal is abbreviated as HT, melting is abbreviated as M, mechanical alloying is abbreviated as MA, and hot-pressing is abbreviated as HP. ‘ \perp ’ and ‘ \parallel ’ denotes the perpendicular and parallel SPS pressing directions respectively.

Product	Synthetic Procedure	κ_{lat} (W m ⁻¹ K ⁻¹)	T (K)	Reference
Sn_{0.97}Ge_{0.03}Se	HT+SPS	0.18 (\perp)	873	This Work
SnSb _{0.02} Se _{0.96}	HT+SPS	0.17 (\perp)	773	15
Sn _{0.95} Se	HT+SPS	0.23 (\parallel)	873	22
SnPb _{0.01} Zn _{0.03} Se	HT+SPS	0.13 (\parallel)	873	31
SnSe+1mol% PbSe	HT+SPS	0.15 (\parallel)	873	13
Sn _{0.882} Cu _{0.118} Se	ST+SPS	0.25 (\perp)	823	23
Ag _{0.01} Sn _{0.99} Se _{0.85} Se _{0.15}	M+HP	0.11 (\parallel)	825	17
K _{0.01} Sn _{0.99} Se	MA+SPS	0.20 (\perp)	773	12
SnSe _{0.67} S _{0.3} I _{0.03}	M+MA+HP	0.25 (\perp)	773	19

We have compared the high temperature κ_{lat} value of Sn_{0.97}Ge_{0.03}Se with the κ_{lat} of other high performance SnSe samples (Table 2.1.3), which is in good agreement.

The zT increases to a maximum value of ~ 2.1 at 873 K for p -type solution processed Sn_{0.97}Ge_{0.03}Se (\perp to the pressing direction, Figure 2.1.10b), which is significantly higher than that of previously reported polycrystalline Ge doped SnSe made by solid state high temperature melting.⁷ We have also obtained a maximum zT of ~ 1.8 at 873 K measured along the pressing direction in Sn_{0.97}Ge_{0.03}Se, Figure 2.1.10a.

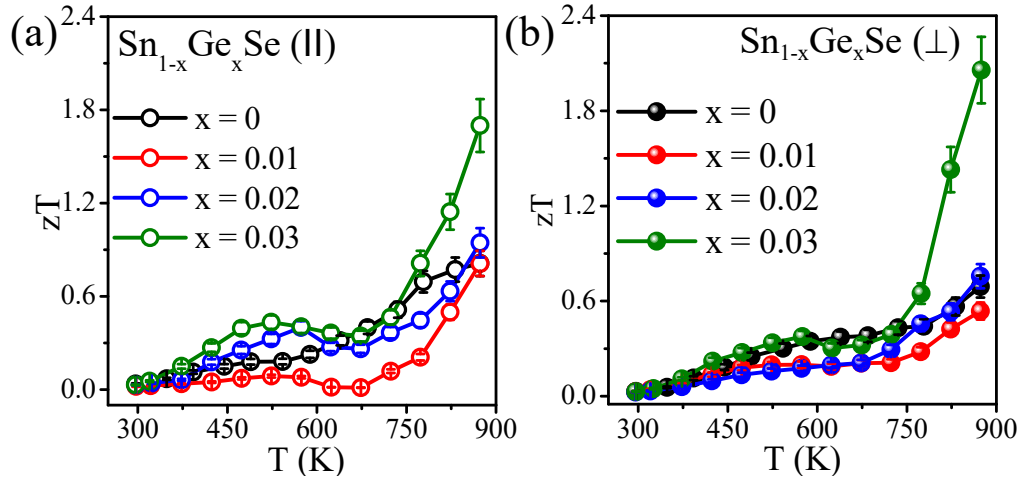


Figure 2.1.10. Temperature dependent zT of $\text{Sn}_{1-x}\text{Ge}_x\text{Se}$ nanoplates measured along (a) parallel and (b) perpendicular to the SPS direction respectively.

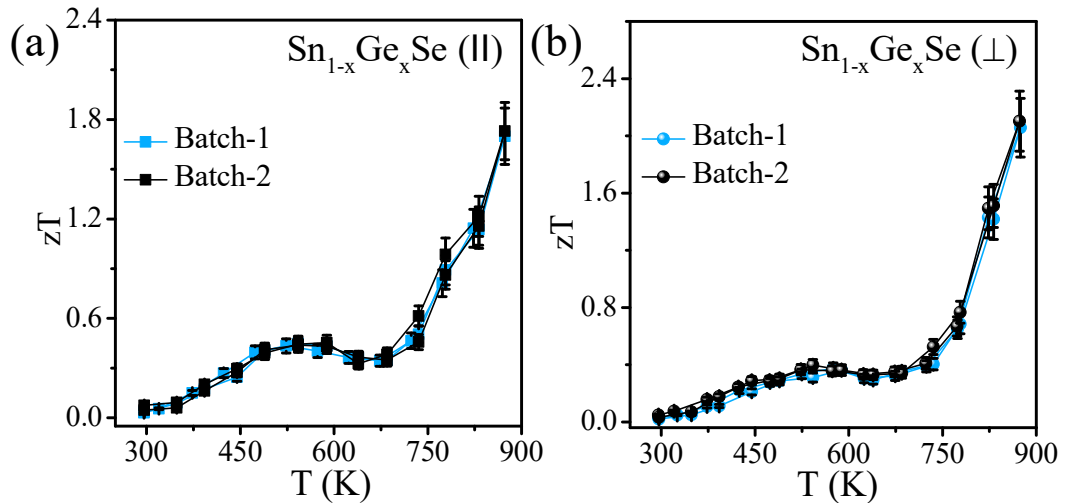


Figure 2.1.11. zT of SPS processed $\text{Sn}_{0.97}\text{Ge}_{0.03}\text{Se}$ sample is reversible (heating-cooling) and reproducible over temperature gradient and different batch of synthesis for both the (a) parallel and (b) perpendicular directions.

The obtained high zT values in $\text{Sn}_{0.97}\text{Ge}_{0.03}\text{Se}$ are reproducible and reversible in several batches of samples synthesized separately (Figure 2.1.11).

2.1.4. Conclusion

In summary, a simple scalable hydrothermal synthesis has been implemented to prepare 2D nanoplates of $\text{Sn}_{1-x}\text{Ge}_x\text{Se}$ ($x = 0-3$ mol%). Ge doping in SnSe increases the p -

type carrier concentration, thereby enhances electrical transport. Synergistic effect of lattice anharmonicity, point defects, nanoscale grains and precipitates decrease the κ_{lat} heavily in $\text{Sn}_{1-x}\text{Ge}_x\text{Se}$. Thus, an extremely high zT of ~ 1.8 and ~ 2.1 at 873 K are obtained for 3 mol % Ge doped SnSe when measured in parallel and perpendicular to the SPS pressing directions, respectively.

2.1.5. References

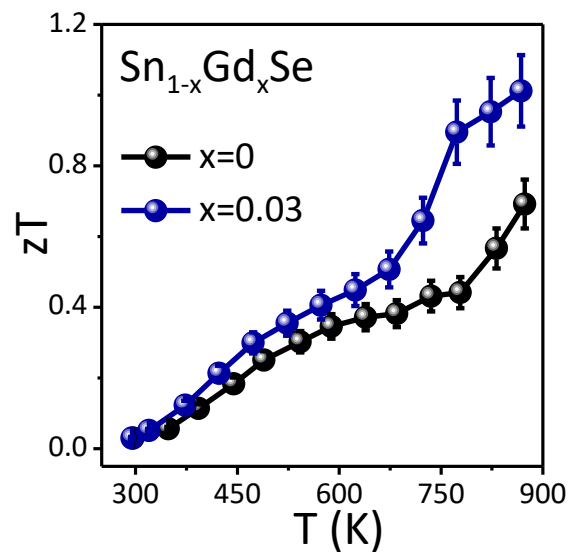
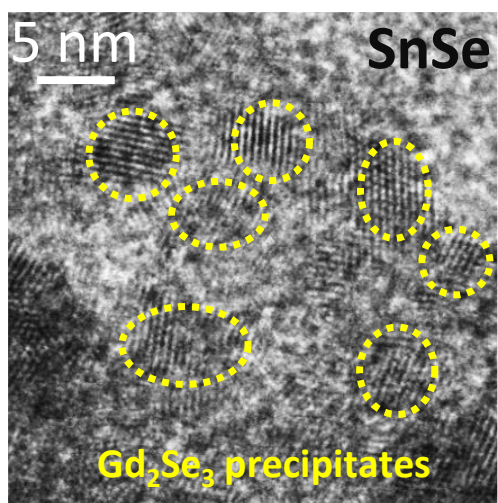
- (1) Zhou, Y.; Zhao, L. D. *Adv. Mater.* **2017**, *29*, 1702676.
- (2) Cao, X.; Tan, C.; Zhang, X.; Zhao, W.; Zhang, H. *Adv. Mater.* **2016**, *28*, 6167–6196.
- (3) Samanta, M.; Pal, K.; Pal, P.; Waghmare, U. V.; Biswas, K. *J. Am. Chem. Soc.* **2018**, *140*, 5866–5872.
- (4) Banik, A.; Biswas, K. *Angew. Chem. Int. Ed.* **2017**, *56*, 14561–14566.
- (5) Chatterjee, A.; Biswas, K. *Angew. Chem. Int. Ed.* **2015**, *54*, 5623–5627.
- (6) Zhao, L.-D.; Lo, S. H.; Zhang, Y.; Sun, H.; Tan, G.; Uher, C.; Wolverton, C.; Dravid, V. P.; Kanatzidis, M. G. *Nature* **2014**, *508*, 373–377.
- (7) Zhao, L. D.; Tan, G.; Hao, S.; He, J.; Pei, Y.; Chi, H.; Wang, H.; Gong, S.; Xu, H.; Dravid, V. P.; Uher, C.; Snyder, G. J.; Wolverton, C.; Kanatzidis, M. G. *Science* **2016**, *351*, 141–144.
- (8) Peng, K.; Lu, X.; Zhan, H.; Hui, S.; Tang, X.; Wang, G. *Energy Environ. Sci.* **2015**, *9*, 454–460.
- (9) Duong, A. T.; Nguyen, V. Q.; Duvjir, G.; Duong, V. T.; Kwon, S.; Song, J. Y.; Lee, J. K.; Lee, J. E.; Park, S.; Min, T.; Lee, J.; Kim, J.; Cho, S. *Nat. Commun.* **2016**, *7*, 13713.
- (10) Zhao, L. D.; Chang, C.; Tan, G.; Kanatzidis, M. G. *Energy Environ. Sci.* **2016**, *9*, 3044–3060.
- (11) Chang, C.; Wu, M.; He, D.; Pei, Y.; Wu, C.-F.; Wu, X.; Yu, H.; Zhu, F.; Wang, K.; Chen, Y.; Huang, L.; Li, J. F.; He, J.; Zhao, L. D. *Science* **2018**, *360*, 778–783.
- (12) Chen, Y.-X.; Ge, Z. H.; Yin, M.; Feng, D.; Huang, X.-Q.; Zhao, W.; He, J. *Adv. Funct. Mater.* **2016**, *26*, 6836–6845.
- (13) Tang, G.; Wei, W.; Zhang, J.; Li, Y.; Wang, X.; Xu, G.; Chang, C.; Wang, Z.; Du, Y.; Zhao, L.-D. *J. Am. Chem. Soc.* **2016**, *138*, 13647–13654.
- (14) Ge, Z.; Song, D.; Chong, X.; Zheng, F.; Jin, L.; Qian, X.; Zheng, L.; Dunin-borkowski, R. E.; Qin, P.; Feng, J.; Zhao, L. *J. Am. Chem. Soc.* **2017**, *139*, 9714–9720.
- (15) Shi, X. L.; Zheng, K.; Liu, W. Di; Wang, Y.; Yang, Y. Z.; Chen, Z. G.; Zou, J. *Adv. Energy Mater.* **2018**, *8*, 1800775.

-
- (16) Li, Y.; Li, F.; Dong, J.; Ge, Z.; Kang, F.; He, J.; Du, H.; Li, B.; Li, J. F. *J. Mater. Chem. C* **2016**, *4*, 2047–2055.
- (17) Lin, C. C.; Lydia, R.; Yun, J. H.; Lee, H. S.; Rhyee, J. S. *Chem. Mater.* **2017**, *29*, 5344–5352.
- (18) Lee, Y. K.; Ahn, K.; Cha, J.; Zhou, C.; Kim, H. S.; Choi, G.; Chae, S. I.; Park, J.-H.; Cho, S.-P.; Park, S. H.; Sung, Y.-E.; Lee, W. B.; Hyeon, T.; Chung, I. *J. Am. Chem. Soc.* **2017**, *139*, 10887–10896.
- (19) Zhang, Q.; Chere, E. K.; Sun, J.; Cao, F.; Dahal, K.; Chen, S.; Chen, G.; Ren, Z. *Adv. Energy Mater.* **2015**, *5*, 1500360.
- (20) Wei, T. R.; Tan, G.; Zhang, X.; Wu, C. F.; Li, J. F.; Dravid, V. P.; Snyder, G. J.; Kanatzidis, M. G. *J. Am. Chem. Soc.* **2016**, *138*, 8875–8882.
- (21) Han, G.; Popuri, S. R.; Greer, H. F.; Bos, J. W. G.; Zhou, W.; Knox, A. R.; Montecucco, A.; Siviter, J.; Man, E. A.; Macauley, M.; Paul, D. J.; Li, W.; Paul, M. C.; Gao, M.; Sweet, T.; Freer, R.; Azough, F.; Baig, H.; Sellami, N.; Mallick, T. K.; Gregory, D. H. *Angew. Chem. Int. Ed.* **2016**, *55*, 6433–6437.
- (22) Wei, W.; Chang, C.; Yang, T.; Liu, J.; Tang, H.; Zhang, J.; Li, Y.; Xu, F.; Zhang, Z.; Li, J. F.; Tang, G. *J. Am. Chem. Soc.* **2018**, *140*, 499–505.
- (23) Shi, X.; Zheng, K.; Hong, M.; Liu, W.; Moshwan, R.; Wang, Y.; Qu, X.; Chen, Z. G.; Zou, J. *Chem. Sci.* **2018**, *9*, 7376–7389.
- (24) Roychowdhury, S.; Ghosh, T.; Arora, R.; Waghmare, U. V.; Biswas, K. *Angew. Chem. Int. Ed.* **2018**, *57*, 15167–15171.
- (25) Huang, Z.; Miller, S. A.; Ge, B.; Yan, M.; Anand, S.; Wu, T.; Nan, P.; Zhu, Y.; Zhuang, W.; Snyder, G. J.; Jiang, P.; Bao, X. *Angew. Chem. Int. Ed.* **2017**, *56*, 14113–14118.
- (26) Roychowdhury, S.; Samanta, M.; Perumal, S.; Biswas, K. *Chem. Mater.* **2018**, *30*, 5799–5813.
- (27) Gharsallah, M.; Serrano-Sánchez, F.; Nemes, N. M.; Mompeán, F. J.; Martínez, J. L.; Fernández-Díaz, M. T.; Elhalouani, F.; Alonso, J. *Sci. Rep.* **2016**, *6*, 26774.
- (28) Fu, Y.; Xu, J.; Liu, G. Q.; Tan, X.; Liu, Z.; Wang, X.; Shao, H.; Jiang, H.; Liang, B.; Jiang, J. *J. Electron. Mater.* **2017**, *46*, 3182–3186.
- (29) Wubieneh, T. A.; Chen, C. L.; Wei, P. C.; Chen, S. Y.; Chen, Y. Y. *RSC Adv.* **2016**,

-
- 6, 114825–114829.
- (30) Ge, Z. H.; Wei, K.; Lewis, H.; Martin, J.; Nolas, G. S. *J. Solid State Chem.* **2015**, 225, 354-358.
- (31) Liu, J.; Wang, P.; Wang, M.; Xu, R.; Zhang, J.; Liu, J.; Li, D.; Liang, N.; Du, Y.; Chen, G.; Tang, G. *Nano Energy* **2018**, 53, 683–689.

Chapter 2.2

Enhancement of the Thermoelectric Performance of 2D SnSe Nanoplates through Incorporation of Magnetic Nanoprecipitates



Enhancement of the Thermoelectric Performance of 2D SnSe Nanoplates through Incorporation of Magnetic Nanoprecipitates[†]

Summary

Recently, it has been observed that enhancement of the thermoelectric performance can be achieved by the incorporation of magnetic nanoprecipitates in a thermoelectric host matrix. Herein, we have demonstrated the significant enhancement in thermoelectric performance of the two-dimensional (2D) nanoplates of SnSe by introducing magnetic Gd dopants, which are synthesized and scaled up (~ 10 g) by low temperature hydrothermal method. The p-type carrier concentration increases significantly upon 3 mol% Gd addition in SnSe nanoplates due to phase separation of Gd₂Se₃ nanoprecipitates (2-5 nm) and subsequent Sn²⁺ vacancy formation. Thus, the thermoelectric power factor has been markedly enhanced to 6.7 μW/cmK² at 868 K compared to that of the pristine SnSe nanoplates. The presence of magnetic fluctuations induced by small nanoprecipitates of Gd₂Se₃ provides additional scattering of the phonons in SnSe, which reduces the lattice thermal conductivity significantly to 0.41 W/mK at 868 K in Sn_{0.97}Gd_{0.03}Se. We have achieved a zT of ~ 1 at 868 K for the spark plasma sintered (SPS) Sn_{0.97}Gd_{0.03}Se nanoplates along the perpendicular to the pressing direction.

[†]S. Chandra, P. Dutta, and K. Biswas. *ACS Appl. Energy Mater.*, 2020, 3, 9051–9057.

2.2.1. Introduction

Recently, researches have come up with an idea that the magnetic interactions induced by magnetic-element in a non-magnetic thermoelectric host could be an effective strategy to elevate the overall thermoelectric performance.¹⁻⁴ Incorporation of a magnetic element can be achieved mainly by two ways; (i) doping of magnetic transition metal ions into the crystalline thermoelectric materials (e.g. Bi₂Te₃),¹ and (ii) embedding magnetic nanoparticles (e.g., Fe₃O₄, Ni) into the thermoelectric matrix (e.g. BiSbTe₃, CoSb₃).^{2,3} In the first method, magnetic doping enhances the thermopower by increasing the carrier effective mass or spin entropy, whereas, in the second approach, a complex thermo-electromagnetic effect plays the key role to refine the thermoelectric properties.¹⁻³ The presence of nanostructures and the magnetic fluctuations synergistically enhance the phonon scattering of the system, resulting in a reduced lattice thermal conductivity. Considering these facts, we have purposefully introduced gadolinium (Gd, [Xe]4f⁷5d¹6s²) in 2D SnSe nanoplates to study the impact of *f*-block magnetic dopant on its thermoelectric properties. As per our best knowledge, it is the first experimental report of magnetic rare earth doping in SnSe nanoplates in the arena of thermoelectrics.⁴

In this chapter, I have demonstrated a simple and scalable hydrothermal synthesis and thermoelectric properties of Gd doped (1-3 mol%) SnSe 2D nanoplates. Incorporation of Gd in SnSe nanoplates enhances the hole concentration in the sample, leading to improved electrical conductivity and power factor. While with Gd concentrations up to 2 mol% in SnSe, the system behaves as a solid solution, but upon 3 mol% Gd addition, nanoprecipitate (2-5 nm) of Gd₂Se₃ starts precipitating out in the SnSe matrix. Sn_{0.97}Gd_{0.03}Se is paramagnetic at room temperature but show antiferromagnetic interaction at low temperatures. An ultralow lattice thermal conductivity of ~ 0.4 W/mK has been achieved at 868 K in the spark plasma sintered (SPS) Sn_{0.97}Gd_{0.03}Se nanoplates (along perpendicular to SPS) owing to the significant phonon scattering by point defects, grain boundaries and magnetic fluctuations induced by nanoprecipitates of Gd₂Se₃. Thus, due to the integrated effects of well-maintained power factor and reduced lattice thermal conductivity, a high *zT* of ~ 1 is obtained in nanocrystalline Sn_{0.97}Gd_{0.03}Se at 868 K along the perpendicular to the SPS pressing direction. We have also measured the anisotropic thermoelectric properties of SPS processed Sn_{0.97}Gd_{0.03}Se and found that the properties

measured perpendicular to the SPS pressing direction provides better thermoelectric performance. This work amalgamates thermoelectric and magnetic properties of Gd doped SnSe and initiates the investigation of new magnetic ion doping in 2D layered chalcogenide based thermoelectric material.

2.2.2. Methods

Reagents. Tin (II) chloride dihydrate ($\text{SnCl}_2 \cdot 2\text{H}_2\text{O}$, 98%, Sigma Aldrich), selenium powder (Se, 99.99%, Alfa Aesar), gadolinium (III) acetate hydrate ($\text{Gd}(\text{OOCCH}_3)_3 \cdot x\text{H}_2\text{O}$, 99.9%, Alfa Aesar) and sodium hydroxide Pellets (NaOH, 98% Sigma Aldrich) were used for the synthesis.

Synthesis. $\text{Sn}_{1-x}\text{Gd}_x\text{Se}$ ($x = 0-3$ mol%) nanoplates were synthesized using simple hydrothermal method. First a mixture of $\text{SnCl}_2 \cdot 2\text{H}_2\text{O}$ (2 mmol) and $\text{Gd}(\text{OOCCH}_3)_3 \cdot x\text{H}_2\text{O}$ (x mmol%) were dissolved in deionized water. The solution was then sonicated at room temperature for 10 min, followed by addition of NaOH (30 mmol) and sonicated again for another 10 min unless a clear solution has been obtained. The mixture was then transferred to a Teflon-lined stainless-steel autoclave of 25 ml capacity and Se powder (1 mmol) was added to it. The autoclaves were then sealed tightly and heated to 130 °C for 36 hrs. After cooling to room temperature, the black precipitate was collected and thoroughly washed with absolute ethanol and deionized water for several times. Finally, the product was vacuum dried at 60 °C for 6 hrs and collected as powder. During the synthesis, NaOH acts as a solubilizing agent. Excess of Sn^{2+} should always be present in the reaction mixture, as Sn^{2+} itself acts as a reductant and precipitant. The yield of the reaction was ~ 95% and the nanoplates were scaled up to ~ 10 gm for the thermoelectric measurements. The nanoplates were dispersed in ethanol for further characterizations.

Powder X-ray diffraction (PXRD) patterns of the samples were collected using $\text{CuK}\alpha$ ($\lambda = 1.5406 \text{ \AA}$) radiation on a Bruker D8 diffractometer at room temperature.

Field emission scanning electron microscopy (FESEM) experiments were performed using NOVANO SEM 600 (FEI, Germany) operated at 15 kV. EDAX compositional analysis was performed during FESEM imaging.

Transmission electron microscopy (TEM) images of the as synthesized materials were taken using a JEOL (JEM3010) TEM instrument (300 kV accelerating voltage) fitted with a Gatan CCD camera and also with a FEI TECNAI G2 20 STWIN TEM instrument (operating at 200 kV). A suspension of the nanosheets was prepared in cyclohexane solution and it was then drop casted in a holey carbon coated Cu grid for TEM imaging.

Scanning transmission electron microscopy (STEM) imaging was carried out using FEITECNAI G² 20 STWIN TEM operating at 200 KV. The sample preparation was same as that of TEM. EDAX compositional analysis and color mapping were performed during STEM imaging. Background was subtracted (using multi-polynomial model) during the data processing for EDAX color mapping (with 500 eV minimum region of interest width). Errors in the determination in compositions of nanosheets in EDAX measurements is nearly 5%.

Inductively coupled plasma atomic emission spectroscopy (ICP-AES). The exact composition of the as synthesized nanosheets was calculated based on ICP-AES data. ICP-AES measurements were carried out using Perkin-Elmer Optima 7000DV instrument. ICP-AES measurement were carried out by dissolving the powder nanosheets in aqua regia (HNO₃:HCl = 1:3) followed by diluting with millipore water. Sn standard (1000 mg/L, Sigma-Aldrich), Se standard (1000 mg/L, Sigma-Aldrich) and Gd standard (1000 mg/L, Sigma-Aldrich) were used to determine the compositions in ICP. In the present measurement, error bar lies below 1.5 %.

Magnetic measurements. The dc magnetic measurements were performed using a vibrating sample magnetometer from Cryogenic Ltd., U.K. Temperature dependent magnetization (M) data were recorded in two different protocols namely zero field cooling (ZFC) and field cooling (FC). In ZFC mode, the sample was first cooled from room temperature to 2 K without any magnetic field (H). Then a magnetic field of 1 kOe is applied and subsequently recorded the M data during heating from 2 K to 300 K. Whereas in FC mode, the sample was first cooled in presence of $H = 1$ kOe and then measured the M during subsequent heating. M - H curves at different constant temperature were recorded in the ± 150 kOe magnetic field range.

Spark plasma sintering (SPS) was done using a SPS211-LX (Dr. Sinter Lab) instrument

The powdered nanoplates were sintered to prepare a rectangular column (8 mm × 8 mm × 8 mm) and coin (2 mm × 10 mm) using graphite dies at 50 MPa pressure and 450 °C temperature for 10 minutes. From the rectangular column, a rectangular bar (2 mm × 2 mm × 8 mm) was made using a typical cutter-polisher. The density of the SPS processed samples were found to be about ~ 95 % of theoretical density.

Electrical transport properties. Electrical conductivity (σ) and Seebeck coefficients (S) were measured simultaneously from the rectangular bar under helium atmosphere from room temperature to 873 K using a ULVAC-RIKO ZEM-3 instrument system. σ and S were measured in both the parallel and perpendicular to the pressing directions.

Hall measurement. Room temperature carrier concentrations were determined from Hall coefficient measurements with the equipment developed by Excel Instrument, India. Four-contact Hall-bar geometry was used for the measurement. The maximum applied magnetic field was 1 Tesla. Room temperature carrier concentration, n , was measured using the formula $n = 1/eR_H$, where e is the electronic charge, R_H is hall coefficient.

Thermal transport properties. The thermal diffusivity (D) of the coin-shaped samples have been measured by laser flash diffusivity technique using NETZSCH LFA 457 instrument in 300–873 K range. Total thermal conductivity (κ_{tot}) was calculated using the formula $\kappa_{tot} = DC_p\rho$, where D is the thermal diffusivity, C_p is specific heat, and ρ is density of the sample. C_p was derived experimentally during the thermal diffusivity measurement using pyroceram as a reference material. Further, the electronic thermal conductivities, κ_{ele} were estimated using Wiedemann-Franz Law, $\kappa_{ele} = L\sigma T$, where L is the Lorenz number which is estimated by fitting reduced chemical potential derived from temperature-dependent Seebeck coefficient using single parabolic band conduction and dominant acoustic phonon scattering of carriers.

2.2.3. Results and Discussions

The powder X-ray diffraction (PXRD) patterns of $\text{Sn}_{1-x}\text{Gd}_x\text{Se}$ ($x = 0-3 \text{ mol}\%$) samples are shown in Figure 2.2.1a. The patterns can be indexed with the orthorhombic phase ($Pnma$) of SnSe ,⁵ whereas, a small amount of Gd_2Se_3 secondary phase was noticed in the

case of $\text{Sn}_{0.97}\text{Gd}_{0.03}\text{Se}$ samples. Gd_2Se_3 crystallises in a cation deficient Th_3P_4 type defected cubic structure (space group, $I-43d$) with lattice parameters of $a = 8.72 \text{ \AA}$ (Figure 2.2.1b). The Se^{2-} ions reside at the five coordinated 16c position whereas the Gd^{3+} cations occupy an eight coordinated 12b sites.⁶⁻⁸

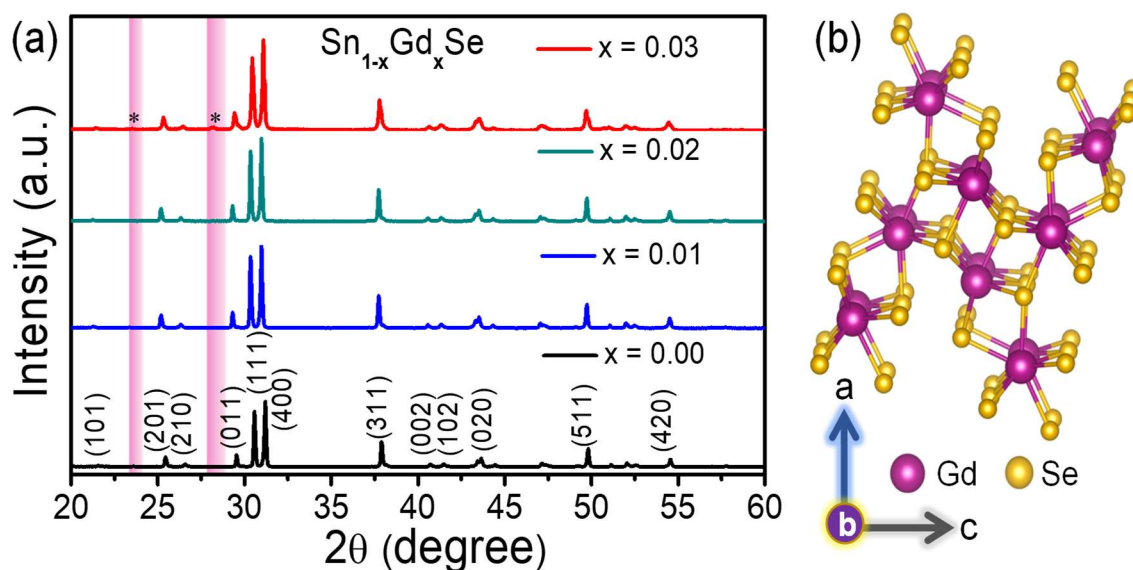


Figure 2.2.1. (a) The PXRD pattern of the as-synthesized $\text{Sn}_{1-x}\text{Gd}_x\text{Se}$ ($x = 0-3 \text{ mol\%}$) samples. The asterisks (*) represents the Gd_2Se_3 secondary phase in SnSe nanoplates. (b) Crystal structure of Gd_2Se_3 as seen along the crystallographic b -direction.

Moreover, lattice parameters of $\text{Sn}_{1-x}\text{Gd}_x\text{Se}$ nanoplates were calculated from the PXRD pattern and it was confirmed that the solid solution limit of Gd in SnSe remains only up to 2 mol% (Figure 2.2.2).

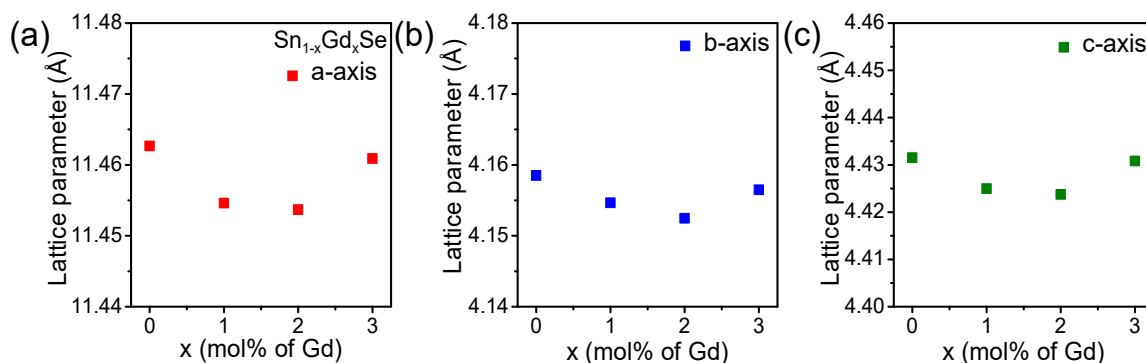


Figure 2.2.2. Experimentally estimated lattice parameters of the $\text{Sn}_{1-x}\text{Gd}_x\text{Se}$ ($x = 0-3 \text{ mol\%}$) nanoplates derived from the PXRD.

To identify the morphology and understand the structure of the samples, FESEM and TEM were performed on the as-synthesized $\text{Sn}_{0.97}\text{Gd}_{0.03}\text{Se}$ samples. The morphology of the samples resembles to that of the 2D nanoplates with a lateral dimension of 0.5 - 1.0 μm which is evident from FESEM (Figure 2.2.3a) and TEM images (Figure 2.2.3b).

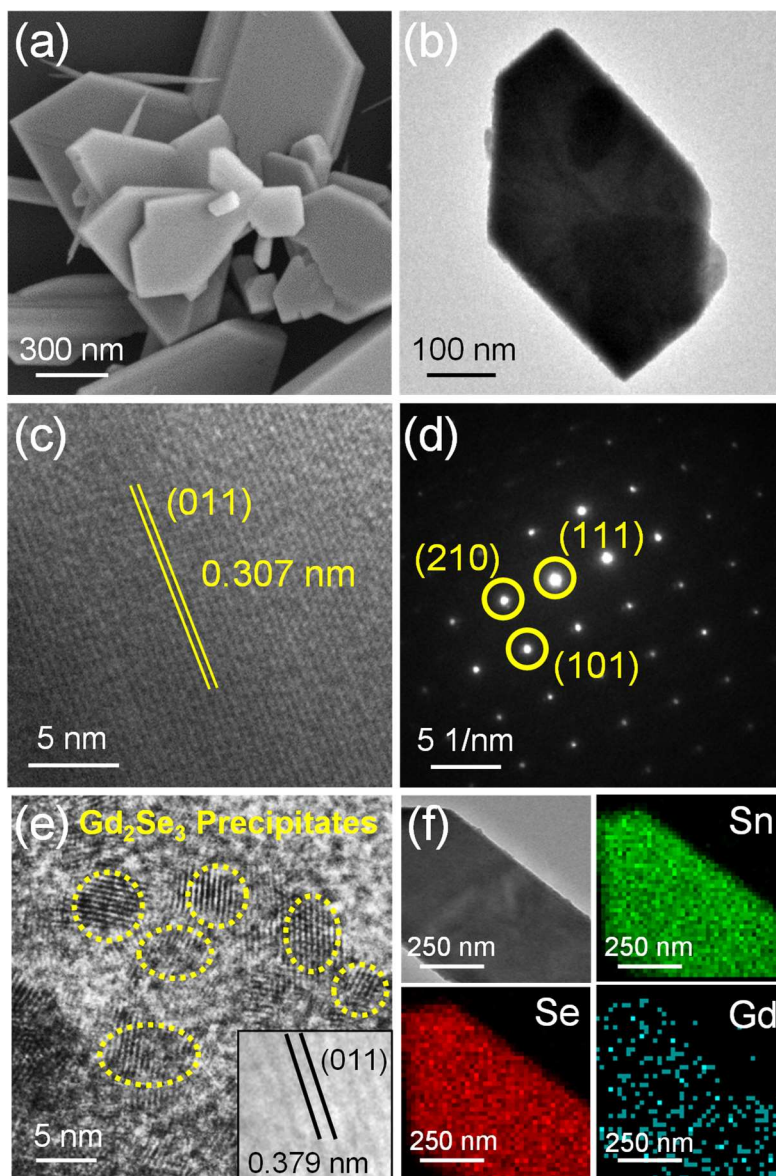


Figure 2.2.3. (a) FESEM, (b) TEM and (c) HRTEM image of $\text{Sn}_{0.97}\text{Gd}_{0.03}\text{Se}$ nanoplates. The SAED pattern for the same has been shown in (d). (e) HRTEM image taken from the edge of the $\text{Sn}_{0.97}\text{Gd}_{0.03}\text{Se}$ nanoplates showing the Gd_2Se_3 nanoprecipitates. The HRTEM image displayed at the inset of (e) shows that the (011) lattice planes of Gd_2Se_3 . (f) STEM image of $\text{Sn}_{0.97}\text{Gd}_{0.03}\text{Se}$ nanoplates along with EDAX color mapping for Sn, Se and Gd.

Figure 2.2.3c shows a high-resolution TEM (HRTEM) image of the nanoplate. The lattice spacing between two apparent planes was estimated to be 0.307 nm which reveals that the (011) set of planes are exposed in $\text{Sn}_{0.97}\text{Gd}_{0.03}\text{Se}$ nanoplates. Figure 2.2.3d shows the corresponding selected area electron diffraction (SAED) pattern, which indicates the single crystalline nature of the nanoplates revealing the typical orthorhombic structure of the $\text{Sn}_{0.97}\text{Gd}_{0.03}\text{Se}$ nanoplates. The presence of the nanoprecipitates in $\text{Sn}_{0.97}\text{Gd}_{0.03}\text{Se}$ can be observed from the HRTEM image as shown in Figure 2.2.3e. The size of the nanoprecipitates is of the order of 2-5 nm. To confirm the structure and composition of the nanoprecipitates, the lattice planes of nanoprecipitates was estimated from HRTEM to be 0.379 nm which can be attributed to the (011) set of planes of Gd_2Se_3 (inset of Figure 2.2.3e). Thus, analysis of HRTEM concludes that the small (2-5 nm) nanoprecipitates are embedded in SnSe nanoplates (lateral dimension of 0.5 - 1.0 μm).

The composition of $\text{Sn}_{1-x}\text{Gd}_x\text{Se}$ nanoplates were obtained from EDAX during FESEM and ICP-AES. Compositions obtained from the two independent experiments are in good agreement with the nominal composition of the nanoplates (Table 2.2.1), which confirms effective control over the composition in the present synthesis. EDAX elemental colour mapping performed during STEM imaging confirms the presence of Gd, Sn, and Se in the $\text{Sn}_{0.97}\text{Gd}_{0.03}\text{Se}$ nanoplates (Figure 2.2.3f).

Table 2.2.1. Analysis of sample compositions from ICP-AES and EDAX.

Nominal Composition	Composition obtained from ICP-AES	Composition obtained from EDAX
SnSe	$\text{SnSe}_{1.03}$	$\text{SnSe}_{0.99}$
$\text{Sn}_{0.99}\text{Gd}_{0.01}\text{Se}$	$\text{Sn}_{0.98}\text{Gd}_{0.0068}\text{Se}_{1.11}$	-
$\text{Sn}_{0.98}\text{Gd}_{0.02}\text{Se}$	$\text{Sn}_{0.987}\text{Gd}_{0.023}\text{Se}_{1.19}$	-
$\text{Sn}_{0.97}\text{Gd}_{0.03}\text{Se}$	$\text{Sn}_{0.969}\text{Gd}_{0.035}\text{Se}_{1.01}$	$\text{Sn}_{0.953}\text{Gd}_{0.031}\text{Se}_{1.31}$

Figure 2.2.4a depicts the magnetization (M) versus T data for $\text{Sn}_{0.97}\text{Gd}_{0.03}\text{Se}$ sample measured in ZFC and FC mode. The $\text{Sn}_{0.97}\text{Gd}_{0.03}\text{Se}$ sample shows a paramagnetic behaviour from room temperature to 5 K. A closer look reveals that at 4.2 K, there is a small kink as shown in the inset of Figure 2.2.4a, which probably related to antiferro-

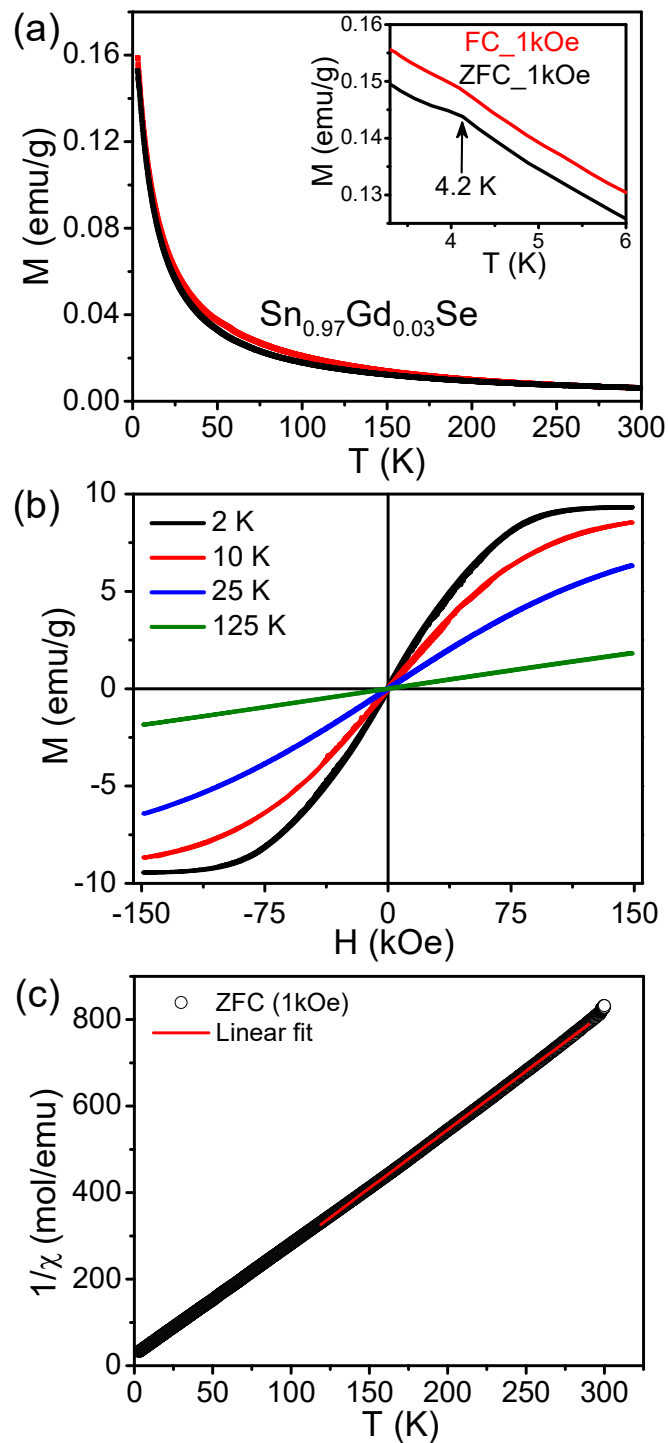


Figure 2.2.4. (a) Magnetization (M) versus temperature (T) curves for $\text{Sn}_{0.97}\text{Gd}_{0.03}\text{Se}$ sample measured in ZFC (black) and FC (red) protocols. Inset shows the antiferromagnetic transition of the sample occurring at ~ 4.2 K. (b) M - H curves of $\text{Sn}_{0.97}\text{Gd}_{0.03}\text{Se}$ sample measured at different constant temperatures. (c) Temperature dependent magnetic susceptibility (χ) of $\text{Sn}_{0.97}\text{Gd}_{0.03}\text{Se}$ nanoplates which obeys the Curie-Weiss law in the temperature range of 100-300 K.

magnetic (AFM) nature of the Gd_2Se_3 which has Neel temperature (T_N) = 6 K in bulk phase.⁷ The slight change in T_N is due to probably presence of small nanoprecipitates (2-5 nm) embedded in diamagnetic host SnSe. To ascertain the magnetic nature of the sample, magnetization (M) versus field (H) isotherms recorded at different constant temperatures are shown in Figure 2.2.4b. Linear behaviour of $M(H)$ isotherm at 125 K indicates that the sample is in paramagnetic state. Whereas the $M(H)$ at 2 K shows almost linear behaviour up to 75 kOe with a significant increase in M value, which supports the AFM nature of the sample at low temperature as observed from the $M(T)$ and $\chi(T)$ data. Mention must be made that above $H = 75$ kOe, the $M(H)$ curve try to saturate, which may be related to the induced ferromagnetic interaction in the sample due to the alignment of the Gd^{3+} moments by the high external magnetic field. The temperature dependent susceptibility (χ) follows the Curie–Weiss law in the temperature range of 100-300 K (Figure 2.2.4c). The Curie–Weiss temperature (Θ_{CW}) is found to be about -10 K. This negative value of Θ_{CW} clearly indicates that the sample has AFM interaction at low temperature.

In order to measure the thermoelectric properties, we have performed spark plasma sintering of $\text{Sn}_{1-x}\text{Gd}_x\text{Se}$ samples. PXRD pattern in both perpendicular and parallel to the SPS direction show the anisotropy (Figure 2.2.5).

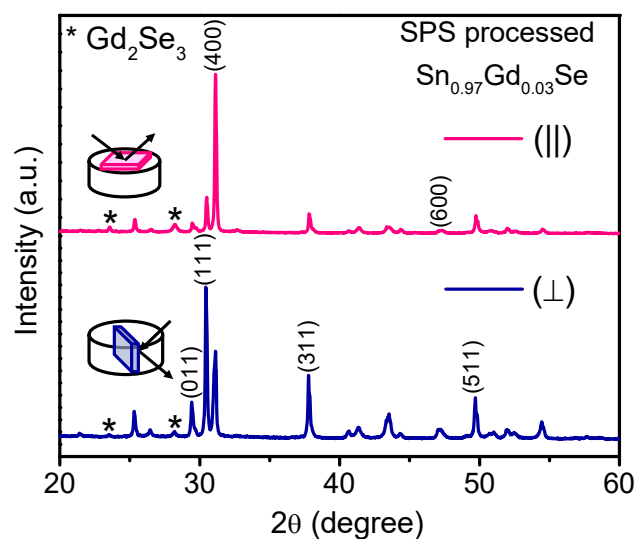


Figure 2.2.5. PXRD patterns of SPS processed 3 mol% Gd-doped SnSe along the parallel and perpendicular directions revealing the anisotropic nature of the sample. The direction of X-ray diffraction has been denoted by the schematic diagrams in inset.

We have measured anisotropic thermoelectric measurement along both the perpendicular and parallel to the SPS direction. We have achieved high thermoelectric performance along the perpendicular to the SPS pressing direction in $\text{Sn}_{1-x}\text{Gd}_x\text{Se}$ samples, thereby presented the data in Figure 2.2.6 and Figure 2.2.7.

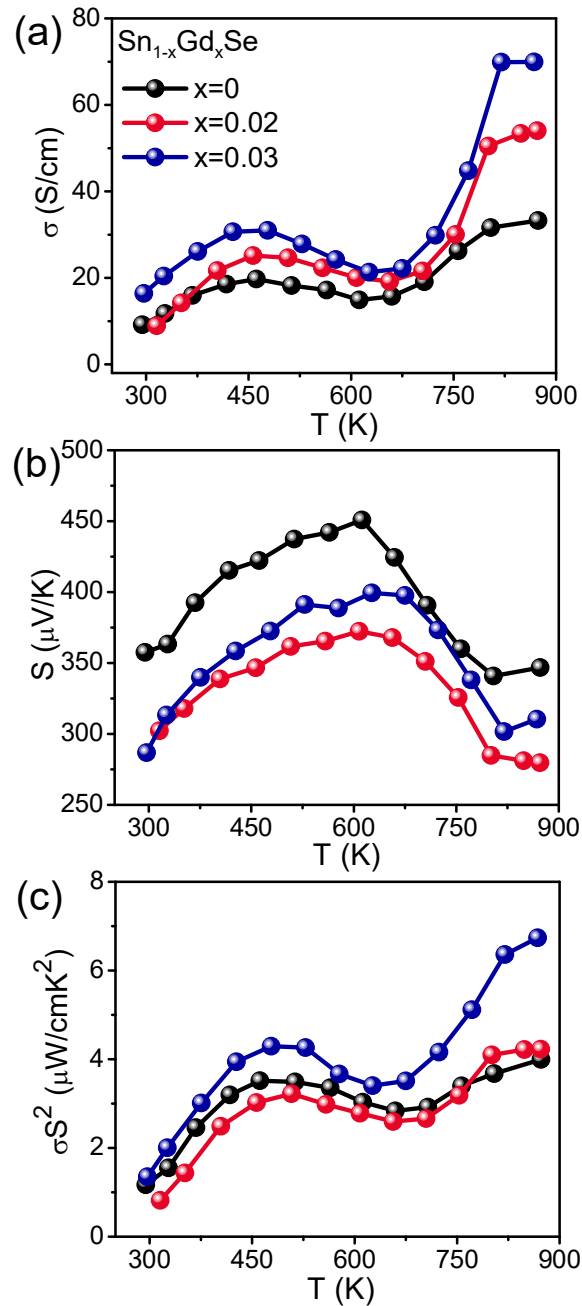


Figure 2.2.6. Temperature dependent (a) electrical conductivity (σ), (b) Seebeck coefficient (S), and (c) power factor (σS^2) of $\text{Sn}_{1-x}\text{Gd}_x\text{Se}$ ($x = 0, 2$ and 3 mol%) nanoplates measured along perpendicular to the SPS pressing direction.

Figure 2.2.6a depicts the temperature dependence of electrical conductivity (σ) of the SPS processed nanoplates of $\text{Sn}_{1-x}\text{Gd}_x\text{Se}$ ($x = 0, 2$ and 3 mol%) measured perpendicular to pressing direction. The values are comparable with those of SnSe single crystals and bulk polycrystalline SnSe.^{9–11} The variation of σ for the $\text{Sn}_{1-x}\text{Gd}_x\text{Se}$ samples can be ascribed as follows: first, a semiconducting transport occurs from 300 to 450 K due to thermal excitation of minority carriers; then it shows a metallic-type behaviour up to 675 K; above that, there is an increasing trend in σ up to 873 K which is due to the displacive phase transition from *Pnma* to *Cmcm* in SnSe. $\text{Sn}_{0.97}\text{Gd}_{0.03}\text{Se}$ sample show a significant increase in the σ value compared to pristine SnSe. The probable reason could be the creation of excess Sn^{2+} vacancies with the phase separation of small Gd_2Se_3 nanoparticles in SnSe matrix in $\text{Sn}_{0.97}\text{Gd}_{0.03}\text{Se}$ (see Figure 2.2.3e), which enhances the overall hole concentration in the $\text{Sn}_{0.97}\text{Gd}_{0.03}\text{Se}$ sample. The σ value for the $\text{Sn}_{0.97}\text{Gd}_{0.03}\text{Se}$ was increased from $\sim 16 \text{ Scm}^{-1}$ at 298 K to $\sim 69 \text{ Scm}^{-1}$ at 825 K. The carrier concentrations of the $\text{Sn}_{1-x}\text{Gd}_x\text{Se}$ ($x = 0, 2$ and 3 mol%) samples were measured by the Hall measurements. For 3 mol% Gd doped SnSe, the *p*-type carrier concentration ($3.1 \times 10^{19} \text{ cm}^{-3}$) is enhanced in two order magnitude than the un-doped sample ($3.9 \times 10^{17} \text{ cm}^{-3}$). Thus, the improved *p*-type carrier concentration in the phase separated $\text{Sn}_{0.97}\text{Gd}_{0.03}\text{Se}$ gives rise to the superior electrical conductivity compared to single-phase SnSe nanoplate.

Figure 2.2.6b portrays the temperature dependent Seebeck coefficient (S) for all the $\text{Sn}_{1-x}\text{Gd}_x\text{Se}$ ($x = 0, 2$ and 3 mol%) samples measured perpendicular to the SPS pressing direction. The $\text{Sn}_{1-x}\text{Gd}_x\text{Se}$ samples exhibit lower S values than the pristine SnSe nanoplates. The lower values of S are consistent with the higher carrier concentrations. Initially Seebeck coefficient increases with the rise in temperature, and reaches to a maximum value in the temperature range of 550–650 K. The peak in Seebeck coefficient indicates an onset of bipolar conduction in the samples.^{5,10} The enhancement of Seebeck coefficient at 823 K arises from the phase transition in SnSe. Due to the significant improvement in carrier concentration and electrical conductivity, remarkable high value of power factor ($\sim 6.7 \mu\text{W}/\text{cmK}^2$) has been obtained for $\text{Sn}_{0.97}\text{Gd}_{0.03}\text{Se}$ nanoplates at 868 K (Figure 2.2.6c) along perpendicular to the SPS pressing direction.

The total thermal conductivity (κ_{tot}) of the $\text{Sn}_{1-x}\text{Gd}_x\text{Se}$ ($x = 0, 2$ and 3 mol%) samples are measured and presented in, Figure 2.2.7a. Figure 2.2.7b shows the temperature depen-

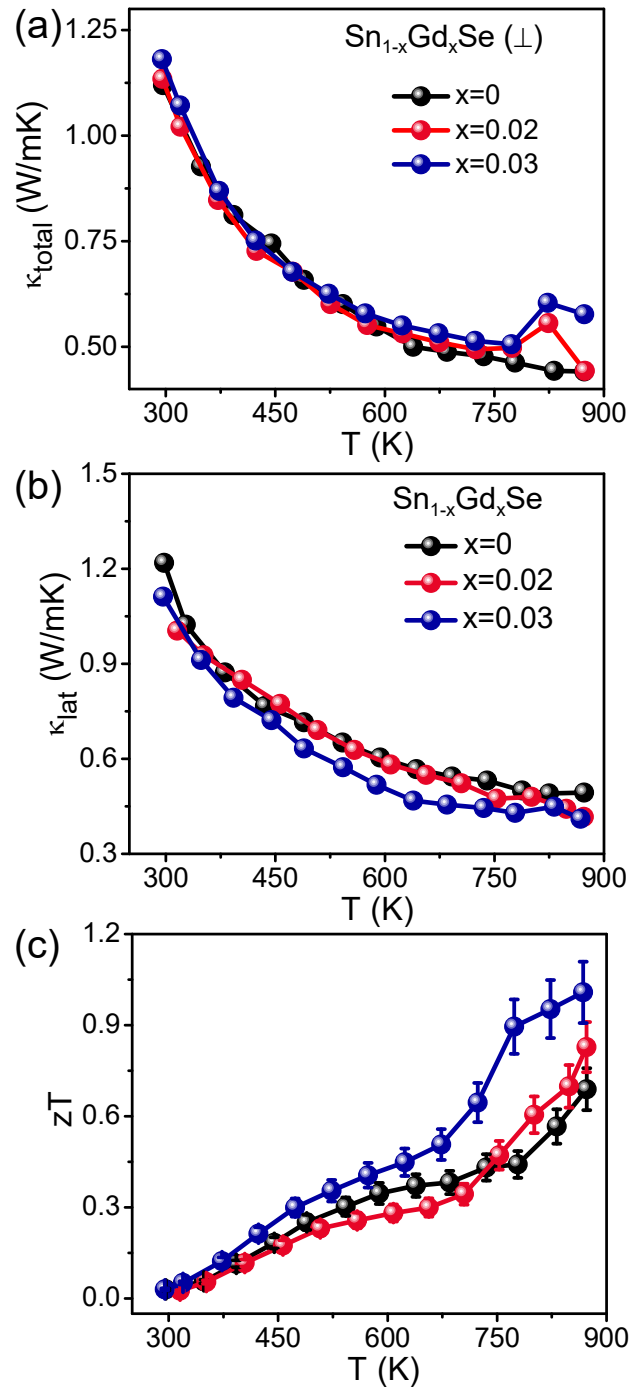


Figure 2.2.7. Temperature dependent (a) total thermal conductivity (κ_{tot}), (b) lattice thermal conductivity (κ_{lat}), and (c) thermoelectric figure of merit (zT) of $\text{Sn}_{1-x}\text{Gd}_x\text{Se}$ ($x = 0, 2$ and 3 mol%) nanoplates measured along perpendicular to the SPS pressing direction.

dence of the lattice thermal conductivity (κ_{lat}) of the $\text{Sn}_{1-x}\text{Gd}_x\text{Se}$ ($x = 0, 2$ and 3 mol%) samples. A room-temperature κ_{lat} value of $\text{Sn}_{0.97}\text{Gd}_{0.03}\text{Se}$ is to be 1.1 W/mK, which

decreases to 0.41 W/mK at 868 K. The κ_{lat} of Sn_{0.97}Gd_{0.03}Se is decreased compared to the pristine SnSe nanoplates throughout the temperature. The additional decrease of κ_{lat} in phase separated Sn_{0.97}Gd_{0.03}Se implies that the low and mid frequency phonon scattering induced by paramagnetic nano-precipitates of Gd₂Se₃ as a result of enhanced magnetic moment fluctuations.^{2,12} Due to the synergistic effect of enhanced electrical conductivity because of improved hole concentration and decreased lattice thermal conductivity, phase-separated Sn_{0.97}Gd_{0.03}Se nanoplate sample exhibits a high zT of ~ 1 at 868 K (Figure 2.2.7c) along the perpendicular to the SPS pressing direction. The maximum zT value is increased by about 45% as compared with the pristine counterpart which is also reversible and reproducible with respect to different batches of samples as well as heat-cooling cycles.

2.2.4. Conclusion

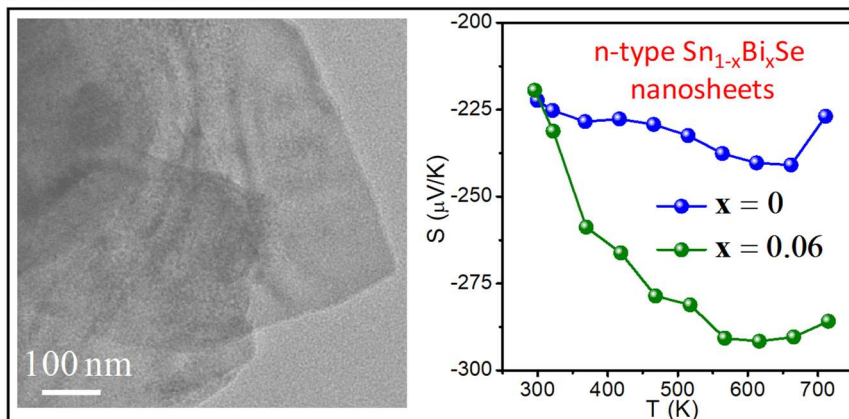
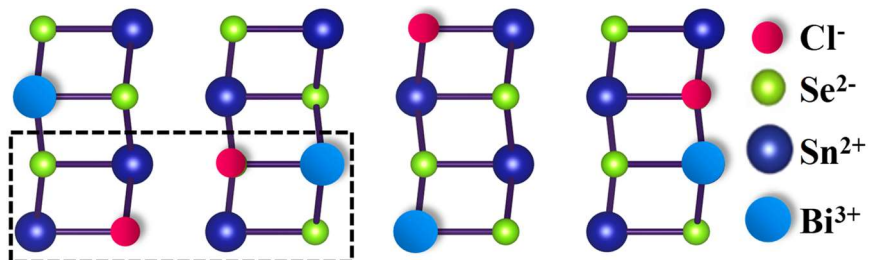
In summary, we have synthesized Gd doped 2D SnSe nanoplates in a simple cost-effective hydrothermal route, which can be scaled up ~ 10 g in a wet chemistry laboratory. With addition of 3 mol% Gd in SnSe, small (2-5 nm) Gd₂Se₃ nanocrystals precipitates in SnSe matrix. Sn_{0.97}Gd_{0.03}Se is paramagnetic at room temperature but show antiferromagnetic interactions at low temperatures. Sn_{0.97}Gd_{0.03}Se sample shows higher p -type carrier concentration and electrical conductivity compared to pristine SnSe nanoplate due to the increased Sn²⁺ vacancies because of phase separation. The lattice thermal conductivity of Sn_{0.97}Gd_{0.03}Se decreased compared to pristine SnSe due to additional phonon scattering by paramagnetic nano-precipitates of Gd₂Se₃. Gd doping simultaneously optimizes both the electronic and phonon transport in 2D SnSe nanoplates. We have achieved a high zT of ~ 1 at 868 K for the Sn_{0.97}Gd_{0.03}Se sample along the perpendicular to SPS pressing direction.

2.2.5. References

- (1) Vaney, J. B.; Aminorroaya Yamini, S.; Takaki, H.; Kobayashi, K.; Kobayashi, N.; Mori, T. *Mater. Today Phys.* **2019**, *9*, 100090.
- (2) Li, C.; Ma, S.; Wei, P.; Zhu, W.; Nie, X.; Sang, X.; Sun, Z.; Zhang, Q.; Zhao, W. *Energy Environ. Sci.* **2020**, *13*, 535–544.
- (3) Zhao, W.; Liu, Z.; Sun, Z.; Zhang, Q.; Wei, P.; Mu, X.; Zhou, H.; Li, C.; Ma, S.; He, D.; Ji, P.; Zhu, W.; Nie, X.; Su, X.; Tang, X.; Shen, B.; Dong, X.; Yang, J.; Liu, Y.; Shi, J. *Nature* **2017**, *549*, 247–251.
- (4) Tang, C.; Li, Q.; Zhang, C.; He, C.; Li, J.; Ouyang, T.; Li, H.; Zhong, J. *J. Phys. D. Appl. Phys.* **2018**, *51*, 245004.
- (5) Chandra, S.; Biswas, K. *J. Am. Chem. Soc.* **2019**, *141*, 6141–6145.
- (6) Folchnandt, M.; Schleid, T. *Zeitschrift Anorg. Allg. Chem.* **2001**, *627*, 1411–1413.
- (7) Pokrzywnicki, S.; Solik, E. *Phys. Stat. Sol.* **1985**, *88*, 619–623.
- (8) Holtzberg, F.; Methfessel, S. *R J. Appl. Phys.* **1966**, *37*, 1433–1435.
- (9) Lee, Y. K.; Ahn, K.; Cha, J.; Zhou, C.; Kim, H. S.; Choi, G.; Chae, S. I.; Park, J.-H.; Cho, S.-P.; Park, S. H.; Sung, Y.-E.; Lee, W. B.; Hyeon, T.; Chung, I. *J. Am. Chem. Soc.* **2017**, *139*, 10887–10896.
- (10) Tang, G.; Wei, W.; Zhang, J.; Li, Y.; Wang, X.; Xu, G.; Chang, C.; Wang, Z.; Du, Y.; Zhao, L.-D. *J. Am. Chem. Soc.* **2016**, *138*, 13647–13654.
- (11) Wei, W.; Chang, C.; Yang, T.; Liu, J.; Tang, H.; Zhang, J.; Li, Y.; Xu, F.; Zhang, Z.; Li, J.-F.; Tang, G. *J. Am. Chem. Soc.* **2018**, *140*, 499–505.
- (12) Gonçalves, A. P.; Godart, C. *Eur. Phys. J. B* **2014**, *87*, 1-29.

Chapter 2.3

n-type Ultrathin Few-layer Nanosheets of Bi-doped SnSe: Synthesis and Thermoelectric Properties



***n*-type Ultrathin Few-layer Nanosheets of Bi-doped SnSe: Synthesis and Thermoelectric Properties[†]**

Summary

Although the stride towards developing superior p-type SnSe as a thermoelectric material is progressing rapidly, synthesis of n-type SnSe is somewhat overlooked. Here, we report the solution phase synthesis and thermoelectric transport properties of two dimensional (2D) ultrathin (1.2-3 nm thick) few layer nanosheets (2-4 layers) of n-type SnSe. The n-type nature of the nanosheets initially originates from chlorination of the material during the synthesis. We could be able to increase the carrier concentration of n-type SnSe significantly from $3.08 \times 10^{17} \text{ cm}^{-3}$ to $1.97 \times 10^{18} \text{ cm}^{-3}$ via further Bi doping which results in the increment of electrical conductivity and power factor. Furthermore, Bi-doped nanosheets exhibit ultralow lattice thermal conductivity ($\sim 0.3 \text{ W/mK}$) throughout the temperature range of 300-720 K which can be ascribed to the effective phonon scattering by interface of SnSe layers, nanoscale grain boundaries and point defects.

[†]S. Chandra, A. Banik, and K. Biswas. *ACS Energy Lett.*, 2018, 3, 1153-1158.

2.3.1. Introduction

Inorganic solid materials with ultralow lattice thermal conductivity (κ_{lat}) are essential for good thermoelectric performance.¹ Recently, layered metal chalcogenides (LMCs) have acquired a momentous attention in the field of thermoelectrics as they exhibit record high thermoelectric figure of merit due to their intrinsically low thermal conductivity owing to their anisotropic crystal and electronic structures.²⁻³ Few layered metal chalcogenides are, in general, held together by weak interlayer van der Waals interactions which provide it with a novel electronic structure and high specific surface area.⁴⁻⁶ Two dimensional (2D) few layer nanosheets/plates of layered Bi_2X_3 ($\text{X} = \text{Se}, \text{Te}$) have displayed promising thermoelectric performance due to their enhanced metallic surface states, high carrier mobility and low κ_{lat} .⁷⁻⁹ Recently, ultralow κ_{lat} in few layered nanosheets of natural 2D van der Waals heterostructure in homologous intergrowth series, $(\text{MX})_m(\text{Bi}_2\text{X}_3)_n$, [$\text{M} = \text{Pb}, \text{Sn}; \text{X} = \text{Te}, \text{Se}$] have been achieved.¹⁰⁻¹² Further, nanosheets/plates of n -type SnSe_2 exhibit good thermoelectric performance at medium temperatures due to low κ_{lat} .¹³⁻¹⁴

Among the layered metal chalcogenides, tin selenide (SnSe), an important p -type semiconductor, has received immense momentum in this area due to its remarkable thermoelectric performance, low toxicity and earth-abundance of the component elements.¹⁵⁻¹⁸ Single crystals of SnSe have lately shown an outstanding zT of 2.6 at 923 K, which can be attributed to its layered structure, soft chemical bonding and lattice anharmonicity.¹⁶ However, polycrystalline SnSe is a better choice for thermoelectric applications for the ease of its production and machinability.¹⁵ There are a number of validating recent reports on p -type bulk polycrystalline SnSe showing good thermoelectric performance.¹⁹⁻²⁵ Though, in most of the cases, reported SnSe materials are p -type while thermoelectric applications demand both p -type and n -type materials. Recently, n -type single crystals of 6 mole% Bi-doped SnSe have been reported to show high zT of 2.2.²⁶ Till date, few nanostructures (*e.g.*, nanowires, nanoplates, nanoflowers and nanosheets) of SnSe have been synthesized by bottom-up wet chemical synthesis,²⁷⁻²⁸ but the materials are mostly p -type.²⁹⁻³⁰ Recently, electronic transport properties of n -type Cl-doped SnSe nanoparticles have been studied, which show moderate power factors.³¹ Thus, n -type SnSe with 2D few-layered nanosheet morphology would be

interesting for thermoelectric investigations as it may exhibit low κ_{lat} due to excess phonon scattering from nanoscale grains and interfaces.

In this chapter, I have demonstrated the low temperature solution phase synthesis and anisotropic thermoelectric properties of *n*-type few-layer (~ 2-4 layers) Bi-doped SnSe nanosheets (1.2-3 nm thick). Nanosheets of Sn_{0.94}Bi_{0.06}Se exhibit a lower band gap compared to the pristine SnSe nanosheets due to the formation of Bi acceptor level near the conduction band. Bi-doped few-layer SnSe nanosheets show enhanced *n*-type carrier concentration compared to SnSe nanosheets, which resulted in superior electrical conductivity and power factor for spark plasma sintering (SPS) processed Sn_{0.94}Bi_{0.06}Se nanosheets compared to SnSe nanosheets. We have achieved higher Seebeck coefficient value in the perpendicular to the SPS pressing direction (*i.e.*, along the *c*-axis in SnSe) compared to parallel to SPS pressing direction (*i.e.*, along the *a*-axis in SnSe) due to high effective mass of the conduction band electron along the crystallographic *c*-axis. Furthermore, Sn_{0.94}Bi_{0.06}Se nanosheets exhibit ultralow lattice thermal conductivity (~ 0.3 W/mK) in the temperature range of 300-720 K due to effective phonon scattering by interface of SnSe layers and point defects. We have achieved a *zT* of 0.21 at 719 K in Sn_{0.94}Bi_{0.06}Se nanosheets, which is higher than that of the controlled *n*-type SnSe nanosheet sample.

2.3.2. Methods

Reagents. Tin (IV) chloride pentahydrate (SnCl₄·5H₂O, 98%, Sigma Aldrich), Selenium dioxide (SeO₂, 99.9%, Sigma Aldrich), Oleylamine (OAm, tech. 90%, Sigma Aldrich), Bismuth neodecanoate (Bi(OCOC(CH₃)₂(CH₂)₅CH₃)₃, Sigma Aldrich) and 1,10-phenanthroline (Phen, C₁₂H₈N₂, 90%, Alfa Aesar) were used for synthesis.

Synthesis. In order to prepare pure phase *n*-type SnSe nanosheets, a typical Schlenk line method with vacuum and N₂ atmosphere has been used. First a mixture of SnCl₄·5H₂O (0.1 mmol), SeO₂ (0.1 mmol), oleylamine (OAM, 10 mL) and 1,10-phenanthroline (Phen, 0.1 mmol) were added into a three-necked flask at room temperature (RT). The mixture was continuously stirred for 10 minutes under vacuum at 70 °C. The white color of the resulting solution indicates the formation of SnCl₄-oleylamine complex (Figure 2.3.1).

The solution mixture was degassed in N_2 atmosphere for 10 min at 120 °C and heated up to 180 °C. The color of the solution changes from white to light yellow and then a black colored suspension was formed immediately at 180 °C. Black colored suspension was further stirred for 5 min to complete the reaction. The reaction mixture was slowly cooled down to room temperature under inert atmosphere with constant stirring. Next the black precipitate was purified by washing several times with ethanol and hexane in an alternative fashion via centrifugation (at a rate of 4000 rpm). Finally, the product was vacuum dried and collected as powder. In the preparation method, OAM acts as both capping reagent as well as reducing agent and 1,10-phenanthroline acts as a morphology controlling agent. To prepare $Sn_{0.94}Bi_{0.06}Se$, Bi-neodecanoate was added in stoichiometric amount along with the other reagents and the rest of the procedure remains the same.

The yield of the reaction was ~ 95% and the products are scaled up to ~ 7 gm for the thermoelectric measurements. The nanosheets are dispersed in cyclohexane for further characterizations.

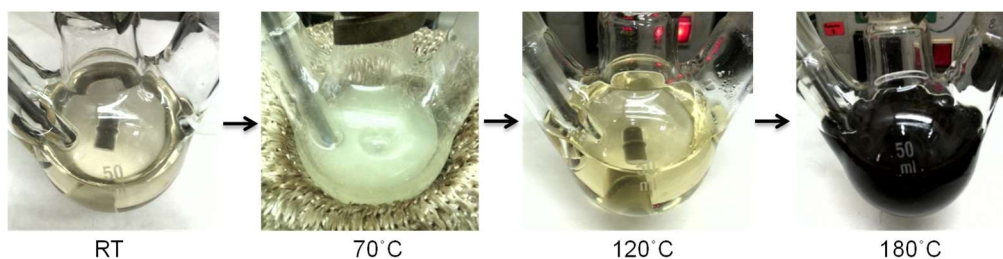


Figure 2.3.1. Color change at different stages of the reaction. At 180 °C the solution became black which indicates the formation of SnSe nanosheets.

Removal of capping ligands. To measure thermoelectric properties, capping reagent has been removed by heat-treatment. The vacuum dried powder samples were taken in an alumina boat and kept inside a tube furnace. Next the tube furnace was heated to 500 °C over 5 hrs and soaked for another 4 hrs under N_2 atmosphere and then slowly cooled down to room temperature. During the annealing process, red colored Se vapours were liberated and oleylamine got detached from the nanosheets.

Powder X-ray diffraction (PXRD) patterns of the samples were collected using $CuK\alpha$ ($\lambda = 1.5406 \text{ \AA}$) radiation on a Bruker D8 diffractometer at room temperature.

Band gap measurements. To estimate the optical band gap, diffuse reflectance measurements were carried out in the range of $\lambda = 250$ to 800 nm by using a Perkin-Elmer Lambda 900 UV/Vis/near-IR spectrometer in reflectance mode. Absorption (α/λ) data were calculated from reflectance data by using the Kubelka–Munk equation: $\alpha/\lambda = (1-R)^2/(2R)$, in which R is the reflectance, α and λ are the absorption and scattering coefficients respectively. The energy band gaps were derived from α/λ vs. E (eV) plots.

Field emission scanning electron microscopy (FESEM) experiments were performed using NOVANO SEM 600 (FEI, Germany) operated at 15 kV. EDAX compositional analysis was performed during FESEM imaging.

Atomic force microscopy (AFM) was performed on a Bruker Innova Microscope in tapping mode with 10 nm diameter containing antimony doped Silicon tip.

X-ray photoelectron spectroscopy (XPS) measurement was performed with MgK α (1253.6 eV) X-ray source with a relative composition detection better than 0.1% on an Omicron Nano-technology spectrometer.

Transmission electron microscopy (TEM) images of the as synthesized materials were taken using a JEOL (JEM3010) TEM instrument (300 kV accelerating voltage) fitted with a Gatan CCD camera and also with a FEI TECNAI G2 20 STWIN TEM instrument (operating at 200 kV). A suspension of the nanosheets was prepared in cyclohexane solution and it was then drop casted in a holey carbon coated Cu grid for TEM imaging.

Scanning transmission electron microscopy (STEM) imaging was carried out using FEITECNAI G² 20 STWIN TEM operating at 200 KV. The sample preparation was the same as that of TEM. EDAX compositional analysis and color mapping were performed during STEM imaging. Background was subtracted (using multi-polynomial model) during the data processing for EDAX color mapping (with 500 eV minimum region of interest width). Errors in the determination in compositions of nanosheets in EDAX measurements is nearly 5%.

Inductively coupled plasma atomic emission spectroscopy (ICP-AES). The exact composition of the as synthesized nanosheets was calculated based on ICP-AES data. ICP-AES measurements were carried out using Perkin-Elmer Optima 7000DV

instrument. ICP-AES measurement were carried out by dissolving the powder nanosheets in aquaregia ($\text{HNO}_3:\text{HCl} = 1:3$) followed by diluting them with millipore water. Sn standard (1000 mg/L, Sigma-Aldrich), Se standard (1000 mg/L, Sigma-Aldrich) and Bi standard (1000 mg/L, Sigma-Aldrich) were used to determine the compositions in ICP. In the present measurement, error bar lies below 1.5 %.

Fourier transform infrared (FTIR) spectra was recorded using a Bruker IFS 66v/S spectrometer.

Spark plasma sintering (SPS) was done using a SPS211-LX (Dr. Sinter Lab) instrument. The powdered nanoplates were sintered to prepare a rectangular column ($8 \text{ mm} \times 8 \text{ mm} \times 8 \text{ mm}$) and coin ($2 \text{ mm} \times 10 \text{ mm}$) using graphite dies at 50 MPa pressure and 450°C temperature for 10 minutes. From the rectangular column, a rectangular bar ($2 \text{ mm} \times 2 \text{ mm} \times 8 \text{ mm}$) was made using a typical cutter-polisher. The density of the SPS processed samples were found to be about $\sim 95\%$ of theoretical density.

For further comparison, powdered samples had been compacted using Inductively heated uniaxial hot press in argon atmosphere at 45 MPa pressure and 500°C temperature.

Electrical transport properties. Electrical conductivity (σ) and Seebeck coefficients (S) were measured simultaneously from the rectangular bar under helium atmosphere from room temperature to 873 K using a ULVAC-RIKO ZEM-3 instrument system. σ and S were measured in both the parallel and perpendicular to the pressing directions.

Hall measurement. Room temperature carrier concentrations were determined from Hall coefficient measurements with the equipment developed by Excel Instrument, India. Four-contact Hall-bar geometry was used for the measurement. The applied magnetic field was 1 Tesla. Room temperature carrier concentration, n , was measured using the formula $n = I/eR_H$, where e is the electronic charge, and R_H is the hall coefficient.

Thermal transport properties. The thermal diffusivity (D) of the coin-shaped samples have been measured by laser flash diffusivity technique using NETZSCH LFA 457 instrument in 300–720 K range. Total thermal conductivity (κ_{total}) was calculated using the formula $\kappa_{total} = DC_p\rho$, where D is the thermal diffusivity, C_p is specific heat, and ρ is density of the sample. Further, the electronic thermal conductivities, κ_{ele} were estimated

using Wiedemann-Franz Law, $\kappa_{ele} = L\sigma T$, where L is the Lorenz number which is estimated by fitting reduced chemical potential derived from temperature-dependent Seebeck coefficient using single parabolic band conduction and dominant acoustic phonon scattering of carriers. The heat capacity value was taken from references 16 and 17.

2.3.3. Results and Discussions

Powder X-ray diffraction patterns of as-synthesized samples have been indexed to pure orthorhombic SnSe (Figure 2.3.2a) with lattice parameters of $a = 11.50 \text{ \AA}$, $b = 4.15 \text{ \AA}$ and $c = 4.45 \text{ \AA}$. The indirect optical band gap of the SnSe nanosheets were measured to be $\sim 1.01 \text{ eV}$. Further, Bi being more electronegative than Sn, is known to create an acceptor level just below the conduction band of Sn, which *in-turn* reduces the band gap of the $\text{Sn}_{0.94}\text{Bi}_{0.06}\text{Se}$ nanosheets to $\sim 0.88 \text{ eV}$ (Figure 2.3.2b).

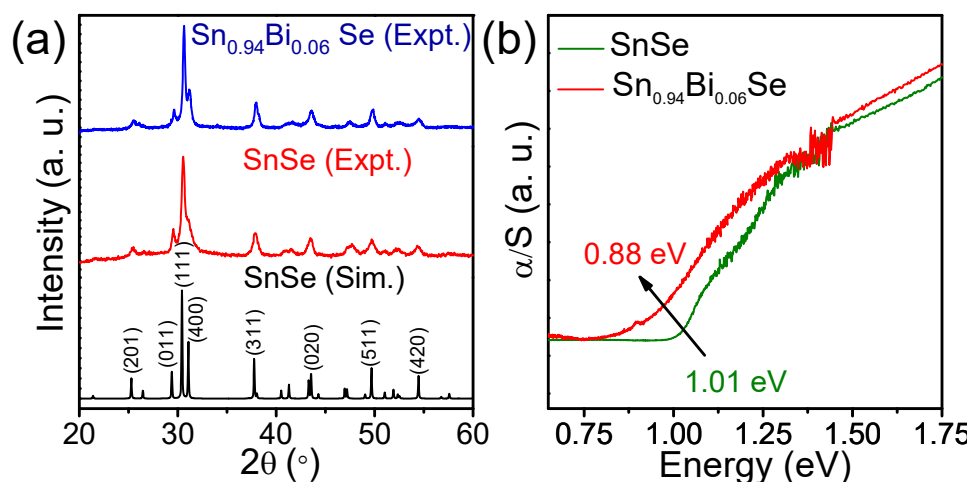


Figure 2.3.2. (a) PXRD patterns of as-synthesized SnSe and $\text{Sn}_{0.94}\text{Bi}_{0.06}\text{Se}$ nanosheets. (b) Optical absorption spectra of SnSe and $\text{Sn}_{0.94}\text{Bi}_{0.06}\text{Se}$ nanosheets.

In order to confirm Bi doping, X-ray photoelectron spectroscopy (XPS) was performed on both SnSe and Bi-doped SnSe nanosheets. Figure 2.3.3 confirms the presence of Sn, Se and Bi in as-synthesized $\text{Sn}_{0.94}\text{Bi}_{0.06}\text{Se}$ nanosheets. The Sn 3d spin-orbit doublet peaks appeared at 488.4 eV and 496.7 eV with splitting of 8.3 eV, which can be assigned to Sn 3d_{5/2} and Sn 3d_{3/2}, respectively.¹⁰ We could be able to deconvolute

the broad peak of selenium as Se 3d_{5/2} and Se 3d_{3/2} at 53.1 eV and 55.45 eV respectively.¹³ Presence of Bi 4f_{7/2} and Bi 4f_{5/2} peaks at 159.6 eV and 164.95 eV can be attributed to Bi (III) states in Bi-doped SnSe sample.¹⁰ *In-situ* chlorination of as-synthesized SnSe and Sn_{0.94}Bi_{0.06}Se nanosheets was further confirmed from the XPS peak at 198.7 eV.¹³

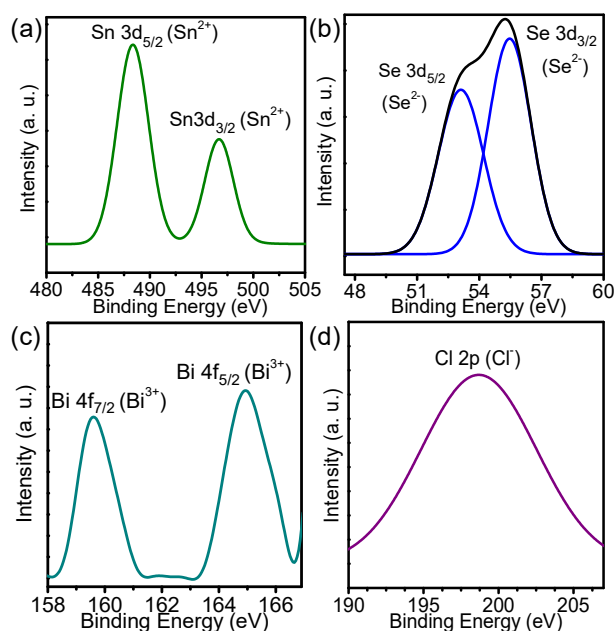


Figure 2.3.3. High-resolution XPS of (a) Sn 3d, (b) Se 3d, (c) Bi 4f, and (d) Cl 2p in Sn_{0.94}Bi_{0.06}Se nanosheets.

The actual elemental compositions of SnSe nanosheet samples were obtained further from inductively coupled plasma atomic emission spectroscopy (ICP-AES) and energy dispersive analysis of X-Rays (EDAX). Compositions determined by these two independent techniques are in good agreement with the nominal compositions (Table 2.3.1), which confirms successful control over the composition in the present synthetic technique.

Table 2.3.1. Analysis of sample compositions from EDAX and ICP-AES.

Nominal Composition	Composition obtained from ICP-AES	Composition obtained from EDAX
SnSe	SnSe _{1.33}	SnSe _{1.05}
Sn _{0.94} Bi _{0.06} Se	Sn _{0.94} Bi _{0.055} Se _{1.42}	Sn _{0.91} Bi _{0.058} Se _{1.47}

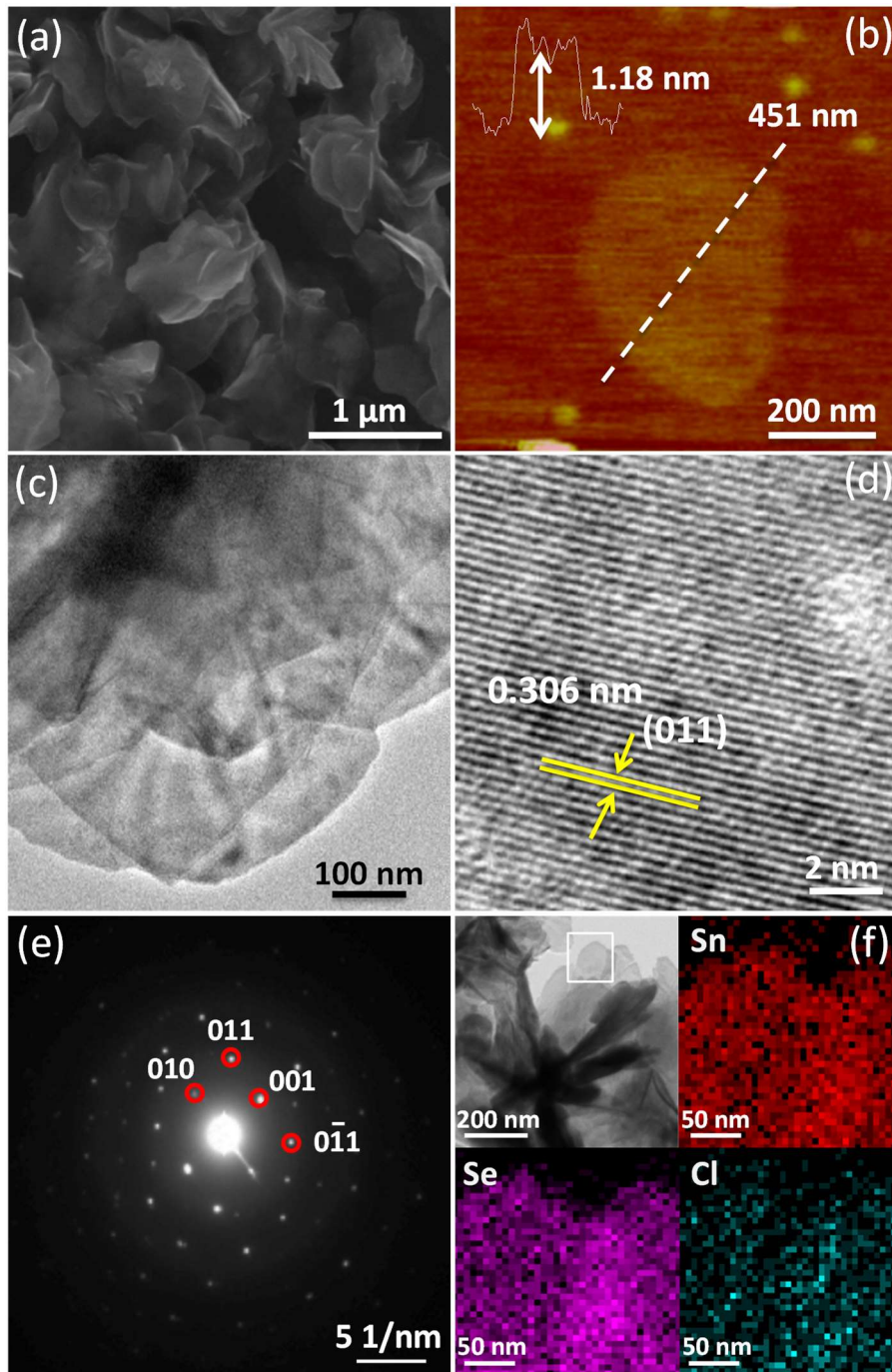


Figure 2.3.4. (a) FESEM image of SnSe nanosheets. (b) AFM image of single nanosheet of SnSe. (c) TEM image of SnSe nanosheets. (d) HRTEM image reveals the crystalline nature of the as-synthesized SnSe nanosheets. (e) SAED pattern of a single SnSe nanosheet. (f) STEM image of nanosheets and EDAX color mapping for Sn, Se and Cl.

Field emission scanning electron microscopy (FESEM) images display the 2D nanosheet morphology of SnSe and $\text{Sn}_{0.94}\text{Bi}_{0.06}\text{Se}$ samples (Figures 2.3.4a and 2.3.5a).

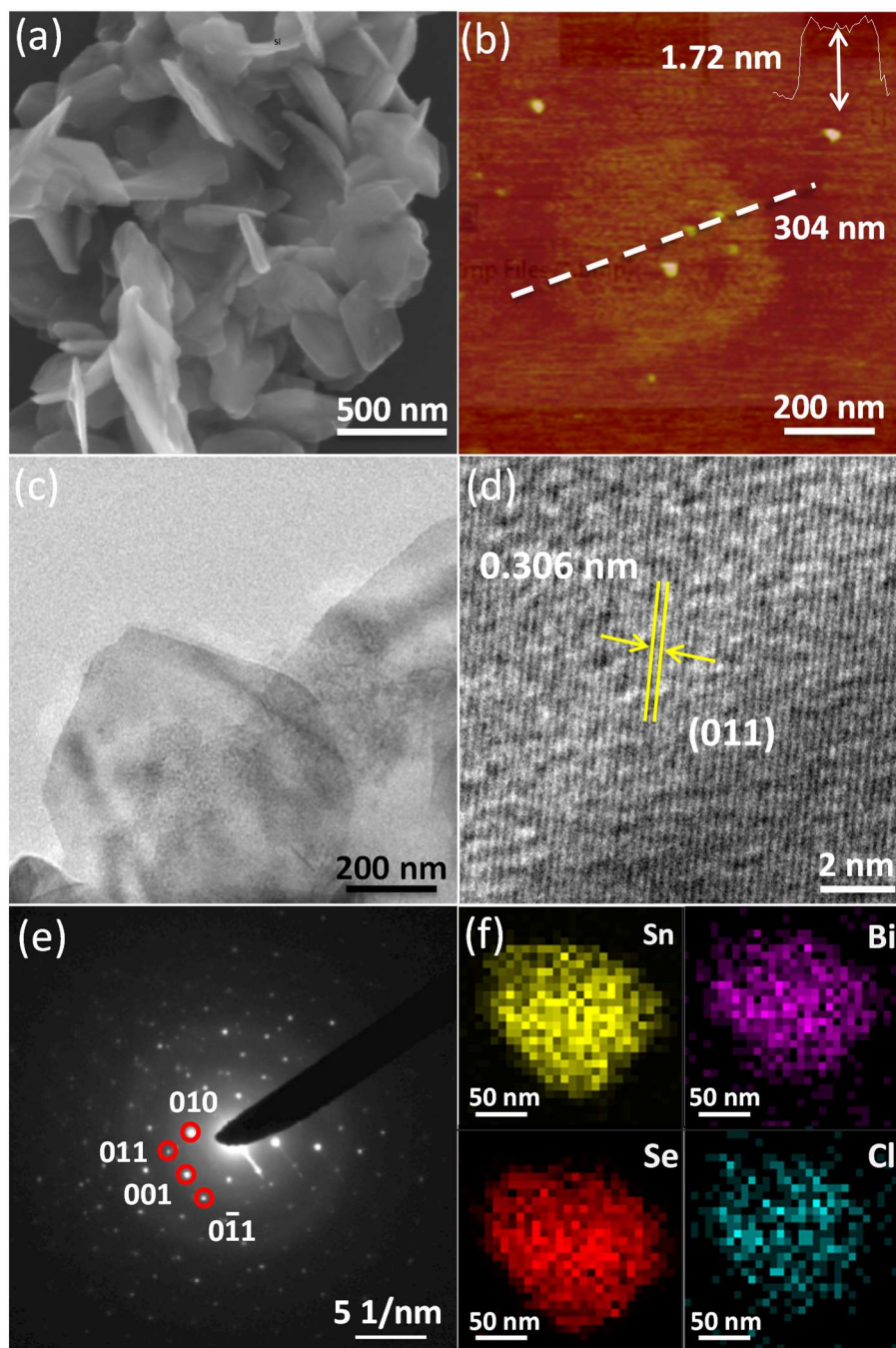


Figure 2.3.5. (a) FESEM image of $\text{Sn}_{0.94}\text{Bi}_{0.06}\text{Se}$ nanosheets. (b) AFM image of single nanosheet of $\text{Sn}_{0.94}\text{Bi}_{0.06}\text{Se}$. (c) TEM image of $\text{Sn}_{0.94}\text{Bi}_{0.06}\text{Se}$ nanosheets. (d) HRTEM image of $\text{Sn}_{0.94}\text{Bi}_{0.06}\text{Se}$ nanosheets. (e) SAED pattern of a single $\text{Sn}_{0.94}\text{Bi}_{0.06}\text{Se}$ nanosheet. Inset of (e) shows the STEM image of single nanosheet of $\text{Sn}_{0.94}\text{Bi}_{0.06}\text{Se}$. (f) EDAX color mapping of Sn, Se, Bi and Cl from the $\text{Sn}_{0.94}\text{Bi}_{0.06}\text{Se}$ nanosheet shown in STEM image.

SnSe and Bi-doped SnSe samples show folded nanosheet like morphology with a thickness of few nanometers (1.2-3 nm). The ultra-thin nature of the nanosheets was

confirmed by AFM, as depicted in Figures 2.3.4b and 2.3.5b. The height profile acquired from a typical AFM micrograph indicates the formation of 1.18 nm thick nanosheets (Figure 2.3.4b), which is nearly the thickness of two-layers SnSe (*i.e.*, *a*-axis of the unit cell). The lateral dimension of the as synthesized nanosheets ranges from 0.3 to 0.5 μm . 2D nanosheet nature of the samples was further verified from transmission electron microscope (TEM) images in Figures 2.3.4c and 2.3.5c. High-resolution TEM (HRTEM) images of SnSe and $\text{Sn}_{0.94}\text{Bi}_{0.06}\text{Se}$ nanosheets clearly show a lattice spacing of 3.06 \AA , which corresponds to the (011) plane of SnSe (Figures 2.3.4d and 2.3.5d).

The single crystalline nature of the nanosheets is confirmed by selected-area electron diffraction (SAED) pattern recorded from single nanosheet region (Figures 2.3.4e and 2.3.5e), which are indexed based on the orthorhombic SnSe structure. EDAX elemental color mapping has been done during scanning transmission electron microscopy (STEM) imaging which shows homogeneous distribution of all the respective elements in SnSe and $\text{Sn}_{0.94}\text{Bi}_{0.06}\text{Se}$ nanosheets (Figures 2.3.4f and 2.3.5f), which also confirms the successful Bi doping in SnSe.

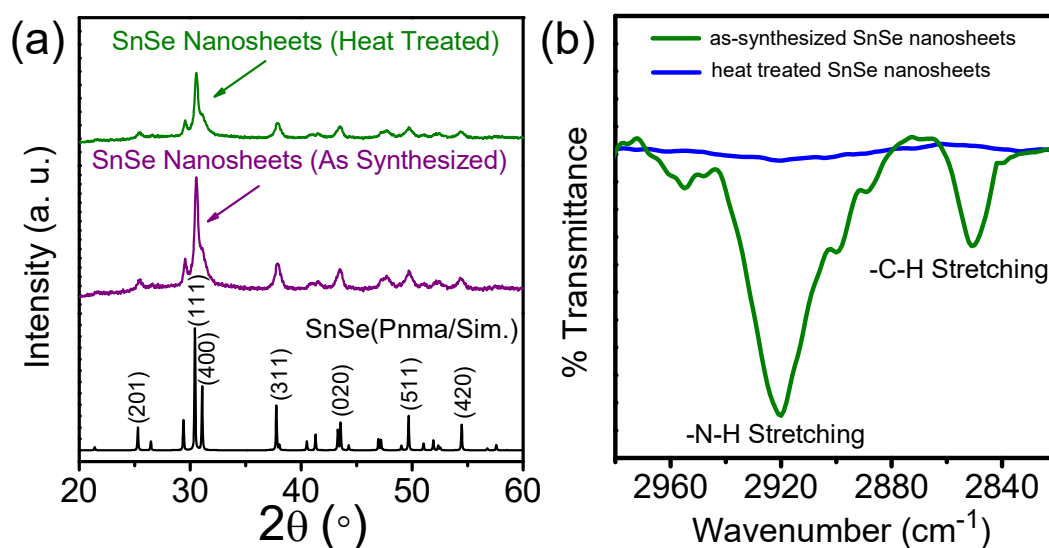


Figure 2.3.6. (a) PXRD pattern of the synthesized SnSe nanosheets before and after the tube-furnace treatment at 500 $^\circ\text{C}$. (b) FT-IR spectra of SnSe nanosheets before and after the heat treatment.

In order to investigate thermoelectric properties of SnSe and Bi-doped SnSe few-layer nanosheets, capping reagent has been removed by heat-treatment of as-synthesized

powder at 500 °C under N₂ flow. The conventional hydrazine treatment route for removal of capping agent was avoided because SnSe reacts with hydrazine to form a SnSe-hydrazine hydrate adduct.³² During this heat treatment, no change in structure and composition was found, as indicated by PXRD patterns (Figure 2.3.6a). The FTIR spectra confirms the removal of organic capping agent in the heating process (Figure 2.3.6b).

To measure the thermoelectric properties, the surface cleaned nanosheets were pressed into pellets using SPS process at a pressure of 40 MPa and 450 °C under vacuum. Figure 2.3.7 presents the temperature dependent electrical transport properties (both in \parallel & \perp to SPS pressing directions) of SnSe and Sn_{0.94}Bi_{0.06}Se nanosheets in the temperature range of 300-720 K. Electrical conductivity (σ) and Seebeck coefficient (S) were measured simultaneously under He atmosphere by a ULVAC-RIKO ZEM-3 instrument. Figure 2.3.7a represents temperature dependence of σ for both SnSe and Sn_{0.94}Bi_{0.06}Se samples. Being a semiconductor, electrical conductivity increases linearly with temperature for both the samples. The electrical conductivity measured along perpendicular to the SPS pressing direction is more than those from parallel to the pressing direction, which can be attributed to favorable electronic transport in perpendicular to pressing direction (*i.e.*, the *c*-axis, along the layers in SnSe, Figure 2.3.7a), as also observed elsewhere.^{23,33,34} Room temperature σ for SnSe nanosheets measured perpendicular to pressing direction is to be 0.28 S/cm, which increases to 9 S/cm at 719 K. Bi-doped nanosheets show superior electrical conductivity as compared to that of pristine SnSe. At room temperature, the σ values for the Sn_{0.94}Bi_{0.06}Se nanosheets (for the \perp to pressing direction) was 1.20 S/cm, which increases to 12.5 S/cm with increase in temperature.

The Hall coefficient of both the SnSe and Sn_{0.94}Bi_{0.06}Se nanosheets is negative at room temperature, which confirms the *n*-type conduction. The *n*-type nature of SnSe can be attributed to the *in-situ* chlorination during synthesis as confirmed from ICP and EDAX analysis (Table 2.3.1). The room temperature *n*-type carrier concentration (*n*) for Sn_{0.94}Bi_{0.06}Se nanosheets was estimated based on Hall measurement to be $1.97 \times 10^{18} \text{ cm}^{-3}$, which is significantly higher compared to that of the pure SnSe nanosheet ($3.08 \times 10^{17} \text{ cm}^{-3}$). Substitution of Bi³⁺ at Sn²⁺ site contributes excess electron to conduction band, which results in enhanced *n*-type carrier concentration and electrical conductivity.

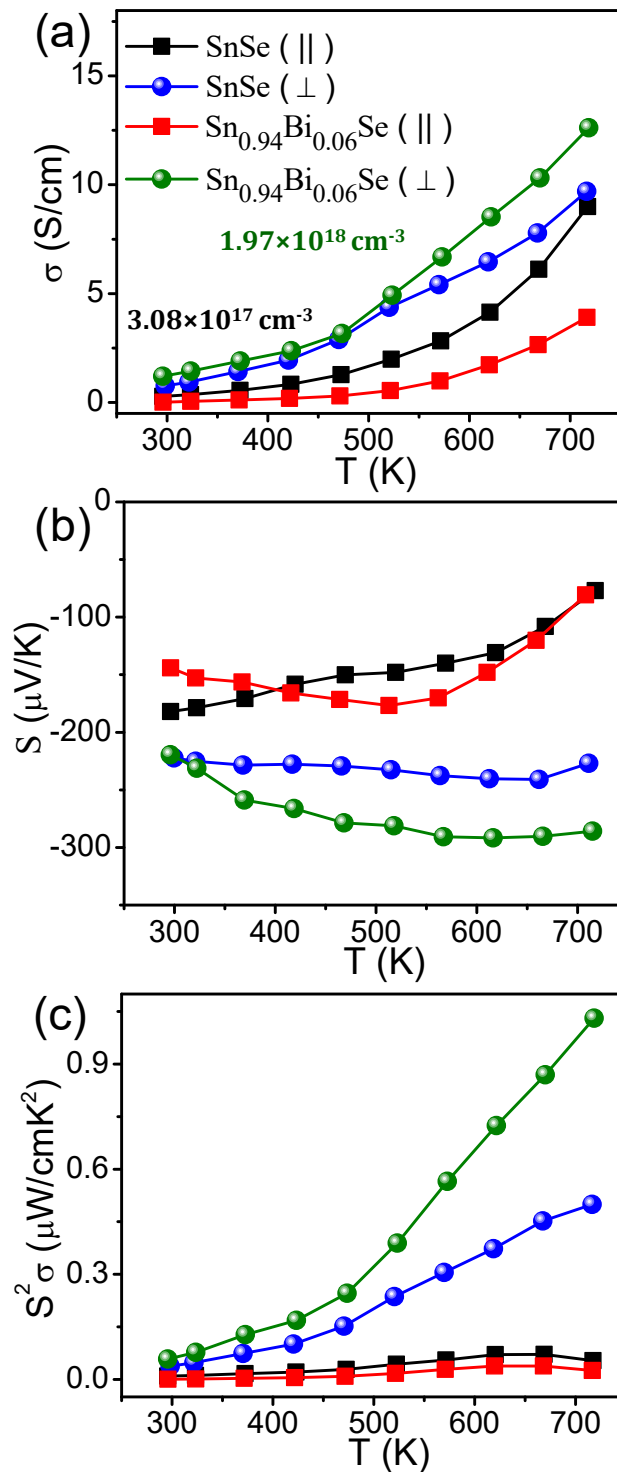


Figure 2.3.7. Temperature dependent (a) electrical conductivity (σ), (b) Seebeck coefficient (S), and (c) power factor ($S^2\sigma$) of SnSe and Sn_{0.94}Bi_{0.06}Se nanosheets measured along the SPS direction (indicated by squares) and perpendicular to the SPS direction (indicated by spheres). Room temperature carrier concentration of SPS-processed SnSe and Sn_{0.94}Bi_{0.06}Se nanosheets were mentioned in (a).

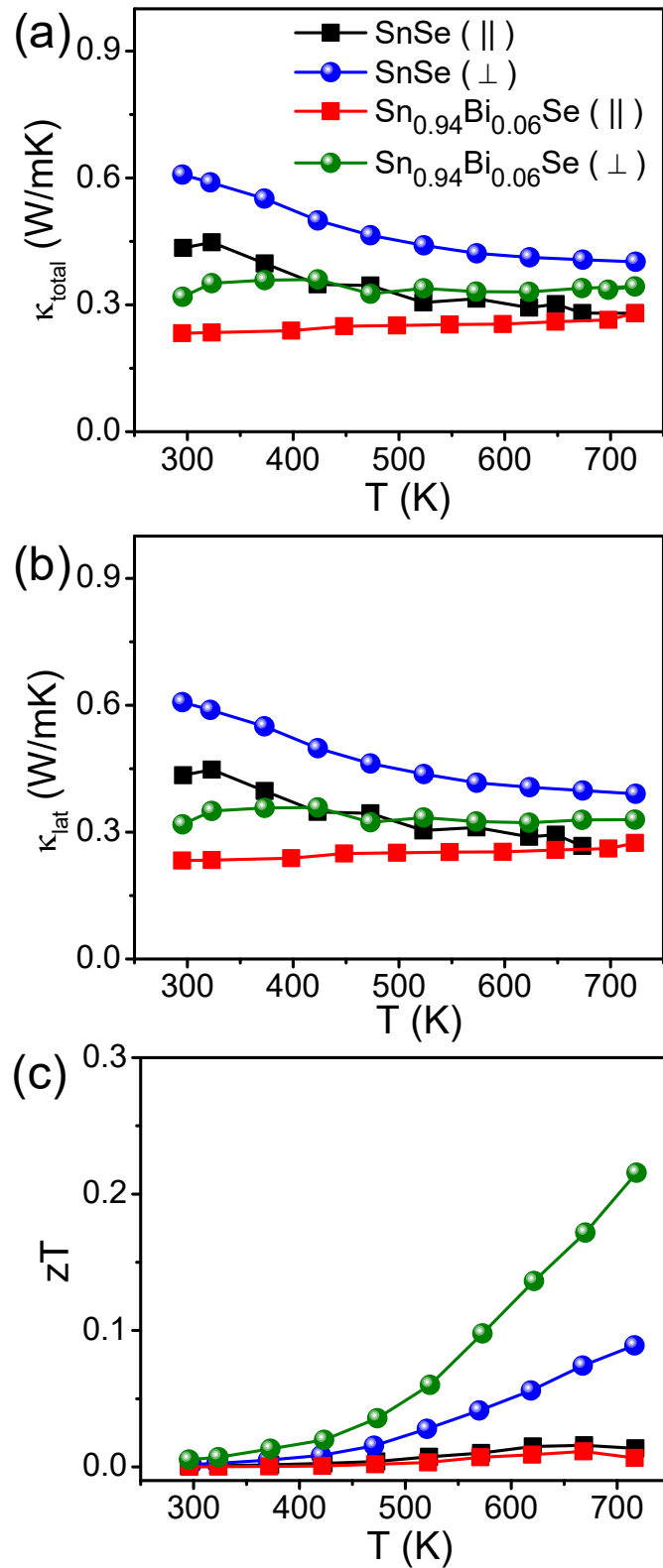


Figure 2.3.8. Temperature dependent total thermal conductivity (κ_{total}), (b) lattice thermal conductivity (κ_{lat}), (c) thermoelectric figure of merit, (zT) of SnSe and Sn_{0.94}Bi_{0.06}Se nanosheets.

Negative Seebeck coefficient (S) indicates the presence of n -type carriers in both the samples (Figure 2.3.7b). Typically, $\text{Sn}_{0.94}\text{Bi}_{0.06}\text{Se}$ nanosheets (\perp to pressing direction) has S value of $-219 \mu\text{V/K}$ at 300 K, which increases to $-285 \mu\text{V/K}$ at 719 K. Interestingly, we observe the S value is higher in the perpendicular to the pressing direction (along the c -axis in SnSe structure) than that of the parallel to the pressing direction, which is earlier observed in n -type Cl/Br-doped bulk SnSe.^{33,34} Previous electronic structure calculation demonstrated the presence of a heavy conduction band (Γ -Z direction *i.e.*, the c -axis in SnSe) along with the principal conduction band in SnSe.³⁵ Thus, high effective mass (m^*) of electron along the c -axis of SnSe (\perp to the pressing direction) resulted high S value compared to that of the parallel to the pressing direction. $\text{Sn}_{0.94}\text{Bi}_{0.06}\text{Se}$ nanosheets sample exhibit higher power factor of $1 \mu\text{W/cmK}^2$ at 719 K which is significantly higher than that of the SnSe (Figure 2.3.7c).

The temperature dependent total thermal conductivity was reported in Figure 2.3.8a. $\text{Sn}_{0.94}\text{Bi}_{0.06}\text{Se}$ nanosheets show lower κ_{lat} in the parallel to SPS pressing direction (*i.e.*, a -axis in SnSe) compared to that of the perpendicular to the SPS pressing direction (*i.e.*, c -axis of SnSe), which is attributed to phonon scattering by the interfaces between the layers (Figure 2.3.8b). Typically, $\text{Sn}_{0.94}\text{Bi}_{0.06}\text{Se}$ nanosheets exhibit ultralow κ_{lat} of $\sim 0.3 \text{ W/mK}$ over 300–720 K measured perpendicular to SPS pressing direction which is in close proximity to the theoretical minimum, κ_{min} of SnSe (0.26 W/mK).²³ n -type $\text{Sn}_{0.94}\text{Bi}_{0.06}\text{Se}$ few-layer nanosheets (\perp to the SPS pressing direction) demonstrate zT of 0.21 at 719 K, which is higher than that of n -type SnSe nanosheet sample (Figure 2.3.8c).

2.3.4. Conclusion

In summary, n -type few-layer (2-4 layers) Bi-doped SnSe 2D nanosheets (1.2-3 nm thick) have been synthesized via facile low temperature solution-based route. The n -type nature of $\text{Sn}_{0.94}\text{Bi}_{0.06}\text{Se}$ can be attributed to the *in-situ* chlorination and donor dopant nature of Bi. The presence of nanoscale grain boundaries and layered anisotropic structure enables the heat carrying phonons to get scattered significantly, thereby decreasing κ_{lat} to as low as $\sim 0.3 \text{ W/mK}$ over 300-720 K range. A combination of low thermal conductivity coupled with high power factor originated due to the enhancement of carrier

concentration to $1.97 \times 10^{18} \text{ cm}^{-3}$, gives rise to a zT of 0.21 at 719 K for 6% Bi-doped SnSe nanosheets, which is higher than that of n -type SnSe nanosheets.

2.3.5. References

- (1) Tan, G.; Zhao, L. D.; Kanatzidis, M. G. *Chem. Rev.* **2016**, *116*, 12123-12149.
- (2) Guin, S. N.; Banik, A.; Biswas, K. In *2D Inorganic Materials Beyond Graphene*, Rao, C. N. R.; Waghmare, U. V., Eds. World Scientific Publishing: Singapore, **2017**, Pages 239-274.
- (3) Poudel, B.; Hao, Q.; Ma, Y.; Lan, Y.; Minnich, A.; Yu, B.; Yan, X.; Wang, D.; Muto, A.; Vashaee, D.; *et al.* *Science* **2008**, *320*, 634-638.
- (4) Nicolosi, V.; Chhowalla, M.; Kanatzidis, M. G.; Strano, M. S.; Coleman, J. N. *Science* **2013**, *340*, 1226419.
- (5) Chhowalla, M.; Shin, H. S.; Eda, G.; Li, L. J.; Loh, K. P.; Zhang, H. *Nat. Chem.* **2013**, *5*, 263-275.
- (6) Cao, X.; Tan, C.; Zhang, X.; Zhao, W.; Zhang, H. *Adv. Mater.* **2016**, *28*, 6167-6196.
- (7) Jana, M. K.; Biswas, K.; Rao, C. N. R. *Chem. Eur. J.* **2013**, *19*, 9110-9113.
- (8) Park, K.; Ahn, K.; Cha, J.; Lee, S.; Chae, S. I.; Cho, S. P.; Ryee, S.; Im, J.; Lee, J.; Park, S.-D.; *et al.* *J. Am. Chem. Soc.* **2016**, *138*, 14458-14468.
- (9) Sun, Y.; Cheng, H.; Gao, S.; Liu, Q.; Sun, Z.; Xiao, C.; Wu, C.; Wei, S.; Xie, Y. *J. Am. Chem. Soc.* **2012**, *134*, 20294-20297.
- (10) Banik, A.; Biswas, K. *Angew. Chem. Int. Ed.* **2017**, *56*, 14561-14566.
- (11) Chatterjee, A.; Biswas, K. *Angew. Chem. Int. Ed.* **2015**, *54*, 5623-5627.
- (12) Chatterjee, A.; Guin, S. N.; Biswas, K. *Phys. Chem. Chem. Phys.* **2014**, *16*, 14635-14639.
- (13) Saha, S.; Banik, A.; Biswas, K. *Chem. Eur. J.* **2016**, *22*, 15634-15638.
- (14) Luo, Y.; Zheng, Y.; Luo, Z.; Hao, S.; Du, C.; Liang, Q.; Li, Z.; Khor, K. A.; Hippalgaonkar, K.; Xu, J.; *et al.* *Adv. Energy Mater.* **2017**, *8*, 1702167.
- (15) Zhao, L.-D.; Chang, C.; Tan, G.; Kanatzidis, M. G. *Energy Environ. Sci.* **2016**, *9*, 3044-3060.
- (16) Zhao, L.-D.; Lo, S.-H.; Zhang, Y.; Sun, H.; Tan, G.; Uher, C.; Wolverton, C.; Dravid, V. P.; Kanatzidis, M. G. *Nature* **2014**, *508*, 373-377.
- (17) Zhao, L.-D.; Tan, G.; Hao, S.; He, J.; Pei, Y.; Chi, H.; Wang, H.; Gong, S.; Xu, H.; Dravid, V. P.; *et al.* *Science* **2016**, *351*, 141-144.
- (18) Peng, K.; Lu, X.; Zhan, H.; Hui, S.; Tang, X.; Wang, G.; Dai, J.; Uher, C.; Wang,

- G.; Zhou, X. *Energy Environ. Sci.* **2015**, *9*, 454-460.
- (19) Ge, Z.-H.; Song, D.; Chong, X.; Zheng, F.; Jin, L.; Qian, X.; Zheng, L.; Dunin-Borkowski, R. E.; Qin, P.; Feng, J.; *et al.* *J. Am. Chem. Soc.* **2017**, *139*, 9714-9720.
- (20) Tang, G.; Wei, W.; Zhang, J.; Li, Y.; Wang, X.; Xu, G.; Chang, C.; Wang, Z.; Du, Y.; Zhao, L. D. *J. Am. Chem. Soc.* **2016**, *138*, 13647-13654.
- (21) Chen, Y.-X.; Ge, Z.-H.; Yin, M.; Feng, D.; Huang, X.-Q.; Zhao, W.; He, J. *Adv. Funct. Mater.* **2016**, *26*, 6836-6845.
- (22) Lee, Y. K.; Ahn, K.; Cha, J.; Zhou, C.; Kim, H. S.; Choi, G.; Chae, S. I.; Park, J.-H.; Cho, S. P.; Park, S. H.; *et al.* *J. Am. Chem. Soc.* **2017**, *139*, 10887-10896.
- (23) Zhang, Q.; Chere, E. K.; Sun, J.; Cao, F.; Dahal, K.; Chen, S.; Chen, G.; Ren, Z. C. *Adv. Energy Mater.* **2015**, *5*, 1500360.
- (24) Wei, T.-R.; Tan, G.; Zhang, X.; Wu, C.-F.; Li, J.-F.; Dravid, V. P.; Snyder, G. J.; Kanatzidis, M. G. *J. Am. Chem. Soc.* **2016**, *138*, 8875-8882.
- (25) Wei, W.; Chang, C.; Yang, T.; Liu, J.; Tang, H.; Zhang, J.; Li, Y.; Xu, F.; Zhang, Z.; Li, J. F.; *et al.* *J. Am. Chem. Soc.* **2018**, *140*, 499-505.
- (26) Duong, A. T.; Nguyen, V. Q.; Duvjir, G.; Duong, V. T.; Kwon, S.; Song, J. Y.; Lee, J. K.; Lee, J. E.; Park, S.; Min, T.; *et al.* *Nat. Commun.* **2016**, *7*, 13713.
- (27) Hu, C.-H.; Chiang, M.-H.; Hsieh, M.-S.; Lin, W.-T.; Fu, Y.-S.; Guo, T.-F. *CrystEngComm* **2013**, *16*, 1786-1792.
- (28) Li, L.; Chen, Z.; Hu, Y.; Wang, X.; Zhang, T.; Chen, W.; Wang, Q. *J. Am. Chem. Soc.* **2013**, *135*, 1213-1216.
- (29) Han, G.; Popuri, S. R.; Greer, H. F.; Bos, J. W. G.; Zhou, W.; Knox, A. R.; Montecucco, A.; Siviter, J.; Man, E. A.; Macauley, M.; *et al.* *Angew. Chem. Int. Ed.* **2016**, *55*, 6433-6437.
- (30) Hong, M.; Chen, Z.-G.; Yang, L.; Chasapis, T. C.; Kang, S. D.; Zou, Y.; Auchterlonie, G. J.; Kanatzidis, M. G.; Snyder, G. J.; Zou, J. *J. Mater. Chem. A* **2017**, *5*, 10713-10721.
- (31) Han, G.; Popuri, S. R.; Greer, H. F.; Llin, L. F.; Bos, J.-W. G.; Zhou, W.; Paul, D. J.; Ménard, H.; Knox, A. R.; Montecucco, A.; *et al.* *Adv. Energy Mater.* **2017**, *7*, 1602328.
- (32) Mitzi, D. B. *Inorg. Chem.* **2005**, *44*, 3755-3761.

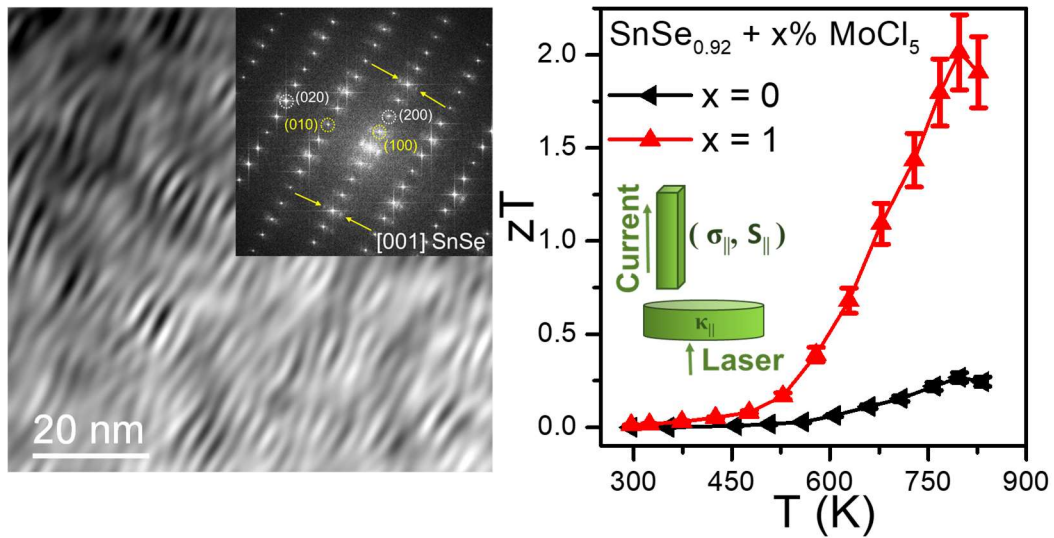
-
- (33) Xue, W.; Jingtao, X.; Guoqiang, L.; Yajie, F.; Zhu, L.; Xiaojian, T.; Hezhu, S.; Haochuan, J.; Tianya, T.; Jun, J. *Appl. Phys. Lett.* **2016**, *108*, 083902.
- (34) Chang, C.; Tan, Q.; Pei, Y.; Xiao, Y.; Zhang, X.; Chen, Y.-X.; Zheng, L.; Gong, S.; Li, J. F.; He, J.; *et al.* *RSC Adv.* **2016**, *6*, 98216-98220.
- (35) Kutorasinski, K.; Wiendlocha, B.; Kaprzyk, S.; Tobola, J. *Phys. Rev. B* **2015**, *91*, 205201.

PART 3

**High Thermoelectric Performance of
Polycrystalline *n*-type SnSe**

Chapter 3.1

Modular Nanostructures Facilitate Low Thermal Conductivity and Ultra-high Thermoelectric Performance in *n*-type SnSe



Modular Nanostructures Facilitate Low Thermal Conductivity and Ultra-high Thermoelectric Performance in *n*-type SnSe[†]

Summary

Single crystals of SnSe have gained considerable attention in thermoelectrics due to their unprecedented thermoelectric performance. However, polycrystalline SnSe is more favourable for practical applications due to its facile chemical synthesis procedure, processability and scalability. Though the thermoelectric figure of merit (zT) of *p*-type bulk SnSe polycrystals has reached >2.5 , the zT of *n*-type counterpart is still lower and lies around ~ 1.5 . Herein, we report record high zT of 2.0 in *n*-type polycrystalline SnSe_{0.92} + *x* mol% MoCl₅ ($x = 0 - 3$) samples when measured parallel to the SPS pressing direction due to the simultaneous optimization of *n*-type carrier concentration and enhanced phonon scattering by incorporating modular nano-heterostructures in SnSe matrix. The successful creation of Se vacancy and substitution of Mo⁵⁺ at Sn²⁺ and Cl⁻ ions at Se²⁻ sites effectively enhance the total *n*-type carrier concentration, thus improving the electrical conductivity. Modular nanostructures of layered intergrowth [(SnSe)_{1.05}]_{*m*}(MoSe₂)_{*n*} like compounds embedded in SnSe matrix scatters the phonons significantly leading to an ultra-low lattice thermal conductivity of ~ 0.26 W/mK at 798 K in SnSe_{0.92} + 3 mol% MoCl₅. Here, the 2D layered modular intergrowth compound resembles the nano-heterostructure and their periodicity of 1.2 - 2.6 nm in the SnSe matrix matches the phonon mean free path of SnSe, thereby block the heat carrying phonons which result in low κ_{lat} and ultra-high thermoelectric performance in *n*-type SnSe.

[†]S. Chandra, U. Bhat, P. Dutta, A. Bhardwaj, R. Datta and K. Biswas, 2022. (Manuscript Submitted)

3.1.1. Introduction

Polycrystalline SnSe is more preferred over single crystals for practical thermoelectric applications due to the ease of synthesis, processability and scalability.¹⁻⁵ But polycrystalline SnSe suffers from surface oxidation which leads to a diminished carrier mobility and higher thermal conductivity (κ) and hence it struggles to display higher thermoelectric figure of merit (zT) as compared to the single crystalline counterparts.^{6,7} Till date, a plethora of research has been carried out to modulate the thermoelectric performance of polycrystalline SnSe by doping with alkali metal ions (Na, K, and Ag)^{1,7,8} or by removing the surface oxidation via H₂ treatment.^{9,10} However, in most of the cases the research is focused to enhance the zT of p -type bulk SnSe polycrystals, whereas thermoelectric applications demand both p and n -type counterparts.¹¹ Recently, halide doping has evolved as an effective strategy to increase the n -type carrier concentration of polycrystalline SnSe.¹²⁻¹⁷ Besides, a couple of thermoelectric studies have also shown moderate zT values (far below the zT 's of n -type single crystal) in n -type polycrystalline SnSe via Re doping and band-gap engineering.^{18,19} As thermoelectric module demands both high performance p - and n -type similar materials, there remains plenty of room to enhance the zT to 2 for the n -type SnSe polycrystals by applying innovative and new strategies.

Lattice thermal conductivity (κ_{lat}) being the only independent parameter in the expression of zT , it plays a major role to determine the performance of a thermoelectric material. Hitherto, numerous strategies have been established for suppressing the lattice thermal conductivity by introducing hierarchical nano/meso architectures over all possible length-scales owing to enhanced phonon scattering.²⁰⁻²² Recently, incorporating nanoscale superstructure domains in a thermoelectric matrix is also found to be an efficient tool to minimize the κ_{lat} to its glass limit.^{23,24} On the other hand, modular inorganic materials like pristine layered intergrowth (*e.g.* Pb_mBi_{2n}Te_{3n+m}, Sn_mBi_{2n}Te_{3n+m}, *etc.*)²⁵⁻²⁷, misfit (*e.g.* SnS₂/SnS, LaS/TaSe₂, *etc.*)^{28,29} compounds and more recently the modular oxides,³⁰ have emerged as interesting candidates in thermoelectrics. These materials are considered as natural heterostructures which show intrinsically low κ_{lat} due to inherent phonon scattering at the interfaces and due to large unit cells. Although modular compounds show great promise in exhibiting low κ_{lat} in pristine form, they lack

high thermoelectric performance due to their poor electrical transport properties.^{26,27} Thus, we believe, if such modular compounds with natural superstructures can be stabilized in the form of 2D nanostructures in bulk thermoelectric matrix (such as here in *n*-type SnSe), it will be greatly beneficial for achieving high thermoelectric performance. However, stabilization of such modulated nanostructures in bulk thermoelectric matrix is a challenging task and hence rarely studied.

In this chapter, I have presented ultra-high thermoelectric figure of merit (zT) of 2.0 in *n*-type polycrystalline $\text{SnSe}_{0.92+x}$ mol% MoCl_5 ($x = 0 - 3$) when measured parallel to the spark plasma sintering (SPS) direction due to the simultaneous effect of significant phonon scattering by modular nanostructures and enhanced electronic charge carrier transport. First, we have synthesized *n*-type polycrystalline $\text{SnSe}_{1-\delta}$ by creating slight Se vacancy (δ) and subsequently MoCl_5 was doped to enhance the overall *n*-type carrier concentration. Detailed high-resolution transmission electron microscopy (HRTEM) analysis indicates the formation of two-dimensional (2D) layered modular nanostructures of layered intergrowth $[(\text{SnSe})_{1.05}]_m(\text{MoSe}_2)_n$ (where, m and n are integers) like compound which are embedded in SnSe matrix. These natural nano-heterostructures with periodicity of 1.2 - 2.6 nm significantly scatter the heat carrying phonons in SnSe and reduce the κ_{lat} drastically to ~ 0.26 W/mK at 798 K in $\text{SnSe}_{0.92+3}$ mol% MoCl_5 sample. To check the anisotropic behavior, we have carefully measured the thermoelectric properties of the present system both along the parallel and perpendicular to spark plasma sintering (SPS) pressing direction. The present strategy of incorporating modular nano-heterostructures (*e.g.*, layered intergrowth or misfit compounds) in *n*-type polycrystalline SnSe matrix is found to be an effective approach to decrease the κ_{lat} thereby enhancing the overall thermoelectric performance and this idea can also be implemented in other thermoelectric materials.

3.1.2. Methods

Reagents. The high purity elements utilized for the synthesis are tin (Alfa Aesar 99.99+%), selenium (Se, Alfa Aesar 99.9999%) and molybdenum (V) chloride (MoCl_5 , Sigma Aldrich 99.9%).

Synthesis. Polycrystalline SnSe_{0.92} samples doped with x mol% MoCl₅ (x = 0, 1, 2, 3) were synthesized by combining stoichiometric amount of elemental Sn, Se and powdered MoCl₅ in high quality quartz tubes. The quartz tubes were sealed under vacuum (Pressure = 10⁻⁵ Torr). The sealed tubes were initially heated to 773 K in a box furnace over a period of 12 hrs, then heated again to 1223 K in next 5 hrs followed by annealing for 10 hrs and subsequently cooled to room temperature for a period of 15 hrs. The resulted ingots were crushed by using a mortar and pestle; and sieved to fine powder. For the ease of representation, the samples are termed as SnSe_{0.92} + x% MoCl₅ throughout the manuscript.

Powder X-ray diffraction (PXRD) patterns of the samples were recorded using a Cu K_α (λ = 1.5406 Å) radiation on a Rigaku Smartlab (9 kW, rotating anode) x-ray diffractometer. Rietveld refinement of the PXRD pattern was performed using FULLPROF software.³¹

Field emission scanning electron microscopy (FESEM) in back-scattered electron (BSE) mode. FESEM-BSE images were taken using ZEISS Gemini SEM – Field Emission Scanning Electron Microscope.

Transmission electron microscopy (TEM). TEM experiments were performed using ThermoFisher TitanTM Themis operating at 300 kV accelerating voltage and ThermoFisher Talos F200 S operating at 200 kV accelerating voltage. The samples for TEM measurement were prepared by the standard mechanical grinding, polishing down to a thickness of ~ 45 μm, and then followed by precision ion polishing system (PIPS). During ion milling, the samples were the first ion milled with the beam voltage = 4.5 keV and milling angle = ±5°. After the sample was perforated, a voltage of 2.0 keV was used to optimize the thin area of the specimen. The EDS mapping was conducted using the SuperX EDS detector. TEM measurements and analysis were performed in the collaboration with Prof. Ranjan Datta, JNCASR, India.

X-ray photoelectron spectroscopy (XPS) measurement has been performed with AlK_α (1.487 keV) monochromatic X-ray source with a relative composition detection better than 0.1% on an Thermo Scientific spectrometer.

Spark plasma sintering (SPS) was done using a SPS211-LX (Dr. Sinter Lab) instrument. The finely powdered samples were sintered to prepare a cylinder (10 mm × 8 mm) using graphite dies at 50 MPa pressure and 450 °C temperature for 10 minutes. The samples were cut and polished in different directions to measure the anisotropic electrical and thermal transport properties of $\text{SnSe}_{0.92} + x\% \text{MoCl}_5$.

Electrical transport properties. Electrical conductivity and Seebeck coefficients were measured simultaneously under helium atmosphere from room temperature to 850 K on a ULVAC-RIKO ZEM-3 instrument system. The SPS processed sample were cut and polished in a bar shape with the dimensions of $\sim 2 \times 2 \times 8 \text{ mm}^3$ to carry out the measurements. Electrical and thermal transport were measured in same direction.

Hall measurement. For determining the carrier concentrations, Hall measurements were carried out on the same rectangular specimens used for electrical transport measurement in four-contact geometry up to a magnetic field of 1 T at room-temperature using custom-built equipment developed by Excel Instruments.

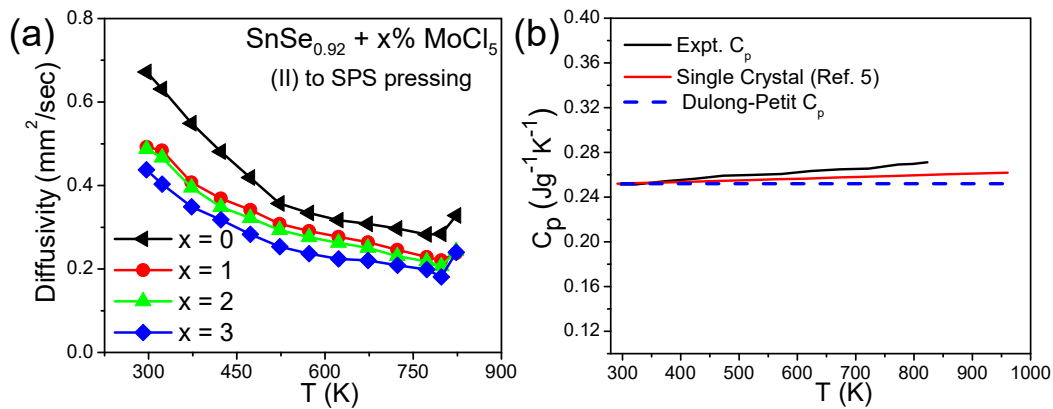


Figure 3.1.1. (a) Temperature dependent diffusivity and (b) typical heat capacity (C_p) of $\text{SnSe}_{0.92} + x\% \text{MoCl}_5$ polycrystals along with the Dulong-Petit limit and C_p value of single crystals of SnSe .³²

Thermal transport properties. Temperature dependent thermal diffusivity (D) was evaluated using a laser flash diffusivity technique in a Netzsch LFA-457 instrument. Next, the total thermal conductivity (κ) was derived using the formula, $\kappa = D \cdot C_p \cdot \rho$, where D is the thermal diffusivity, C_p is specific heat, and ρ is density of the sample. Diffusivity

of the samples are provided in Figure 3.1.1a. C_p was derived experimentally using pyroceram as a reference material during the thermal diffusivity measurements and provided in Figure 3.1.1b. The experimentally determined density was found to be $\sim 97\%$ of the theoretical density. Further, the electrical thermal conductivity, κ_{ele} were derived using Wiedemann-Franz Law, $\kappa_{ele} = L\sigma T$, where L denotes the Lorenz number which was estimated by fitting the temperature dependent Seebeck data^{33–35}.

3.1.3. Results and Discussions

Stoichiometric SnSe is a *p*-type semiconductor due to its intrinsic Sn vacancy.^{36,37} Thus, creation of Se vacancy could be useful in two ways: (i) it can compensate the inherent Sn vacancy in SnSe and (ii) depending on the concentration of Se vacancy (δ), it may lead to a desired *n*-type SnSe system.³⁸ Further, introduction of a small concentration of MoCl₅ in the SnSe_{1- δ} can further enhance the *n*-type carrier density which is beneficial for its thermoelectric performance. Polycrystalline SnSe_{0.92} samples doped with x mol% MoCl₅ ($x = 0, 1, 2, 3$) were synthesized via vacuum ($\sim 10^{-5}$ torr) sealed tube melting reaction followed by spark plasma sintering (SPS) and the composition is termed as SnSe_{0.92} + $x\%$ MoCl₅. Figure 3.1.2a depicts the room temperature powder X-ray diffraction (PXRD) patterns of as-synthesized SnSe_{0.92} + $x\%$ MoCl₅ ($x = 0, 1, 2, 3$) polycrystals. All the major peaks in the PXRD pattern are indexed to the *Pnma* orthorhombic phase of SnSe, whereas minute amount of MoSe₂ secondary phase (marked with asterisk) started to emerge from 2 mol% doping of MoCl₅. MoSe₂ also possess a layered structure with space group *P6₃/mmc* where the individual layers are stacked along *c*-direction by van der Waals interactions.³⁹ Presence of MoSe₂ secondary phase in the PXRD pattern indicates that the solid solution limit of MoCl₅ in SnSe_{0.92} is only up to 1 mol%. Furthermore, to check the phase purity of the Se vacant SnSe sample, Rietveld refinement has been performed on the room temperature PXRD patterns of SnSe_{0.92} as shown in Figure 3.1.2b. The obtained lattice parameters from the refinement are ($a = 11.4837$ Å, $b = 4.1491$ Å, and $c = 4.4393$ Å) which are in good agreement with previously reported values.³²

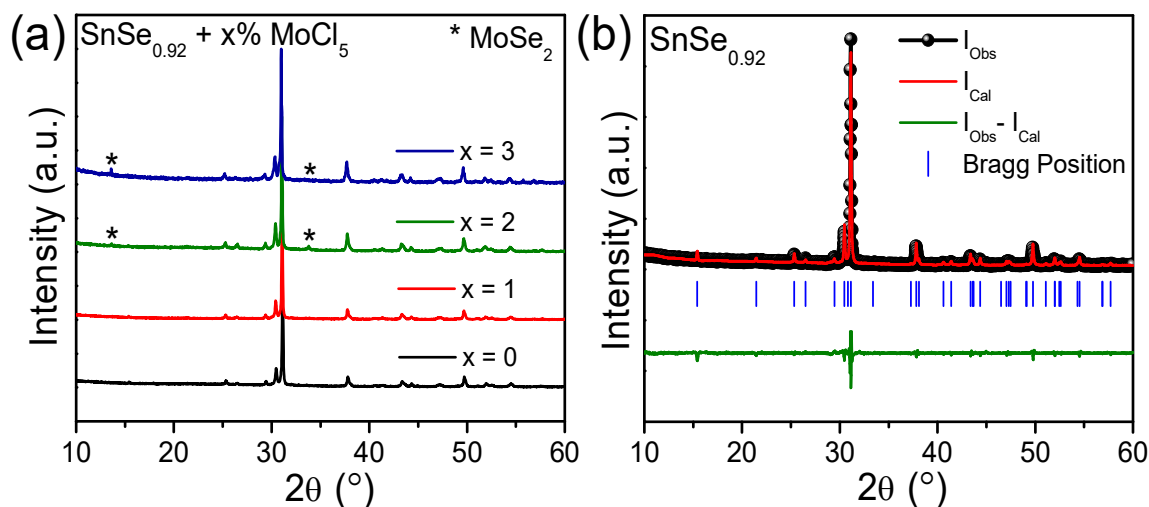


Figure 3.1.2. (a) Room temperature PXRD patterns of as-synthesized $\text{SnSe}_{0.92} + x\%$ MoCl_5 ($x = 0, 1, 2, 3$) polycrystals. The peaks marked with asterisk (*) denotes the presence of MoSe_2 as secondary phase. (b) Rietveld refinement of PXRD data of polycrystalline $\text{SnSe}_{0.92}$.

Further, to investigate the microstructural compositions, field-emission scanning electron microscopy (FESEM) in the backscattered electron imaging (BSE) mode was performed on SPS-processed $\text{SnSe}_{0.92} + 3\%$ MoCl_5 (Figure 3.1.3).

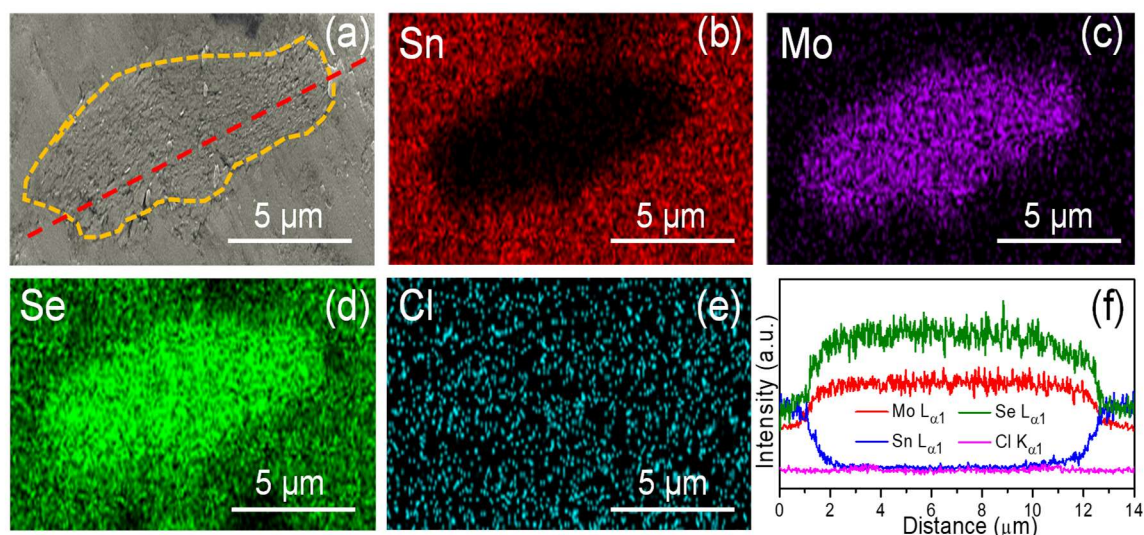


Figure 3.1.3. (a) Backscattered electron image taken during FESEM for SPS processed $\text{SnSe}_{0.92} + 3\%$ MoCl_5 polycrystals. (b) – (e) EDAX elemental color mapping for Sn, Mo, Se and Cl. (f) EDAX line scan performed on the precipitate along with the matrix (denoted by dotted red line) clearly indicates the higher concentration of Mo and Se in the precipitate region.

It confirms the presence of a few Mo and Se rich microprecipitates of size $\sim 5\text{--}10\ \mu\text{m}$ encapsulated in the matrix of SnSe. The energy dispersive analysis of X-ray (EDAX) line scan performed on the precipitate along with the matrix (Figure 3.1.3a, denoted by a dotted red line) clearly indicates the higher concentration of Mo and Se in the precipitate region (Figure 3.1.3f). Thereby, addition of higher concentration of MoCl_5 ($\sim 3\ \text{mol}\%$) results in phase separation of MoSe_2 in SnSe matrix.

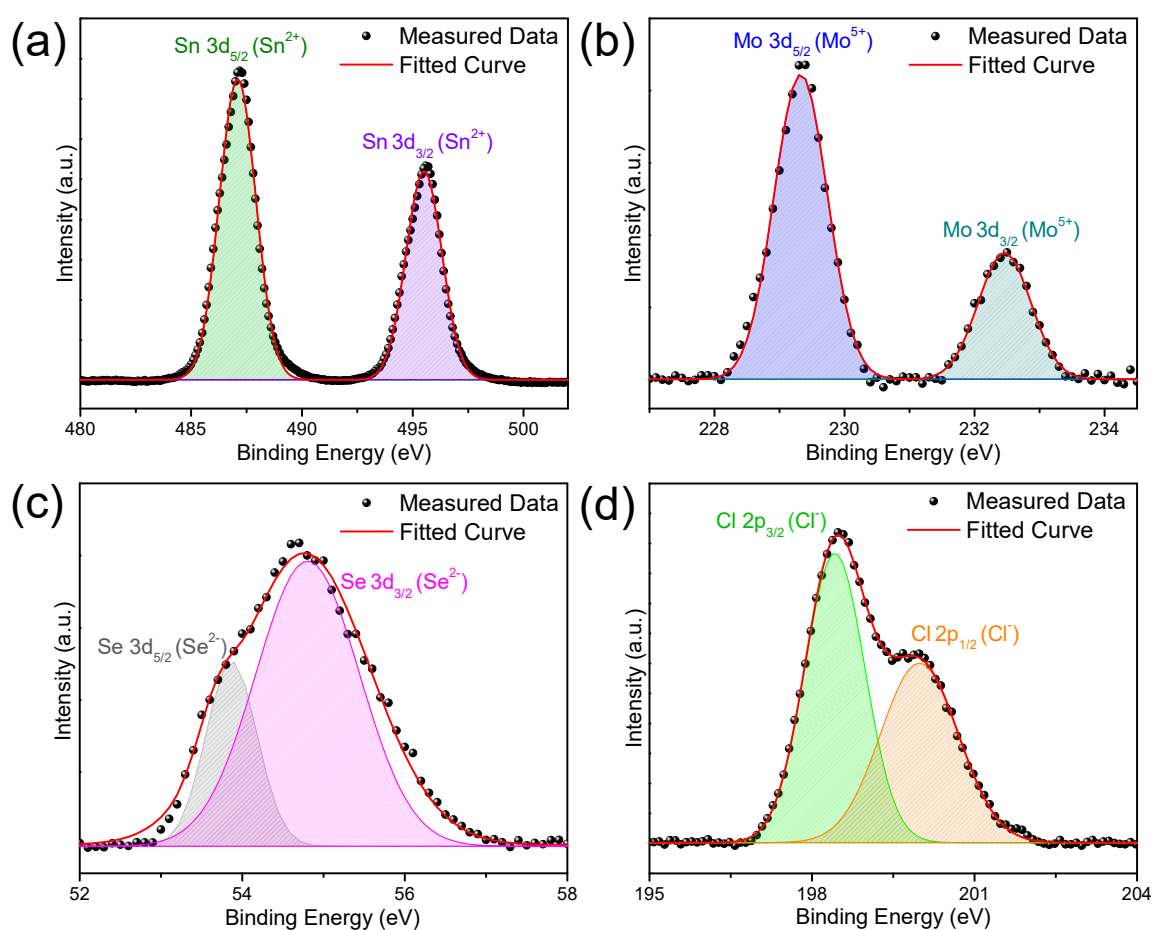


Figure 3.1.4. High-resolution XPS of (a) Sn 3d, (b) Mo 3d, (c) Se 3d, and (d) Cl 2p in $\text{SnSe}_{0.92} + 1\% \text{MoCl}_5$ polycrystals.

In order to confirm the ionic states of the elements, X-ray photoelectron spectroscopy (XPS) was performed on $\text{SnSe}_{0.92} + 1\% \text{MoCl}_5$ sample (Figure 3.1.4). The Sn 3d spin-orbit coupling peaks appearing at 487.1 eV and 495.5 eV can be assigned as $3d_{5/2}$ and $3d_{3/2}$ respectively, stating the existence of Sn^{2+} ions in the system.⁹ The splitting of spin-orbit coupling peaks of Se 3d and Mo 3d orbitals were in good agreement with the

previously reported results and confirms the valence states of Se and Mo to be 2^- and 5^+ state, respectively.^{11,40} Further, the substitution of Cl^- at Se^{2-} was verified by the occurrence of the $2p_{3/2}$ and $2p_{1/2}$ peaks of Cl^- at 198.4 eV and 199.9 eV,^{41,42} which are important for n -type electronic properties in SnSe.

We have performed SPS on powdered samples of $\text{SnSe}_{0.92} + x\% \text{MoCl}_5$ to measure the thermoelectric properties. Since SnSe is a layered material, we have measured the thermoelectric properties along both the perpendicular and parallel to the SPS direction. A schematic diagram has been drawn to visualize the direction of the measurements (Figure 3.1.5a). All the compositions exhibit superior thermoelectric properties along parallel to the SPS pressing direction in comparison to that of the perpendicular direction. Therefore, we have mainly reported the electrical and thermal transport properties along parallel to SPS pressing direction, but we have also reported the thermoelectric properties of highest performance sample measured in both parallel and perpendicular to the SPS pressing directions.

Figure 3.1.5b depicts the temperature dependence of electrical conductivity (σ) of the SPS processed polycrystalline $\text{SnSe}_{0.92} + x\% \text{MoCl}_5$ ($x = 0, 1, 2, 3$) samples measured parallel to pressing direction. The electrical conductivity for all the $\text{SnSe}_{0.92} + x\% \text{MoCl}_5$ ($x = 0, 1, 2, 3$) samples rises with the increase in temperature showing a semiconducting transport which is typical of SnSe.^{13,17-19} The room temperature electrical conductivity of polycrystalline $\text{SnSe}_{0.92}$ was measured to be 0.33 S/cm which has substantially increased to 6.55 S/cm with the addition of 1 mol% MoCl_5 . However, with the further increase in MoCl_5 concentration, the σ value has dropped to 2.64 S/cm and 0.265 S/cm for 2 mol% and 3 mol% MoCl_5 doped $\text{SnSe}_{0.92}$ samples, respectively. Typically, the $\text{SnSe}_{0.92} + 1\% \text{MoCl}_5$ samples demonstrate a σ value of 41 S/cm at 827 K. To explain the variation of σ (at room temperature) for different compositions, we have measured the carrier concentration from Hall measurements and the presented the data in Table 3.1.1. The negative value of Hall coefficient confirms the n -type conduction which is further supported by the negative value of Seebeck-coefficient (discussed later).

For 1 mol% MoCl_5 doped $\text{SnSe}_{0.92}$, the n -type carrier concentration ($5.2 \times 10^{19} \text{cm}^{-3}$) is enhanced in two order magnitude than the controlled $\text{SnSe}_{0.92}$ sample ($3.4 \times 10^{17} \text{cm}^{-3}$).

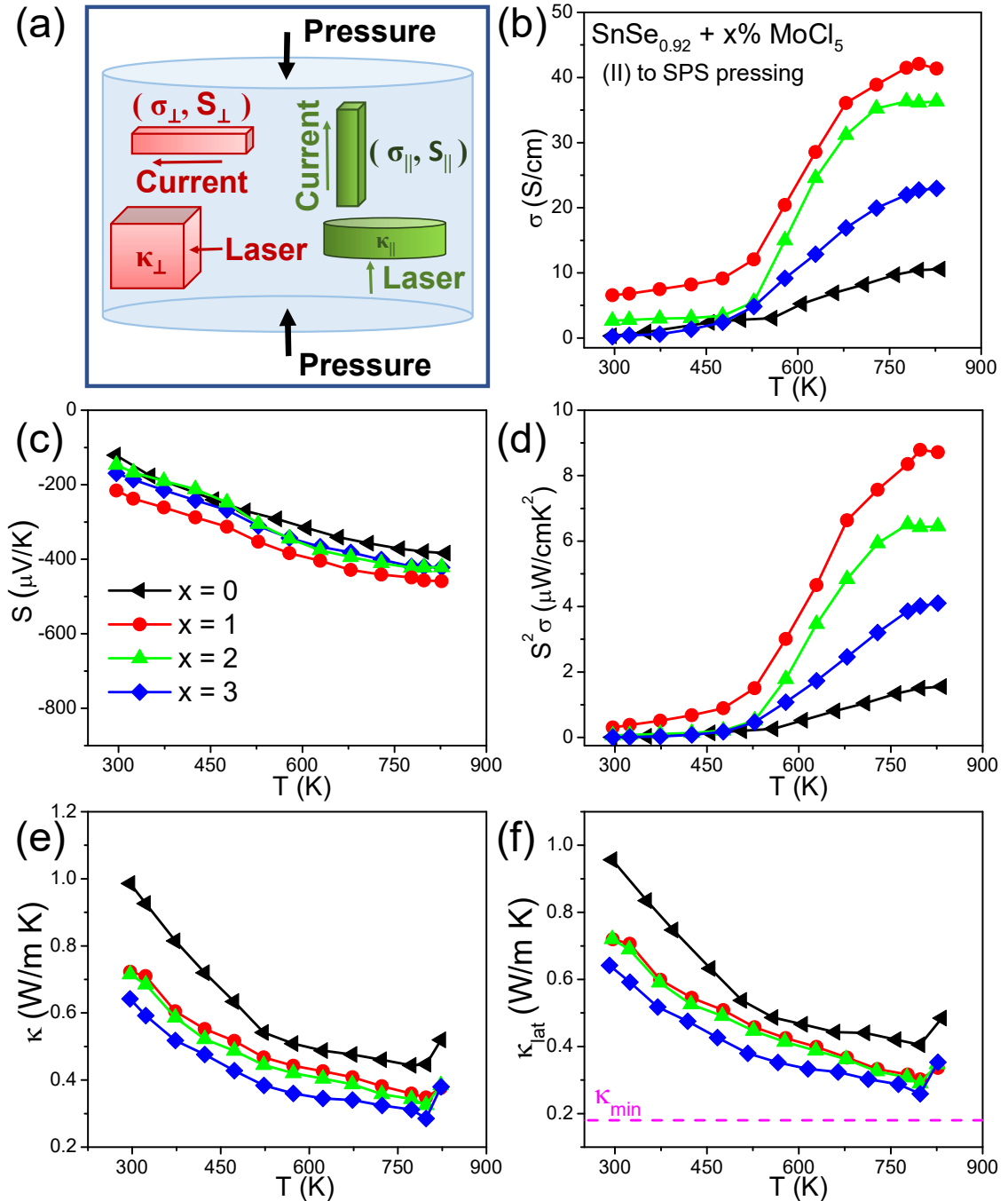
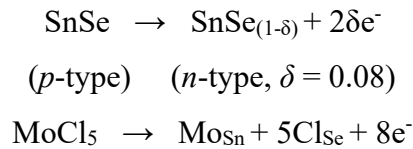


Figure 3.1.5. (a) A schematic diagram to elucidate how a SPS-processed sample has been prepared in desired shapes to measure the anisotropic transport properties of $\text{SnSe}_{0.92} + x\% \text{MoCl}_5$ ($x = 0, 1, 2, 3$). Temperature dependent (b) electrical conductivity (σ), (c) Seebeck coefficient (S), (d) power factor ($S^2\sigma$), (e) total thermal conductivity (κ) and (f) lattice thermal conductivity (κ_{lat}) of polycrystalline $\text{SnSe}_{0.92} + x\% \text{MoCl}_5$ ($x = 0, 1, 2, 3$) samples measured along parallel (\parallel) to the SPS pressing direction.

Table 3.1.1. Room temperature carrier concentration and carrier type of the bulk $\text{SnSe}_{0.92} + x\% \text{MoCl}_5$ ($x = 0, 1, 2, 3$) samples along with the comparison of other halide-doped samples.

Composition	Carrier Type	Carrier concentration n (10^{18} cm^{-3})
$x = 0$	n	0.34
$x = 1$	n	52.0
$x = 2$	n	1.1
$x = 3$	n	0.58
$\text{SnSe}_{0.96}\text{I}_{0.04}$ ¹²	n	0.24
$\text{Sn}_{1.005}\text{Se}_{0.94}\text{Br}_{0.06}$ ¹³	n	3.20
$\text{SnSe}_{0.95} + 0.2\% \text{BiCl}_3$ ¹⁵	n	12.70
$\text{SnSe}_{0.95} + 3\% \text{PbBr}_2$ ¹⁶	n	18.60

With further increase of MoCl_5 concentration, the carrier density starts to decrease and finally reaches a value of $5.8 \times 10^{17} \text{ cm}^{-3}$ for 3 mol% MoCl_5 sample (Table 3.1.1). The declined trend in electrical conductivity with the increasing MoCl_5 concentration (when $x > 1$ in $\text{SnSe}_{0.92} + x\% \text{MoCl}_5$) could be due to the formation of more Sn^{2+} vacancies with the phase separation of MoSe_2 in the SnSe matrix which diminishes the overall n -type carrier concentration of the system. In comparison to the other halide dopants like SnI_2 ,¹² SnBr_2 ,¹³ BiCl_3 ,¹⁵ PbBr_2 ,¹⁶ and ReCl_2 ¹⁸ it is observed that MoCl_5 is more efficient in improving the n -type carrier concentration of SnSe (see Table 3.1.1). Moreover, Mo^{5+} contains more positive charge in comparison to Sn^{2+} , Bi^{3+} , Re^{4+} and Pb^{2+} ions, and thus the substitution of Mo^{5+} at Sn^{2+} sites induce more free electrons. A possible two step defect formation mechanism can be given as:



where Mo_{Sn} and Cl_{Se} represent the substitution of Mo in Sn sites and Cl in Se sites respectively.

The temperature variation of S for the polycrystalline $\text{SnSe}_{0.92} + x\% \text{MoCl}_5$ ($x = 0, 1, 2, 3$) samples measured parallel to SPS pressing direction has been reported in Figure

3.1.5c. The negative values of Seebeck coefficient further confirms the presence of *n*-type carriers in the samples. The increasing trend of *S* with the increase in temperature is in good agreement with the previously reported *n*-type SnSe polycrystals.¹³ The SnSe_{0.92} + 1% MoCl₅ shows a maximum *S* value of ~ 470 μV/K at 827 K. Due to the enhancement in the electrical conductivity and Seebeck coefficient, a remarkably high power factor of ~ 8.7 μW/cmK² has been obtained for *n*-type polycrystalline SnSe_{0.92} + 1% MoCl₅ at 827 K (Figure 3.1.5d) along parallel to the SPS pressing direction which is almost six times higher in magnitude as compared to the pristine SnSe_{0.92}.

The temperature variation of total κ and κ_{lat} of SnSe_{0.92} + x% MoCl₅ (x = 0, 1, 2, 3) samples measured parallel to SPS pressing direction have been depicted in Figure 3.1.5e and Figure 3.1.5f respectively. The κ of the SnSe_{0.92} + x% MoCl₅ polycrystals were considerably lower in comparison to controlled SnSe_{0.92} (Figure 3.1.5e). The up-turn around 798 K in thermal conductivity is attributed to the phase transition from *Pnma* to *Cmcm* structure of SnSe.¹⁷

The contribution from the electronic thermal conductivity is almost negligible and hence the lattice thermal conduction dominates the total thermal transport in SnSe_{0.92} + x% MoCl₅ (x = 0, 1, 2, 3) samples. We have obtained ultra-low κ_{lat} of ~ 0.30 W/mK and ~ 0.26 W/mK at 798 K for the 1 mol% and 3 mol% MoCl₅ doped SnSe_{0.92} samples, respectively which nearly reaches the theoretical minimum value (κ_{min}) of SnSe.⁴³

To understand the origin of this ultra-low κ_{lat} , an extensive transmission electron microscopy (TEM) study has been performed on SnSe_{0.92} + x% MoCl₅ (x = 1 and 3) samples. Figure 3.1.6a and Figure 3.1.6b portray the high-resolution transmission electron microscope (HRTEM) images showing the ripple like modular nanostructures in the SnSe_{0.92} + 1% MoCl₅ sample. Fast Fourier transform (FFT) of the HRTEM image in Figure 3.1.6b reveals the diffraction spots corresponding to the SnSe lattice along [001] zone axis with the superlattice spots appearing at ½ (200) and (020) (Figure 3.1.6c). Pair of weak diffraction spots around the primary diffraction spots (marked by yellow arrows in Figure 3.1.6c) represents the periodicity in the nanodomain of the modular superstructure. The superlattice spots are formed along the (200) of SnSe which are perpendicular to the direction of ripples. The appearance of the superlattice spots at the half distance of (200) (otherwise forbidden in pristine orthorhombic SnSe) is due to the

probable incorporation of the Mo in SnSe in the nanoscale domains. We have also represented the corresponding inverse FFT (IFFT) image in Figure 3.1.6d which confirms the clear presence of such nanostructure modulations.

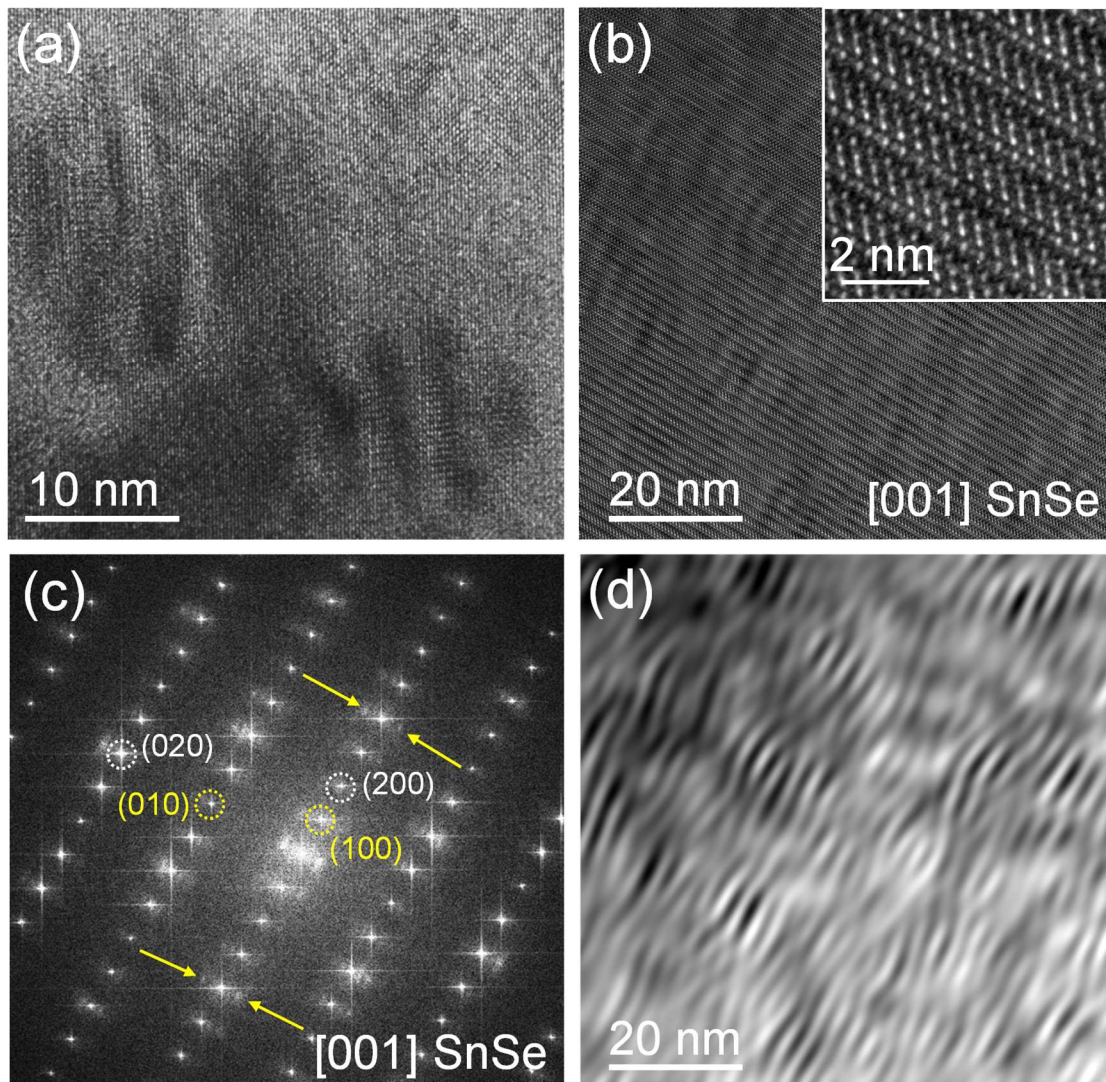


Figure 3.1.6. (a) and (b) HRTEM images revealing the presence of modular nanostructure in the $\text{SnSe}_{0.92} + 1\% \text{MoCl}_5$ sample. The atomic arrangement along $[001]$ zone axis is shown in the inset of (b). (c) Fast Fourier transform (FFT) of image b shows the diffraction spots corresponding to SnSe lattice along $[001]$ zone axis (marked with white circle) with superlattice spots appearing at $\frac{1}{2}(200)$ and (020) (marked with yellow circle). The yellow arrows indicate the weak diffraction spots due to the periodicity of the modular nanostructure. (d) Masked inverse FFT (IFFT) image (where only the superlattice spots are selected) from (c), displaying the modular nanostructure more prominently which have a periodicity of 2.3 - 2.6 nm.

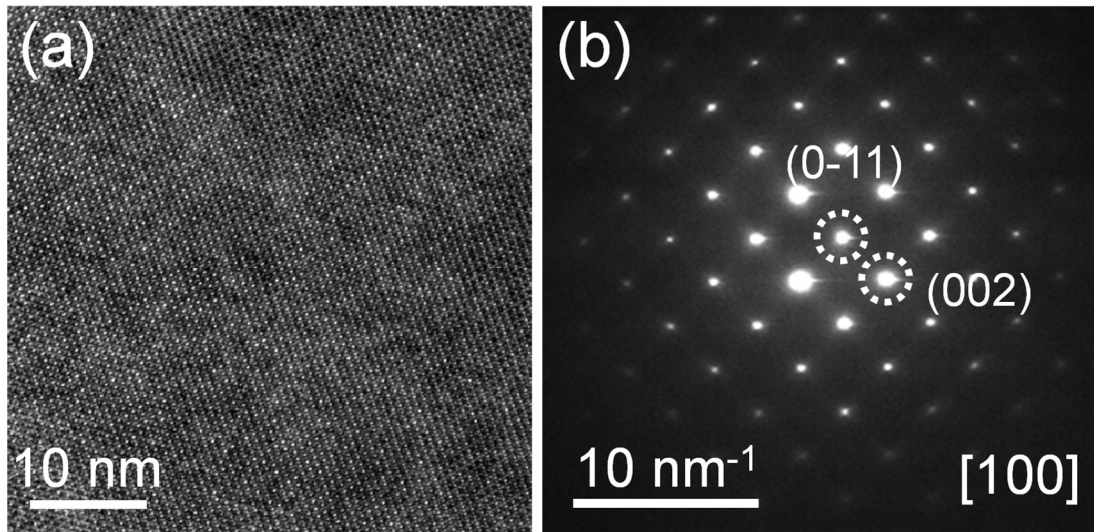


Figure 3.1.7. (a) HRTEM image of the controlled $\text{SnSe}_{0.92}$ and (b) the corresponding electron diffraction (ED) pattern.

The IFFT image is obtained by selecting only the superlattice spots and masking the Bragg's spots. We have estimated that the periodicity of the modular nanoscale superstructures to be in the ranges from 2.3 to 2.6 nm, which is in order of phonon mean free path of SnSe .⁴⁴⁻⁴⁶ TEM analysis indicate the formation of layered intergrowth $[(\text{SnSe})_{1.05}]_m(\text{MoSe}_2)_n$ (where, m and n are integers)⁴⁷ like compounds in the form of modular nanostructure with periodicity of 2.3-2.6 nm in SnSe matrix, which are important for phonon scattering due to its modular heterostructure and size. However, we have not observed such modular nanostructure in controlled $\text{SnSe}_{0.92}$ sample (Figure 3.1.7).

Similarly, in the case of $\text{SnSe}_{0.92} + 3\% \text{MoCl}_5$ sample, same type of modular nanostructures is observed as shown in the HRTEM images (Figure 3.1.8a and Figure 3.1.8b). The corresponding FFT and IFFT images are provided in Figure 3.1.8c and Figure 3.1.8d where the zone axis is determined to be $[100]$ and the ripple periodicity varies from 1.2 - 1.3 nm. The EDAX measured during HRTEM of $\text{SnSe}_{0.92} + x\% \text{MoCl}_5$ ($x = 1, 3$) samples confirm the presence of Mo in the SnSe (Figure 3.1.9). Thereby, due to the presence of nanodomains of layered intergrowth $[(\text{SnSe})_{1.05}]_m(\text{MoSe}_2)_n$ like modular structure in the SnSe matrix, heat carrying phonons get scattered heavily at the (i) the interface between nanostructures and SnSe matrix, and (ii) the interfaces between the modulated heterostructured layers within $[(\text{SnSe})_{1.05}]_m(\text{MoSe}_2)_n$. In addition to this,

substitution of some amount of Mo at the Sn and Cl at Se sites create mass and strain fluctuations in the system which is also helpful to suppress the κ_{lat} .

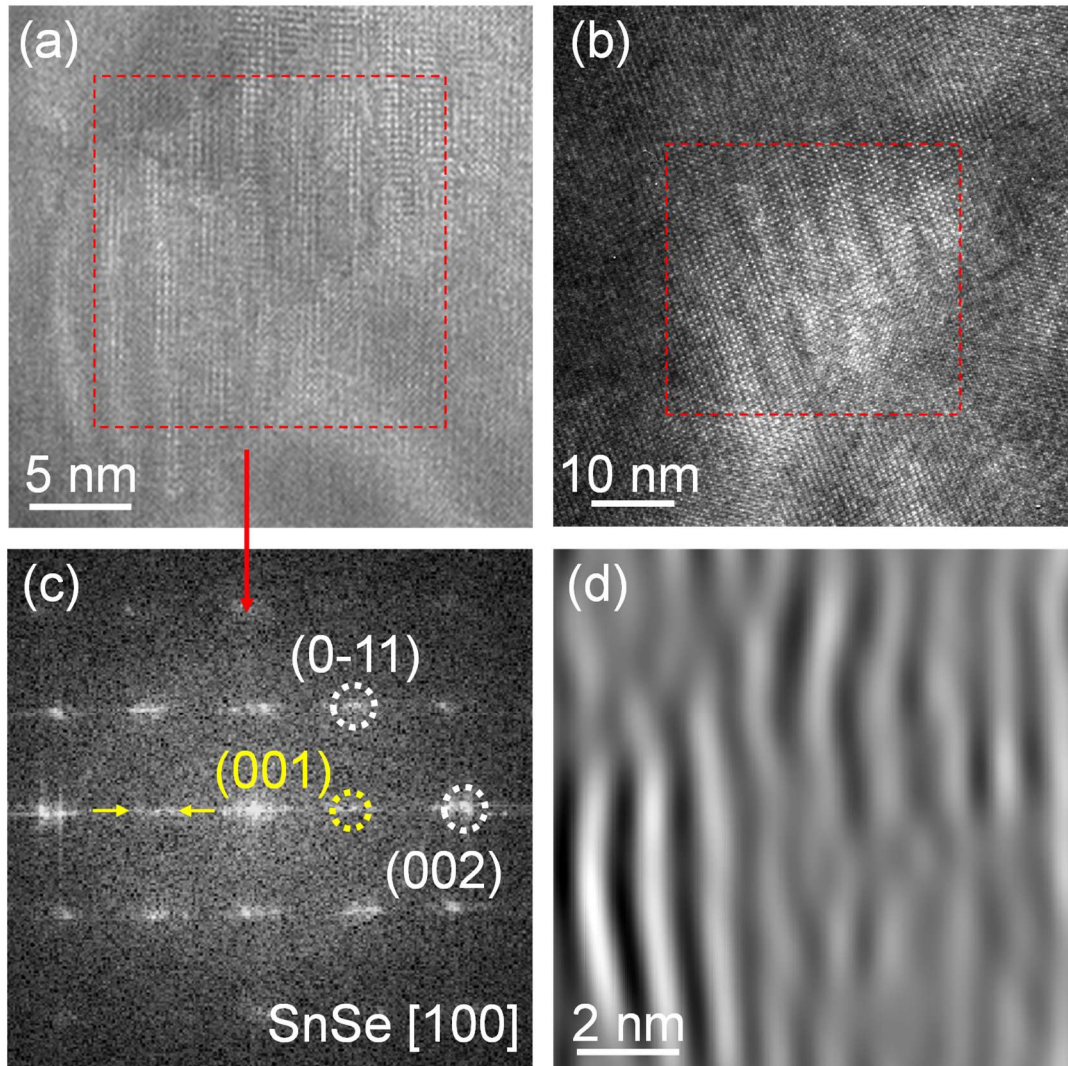


Figure 3.1.8. (a) and (b) HRTEM images showing the nanoscale superstructure in $\text{SnSe}_{0.92} + 3 \text{ mol\% MoCl}_5$ (marked with the red boxes). (c) The corresponding FFT of a from the area marked confirms the presence of superlattice spots at $\frac{1}{2} (002)$ along $[100]$ zone axis. Splitting of superlattices spots (marked with yellow arrows) is observed due to the periodicity of the modular structure. (d) Masked IFFT image (where only the superlattice spots are selected) showing the ripples with a periodicity of 1.2-1.3 nm.

Finally, due to the simultaneous effects of high electrical properties and decreased lattice thermal conductivity, a record high zT of ~ 2.0 at 798 K has been achieved in n -type polycrystalline $\text{SnSe}_{0.92} + 1\% \text{ MoCl}_5$ when measured along parallel to SPS pressing

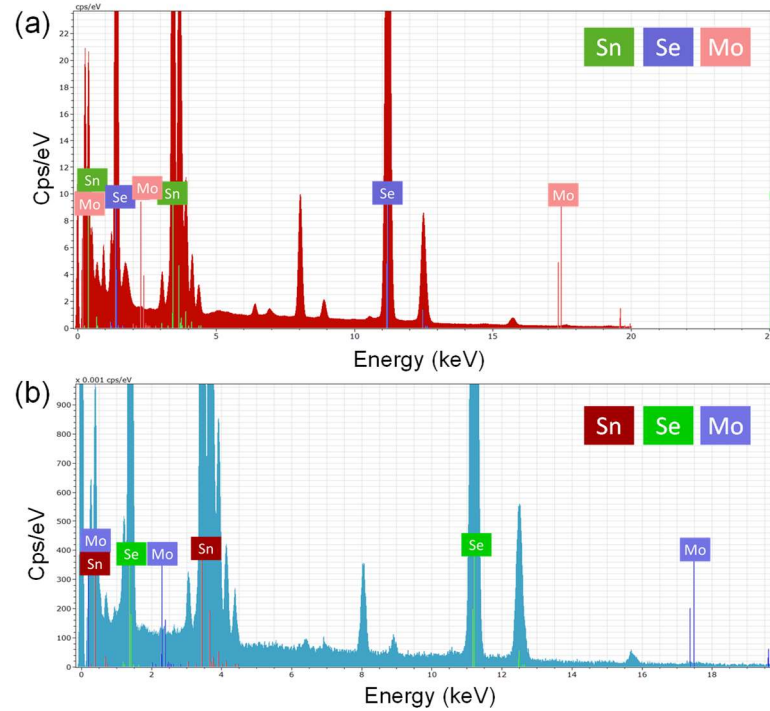


Figure 3.1.9. EDAX scan recorded during TEM measurement shows the presence of Sn, Se, and Mo in both the (a) $\text{SnSe}_{0.92} + 1\% \text{MoCl}_5$ and (b) $\text{SnSe}_{0.92} + 3\% \text{MoCl}_5$ samples.

direction (Figure 3.1.10a). The zT is reversible and reproducible with respect to different batches of samples and several heat-cooling cycles.

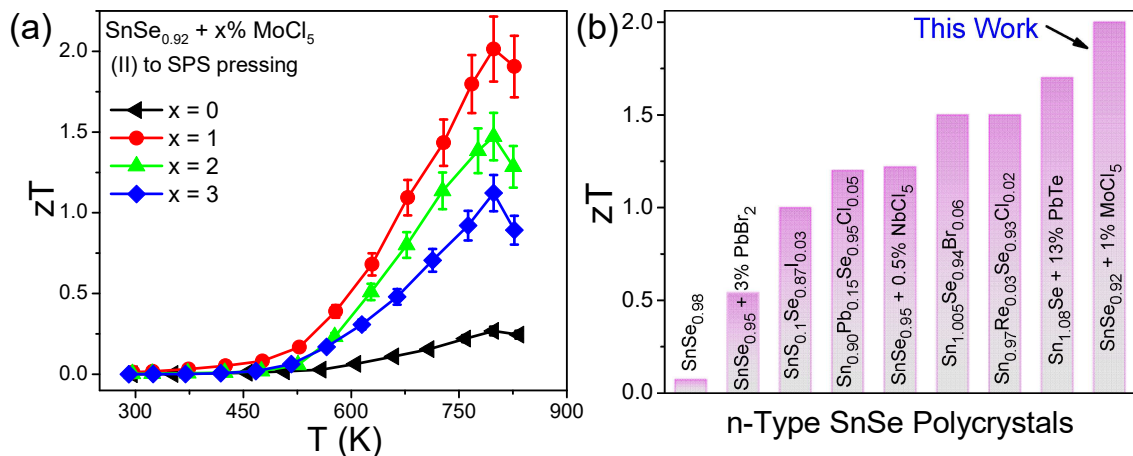


Figure 3.1.10. (a) Temperature dependent thermoelectric figure of merit (zT) of polycrystalline $\text{SnSe}_{0.92} + x\% \text{MoCl}_5$ ($x = 0, 1, 2, 3$) measured along parallel to the SPS pressing direction. The vertical bars denote the standard error in the zT measurement. (b) A comparison of zT of the present n-type SnSe polycrystalline sample with few other n-type SnSe polycrystalline samples.^{12–14,16–19,38}

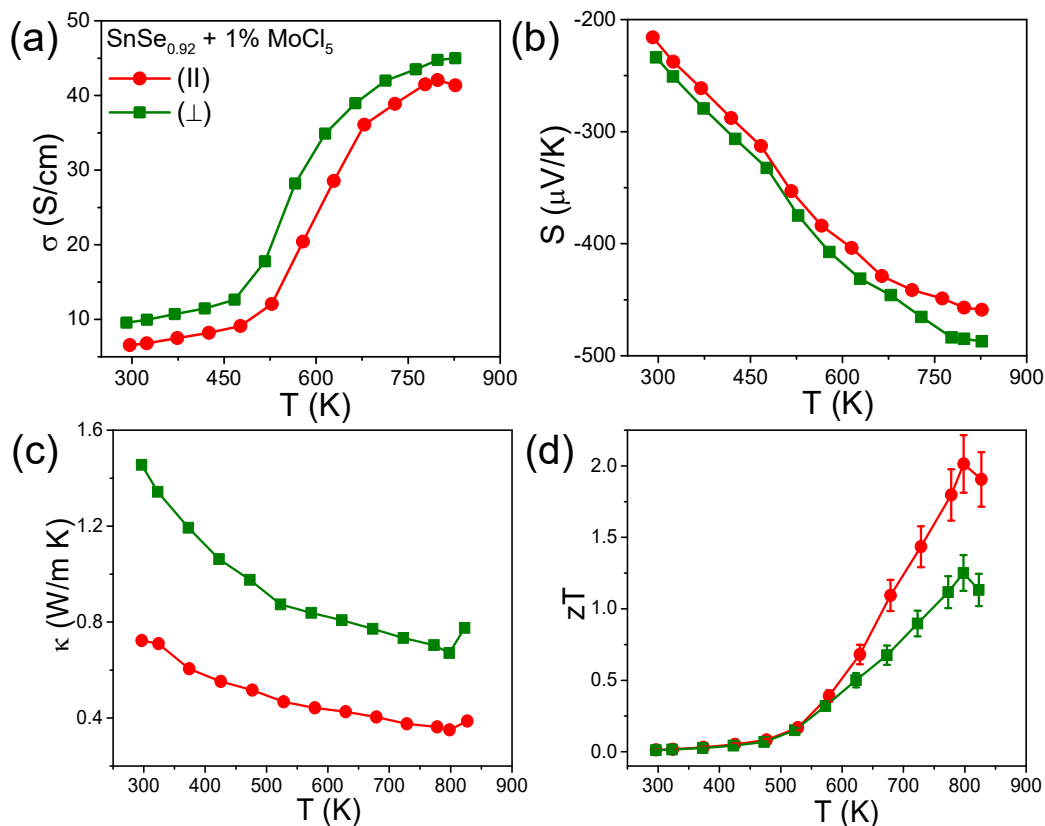


Figure 3.1.11. Temperature dependent (a) electrical conductivity (σ), (b) Seebeck coefficient (S), (c) total thermal conductivity (κ), and (d) thermoelectric figure of merit (zT) of SPS processed $\text{SnSe}_{0.92} + 1\% \text{MoCl}_5$ sample measured along parallel (\parallel) and perpendicular (\perp) to SPS pressing directions.

To the best of our knowledge, it is the highest reported zT among all other n -type polycrystalline SnSe samples (Figure 3.1.10b). We have presented the thermoelectric properties of the best performing sample ($\text{SnSe}_{0.92} + 1\% \text{MoCl}_5$) both along parallel and perpendicular to the SPS pressing direction in Figure 3.1.11. A clear anisotropic behaviour has been observed and we have obtained a relatively lower zT of ~ 1.2 at 798 K for the perpendicular direction, which is a typical trend in n -type polycrystalline SnSe.^{17–19}

3.1.4. Conclusion

In conclusion, we have synthesized polycrystalline $\text{SnSe}_{0.92} + x\% \text{MoCl}_5$ ($x = 0, 1, 2, 3$) samples via simple solid-state melting followed by SPS which show record high zT of

2 among *n*-type SnSe polycrystals due to the collective effects of enhancement of *n*-type carrier concentration and effective phonon scattering by modular nanostructures in SnSe matrix. Creation of Se vacancy and successful substitution of Mo⁵⁺ at Sn²⁺ and Cl⁻ ions at Se²⁻ sites significantly enhances the *n*-type carrier concentration, thus improving its electrical transport. The detailed nano/microstructural analysis on SnSe_{0.92} + x% MoCl₅ samples have revealed the presence of layered 2D modular nanostructures of intergrowth [(SnSe)_{1.05}]_m(MoSe₂)_n (where, m, n = integers) like compound which are embedded in SnSe matrix. These layered intergrowth compounds resemble natural nano-heterostructures and have a periodicity of 1.2 - 2.6 nm in SnSe matrix which scatters the heat carrying phonons to a greater extent due to their size and heterostructure interface leading to an ultra-low lattice thermal conductivity of ~ 0.26 W/mK at 798 K in SnSe_{0.92} + 3% MoCl₅ polycrystals. Owing to the combined effects of high electrical properties and decreased lattice thermal conductivity, a significantly high *zT* of ~ 2.0 at 798 K has been achieved in polycrystalline SnSe_{0.92} + 1% MoCl₅ when measured along parallel to SPS. Further, to provide a more detailed insight, we have also measured the anisotropic thermoelectric properties of SnSe_{0.92} + x% MoCl₅ sample along both parallel and perpendicular to SPS pressing. The concept of introducing modular 2D nano-heterostructures (*e.g.*, layered intergrowth and misfit compounds) in bulk thermoelectric matrix for the reduction of lattice thermal conductivity can provide a new and general path to enhance the performance of several other thermoelectric materials.

3.1.5. References

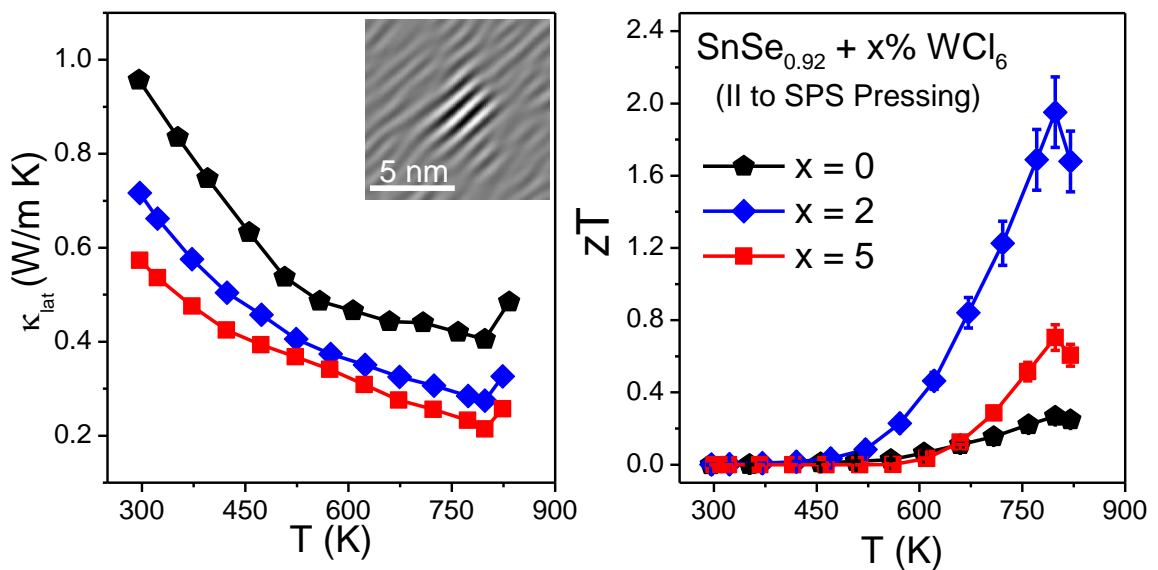
- (1) Wei, T. R.; Tan, G.; Zhang, X.; Wu, C. F.; Li, J. F.; Dravid, V. P.; Snyder, G. J.; Kanatzidis, M. G. *J. Am. Chem. Soc.* **2016**, *138*, 8875–8882.
- (2) Wei, T. R.; Wu, C. F.; Zhang, X.; Tan, Q.; Sun, L.; Pan, Y.; Li, J. F. *Phys. Chem. Chem. Phys.* **2015**, *17*, 30102–30109.
- (3) Tang, G.; Wei, W.; Zhang, J.; Li, Y.; Wang, X.; Xu, G.; Chang, C.; Wang, Z.; Du, Y.; Zhao, L.-D. *J. Am. Chem. Soc.* **2016**, *138*, 13647–13654.
- (4) Shi, X.; Zheng, K.; Hong, M.; Liu, W.; Moshwan, R.; Wang, Y.; Qu, X.; Chen, Z.-G.; Zou, J. *Chem. Sci.* **2018**, *9*, 7376–7389.
- (5) Wei, W.; Chang, C.; Yang, T.; Liu, J.; Tang, H.; Zhang, J.; Li, Y.; Xu, F.; Zhang, Z.; Li, J.-F.; Tang, G. *J. Am. Chem. Soc.* **2018**, *140*, 499–505.
- (6) Ge, Z.; Song, D.; Chong, X.; Zheng, F.; Jin, L.; Qian, X.; Zheng, L.; Dunin-borkowski, R. E.; Qin, P.; Feng, J.; Zhao, L. D. *J. Am. Chem. Soc.* **2017**, *139*, 9714–9720.
- (7) Chen, Y. X.; Ge, Z. H.; Yin, M.; Feng, D.; Huang, X. Q.; Zhao, W.; He, J. *Adv. Funct. Mater.* **2016**, *26*, 6836–6845.
- (8) Chen, C.-L.; Wang, H.; Chen, Y.; Day, T.; Snyder, G. J. *J. Mater. Chem. A* **2014**, *2*, 11171–11176.
- (9) Lee, Y. K.; Luo, Z.; Cho, S. P.; Kanatzidis, M. G.; Chung, I. *Joule* **2019**, *3*, 719–731.
- (10) Zhou, C.; Lee, Y. K.; Yu, Y.; Byun, S.; Luo, Z.; Lee, H.; Ge, B.; Lee, Y.-L.; Chen, X.; Lee, J. Y.; Cojocaru-Mirédin, O.; Chang, H.; Im, J.; Cho, S.; Wuttig, M.; Dravid, V. P.; Kanatzidis, M. G.; Chung, I. *Nat. Mater.* **2021**, *20*, 1378–1384.
- (11) Chandra, S.; Banik, A.; Biswas, K. *ACS Energy Lett.* **2018**, *3*, 1153–1158.
- (12) Zhang, Q.; Chere, E. K.; Sun, J.; Cao, F.; Dahal, K.; Chen, S.; Chen, G.; Ren, Z. *Adv. Energy Mater.* **2015**, *5*, 1500360.
- (13) Shang, P.-P.; Dong, J.; Pei, J.; Sun, F.-H.; Pan, Y.; Tang, H.; Zhang, B. P.; Zhao, L.-D.; Li, J.-F. *Research* **2019**, *2019*, 9253132.
- (14) Cha, J.; Zhou, C.; Lee, Y. K.; Cho, S.-P.; Chung, I. *ACS Appl. Mater. Interfaces* **2019**, *11*, 21645–21654.
- (15) Wang, X.; Xu, J.; Liu, G.; Fu, Y.; Liu, Z.; Tan, X.; Shao, H.; Jiang, H.; Tan, T.;

- Jiang, J. *Appl. Phys. Lett.* **2016**, *108*, 083902.
- (16) Li, D.; Tan, X.; Xu, J.; Liu, G.; Jin, M.; Shao, H.; Huang, H.; Zhang, J.; Jiang, J. *RSC Adv.* **2017**, *7*, 17906–17912.
- (17) Cai, J.; Zhang, Y.; Yin, Y.; Tan, X.; Duan, S.; Liu, G.; Hu, H.; Xiao, Y.; Ge, Z.; Jiang, J. *J. Mater. Chem. C* **2020**, *8*, 13244–13252.
- (18) Ge, Z.; Qiu, Y.; Chen, Y.; Chong, X.; Feng, J.; Liu, Z.; He, J. *Adv. Funct. Mater.* **2019**, *29*, 1902893.
- (19) Su, L.; Hong, T.; Wang, D.; Wang, S.; Qin, B.; Zhang, M.; Gao, X.; Chang, C.; Zhao, L. D. *Mater. Today Phys.* **2021**, *20*, 100452.
- (20) Biswas, K.; He, J.; Blum, I. D.; Wu, C.-I.; Hogan, T. P.; Seidman, D. N.; Dravid, V. P.; Kanatzidis, M. G. *Nature* **2012**, *489*, 414–418.
- (21) Biswas, K.; He, J.; Zhang, Q.; Wang, G.; Uher, C.; Dravid, V. P.; Kanatzidis, M. G. *Nat. Chem.* **2011**, *3*, 160–166.
- (22) Lou, X.; Li, S.; Chen, X.; Zhang, Q.; Deng, H.; Zhang, J.; Li, D.; Zhang, X.; Zhang, Y.; Zeng, H.; Tang, G. *ACS Nano* **2021**, *15*, 8204–8215.
- (23) Banik, A.; Vishal, B.; Perumal, S.; Datta, R.; Biswas, K. *Energy Environ. Sci.* **2016**, *9*, 2011–2019.
- (24) Roychowdhury, S.; Ghosh, T.; Arora, R.; Samanta, M.; Xie, L.; Singh, N. K.; Soni, A.; He, J.; Waghmare, U. V.; Biswas, K. *Science* **2021**, *371*, 722–727.
- (25) Kanatzidis, M. G. *Acc. Chem. Res.* **2005**, *38*, 359–368.
- (26) Banik, A.; Biswas, K. *Angew. Chem. Int. Ed.* **2017**, *129*, 14753–14758.
- (27) Chatterjee, A.; Biswas, K. *Angew. Chem. Int. Ed.* **2015**, *127*, 5715–5719.
- (28) Radovsky, G.; Popovitz-Biro, R.; Stroppa, D. G.; Houben, L.; Tenne, R. *Acc. Chem. Res.* **2014**, *47*, 406–416.
- (29) Sreedhara, M. B.; Hettler, S.; Kaplan-Ashiri, I.; Rechav, K.; Feldman, Y.; Enyashin, A.; Houben, L.; Arenal, R.; Tenne, R. *Proc. Natl. Acad. Sci.* **2021**, *118*, e2109945118.
- (30) Gibson, Q. D.; Zhao, T.; Daniels, L. M.; Walker, H. C.; Daou, R.; Hébert, S.; Zanella, M.; Dyer, M. S.; Claridge, J. B.; Slater, B.; Gaultois, M. W.; Corà, F.; Alaria, J.; Rosseinsky, M. J. *Science* **2021**, *373*, 1017–1022.
- (31) Rodríguez-Carvajal, J. *Phys. B Condens. Matter* **1993**, *192*, 55–69.

- (32) Zhao, L. D.; Lo, S.-H.; Zhang, Y.; Sun, H.; Tan, G.; Uher, C.; Wolverton, C.; Dravid, V. P.; Kanatzidis, M. G. *Nature* **2014**, *508*, 373–377.
- (33) Banik, A.; Shenoy, U. S.; Saha, S.; Waghmare, U. V.; Biswas, K. *J. Am. Chem. Soc.* **2016**, *138*, 13068–13075.
- (34) Sarkar, D.; Ghosh, T.; Banik, A.; Roychowdhury, S.; Sanyal, D.; Biswas, K. *Angew. Chem. Int. Ed.* **2020**, *59*, 11115–11122.
- (35) Perumal, S.; Roychowdhury, S.; Negi, D. S.; Datta, R.; Biswas, K. *Chem. Mater.* **2015**, *27*, 7171–7178.
- (36) Chandra, S.; Biswas, K. *J. Am. Chem. Soc.* **2019**, *141*, 6141–6145.
- (37) Chandra, S.; Dutta, P.; Biswas, K. *ACS Appl. Energy Mater.* **2020**, *3*, 9051–9057.
- (38) Li, Q.; Zhang, L.; Yin, J.; Sheng, Z.; Chu, X.; Wang, F.; Zhu, F. *J. Alloys Compd.* **2018**, *745*, 513–518.
- (39) Zhang, Y.; Gong, Q.; Li, L.; Yang, H.; Li, Y.; Wang, Q. *Nano Res.* **2015**, *8*, 1108–1115.
- (40) Lee, Y.-J.; Barrera, D.; Luo, K.; Hsu, J. W. P. *J. Nanotechnol.* **2012**, *2012*, 195761.
- (41) Bouša, D.; Luxa, J.; Mazánek, V.; Jankovský, O.; Sedmidubský, D.; Klímová, K.; Pumera, M.; Sofer, Z. *RSC Adv.* **2016**, *6*, 66884–66892.
- (42) Araujo, J. R.; Archanjo, B. S.; de Souza, K. R.; Kwapinski, W.; Falcão, N. P. S.; Novotny, E. H.; Achete, C. A. *Biol. Fertil. Soils* **2014**, *50*, 1223–1232.
- (43) Chang, C.; Wu, M.; He, D.; Pei, Y.; Wu, C.-F.; Wu, X.; Yu, H.; Zhu, F.; Wang, K.; Chen, Y.; Huang, L.; Li, J.-F.; He, J.; Zhao, L.-D. *Science* **2018**, *360*, 778–783.
- (44) Ma, J.; Chen, Y.; Li, W. *Phys. Rev. B* **2018**, *97*, 205207.
- (45) Xiao, Y.; Chang, C.; Pei, Y.; Wu, D.; Peng, K.; Zhou, X.; Gong, S.; He, J.; Zhang, Y.; Zeng, Z.; Zhao, L.-D. *Phys. Rev. B* **2016**, *94*, 125203.
- (46) Guo, R.; Wang, X.; Kuang, Y.; Huang, B. *Phys. Rev. B* **2015**, *92*, 115202.
- (47) Gunning, N. S.; Feser, J.; Beekman, M.; Cahill, D. G.; Johnson, D. C. *J. Am. Chem. Soc.* **2015**, *137*, 8803–8809.

Chapter 3.2

Realization of Excellent Thermoelectric Performance in *n*-type SnSe via WCl_6 Doping



Realization of Excellent Thermoelectric Performance in *n*-type SnSe via WCl₆ Doping[†]

Summary

SnSe has attracted extensive attention due to the excellent thermoelectric (TE) properties of both p- and n-type single crystals. However, the TE performance of polycrystalline SnSe is still low, especially in n-type materials, because SnSe is an intrinsic p-type semiconductor. In this work, we have employed the strategy of incorporating a transition metal halide WCl₆ to enhance the thermoelectric performance of n-type polycrystalline SnSe_{0.92} by synergistically improving the charge transport and reducing the lattice thermal conductivity. It is found that the successful creation of Se vacancy and substitution of W⁶⁺ at Sn²⁺ and Cl⁻ ions at Se²⁻ sites effectively enhance the total n-type carrier concentration, thus improving the electrical conductivity. In addition to this, incorporation of WCl₆ at SnSe lattice results in the formation of ripple like coherently modulated nanostructures as revealed from high-resolution transmission electron microscopy analysis. The periodicity of these ripples is in the range of 1 - 2.5 nm which is in the order of phonon mean free path of SnSe. As a result of which the heat carrying acoustic phonons get scattered effectively leading to an ultralow-lattice thermal conductivity of ~0.21 W/mK at 798 K in 5 mol% WCl₆ doped SnSe_{0.92}. Finally, due to the synergistic effects of superior electrical conductivity and decreased lattice thermal conductivity, a record high zT of ~1.9 at 798 K has been achieved in polycrystalline SnSe_{0.92} + 2% WCl₆ sample when measured along parallel to SPS pressing direction.

[†]S. Chandra, P. Dutta, U. Bhat, A. Bhardwaj, R. Datta and K. Biswas. 2022. (Manuscript Under Preparation)

3.2.1. Introduction

In contrast to the advance in *p*-type polycrystalline SnSe, *n*-type counterparts are less explored in thermoelectrics (TE).^{1,2} The main reason is difficulty in stabilizing the *n*-type charge carrier at the optimal level because of a substantial amount of inherent Sn vacancies and ubiquitous Sn⁴⁺ defects, making SnSe intrinsic *p*-type semiconductor.^{3,4} Till date, only a few dopants have been reported to be effective for improving the thermoelectric performance of *n*-type polycrystalline SnSe, such as, addition of halide ions, BiCl₃, ReCl₂, NbCl₅, and PbBr₂.^{1,5-9,10} However, the *zT* values in all these cases remain far below than that of *n*-type single crystals. Since compatibility in a thermoelectric device requires both *p*- and *n*-type materials of similar composition, there remains a plenty of room to improve the performance of *n*-type bulk SnSe thermoelectrics.

In this chapter, I have chosen a transition metal halide dopant WCl₆ to enhance the thermoelectric performance of *n*-type polycrystalline SnSe_{0.92} by synergistically improving the charge transport and reducing the thermal conductivity. First, introduction of Se vacancies compensates for the intrinsic Sn vacancies in SnSe, whereas WCl₆ plays a dual role in this process by significantly enhancing the electrical transport properties due to improved *n*-type carrier concentration and by largely reducing the thermal conductivity due to formation of ripple like coherently modulated nanostructures in SnSe matrix. Detailed high-resolution transmission electron microscopy (HRTEM) analysis has revealed that the periodicity of these ripples is in the range of 1 - 2.5 nm which is in the order of phonon mean free path of SnSe. As a result of which the heat carrying acoustic phonons get scattered effectively leading to an ultralow-lattice thermal conductivity of ~ 0.21 W/mK at 798 K in 5 mol% WCl₆ doped SnSe_{0.92}. Finally, due to the synergistic effects of superior electrical conductivity and decreased lattice thermal conductivity, a record high *zT* of ~ 1.9 at 798 K has been achieved in polycrystalline SnSe_{0.92} + 2% WCl₆ sample when measured along parallel to SPS (spark plasma sintering) pressing direction. These results indicate that incorporation of transition metal halides significantly improves the thermoelectric properties of *n*-type polycrystalline SnSe, and it should also be a useful method for improving the thermoelectric properties of other thermoelectric system.

3.2.2. Methods

Reagents. The high purity elements utilized for the synthesis are tin (Alfa Aesar 99.99 + %), selenium (Se, Alfa Aesar 99.9999%) and tungsten (VI) hexachloride (WCl_6 , Sigma Aldrich 99.9%).

Synthesis. Polycrystalline $\text{SnSe}_{0.92}$ samples doped with x mol% WCl_6 ($x = 0, 1, 2, 3, 5$) were synthesized by combining stoichiometric amount of elemental Sn, Se and powder WCl_6 in high quality quartz tubes. The quartz tubes were sealed under vacuum (Pressure = 10^{-5} Torr). The sealed tubes were initially heated to 773 K in a box furnace over a period of 12 hrs, then heated again to 1223 K in next 5 hrs followed by annealing for 10 hrs and subsequently cooled to room temperature for a period of 15 hrs. The resulted ingots were crushed by using a mortar and pestle; and sieved to fine powder. For the ease of representation, the samples are termed as $\text{SnSe}_{0.92} + x\% \text{WCl}_6$ throughout the manuscript.

Powder X-ray diffraction (PXRD) patterns of the samples were recorded using a Cu K_α ($\lambda = 1.5406 \text{ \AA}$) radiation on a Rigaku Smartlab (9 kW, rotating anode) x-ray diffractometer.

Field emission scanning electron microscopy (FESEM) in back-scattered electron (BSE) mode. FESEM-BSE images were taken using ZEISS Gemini SEM – Field Emission Scanning Electron Microscope.

Transmission electron microscopy (TEM). TEM experiments were performed using ThermoFisher Talos F200 S operating at 200 kV accelerating voltage. The samples for TEM measurement were prepared by the standard mechanical grinding, polishing down to a thickness of $\sim 45 \mu\text{m}$, and then followed by precision ion polishing system (PIPS). During ion milling, the samples were the first ion milled with the beam voltage = 4.5 keV and milling angle = $\pm 5^\circ$. After the sample was perforated, a voltage of 2.0 keV was used to optimize the thin area of the specimen. The EDS mapping was conducted using the SuperX EDS detector.

TEM measurements and analysis were performed in the collaboration with Prof. Ranjan Datta, JNCASR, India.

X-ray photoelectron spectroscopy (XPS) measurement has been performed with AlK α (1.487 keV) monochromatic X-ray source with a relative composition detection better than 0.1% on an Thermo Scientific spectrometer.

Spark plasma sintering (SPS) was done using a SPS211-LX (Dr. Sinter Lab) instrument. The finely powdered samples were sintered to prepare a cylinder (10 mm \times 8 mm) using graphite dies at 50 MPa pressure and 450 °C temperature for 10 minutes.

Electrical transport properties. Electrical conductivity and Seebeck coefficients were measured simultaneously under helium atmosphere from room temperature to 850 K on a ULVAC-RIKO ZEM-3 instrument system. The SPS processed sample were cut and polished in a bar shape with the dimensions of $\sim 2 \times 2 \times 8$ mm³ to carry out the measurements. Electrical and thermal transport were measured in same direction.

Hall measurement. For determining the carrier concentrations, Hall measurements were carried out on the same rectangular specimens used for electrical transport measurement in four-contact geometry up to a magnetic field of 1 T at room-temperature using custom-built equipment developed by Excel Instruments.

Thermal transport properties. Temperature dependent thermal diffusivity (D) was evaluated using a laser flash diffusivity technique in a Netzsch LFA-457 instrument. Next, the total thermal conductivity (κ) was derived using the formula, $\kappa = D.C_p.\rho$, where D is the thermal diffusivity, C_p is specific heat, and ρ is density of the sample. C_p was derived experimentally using pyroceram as a reference material during the thermal diffusivity measurements. The experimentally determined density was found to be $\sim 97\%$ of the theoretical density. Further, the electrical thermal conductivity, κ_{ele} were derived using Wiedemann-Franz Law, $\kappa_{ele} = L\sigma T$, where L denotes the Lorenz number which was estimated by fitting the temperature dependent Seebeck data¹¹⁻¹³.

3.2.3. Results and Discussions

Figure 3.2.1a shows the XRD patterns of the as-synthesized SnSe_{0.92} + x% WCl₆ (x = 0, 1, 2, 3, 5) samples. All the PXRD patterns can be indexed to the *Pnma* orthorhombic phase of SnSe, while a trace amount of WSe₂ secondary phase (marked with asterisk)

started to appear from 5 mol% WCl_6 addition. WSe_2 possess a layered hexagonal structure¹⁴ with space group $P6_3/mmc$ where the individual layers are stacked along c -direction by van der Waals interactions (Figure 3.2.1b). Presence of WSe_2 secondary phase in the PXRD pattern indicates that the solid solution limit of WCl_6 in $\text{SnSe}_{0.92}$ is up to 3 mol%.

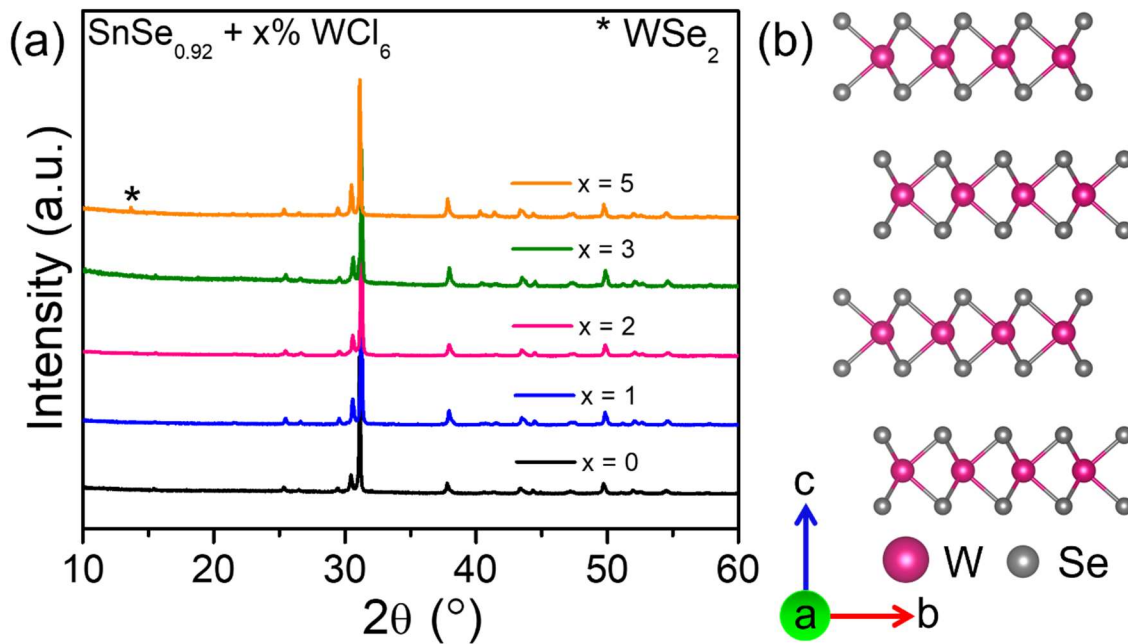


Figure 3.2.1. (a) Room temperature PXRD patterns of as-synthesized $\text{SnSe}_{0.92} + x\% \text{WCl}_6$ ($x = 0, 1, 2, 3, 5$) polycrystals. The peaks marked with asterisk (*) denotes the presence of WSe_2 as secondary phase. (b) Crystal structure of WSe_2 viewed along a -direction.

The XPS spectra performed on the $\text{SnSe}_{0.92} + 2\% \text{WCl}_6$ sample provide the information on the chemical composition and ionic states of the elements (Figure 3.2.2). The Sn 3d spin-orbit coupling peaks appearing at 487.3 eV and 496.1 eV can be assigned as $3d_{5/2}$ and $3d_{3/2}$ respectively, stating the existence of Sn^{2+} ions in the system.¹⁵ The splitting of spin-orbit coupling peaks of Se 3d and W 4f orbitals were in good agreement with the previously reported results and confirms the valence states of Se and W to be 2^- and 6^+ state, respectively.^{16,17} Further, the presence of Cl^- was verified by the occurrence of the $2p_{3/2}$ and $2p_{1/2}$ peaks of Cl^- at 198.5 eV and 199.8 eV.^{18,19} These results confirm the successful doping of W and Cl at Sn and Se sites respectively and plays an imperative role to improve the electronic transport properties of n -type SnSe.

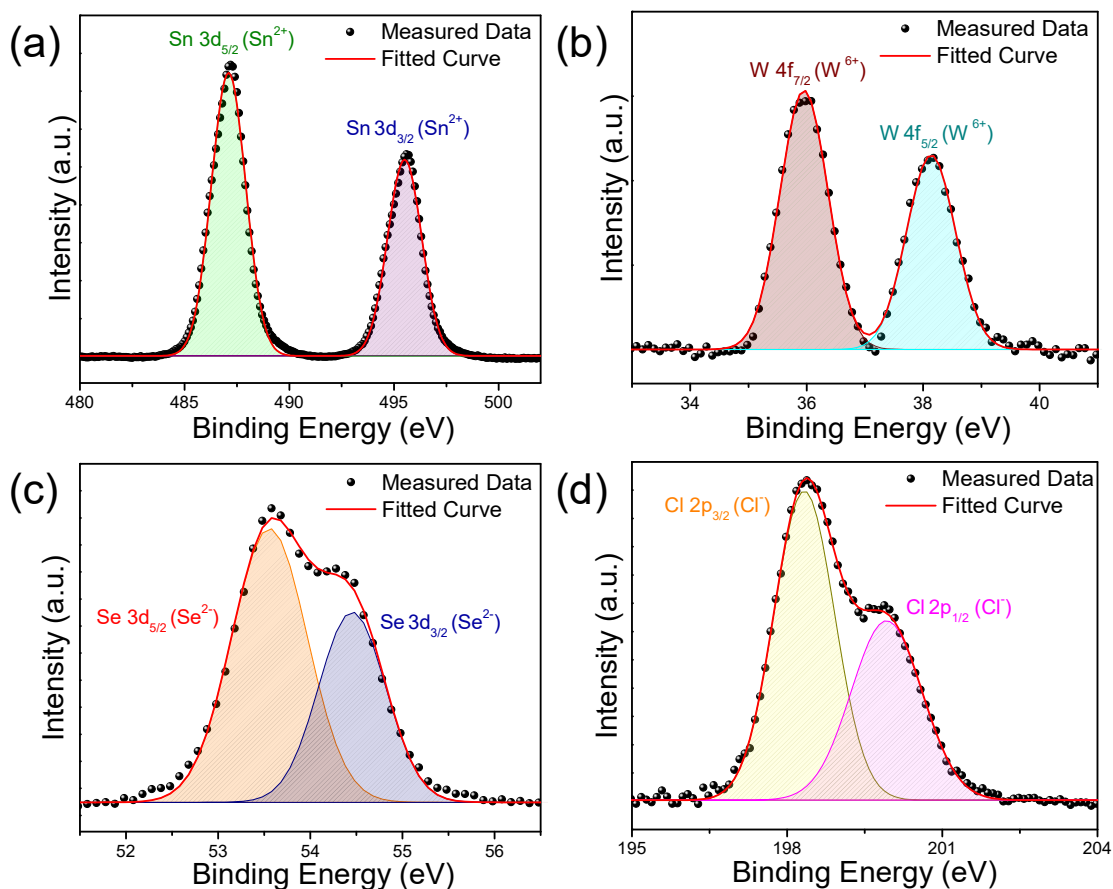


Figure 3.2.2. High-resolution XPS of (a) Sn 3d, (b) W 4f, (c) Se 3d, and (d) Cl 2p in $\text{SnSe}_{0.92} + 2\% \text{WCl}_6$ polycrystals.

In addition to this, the BSE-FESEM analysis of SPS-processed $\text{SnSe}_{0.92} + 5\% \text{WCl}_6$ reveals the occurrence of a few W and Se rich microprecipitates on the SnSe matrix (Figure 3.2.3). The lateral dimension of these precipitates is in the order of $\sim 5\text{--}50 \mu\text{m}$. EDAX line scan performed on the precipitate along with the matrix (Figure 3.2.3a, denoted by a yellow dotted line) clearly indicates the higher concentration of W and Se in the precipitate region (Figure 3.2.3f). Thereby, addition of higher concentration of WCl_6 ($\sim 5 \text{ mol}\%$) results in phase separation of WSe_2 in SnSe matrix.

In order to measure the thermoelectric properties, we have performed SPS on the powdered samples of $\text{SnSe}_{0.92} + x\% \text{WCl}_6$. Since SnSe is a layered material, we have performed the transport measurements both along the perpendicular and parallel to the SPS pressing direction to check the anisotropic behavior. However, we have noticed that thermoelectric figure of merit is greater for all the compositions of $\text{SnSe}_{0.92} + x\% \text{WCl}_6$

when measured along parallel to the SPS pressing. Hence, we have only presented the electrical and thermal transport properties along parallel to SPS pressing direction.

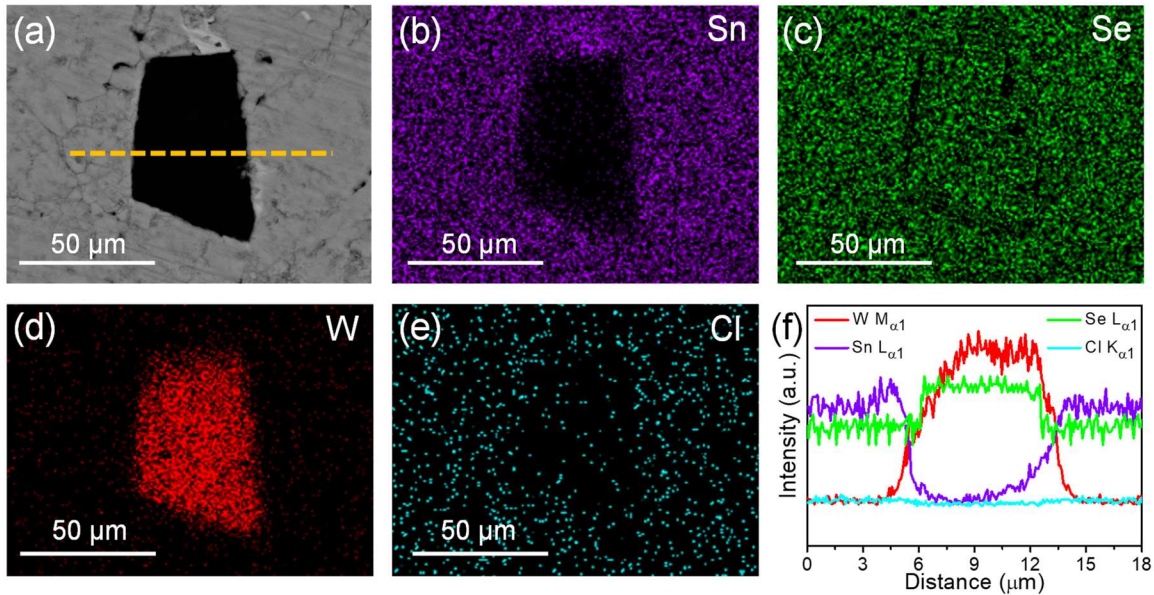


Figure 3.2.3. (a) Backscattered electron image taken during FESEM for SPS processed $\text{SnSe}_{0.92} + 5\% \text{WCl}_6$ polycrystals showing the presence of micro-precipitates (dark contrast) in the SnSe matrix (lighter contrast). (b) – (e) EDAX elemental color mapping for Sn, Se, W, and Cl. (f) EDAX line scan performed on the precipitate along with the matrix (denoted by yellow dotted line) clearly indicates the higher concentration of W and Se in the precipitate region.

Figure 3.2.4a shows the temperature dependence of electrical conductivity of the SPS processed polycrystalline $\text{SnSe}_{0.92} + x\% \text{WCl}_6$ ($x = 0, 1, 2, 3, 5$) samples measured parallel to pressing direction. We have observed that the electrical conductivity increases with increase in temperature indicating a semiconducting transport for all the WCl_6 doped samples which is a typical behaviour of SnSe .^{2,5,9,10} The room temperature electrical conductivity of polycrystalline $\text{SnSe}_{0.92}$ was found to be 0.33 S/cm which has substantially increased to ~ 1 S/cm and ~ 4 S/cm with the addition of 1 mol% and 2 mol% WCl_6 respectively. Interestingly, the $\text{SnSe}_{0.92} + 2\% \text{WCl}_6$ sample demonstrate a σ value of 42 S/cm at 820 K. However, with the further increase in WCl_6 concentration, the room temperature electrical conductivity decreases drastically and the 3 mol% and 5 mol% WCl_6 doped samples show σ values even below 1 S/cm. To explain the variation of σ (at

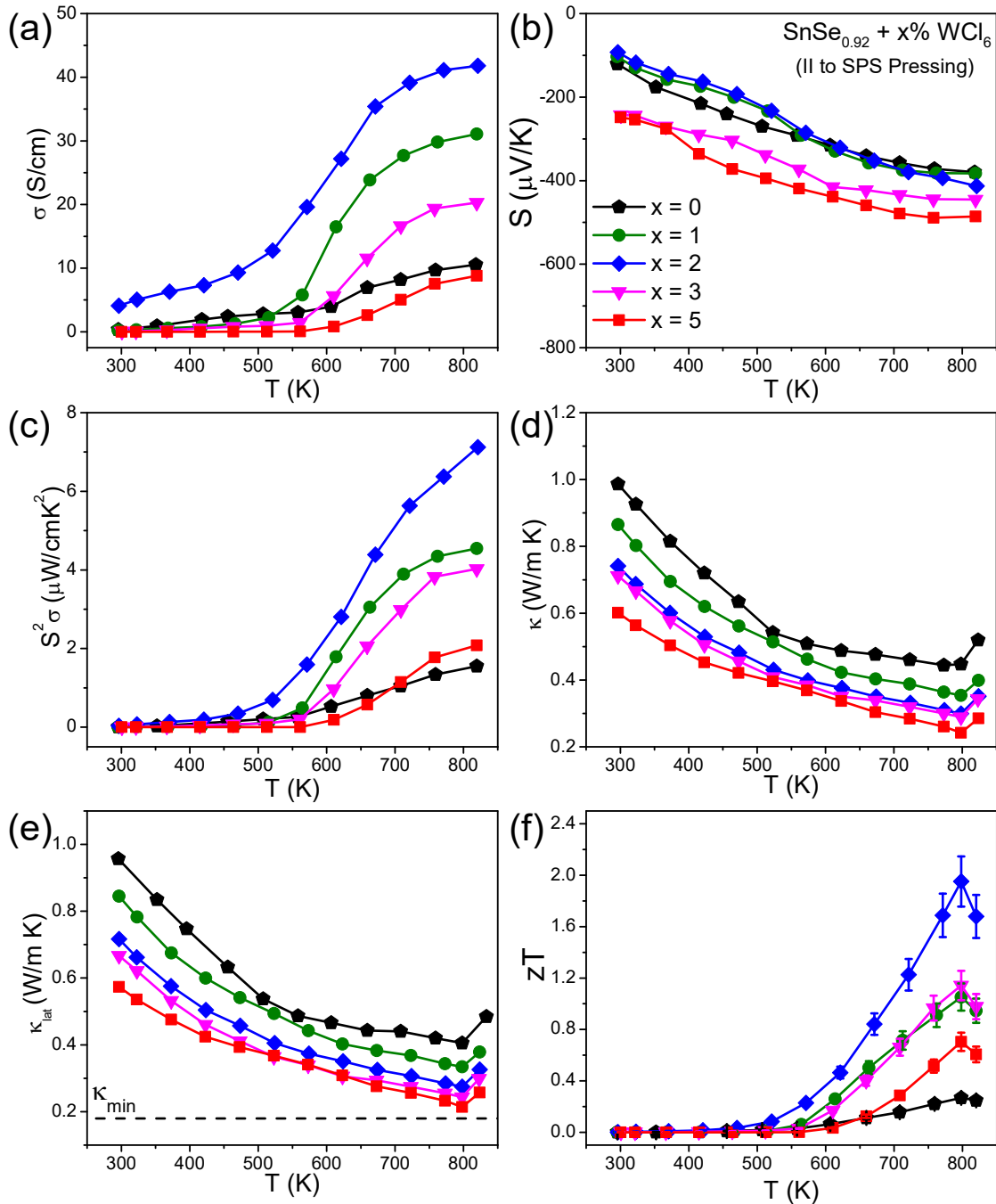


Figure 3.2.4. Temperature dependent (a) electrical conductivity (σ), (b) Seebeck coefficient (S), (c) power factor ($S^2\sigma$), (d) total thermal conductivity (κ) and (e) lattice thermal conductivity (κ_{lat}), and (f) thermoelectric figure of merit (zT) of polycrystalline $\text{SnSe}_{0.92} + x\% \text{WCl}_6$ ($x = 0, 1, 2, 3, 5$) samples measured along parallel (\parallel) to the SPS pressing direction.

room temperature) for different compositions, we have measured the carrier concentration from Hall measurements and the presented the data in Table 3.2.1.

Table 3.2.1. Room temperature carrier concentration and carrier type of the bulk $\text{SnSe}_{0.92} + x\% \text{WCl}_6$ ($x = 0, 1, 2, 3, 5$).

Composition	Carrier Type	Carrier concentration n (10^{18} cm^{-3})
x = 0	n	0.34
x = 1	n	1.90
x = 2	n	18.5
x = 3	n	1.13
x = 5	n	0.72

As shown in Table 3.2.1, the carrier concentration is monotonically increased from $3.4 \times 10^{17} \text{ cm}^{-3}$ for $x = 0$ to $1.85 \times 10^{19} \text{ cm}^{-3}$ for $x = 2$ at 300 K, which is nearly two orders of magnitude higher than that of the undoped sample confirming the increase in electron concentration upon substitution of W and Cl at Sn and Se sites respectively. With further increase of WCl_6 concentration, the carrier density starts to decrease and finally reaches a value of $7.2 \times 10^{17} \text{ cm}^{-3}$ for 5 mol% WCl_6 sample. The declined trend in electrical conductivity with the increasing WCl_6 concentration (when $x > 3$ in $\text{SnSe}_{0.92} + x\% \text{WCl}_6$) could be due to the formation of more Sn^{2+} vacancies with the phase separation of WSe_2 in the SnSe matrix which diminishes the overall n -type carrier concentration of the system.

The temperature variation of S for the polycrystalline $\text{SnSe}_{0.92} + x\% \text{WCl}_6$ ($x = 0, 1, 2, 3, 5$) samples measured parallel to SPS pressing direction has been shown in Figure 3.2.4.b. The negative values of Seebeck coefficient further confirms the presence of n -type carriers in the samples. The increasing trend of S with the increase in temperature is in good agreement with the previously reported n -type SnSe polycrystals.⁵ The $\text{SnSe}_{0.92} + 2\% \text{WCl}_6$ shows a maximum S value of $-413 \mu\text{V/K}$ at 820 K. Due to the enhancement in the electrical conductivity and Seebeck coefficient, a remarkably high power factor of $\sim 7.1 \mu\text{W/cmK}^2$ has been obtained for n -type polycrystalline $\text{SnSe}_{0.92} + 2\% \text{WCl}_6$ at 820 K (Figure 3.2.4c) along parallel to the SPS pressing direction which is almost five times higher in magnitude as compared to the pristine $\text{SnSe}_{0.92}$.

The temperature variation of total κ and κ_{lat} of $\text{SnSe}_{0.92} + x\% \text{WCl}_6$ ($x = 0, 1, 2, 3, 5$) samples measured parallel to SPS pressing direction have been displayed in Figure 3.2.4d

and Figure 3.2.4e respectively. The κ of the $\text{SnSe}_{0.92} + x\% \text{WCl}_6$ polycrystals were considerably lower in comparison to controlled $\text{SnSe}_{0.92}$. The up-turn around 798 K in thermal conductivity is attributed to the second order structural transition from $Pnma$ to $Cmcm$ structure of SnSe .⁹

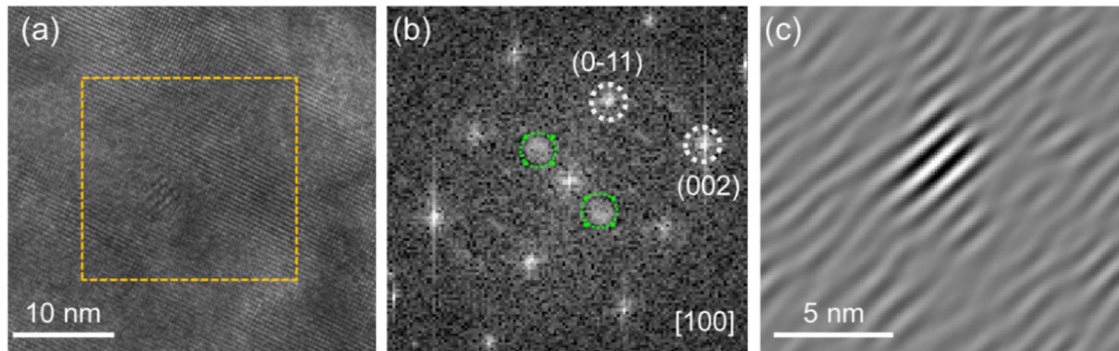


Figure 3.2.5. (a) HRTEM image of $\text{SnSe}_{0.92} + 2\% \text{WCl}_6$ showing the presence of modulation in the lattice. (b) Fast Fourier transform (FFT) of image (a) shows the diffraction spots corresponding to SnSe lattice along $[100]$ zone axis (marked with white circle). The green circles indicate the weak diffraction spots arising due to the substitution of W at Sn site. (c) Masked inverse FFT (IFFT) image (where the weak diffraction spots are selected) from (b), displaying the modular nanostructure more prominently which have a periodicity of 1 - 1.5 nm.

The contribution from the electronic thermal conductivity is almost negligible and hence the lattice thermal conduction dominates the total thermal transport in $\text{SnSe}_{0.92} + x\% \text{WCl}_6$ ($x = 0, 1, 2, 3, 5$) samples. We have obtained ultra-low κ_{lat} of $\sim 0.27 \text{ W/mK}$ and $\sim 0.21 \text{ W/mK}$ at 798 K for the 2 mol% and 5 mol% WCl_6 doped $\text{SnSe}_{0.92}$ samples (Figure 3.2.4e), respectively which nearly reaches the theoretical minimum value (κ_{min}) of SnSe .²⁰

To understand the origin of the ultra-low low lattice thermal conductivity, an extensive transmission electron microscopy study has been performed on $\text{SnSe}_{0.92} + x\% \text{WCl}_6$ ($x = 2, 5$) polycrystals. Figure 3.2.5a and Figure 3.2.6a portray the HRTEM images showing the presence of ripple like coherently modulated nanostructures in both 2 mol% and 5 mol% WCl_6 doped $\text{SnSe}_{0.92}$ samples. Fast Fourier transform (FFT) of the HRTEM images reveal the occurrence of the Bragg's spots corresponding to the SnSe lattice along $[100]$ and $[001]$ zone axis for the 2 mol% and 5 mol% WCl_6 doped $\text{SnSe}_{0.92}$ samples, respectively (Figure 3.2.5b and Figure 3.2.6b). Pair of weak diffraction spots around the

primary diffraction spots (marked by green circles in Figure 3.2.5b and Figure 3.2.6b) represent the periodicity of the modular nanostructures. The appearance of the weak diffraction spots is due to the probable incorporation of the W in SnSe lattice which is visible in HRTEM images as ripples. The inverse FFT (IFFT) images were obtained by selecting only the pair of weak diffraction spots and masking the Bragg's spots (Figure 3.2.5c and Figure 3.2.6c). We have estimated that the periodicity of these modular nanoscale superstructures are in the range of 1 to 2.5 nm, which is in order of phonon mean free path of SnSe.^{21–23} Thereby, due to the presence of such ripple like coherently modulated nanostructures, heat carrying phonons get scattered heavily at the interface between nanostructures and SnSe matrix. In addition to this, substitution of some amount of W at the Sn and Cl at Se sites create mass and strain fluctuations in the system which also assists to suppress the κ_{lat} .

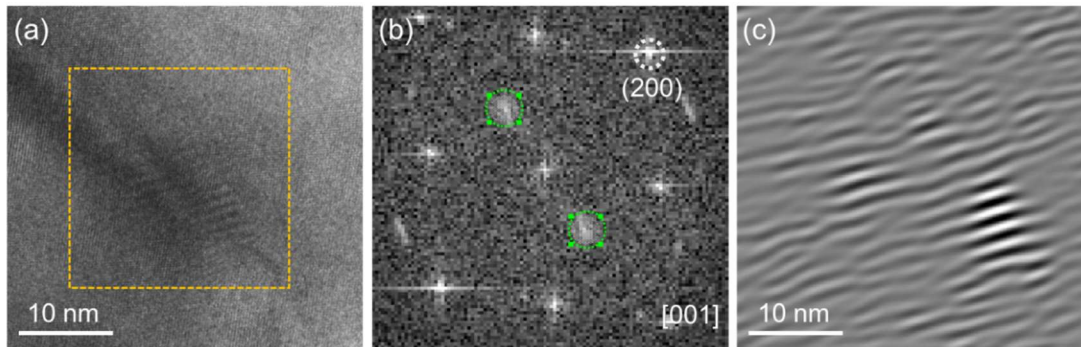


Figure 3.2.6. (a) HRTEM image showing the presence of nanoscale superstructures in $\text{SnSe}_{0.92} + 5\% \text{WCl}_6$. (b) The corresponding FFT of (a) and (c) the corresponding masked IFFT image showing the ripples with a periodicity of 2.2–2.5 nm.

Finally, due to the simultaneous effects of high electrical properties and decreased lattice thermal conductivity, a record high zT of ~ 1.9 at 798 K has been achieved in n -type polycrystalline $\text{SnSe}_{0.92} + 2\% \text{WCl}_6$ when measured along parallel to SPS pressing direction (Figure 3.2.4f).

3.2.4. Conclusion

In conclusion, we have synthesized polycrystalline $\text{SnSe}_{0.92} + x\% \text{WCl}_6$ ($x = 0, 1, 2, 3, 5$) samples via simple solid-state melting reaction followed by SPS which show

improved thermoelectric performance due to the synergistic effects of enhancement of *n*-type carrier concentration and effective phonon scattering by coherently modulated nanostructures in SnSe matrix. Creation of Se vacancy and successful substitution of W^{6+} at Sn^{2+} and Cl^- ions at Se^{2-} sites significantly enhances the *n*-type carrier concentration, thus improving its electrical transport. In addition to this, incorporation of WCl_6 at SnSe lattice results in the formation of ripple like coherently modulated nanostructures as revealed from high-resolution transmission electron microscopy analysis. The periodicity of these ripples is in the range of 1 - 2.5 nm which is in the order of phonon mean free path of SnSe. As a result of which the heat carrying acoustic phonons get scattered effectively leading to an ultralow-lattice thermal conductivity of ~ 0.21 W/mK at 798 K in 5 mol% WCl_6 doped $SnSe_{0.92}$. Finally, due to the combined effects of superior electrical conductivity and decreased lattice thermal conductivity, a record high zT of ~ 1.9 at 798 K has been achieved in polycrystalline $SnSe_{0.92} + 2\% WCl_6$ sample when measured along parallel to SPS pressing direction. The achievement of high-performance in *n*-type SnSe polycrystals should improve the fabrication of SnSe-based TE devices and this concept can be easily extended to other 2D layered materials in future.

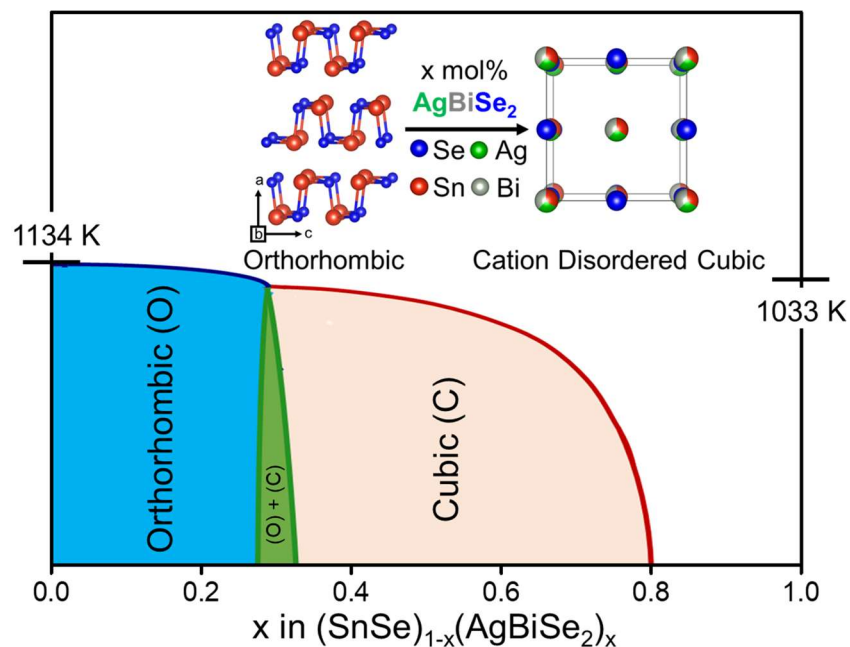
3.2.5. References

- (1) Zhang, Q.; Chere, E. K.; Sun, J.; Cao, F.; Dahal, K.; Chen, S.; Chen, G.; Ren, Z. *Adv. Energy Mater.* **2015**, *5*, 1500360.
- (2) Su, L.; Hong, T.; Wang, D.; Wang, S.; Qin, B.; Zhang, M.; Gao, X.; Chang, C.; Zhao, L. D. *Mater. Today Phys.* **2021**, *20*, 100452.
- (3) Li, Q.; Zhang, L.; Yin, J.; Sheng, Z.; Chu, X.; Wang, F.; Zhu, F. *J. Alloys Compd.* **2018**, *745*, 513–518.
- (4) Zhou, C.; Lee, Y. K.; Yu, Y.; Byun, S.; Luo, Z.; Lee, H.; Ge, B.; Lee, Y.-L.; Chen, X.; Lee, J. Y.; Cojocaru-Mirédin, O.; Chang, H.; Im, J.; Cho, S.; Wuttig, M.; Dravid, V. P.; Kanatzidis, M. G.; Chung, I. *Nat. Mater.* **2021**, *20*, 1378–1384.
- (5) Shang, P.-P.; Dong, J.; Pei, J.; Sun, F.-H.; Pan, Y.; Tang, H.; Zhang, B.-P.; Zhao, L.-D.; Li, J.-F. *Research* **2019**, *2019*, 9253132.
- (6) Cha, J.; Zhou, C.; Lee, Y. K.; Cho, S.-P.; Chung, I. *ACS Appl. Mater. Interfaces* **2019**, *11*, 21645–21654.
- (7) Wang, X.; Xu, J.; Liu, G.; Fu, Y.; Liu, Z.; Tan, X.; Shao, H.; Jiang, H.; Tan, T.; Jiang, J. *Appl. Phys. Lett.* **2016**, *108*, 083902.
- (8) Li, D.; Tan, X.; Xu, J.; Liu, G.; Jin, M.; Shao, H.; Huang, H.; Zhang, J.; Jiang, J. *RSC Adv.* **2017**, *7*, 17906–17912.
- (9) Cai, J.; Zhang, Y.; Yin, Y.; Tan, X.; Duan, S.; Liu, G.; Hu, H.; Xiao, Y.; Ge, Z.; Jiang, J. *J. Mater. Chem. C* **2020**, *8*, 13244–13252.
- (10) Ge, Z.; Qiu, Y.; Chen, Y.; Chong, X.; Feng, J.; Liu, Z.; He, J. *Adv. Funct. Mater.* **2019**, *29*, 1902893.
- (11) Banik, A.; Shenoy, U. S.; Saha, S.; Waghmare, U. V.; Biswas, K. *J. Am. Chem. Soc.* **2016**, *138*, 13068–13075.
- (12) Sarkar, D.; Ghosh, T.; Banik, A.; Roychowdhury, S.; Sanyal, D.; Biswas, K. *Angew. Chem. Int. Ed.* **2020**, *59*, 11115–11122.
- (13) Perumal, S.; Roychowdhury, S.; Negi, D. S.; Datta, R.; Biswas, K. *Chem. Mater.* **2015**, *27*, 7171–7178.
- (14) Coehoorn, R.; Haas, C.; Dijkstra, J.; Flipse, C. J. F.; de Groot, R. A.; Wold, A. *Phys. Rev. B* **1987**, *35*, 6195–6202.
- (15) Lee, Y. K.; Luo, Z.; Cho, S. P.; Kanatzidis, M. G.; Chung, I. *Joule* **2019**, *3*, 719–

- 731.
- (16) Chandra, S.; Banik, A.; Biswas, K. *ACS Energy Lett.* **2018**, *3*, 1153–1158.
- (17) Baig, U.; Gondal, M. A.; Rehman, S.; Akhtar, S. *Appl. Nanosci.* **2020**, *10*, 851–860.
- (18) Bouša, D.; Luxa, J.; Mazánek, V.; Jankovský, O.; Sedmidubský, D.; Klímová, K.; Pumera, M.; Sofer, Z. *RSC Adv.* **2016**, *6*, 66884–66892.
- (19) Araujo, J. R.; Archanjo, B. S.; de Souza, K. R.; Kwapinski, W.; Falcão, N. P. S.; Novotny, E. H.; Achete, C. A. *Biol. Fertil. Soils* **2014**, *50*, 1223–1232.
- (20) Chang, C.; Wu, M.; He, D.; Pei, Y.; Wu, C.-F.; Wu, X.; Yu, H.; Zhu, F.; Wang, K.; Chen, Y.; Huang, L.; Li, J.-F.; He, J.; Zhao, L.-D. *Science* **2018**, *360*, 778–783.
- (21) Ma, J.; Chen, Y.; Li, W. *Phys. Rev. B* **2018**, *97*, 205207.
- (22) Xiao, Y.; Chang, C.; Pei, Y.; Wu, D.; Peng, K.; Zhou, X.; Gong, S.; He, J.; Zhang, Y.; Zeng, Z.; Zhao, L.-D. *Phys. Rev. B* **2016**, *94*, 125203.
- (23) Guo, R.; Wang, X.; Kuang, Y.; Huang, B. *Phys. Rev. B* **2015**, *92*, 115202.

PART 4

Modulation of the Electronic Structure and Thermoelectric Properties of Orthorhombic and Cubic SnSe by AgBiSe₂ Alloying



Modulation of the Electronic Structure and Thermoelectric Properties of Orthorhombic and Cubic SnSe by AgBiSe₂ Alloying[†]

Summary

Layered SnSe attains an orthorhombic crystal structure (*Pnma*) at ambient conditions. However, the cubic rock-salt phase (*Fm $\bar{3}$ m*) of SnSe can only be stabilized at very high pressure and thus experimental realization of the cubic phase remains elusive. Herein, we have successfully stabilized the high-pressure cubic rock-salt phase of SnSe by alloying with AgBiSe₂ ($0.30 \leq x \leq 0.80$) at ambient temperature and pressure. Orthorhombic polycrystalline phase is stable in (SnSe)_{1-x}(AgBiSe₂)_x for composition range of $0.00 \leq x < 0.28$ and these are measured to be narrow band gap semiconductors, whereas the band gap closes upon increasing the concentration of AgBiSe₂ ($0.30 \leq x < 0.70$) with the cubic rock-salt structure. We confirm stabilization of cubic structure at $x = 0.30$ and associated changes in electronic structure using first-principles theoretical calculations. Pristine cubic SnSe exhibits topological crystalline insulator (TCI) quantum phase, but the cubic (SnSe)_{1-x}(AgBiSe₂)_x ($x = 0.33$) possesses semi-metallic electronic structure with overlapping conduction and valence bands. Cubic polycrystalline (SnSe)_{1-x}(AgBiSe₂)_x ($x = 0.30$) sample shows n-type conduction at room temperature while the orthorhombic (SnSe)_{1-x}(AgBiSe₂)_x ($0.00 \leq x < 0.28$) samples retain its p-type character. Thus, by optimizing the electronic structure and the thermoelectric properties of polycrystalline SnSe, a high *zT* of 1.3 at 823 K has been achieved in (SnSe)_{0.78}(AgBiSe₂)_{0.22}.

[†]S. Chandra, R. Arora, U. V. Waghmare, and K. Biswas. *Chem. Sci.*, 2021, 12, 13074–13082.

4.1. Introduction

SnSe crystalizes in three different structures: stable orthorhombic ($Pnma$) phase at ambient temperature and pressure,^{1,2} metastable orthorhombic ($Cmcm$) phase at high temperature,³ and unstable rock-salt cubic ($Fm\bar{3}m$) phase at high pressure.⁴⁻⁶ SnSe undergoes a displacive phase transition from low symmetric $Pnma$ phase to high symmetric $Cmcm$ phase at ~ 800 K.³ This phase transition at elevated temperature results in extended defects and enhancement in the lattice strain which degrades the mechanical properties of SnSe and limits its long-term power generation applications at high temperature.⁷ Furthermore, it has been reported that the high symmetric cubic phase can only be stabilized at very high pressure or by inducing strain.^{4-6,8} However, the formation energy calculated from the density functional theory (DFT) for orthorhombic $Pnma$ and cubic $Fm\bar{3}m$ states are thermodynamically comparable.^{4,9} In addition, the cubic SnSe has been theoretically predicted to show large anharmonicity, high Seebeck coefficient and intrinsically low lattice thermal conductivity.^{5,9} Previously, cubic rock-salt SnSe has been obtained in thin films grown on Bi_2Se_3 substrate using molecular beam epitaxy,¹⁰ but as it is a resource-consuming physical preparation process, an alternative method to prepare the cubic SnSe in bulk form is desired. Therefore, in this work, a chemical approach has been explored to stabilize the cubic rock-salt structure of SnSe and study the crystal and electronic structural evolution. Hitherto, stabilization of cubic rock-salt polycrystalline SnSe has only been achieved via alloying with cubic rock salt $AgSbSe_2$ and $AgSbTe_2$.^{7,9,11} On the other hand, hexagonal $AgBiSe_2$ has been successfully used to tune the carrier concentration and reduce the lattice thermal conductivity in cubic phase of GeTe and GeSe systems.^{12,13} Hence, $AgBiSe_2$ can be chosen as a suitable alloying material to tune the crystal structure, electrical and thermal properties of SnSe as it is isostructural to GeSe.

In this part, I have successfully stabilized the high-pressure cubic rock-salt phase of SnSe by alloying with $AgBiSe_2$ ($0.30 \leq x \leq 0.80$) at ambient temperature and pressure. Solid solution mixing of $AgBiSe_2$ with SnSe increases the configurational entropy by introducing atomic disorder into the system and consequently stabilizes the cubic phase at ambient condition. Orthorhombic polycrystalline phase is stable in $(SnSe)_{1-x}(AgBiSe_2)_x$ for composition range of $0.00 \leq x < 0.28$ and these are narrow band gap

semiconductors, whereas the band gap closes upon increasing the concentration of AgBiSe_2 ($0.30 \leq x < 0.70$) in the cubic rock-salt phase, which is consisted with electronic structure calculated by DFT with the inclusion of spin orbit coupling. Interestingly, pristine cubic SnSe exhibits topological crystalline insulator (TCI) quantum phase where the metallic surface states are protected by mirror symmetry, but the cubic $(\text{SnSe})_{1-x}(\text{AgBiSe}_2)_x$ ($x = 0.33$) possess semi-metallic electronic structure with overlapping conduction and valence band. Cubic polycrystalline $(\text{SnSe})_{1-x}(\text{AgBiSe}_2)_x$ ($x = 0.30$) samples show n -type conduction at room temperature but the orthorhombic $(\text{SnSe})_{1-x}(\text{AgBiSe}_2)_x$ ($0.00 \leq x < 0.28$) samples retain its p -type character. Orthorhombic $(\text{SnSe})_{0.78}(\text{AgBiSe}_2)_{0.22}$ exhibits superior electrical conductivity and power factor of $\sim 685 \text{ Scm}^{-1}$ and $\sim 6.50 \mu\text{Wcm}^{-1}\text{K}^{-2}$, respectively, at 823 K. As a result, a peak zT of 1.3 at 823 K has been obtained in polycrystalline orthorhombic $(\text{SnSe})_{0.78}(\text{AgBiSe}_2)_{0.22}$ system. This study provides a profound insight into the crystal and electric structural modulations and thermoelectric properties of polycrystalline $(\text{SnSe})_{1-x}(\text{AgBiSe}_2)_x$.

4.2. Methods

Reagents. The high purity elements utilized for the synthesis of $(\text{SnSe})_{1-x}(\text{AgBiSe}_2)_x$ ($0.00 \leq x \leq 1.00$) samples are tin (Alfa Aesar 99.99+ %), silver (Ag, Sigma Aldrich 99.999%), bismuth (Alfa Aesar 99.9999%), and selenium (Se, Alfa Aesar 99.9999%).

Synthesis. Polycrystalline $(\text{SnSe})_{1-x}(\text{AgBiSe}_2)_x$ ($0.00 \leq x \leq 1.00$) samples were synthesized by combining stoichiometric ratios of elemental Ag, Bi, Sn and Se in high quality quartz tubes. The quartz tubes were maintained at a pressure of 10^{-5} Torr and sealed under vacuum. The seal tubes were initially heated to 773 K over a period of 12 hrs, then heated again to 1223 K in next 5 hrs followed by annealing for 10 hrs and subsequently cooled to room temperature for a period of 15 hrs. The resulted ingots were crushed by using a mortar and pestle and sieved to fine powder. After that, ball-milling has been carried out at a speed of 250 rpm for 4 hrs at N_2 atmosphere in stainless-steel containers using a planetary Ball Mill (FRITSCH PULVERISETTE 7, Germany).

Spark plasma sintering (SPS) was done using a SPS211-LX (Dr. Sinter Lab) instrument. The finely powdered samples were sintered to prepare a cylinder (10 mm \times 8

mm) using graphite dies at 40 MPa pressure and 450 °C temperature for 10 minutes. The samples were cut and polished in different directions to measure the anisotropic electrical and thermal transport properties of $(\text{SnSe})_{1-x}(\text{AgBiSe}_2)_x$ ($0.00 \leq x \leq 0.80$).

Powder X-ray diffraction (PXRD) patterns of all the samples were recorded using a CuK_α ($\lambda = 1.5406 \text{ \AA}$) radiation on a Bruker D8 Diffractometer. Rietveld refinement of the PXRD pattern was performed using FULLPROF software.

Field emission scanning electron microscopy (FESEM) in back-scattered electron (BSE) mode. FESEM-BSE images were taken using ZEISS Gemini SEM – Field Emission Scanning Electron Microscope.

Band gap measurement. To estimate optical band gap of the as-synthesized specimens of $(\text{SnSe})_{1-x}(\text{AgBiSe}_2)_x$ ($0.00 \leq x \leq 1.00$), diffuse reflectance measurements were carried out with finely grounded powder at room temperature using a Perkin-Elmer Lambda 900 UV/Vis/near-IR spectrometer in reflectance mode ($\lambda = 2500\text{-}250 \text{ nm}$) and FT-IR Bruker IFS 66V/S spectrometer ($\lambda = 4000\text{-}400 \text{ cm}^{-1}$), respectively. Absorption (α/λ) data were calculated from the reflectance data using Kubelka-Munk equation: $\alpha/\lambda = (1-R)^2/(2R)$, where R is the reflectance, α and λ are respectively the absorption and scattering coefficients. The energy band gap was then determined from α/λ vs. E (eV) plot.

Thermal gravimetric analysis (TGA). TGA was performed by using a PerkinElmer TGA8000 instrument. Samples were heated at a rate of $5 \text{ }^\circ\text{C min}^{-1}$ in N_2 atmosphere (40 mL min^{-1}) throughout a temperature range of $30\text{-}700 \text{ }^\circ\text{C}$.

Differential scanning calorimetry (DSC). Finely ground powder samples were used for DSC measurements, in which the data were collected in a wide temperature range from $30\text{-}500 \text{ }^\circ\text{C}$. by using a METTLER TOLEDO DSC 822e at fixed heating/cooling rate of $1 \text{ }^\circ\text{C min}^{-1}$.

Electrical transport properties. Electrical conductivity and Seebeck coefficients were measured simultaneously under helium atmosphere from room temperature to 850 K on a ULVAC-RIKO ZEM-3 instrument system. The SPS processed sample were cut and polished in a rectangular shape with the dimensions of $\sim 2 \times 2 \times 8 \text{ mm}^3$ to carry out the measurements. Electrical and thermal transport were measured in same direction.

Hall measurement. For determining the carrier concentrations, Hall measurements were carried out on the same rectangular specimens used for electrical transport measurement in four-contact geometry up to a magnetic field of 0.57 T at room-temperature using custom-built equipment developed by Excel Instruments.

Thermal transport properties. Temperature dependent thermal diffusivity (D) was evaluated using a laser flash diffusivity technique in a Netzsch LFA-457 instrument. In addition, temperature dependent heat capacity (C_p) was also measured in the same instrument by using a standard pyroceram. Next, the total thermal conductivity (κ) was derived using the formula, $\kappa = D.C_p.\rho$, where ρ is density of the sample and the experimentally determined density was found to be $\sim 97\%$ of the theoretical density. Further, the electrical thermal conductivity, κ_{ele} were derived using Wiedemann-Franz Law, $\kappa_{ele} = L\sigma T$, where L denotes the Lorenz number which was estimated by fitting the temperature dependent Seebeck data.¹⁴⁻¹⁶

Computational details. Our first-principles calculations within density functional theory (DFT) were performed with QUANTUM ESPRESSO Package (QE) and projector augmented wave (PAW) potentials.¹⁷ Electronic exchange and correlation energy was treated within a generalized gradient approximated (GGA)¹⁸ functional with Perdew, Burke, and Ernzerhof (PBE) parametrization.¹⁹

Electronic wave functions and charge density were represented using plane wave basis sets truncated at cut-off energies of 45 Ry and 360 Ry respectively. The discontinuity in occupation numbers of electronic states was smeared with broadening temperature of $k_B T = 0.003$ Ry in a Fermi-Dirac distribution function. We determined electronic structure of $(\text{SnSe})_{1-x}(\text{AgBiSe}_2)_x$ in crystal structures with optimized (minimum energy) lattice parameters. At ambient conditions, SnSe stabilizes in the orthorhombic $Pnma$ phase containing eight atoms in the periodic unit cell. Integrations over its Brillouin Zone (BZ) were sampled on a uniform $8 \times 8 \times 8$ mesh of k-points. Electronic spectrum was determined at Bloch vectors along high symmetry lines ($X - \Gamma - Y - P - \Gamma - A - Z - \Gamma - T$) in the BZS. Our optimized lattice parameters for pristine SnSe in the orthorhombic structure ($Pnma$) are $a = 11.77 \text{ \AA}$, $b = 4.22 \text{ \AA}$, $c = 4.53 \text{ \AA}$, which are within the typical GGA errors of experimental lattice parameters ($a = 11.57 \text{ \AA}$, $b = 4.19 \text{ \AA}$, $c = 4.46 \text{ \AA}$). The cubic phase of $(\text{SnSe})_{0.67}(\text{AgBiSe}_2)_{0.33}$ was simulated using a $\sqrt{2} \times \sqrt{2} \times 1$ supercell of conventional $Fm\bar{3}m$

structure containing 16 atoms. Our estimates of lattice parameters of $(\text{SnSe})_{0.67}(\text{AgBiSe}_2)_{0.33}$ in this structure ($\sqrt{2} \times \sqrt{2} \times 1$ supercell) are $a = 8.43 \text{ \AA}$, $b = 8.43 \text{ \AA}$, $c = 5.96 \text{ \AA}$, which are within the typical GGA errors of experimental values of $a = 8.36 \text{ \AA}$, $b = 8.36 \text{ \AA}$, $c = 5.91 \text{ \AA}$. Electronic spectrum was determined at Bloch vectors along high symmetry lines ($\Gamma - X - M - \Gamma - Z - R - A - Z - X - R - M - A$) in the BZ of its tetragonal unit by including the spin-orbit coupling (SOC) in calculations with fully relativistic potentials.²⁰

The special quasirandom structures (SQS) of $(\text{SnSe})_{0.67}(\text{AgBiSe}_2)_{0.33}$ in the cubic phase and of $(\text{SnSe})_{0.8}(\text{AgBiSe}_2)_{0.2}$ in the orthorhombic phase were generated using the Monte Carlo SQS tool in the Alloy Theoretical Automated Toolkit (ATAT).²¹ Our estimates of lattice parameters of the cubic structure of $(\text{SnSe})_{0.67}(\text{AgBiSe}_2)_{0.33}$ are $a = b = c = 5.98 \text{ \AA}$, and of orthorhombic $(\text{SnSe})_{0.8}(\text{AgBiSe}_2)_{0.2}$ are $a = 12.05 \text{ \AA}$, $b = 4.26 \text{ \AA}$ and $c = 4.52 \text{ \AA}$. To determine the bulk electronic topology of cubic SnSe, we used Z2PACKcode²² to calculate the Z_2 topological invariants and mirror Chern number (n_M). This code uses hybrid Wannier functions^{23,24} and employs the ideas of time-reversal polarization in determination of the Z_2 invariants.

Theoretical calculations were performed in collaboration with Prof. U. V. Waghmare, JNCASR, India.

4.3. Results and Discussions

Polycrystalline $(\text{SnSe})_{1-x}(\text{AgBiSe}_2)_x$ ($0.00 \leq x \leq 1.00$) samples were synthesized by vacuum sealed tube reaction followed by ball milling and spark plasma sintering (SPS). Orthorhombic SnSe ($Pnma$), when alloyed with AgBiSe_2 , gradually transforms from orthorhombic to the face-centered cubic structure at ambient condition. With the addition of 30 mol% AgBiSe_2 in SnSe, a disordered rock-salt ($Fm\bar{3}m$) phase gets stabilized (Figure 4.1a), which perceives up to 80 mol% AgBiSe_2 addition in SnSe. The room-temperature powder X-ray diffraction (PXRD) patterns of bulk $(\text{SnSe})_{1-x}(\text{AgBiSe}_2)_x$ samples can be indexed to phase-pure orthorhombic phase when $0.00 \leq x < 0.28$, and to the face-centered cubic phase when $0.30 \leq x \leq 0.80$. On contrary, the AgBiSe_2 rich polycrystalline $(\text{SnSe})_{1-x}(\text{AgBiSe}_2)_x$ (when $x > 0.80$) samples resemble to the room temperature hexagonal crystal

structure of AgBiSe_2 (space group $P\bar{3}m1$). The Rietveld refinement of the room temperature PXRD patterns of orthorhombic $(\text{SnSe})_{0.78}(\text{AgBiSe}_2)_{0.22}$ and cubic $(\text{SnSe})_{0.70}(\text{AgBiSe}_2)_{0.30}$ have been shown in Figures 4.1b and 4.1c respectively, which indicate when AgBiSe_2 is added into the SnSe system, the Ag and Bi atoms preferentially occupy the Sn sites and induce disorder (Tables 4.1 and 4.2). This leads to the enhancement of configurational entropy and the consequent stabilization of the high symmetry cubic phase at ambient condition. Similar phenomenon can also be observed in other alloys where, the addition of extra elements can boost the total entropy of the system resulting in stabilization of higher symmetric phases.^{12,25,26}

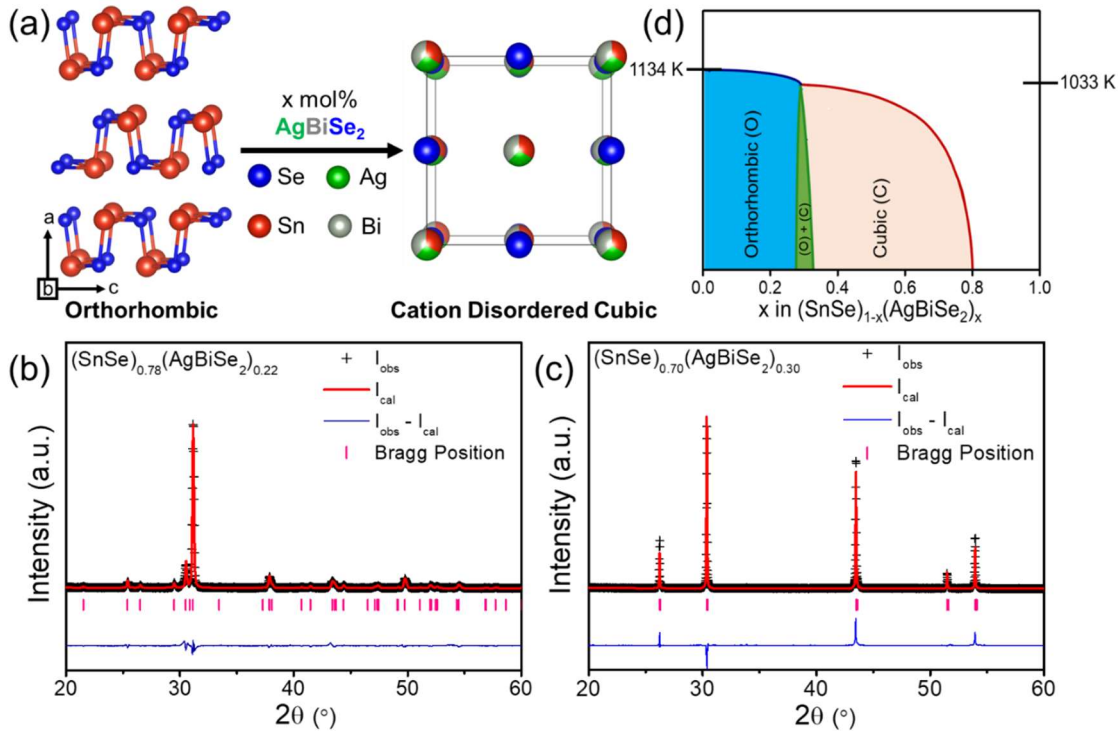


Figure 4.1. (a) Structural transformation of orthorhombic SnSe to rock-salt cubic structure upon AgBiSe_2 alloying. Rietveld refinement of room-temperature PXRD data of (b) orthorhombic $(\text{SnSe})_{0.78}(\text{AgBiSe}_2)_{0.22}$ and (c) cubic $(\text{SnSe})_{0.70}(\text{AgBiSe}_2)_{0.30}$ samples. (d) A schematic phase diagram of the SnSe-AgBiSe_2 system.

Field emission scanning electron microscopy (FESEM) in the backscattered electron mode (BSE) was performed on orthorhombic $(\text{SnSe})_{0.78}(\text{AgBiSe}_2)_{0.22}$ and cubic $(\text{SnSe})_{0.70}(\text{AgBiSe}_2)_{0.30}$ to check the purity of the polycrystals which confirm the absence

of any secondary microprecipitates in both the samples. Energy dispersive X-ray (EDAX) elemental color mapping of Sn, Ag, Bi, and Se during FESEM for both the orthorhombic and cubic $(\text{SnSe})_{1-x}(\text{AgBiSe}_2)_x$ (Figures 4.2 and 4.3) confirm that all the elements are uniformly distributed in the samples indicating the homogeneity of the polycrystals.

Table 4.1. Structural parameters of Rietveld refinement for orthorhombic $(\text{SnSe})_{0.78}(\text{AgBiSe}_2)_{0.22}$ sample.

Space group: $Pnma$; $a = 11.50 (3) \text{ \AA}$, $b = 4.15 (3) \text{ \AA}$, $c = 4.44 (3) \text{ \AA}$, $\alpha = \beta = \gamma = 90^\circ$

Constituent Elements	x/a	y/b	z/c	$U_{\text{iso}} (\text{\AA}^2)$	Occupancy	χ^2
Sn	0.8564(5)	0.25	0.4755(4)	0.1148(4)	0.63(2)	2.37
Ag	0.8564(5)	0.25	0.4755(4)	0.1148(4)	0.21(2)	
Bi	0.8564(5)	0.25	0.4755(4)	0.1148(4)	0.16(2)	
Se	0.1181(4)	0.25	0.1091(5)	0.0380(5)	1	

R-factors: R_{wp} : 12.61; R_{exp} : 8.19

The schematic phase diagram of the SnSe-AgBiSe₂ system, as inferred from PXRD, DSC and TGA analysis is shown in Figure 4.1d. The phase boundaries are, however, relative to the position of the orthorhombic, and cubic phases with respect to the AgBiSe₂ concentration. However, this schematic phase diagram clearly states that the increase of AgBiSe₂ concentration in SnSe causes a structural phase evolution from orthorhombic to a rock-salt crystal structure.

Table 4.2. Structural parameters of Rietveld refinement for cubic $(\text{SnSe})_{0.70}(\text{AgBiSe}_2)_{0.30}$ sample.

Space group: $Fm\bar{3}m$; $a = b = c = 5.8819 (5) \text{ \AA}$, $\alpha = \beta = \gamma = 90^\circ$

Constituent Elements	x/a	y/b	z/c	$U_{\text{iso}} (\text{\AA}^2)$	Occupancy	χ^2
Sn	0.0	0.0	0.0	0.1558(3)	0.54(2)	4.43
Ag	0.0	0.0	0.0	0.1558(3)	0.27(2)	
Bi	0.0	0.0	0.0	0.1558(3)	0.19(2)	
Se	0.5	0.5	0.5	0.0815(4)	1	

R-factors: R_{wp} : 11.93; R_{exp} : 5.6

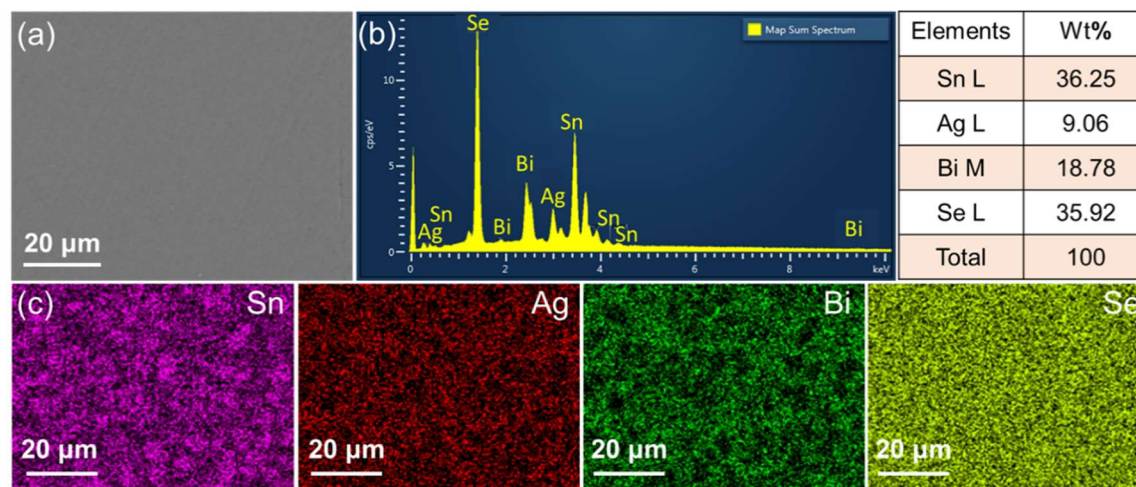


Figure 4.2. (a) Backscattered electron images taken during FESEM for ball milled and SPS processed orthorhombic $(\text{SnSe})_{0.78}(\text{AgBiSe}_2)_{0.22}$ polycrystal with corresponding EDAX spectra in (b). (c) EDAX elemental color mapping for Sn, Ag, Bi and Se for the area in (a).

The band gap of the pristine orthorhombic SnSe is measured to be about 0.90 eV (Figure 4.4a) which is consistent with previous literature reports.^{1,2} However, when SnSe is alloyed with AgBiSe_2 , band gap closes rapidly near to zero at $x = 0.30$ (Figures 4.4a and 4.4b) owing to the increase in chemical pressure originating from a decrease in unit cell volume from 213 \AA^3 (orthorhombic) to 206 \AA^3 (cubic) as shown in Figure 4.4c.

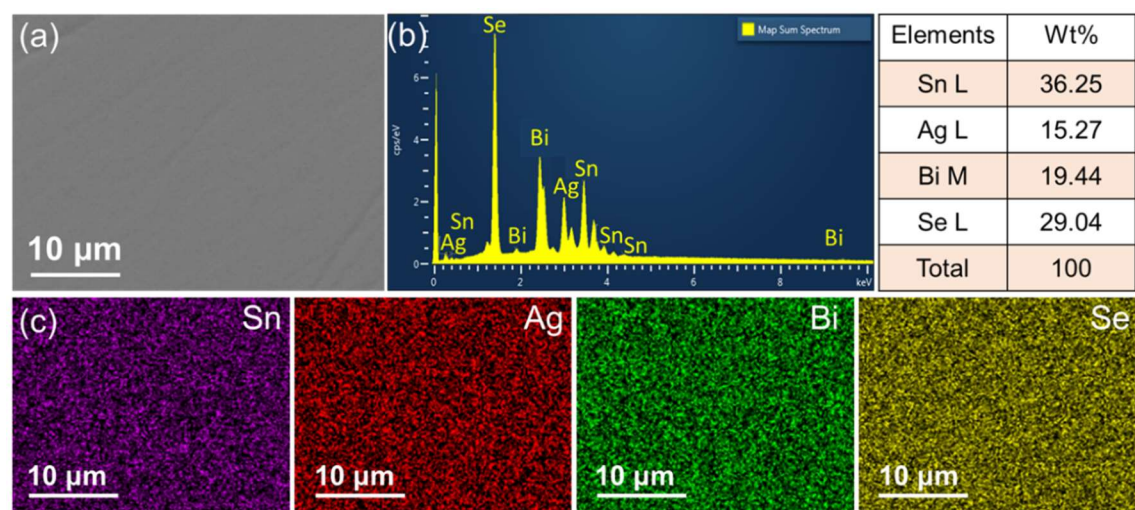


Figure 4.3. (a) Backscattered electron images taken during FESEM for ball milled and SPS processed cubic $(\text{SnSe})_{0.70}(\text{AgBiSe}_2)_{0.30}$ polycrystal with corresponding EDAX spectra in (b). (c) EDAX elemental color mapping for Sn, Ag, Bi and Se for the area in (a).

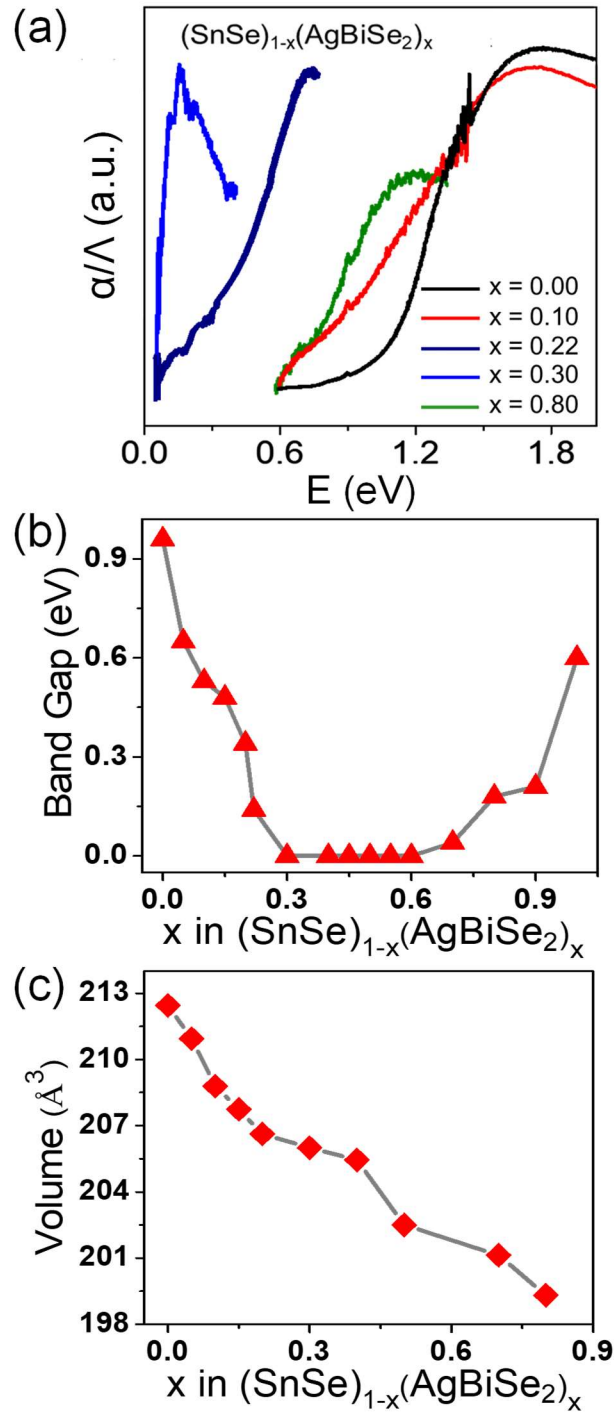


Figure 4.4. (a) Electronic absorption spectra, (b) band gap evolution and (c) unit cell volume of $(\text{SnSe})_{1-x}(\text{AgBiSe}_2)_x$ ($0.00 \leq x \leq 0.80$) as a function of AgBiSe_2 concentration.

The band-gap evolution plot has been shown in Figure 4.4b which depicts that upon increasing the concentration of AgBiSe_2 above $x = 0.24$, the band gap closes. The probable reason could be the structural phase transition induced contraction of the unit

cell volume which increases the chemical pressure and consequently reduces the band gap.

To study the evolution of band gap with respect to alloying concentration, we use first principles DFT calculation to determine its electronic band structure at three concentrations: pure SnSe (orthorhombic and cubic), $(\text{SnSe})_{0.80}(\text{AgBiSe}_2)_{0.20}$ (orthorhombic) and $(\text{SnSe})_{0.67}(\text{AgBiSe}_2)_{0.33}$ (cubic). The theoretical band gap of SnSe in the orthorhombic structure is 0.71 eV, with inclusion of the spin-orbit coupling in calculations. Such underestimation of band gap relative to the experimental band gap of 0.90 eV is typical of DFT calculations.

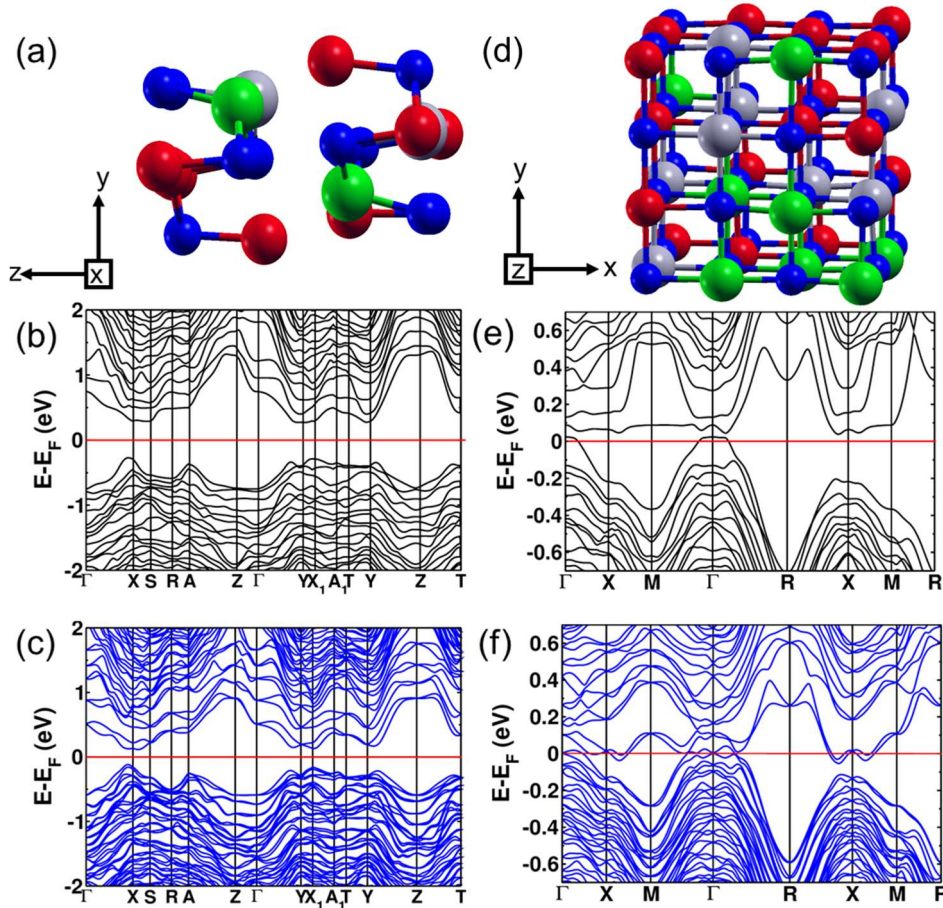


Figure 4.5. (a) SQS unit cell of modelled orthorhombic $(\text{SnSe})_{0.80}(\text{AgBiSe}_2)_{0.20}$ and its electronic structure calculated at the theoretical lattice constant (b) without the inclusion of spin-orbit interaction (SOI) and (c) with SOI. (d) SQS unit cell of modelled cubic $(\text{SnSe})_{0.67}(\text{AgBiSe}_2)_{0.33}$. Electronic structure of cubic $(\text{SnSe})_{0.67}(\text{AgBiSe}_2)_{0.33}$ calculated at the theoretical lattice constant (e) without the inclusion of SOI and (f) with SOI. (Red, green, blue and grey atoms represent Sn, Ag, Se and Bi respectively).

We find that the theoretical band gap of SnSe reduces with AgBiSe₂ alloying, consistent with the trend observed in experimental measurements using diffuse reflectance spectroscopy. The modelled structure of orthorhombic (SnSe)_{0.80}(AgBiSe₂)_{0.20} generated using the special quasirandom structures (SQS) algorithm is shown in Figure 4.5a. Our estimation of the band gap of (SnSe)_{0.80}(AgBiSe₂)_{0.20} are ~ 0.51 eV and ~ 0.24 eV without and with inclusion of the spin-orbit coupling respectively as shown in Figures 4.5b and 4.5c. The band gap obtained from calculations with spin orbit coupling is smaller than the experimentally observed value of ~ 0.34 eV, as expected.

(SnSe)_{1-x}(AgBiSe₂)_x with $x = 0.33$ exists in the cubic phase ($Fm\bar{3}m$). Electronic structure of pure cubic SnSe exhibits band gap of 0.12 eV estimated with the inclusion of the spin-orbit coupling in calculations as shown in Figures 4.6a and 4.6b.

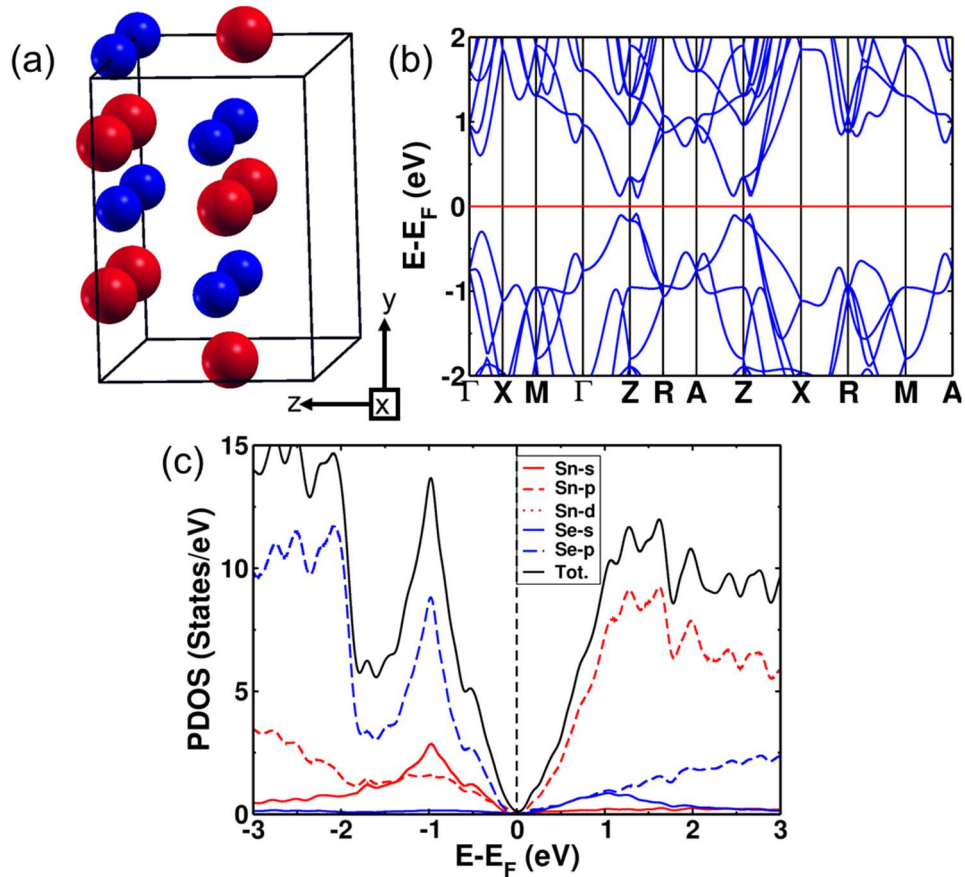


Figure 4.6. (a) Crystal structure of supercell of cubic SnSe (Sn Red, Se blue). (b) Electronic structures of the $\sqrt{2}\times\sqrt{2}\times 1$ tetragonal supercell of the cubic structure of SnSe with the inclusion of the effects of spin-orbit coupling. (c) Electronic density of states (DOS) and projected density of states (PDOS) of cubic SnSe.

Examination of the projected density of states (PDOS) (Figure 4.6c) reveals that its valence band (VB) is contributed mostly by p orbitals of Se, and weakly by s and p orbitals of Sn. Its conduction band (CB) is contributed primarily by p orbitals of Sn. Foremost, we have determined the mirror Chern number (n_M)^{4,27} and Z_2 topological invariant of pure cubic SnSe. Z_2 characterizes the topological insulators (TI) ($Z_2=0$ trivial insulator and $Z_2=1$ nontrivial insulator) and the mirror Chern number is the topological invariant describing a topological crystalline insulator (TCI). In topological crystalline insulators (TCI)^{27,28}, the gapless surface states are protected by mirror symmetry in contrast to topological insulators where the time-reversal symmetry protects the surface states. The presence of mirror symmetry in the crystal structure of a material results in

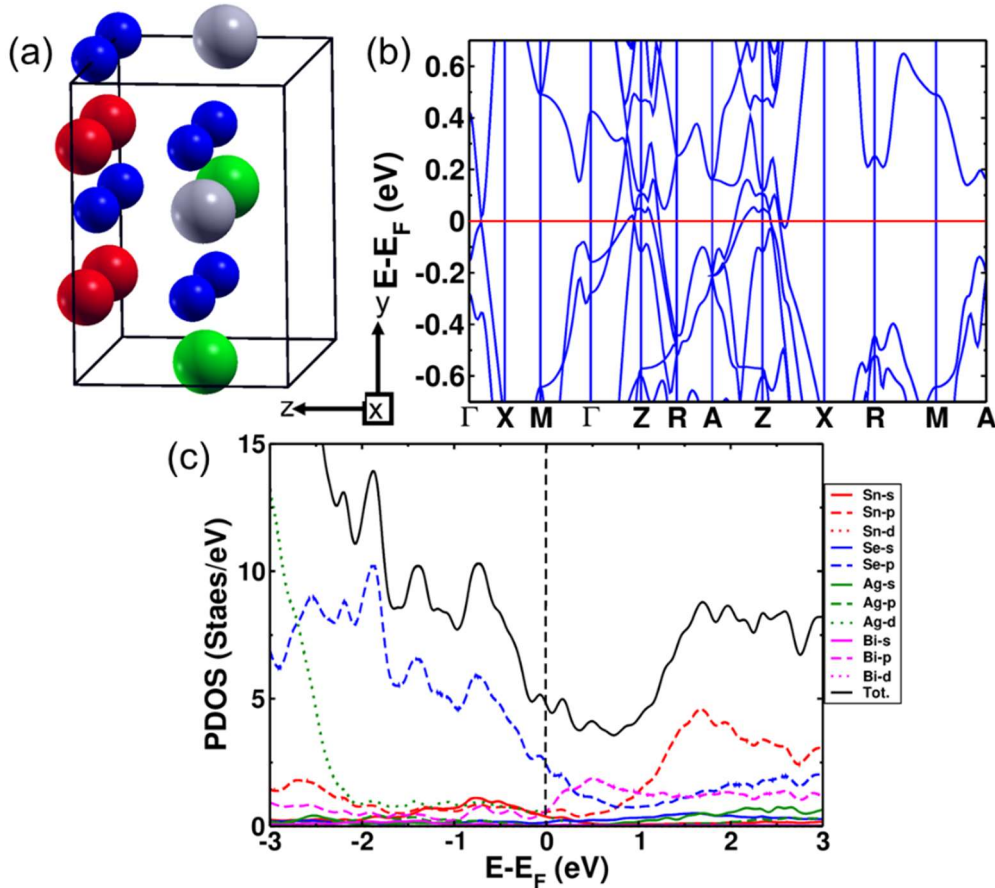


Figure 4.7. (a) Crystal structure of disordered cubic $(\text{SnSe})_{0.67}(\text{AgBiSe}_2)_{0.33}$ (Sn Red, Se blue, Ag green, Bi grey). (b) Electronic structures of the $\sqrt{2} \times \sqrt{2} \times 1$ tetragonal supercell of the cubic phase of $(\text{SnSe})_{0.67}(\text{AgBiSe}_2)_{0.33}$ with the inclusion of the effect of spin-orbit coupling. (c) Electronic density of states (DOS) and projected density of states (PDOS) of cubic $(\text{SnSe})_{0.67}(\text{AgBiSe}_2)_{0.33}$.

the presence of planes in the BZ giving rise to mirror symmetry protected Dirac cones in the surface electronic structure. A TCI supports even number of Dirac cones and band inversions in sharp contrast to a TI characterized by odd number of band inversions. TCIs are characterized by a nonzero mirror Chern number. The individual Chern numbers C_{+i} and C_{-i} are defined on a mirror-invariant plane for TCI. The mirror Chern number²⁷ defined as $n_M = (C_{+i} - C_{-i})/2$ can be used as a topological invariant for TCI. The strong Z_2 topological invariant (ν_0) of the cubic SnSe is 0 (normal insulator) confirming its trivial electronic topology with respect to time reversal symmetry, while its $n_M = 2$ establishes its non-trivial band topology with respect to crystalline symmetry. Therefore, the cubic phase of SnSe is a TCI.

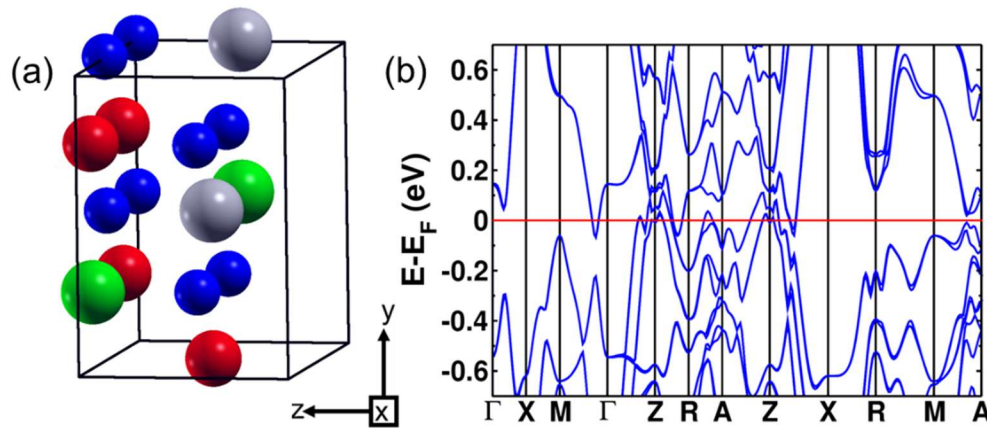


Figure 4.8. (a) Crystal structure of lower-symmetric disordered cubic $(\text{SnSe})_{0.67}(\text{AgBiSe}_2)_{0.33}$ (Sn Red, Se blue, Ag green, Bi grey) obtained by interchanging a pair of Sn and Ag atoms in Fig. S3a. (b) Electronic structure of the second configuration of $\sqrt{2} \times \sqrt{2} \times 1$ tetragonal supercell of cubic structure of $(\text{SnSe})_{0.67}(\text{AgBiSe}_2)_{0.33}$ with the inclusion of the effect of spin-orbit coupling.

We have examined the electronic structure of cubic $(\text{SnSe})_{1-x}(\text{AgBiSe}_2)_x$ in two disordered configurations at $x = 0.33$ (Figures 4.7 and 4.8) simulated with model $\sqrt{2} \times \sqrt{2} \times 1$ supercell of the conventional cell of $Fm\bar{3}m$ structure. The lower-symmetric disordered structure (Figure 4.8) is simulated by interchanging a pair of Sn and Ag atoms in the first disordered structure (Figure 4.7). The electronic structures in both the cases show vanishing band gap with overlapping valence and conduction bands at the Fermi level consistent with the trend observed in our experiments. In cubic SnSe (Figure 4.6a), Sn

occupies 4a (0.0, 0.0, 0.0) Wyckoff positions and Se occupy 4b (0.5, 0.5, 0.5) positions in the $Fm\bar{3}m$ space group. In the cubic phase of SnSe alloyed with 33 mol% AgBiSe₂, the Ag and Bi atoms occupy any of the 4a (0, 0, 0) sites randomly; therefore, to take into account the effect of realistic chemical disorder we generated a model structure using the SQS algorithm. In the 2×2×2 supercell having 16 Sn, 8 Ag, 8 Bi and 32 Se atoms, 4b Wyckoff sites are occupied by Se atoms while Ag, Bi and Sn atoms randomly occupy 4a sites (Figure 4.5d). Our estimation of the band gap of cubic (SnSe)_{0.67}(AgBiSe₂)_{0.33} calculated without spin-orbit coupling (Figure 4.5e) is ~0.07 eV whereas inclusion of the spin-orbit coupling closes this small gap and confirms its semi metallic nature (Figure 4.5f). For deeper understanding of the electronic properties, we examined the projected density of states (PDOS) of cubic phase of (SnSe)_{0.67}(AgBiSe₂)_{0.33} (Figure 4.7c). The valence band is dominated by contribution from *p*-orbitals of Se, similar to pure cubic SnSe, while the CB is contributed majorly by *p* orbitals of Sn and along with additional new contributions of *p* orbitals of Bi.

We calculated the relative stability of orthorhombic and cubic phases of (SnSe)_{1-x}(AgBiSe₂)_x with varied *x* (where *x* = 0, 0.20, 0.33) to confirm the transformation of orthorhombic SnSe (*Pnma*) to face-centered cubic structure with AgBiSe₂ alloying. Here, we used the same SQS supercell in calculation of cubic and orthorhombic structures at each value of *x* by deforming and distorting cubic structure to the orthorhombic structure and relaxing it further. For pristine SnSe, the orthorhombic phase is lower in energy with respect to its cubic phase by 2 meV/f.u. confirming its greater stability as seen in the experimental results. At 20% AgBiSe₂ alloying the orthorhombic phase remains lower in energy by ~ 46 meV/f.u. with respect to its cubic phase, consistent with experimentally observed orthorhombic structure of (SnSe)_{0.80}(AgBiSe₂)_{0.20}. Our estimation of the energy difference between the orthorhombic and cubic (SnSe)_{0.67}(AgBiSe₂)_{0.33} is 1620 meV/fu stabilizing the cubic phase over its orthorhombic phase confirming that the rock-salt ($Fm\bar{3}m$) phase gets stabilized with the addition of 30 mol% AgBiSe₂ in SnSe.

Thermoelectric properties were measured for the ball-milled and SPS processed anisotropic orthorhombic and isotropic cubic polycrystalline (SnSe)_{1-x}(AgBiSe₂)_x (0.00 ≤ *x* ≤ 0.30) samples. The cubic polycrystalline (SnSe)_{0.70}(AgBiSe₂)_{0.30} sample shows lower thermoelectric performance as compared to the orthorhombic (SnSe)_{0.78}(AgBiSe₂)_{0.22}. On

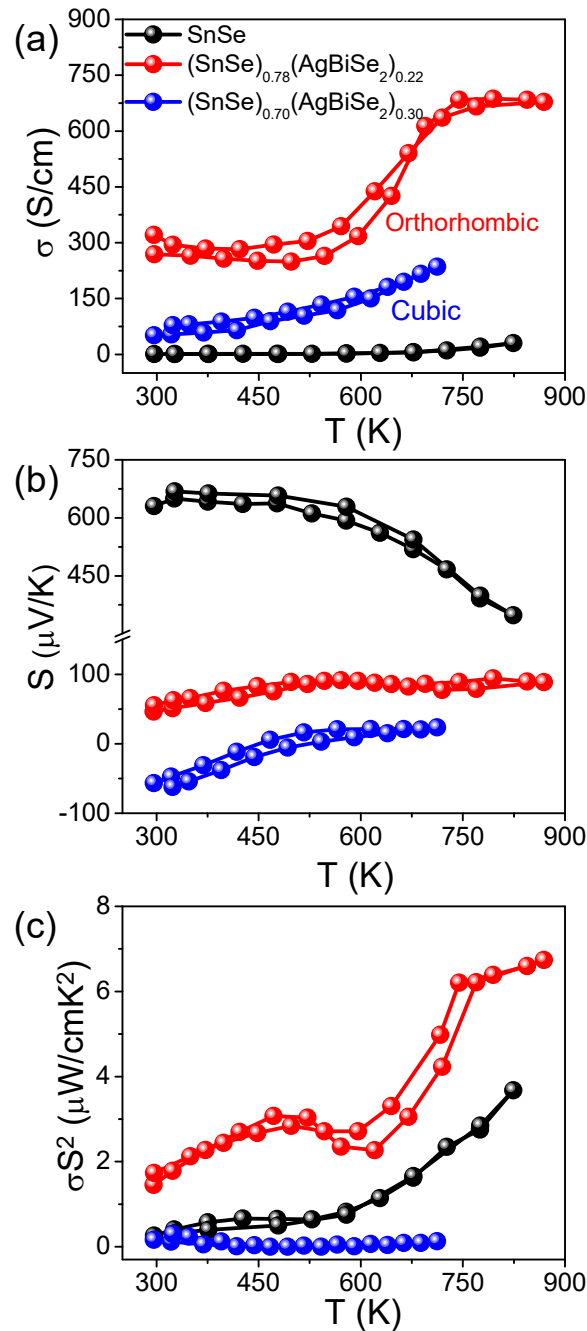


Figure 4.9. Temperature dependent (a) electrical conductivity, (b) Seebeck coefficient and (c) power factor of ball-milled polycrystalline $(\text{SnSe})_{1-x}(\text{AgBiSe}_2)_x$ (where, $x = 0, 0.22$ are orthorhombic and $x = 0.30$ is cubic in nature) samples for both heating-cooling cycle measured along parallel to the SPS pressing direction.

the other hand, improved thermoelectric performance has been observed in anisotropic orthorhombic phase when measurements are carried out along the parallel to the SPS pressing direction.

Figure 4.9 presents the thermoelectric properties of $(\text{SnSe})_{1-x}(\text{AgBiSe}_2)_x$ ($0.00 \leq x \leq 0.30$) measured parallel to the SPS pressing direction. Figure 4.9a depicts the temperature dependent electrical conductivity of pristine orthorhombic SnSe, orthorhombic $(\text{SnSe})_{0.78}(\text{AgBiSe}_2)_{0.22}$ and cubic $(\text{SnSe})_{0.70}(\text{AgBiSe}_2)_{0.30}$. The σ of pristine orthorhombic SnSe is 1.18 S cm^{-1} at 300 K, which increases to about 270 S cm^{-1} upon 22 mol% AgBiSe₂ alloying at room temperature. For all the $(\text{SnSe})_{1-x}(\text{AgBiSe}_2)_x$ ($0.00 \leq x < 0.28$) samples, electrical conductivity increases with increasing temperature which indicates the semiconducting transport (Figure 4.9a). The sharp increase in electrical conductivity at 610 K for orthorhombic $(\text{SnSe})_{0.78}(\text{AgBiSe}_2)_{0.22}$ is an indication of the phase transition from lower symmetric *Pnma* to higher symmetric *Cmcm* phase.^{29,30} Solid solution mixing of AgBiSe₂ with SnSe significantly increases σ due to the enhancement in the carrier concentration from $8.9 \times 10^{17} \text{ cm}^{-3}$ for pristine SnSe to $8.2 \times 10^{19} \text{ cm}^{-3}$ in $(\text{SnSe})_{0.78}(\text{AgBiSe}_2)_{0.22}$. Positive value of Hall coefficient indicates that holes are the majority carriers in orthorhombic $(\text{SnSe})_{1-x}(\text{AgBiSe}_2)_x$ ($0.00 \leq x < 0.28$) making it a *p*-type semiconductor (Table 4.3). Further, on addition of 30 mol% AgBiSe₂, the sample becomes *n*-type in nature as confirmed from the negative sign of the Hall coefficient and the room temperature carrier concentration was obtained to be $6.17 \times 10^{18} \text{ cm}^{-3}$ for the cubic $(\text{SnSe})_{0.70}(\text{AgBiSe}_2)_{0.30}$.

Table 4.3. Charge carrier concentration and mobility of the ball milled and SPS processed polycrystalline $(\text{SnSe})_{1-x}(\text{AgBiSe}_2)_x$ ($x = 0, 0.22, 0.30$) samples.

Composition	Carrier concentration $n \text{ (cm}^{-3}\text{)}$	Carrier Mobility $\mu \text{ (cm}^2 \text{ V}^{-1} \text{ s}^{-1}\text{)}$
SnSe	8.9×10^{17} (<i>p</i> -type)	8.3
$(\text{SnSe})_{0.78}(\text{AgBiSe}_2)_{0.22}$ (Orthorhombic)	8.2×10^{19} (<i>p</i> -type)	20.8
$(\text{SnSe})_{0.70}(\text{AgBiSe}_2)_{0.30}$ (Cubic)	6.17×10^{18} (<i>n</i> -type)	54.6

The measured value of the Seebeck coefficient of pristine orthorhombic SnSe is $631 \mu\text{V K}^{-1}$ at 300 K (Figure 4.9b), which decreases to $46 \mu\text{V K}^{-1}$ for orthorhombic

(SnSe)_{0.78}(AgBiSe₂)_{0.22} and with further increase of AgBiSe₂ concentration, the sample shows *n*-type conduction with a *S* value of -57 μV K⁻¹ for (SnSe)_{0.70}(AgBiSe₂)_{0.30}. The lower value of Seebeck coefficient is consistent with the high carrier concentration in these samples. However, the cubic (SnSe)_{0.70}(AgBiSe₂)_{0.30} shows anomalous trend in *S* values arising mainly due to the onset of bipolar conduction. Due to the optimization in carrier concentration and electrical conductivity, a moderate power factor of ~ 6.52 μW cm⁻¹ K⁻² has been achieved in (SnSe)_{0.78}(AgBiSe₂)_{0.22} sample at 873 K (Figure 4.9c).

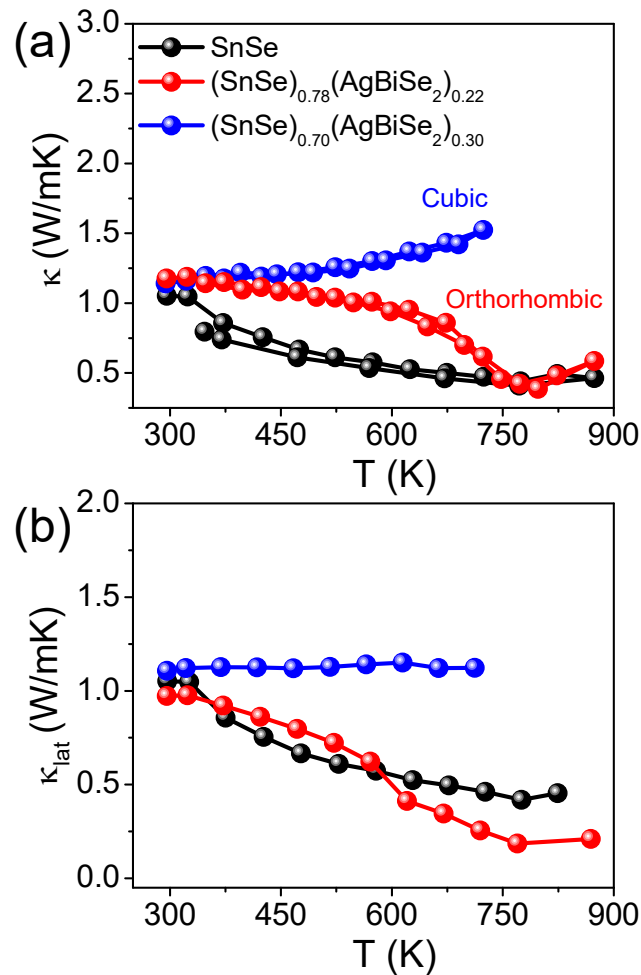


Figure 4.10. (a) Temperature dependent (a) total thermal conductivity (for both heating-cooling cycle), and (b) lattice thermal conductivity of polycrystalline (SnSe)_{1-x}(AgBiSe₂)_x (where, *x* = 0, 0.22 are orthorhombic and *x* = 0.30 is cubic) samples measured along parallel to the SPS pressing direction.

The total thermal conductivity of pristine orthorhombic SnSe, orthorhombic (SnSe)_{0.78}(AgBiSe₂)_{0.22} and cubic (SnSe)_{0.70}(AgBiSe₂)_{0.30} measured parallel to the SPS

pressing direction have been presented in Figure 4.10a. However, the room temperature total thermal conductivity is higher for the $(\text{SnSe})_{1-x}(\text{AgBiSe}_2)_x$ ($x = 0.22$ and 0.30) samples as compared to the pristine SnSe which arises mainly due to the greater contributions from the electrical thermal conductivity. Ball milled and SPS processed pristine SnSe exhibits a lattice thermal conductivity (κ_{lat}) of $1.08 \text{ W m}^{-1} \text{ K}^{-1}$ at 300 K, which decreases to $0.43 \text{ W m}^{-1} \text{ K}^{-1}$ at 773 K (Figure 4.10b). When SnSe is alloyed with AgBiSe_2 , κ_{lat} in the cubic $(\text{SnSe})_{0.70}(\text{AgBiSe}_2)_{0.30}$ increases significantly to $\sim 1.13 \text{ W m}^{-1} \text{ K}^{-1}$ at 300 K (Figure 4.10b). The low lattice thermal conductivity in orthorhombic SnSe mainly caused by the damping phonon vibrations due to the presence of significant lattice anharmonicity.^{1,2} But in the as-prepared cubic $(\text{SnSe})_{0.70}(\text{AgBiSe}_2)_{0.30}$, the higher lattice thermal conductivity can be attributed to the destruction of the layered orthorhombic crystal structure of SnSe.

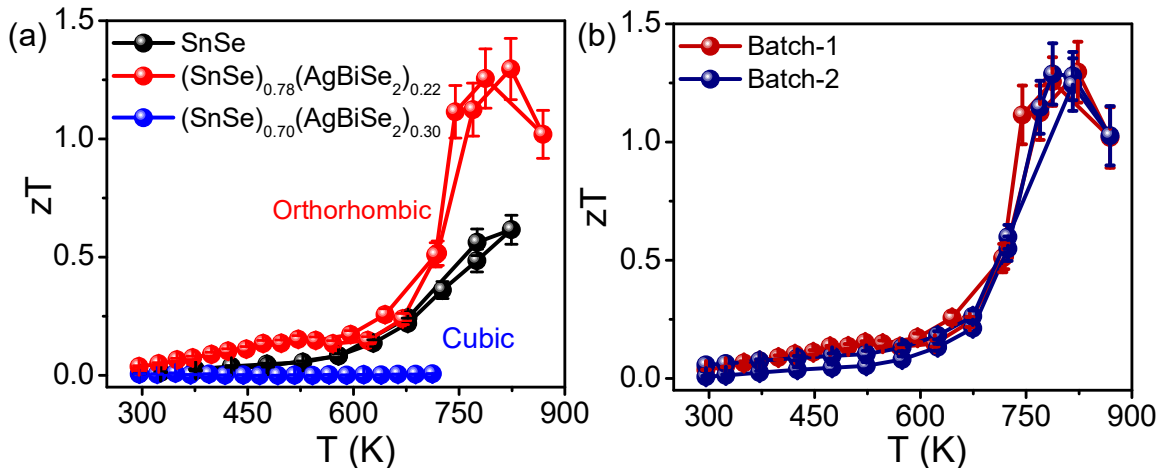


Figure 4.11. (a) Temperature dependent thermoelectric figure of merit of polycrystalline $(\text{SnSe})_{1-x}(\text{AgBiSe}_2)_x$ (where, $x = 0, 0.22$ are orthorhombic and $x = 0.30$ is cubic) samples measured along parallel to the SPS pressing direction. (b) The reversibility and reproducibility of the thermoelectric figure of merit of the SPS processed ball milled orthorhombic $(\text{SnSe})_{0.78}(\text{AgBiSe}_2)_{0.22}$ sample measured for different batches (synthesized separately) with the heating cooling cycles. The zT is measured along the parallel to SPS pressing direction.

The orthorhombic $(\text{SnSe})_{0.78}(\text{AgBiSe}_2)_{0.22}$ sample shows an ultralow lattice thermal conductivity of $\sim 0.19 \text{ W m}^{-1} \text{ K}^{-1}$ at 773 K due to the enhanced phonon scattering induced by the point defects owing to entropy-driven solid solution in SnSe- AgBiSe_2 system in

addition to lattice anharmonicity. Thus, as a collective result of improved carrier concentration, elevated power factor and low thermal conductivity, a high zT of 1.3 has been achieved in polycrystalline orthorhombic $(\text{SnSe})_{0.78}(\text{AgBiSe}_2)_{0.22}$ sample at 823 K (Figure 4.11a) when measured along parallel to SPS pressing direction which is reversible and reproducible for different batches of samples as well as for heating-cooling cycles (Figure 4.11b).

4.4. Conclusion

In conclusion, electronic and crystal structure of SnSe has been tailored with addition of AgBiSe₂. Layered orthorhombic phase is stable in $(\text{SnSe})_{1-x}(\text{AgBiSe}_2)_x$ for the composition range of $0.00 \leq x < 0.28$, which are narrow band gap semiconductors. High-pressure cubic rock-salt phase of SnSe has been stabilized at ambient condition with increasing AgBiSe₂ concentration to $0.30 \leq x \leq 0.80$. Solid solution mixing of AgBiSe₂ with SnSe increases the configurational entropy by introducing atomic disorder into the system and consequently stabilizes the cubic phase at ambient conditions. The anomalous closing of the band gap of SnSe with increasing AgBiSe₂ concentration is caused by the influence of increase in chemical pressure. Electronic structures of orthorhombic and cubic phases of $(\text{SnSe})_{1-x}(\text{AgBiSe}_2)_x$ show emergence of band gap at higher AgBiSe₂ concentration in SnSe. Pristine cubic SnSe exhibits topological crystalline insulator (TCI) phase, but the cubic $(\text{SnSe})_{1-x}(\text{AgBiSe}_2)_x$ ($x = 0.33$) possesses semi-metallic electronic structure with overlapping conduction and valence bands. While the cubic $(\text{SnSe})_{0.70}(\text{AgBiSe}_2)_{0.30}$ sample shows *n*-type conduction, orthorhombic $(\text{SnSe})_{0.78}(\text{AgBiSe}_2)_{0.22}$ retains the *p*-type nature at room temperature. We have achieved a high zT of 1.3 in *p*-type polycrystalline orthorhombic $(\text{SnSe})_{0.78}(\text{AgBiSe}_2)_{0.22}$ at 823 K via optimization of carrier concentration and electronic properties.

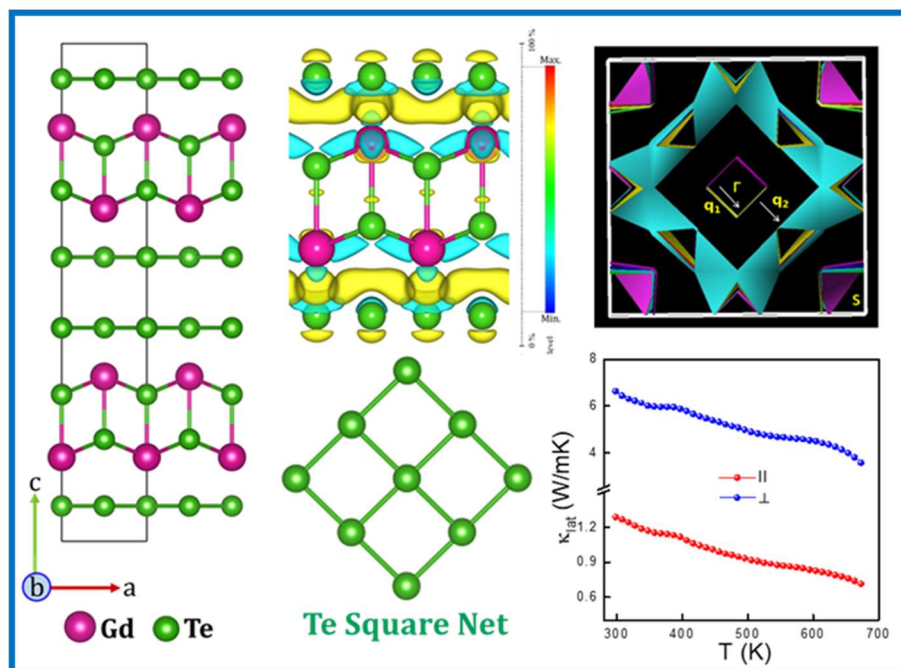
4.5. References

- (1) Zhao, L.-D.; Lo, S.-H.; Zhang, Y.; Sun, H.; Tan, G.; Uher, C.; Wolverton, C.; Dravid, V. P.; Kanatzidis, M. G. *Nature* **2014**, *508*, 373–377.
- (2) Zhao, L.-D.; Tan, G.; Hao, S.; He, J.; Pei, Y.; Chi, H.; Wang, H.; Gong, S.; Xu, H.; Dravid, V. P.; Uher, C.; Snyder, G. J.; Wolverton, C.; Kanatzidis, M. G. *Science* **2016**, *351*, 141–144.
- (3) Zhao, L.-D.; Chang, C.; Tan, G.; Kanatzidis, M. G. *Energy Environ. Sci.* **2016**, *9*, 3044–3060.
- (4) Sun, Y.; Zhong, Z.; Shirakawa, T.; Franchini, C.; Li, D.; Li, Y.; Yunoki, S.; Chen, X.-Q. *Phys. Rev. B* **2013**, *88*, 235122.
- (5) Wang, D.; He, W.; Chang, C.; Wang, G.; Wang, J.; Zhao, L.-D. *J. Mater. Chem. C* **2018**, *6*, 12016–12022.
- (6) Rehman, S. ur; Butt, F. K.; Tariq, Z.; Hayat, F.; Gilani, R.; Aleem, F. *J. Alloys Compd.* **2017**, *695*, 194–201.
- (7) Luo, Y.; Hao, S.; Cai, S.; Slade, T. J.; Luo, Z. Z.; Dravid, V. P.; Wolverton, C.; Yan, Q.; Kanatzidis, M. G. *J. Am. Chem. Soc.* **2020**, *142*, 15187–15198.
- (8) Wang, Z.; Wang, J.; Zang, Y.; Zhang, Q.; Shi, J.-A.; Jiang, T.; Gong, Y.; Song, C.-L.; Ji, S.-H.; Wang, L.-L.; Gu, L.; He, K.; Duan, W.; Ma, X.; Chen, X.; Xue, Q.-K. *Adv. Mater.* **2015**, *27*, 4150–4154.
- (9) Wang, H.; Hu, H.; Man, N.; Xiong, C.; Xiao, Y.; Tan, X.; Liu, G.; Jiang, J. *Mater. Today Phys.* **2021**, *16*, 100298.
- (10) Jin, W.; Vishwanath, S.; Liu, J.; Kong, L.; Lou, R.; Dai, Z.; Sadowski, J. T.; Liu, X.; Lien, H. H.; Chaney, A.; Han, Y.; Cao, M.; Ma, J.; Qian, T.; Dadap, J. I.; Wang, S.; Dobrowolska, M.; Furdyna, J.; Muller, D. A.; Pohl, K.; Ding, H.; Xing, H. G.; Osgood, R. M. *Phys. Rev. X* **2017**, *7*, 041020.
- (11) Wang, H. X.; Mao, L. S.; Tan, X. J.; Liu, G. Q.; Xu, J. T.; Shao, H. Z.; Hu, H. Y.; Jiang, J. *Nano Energy* **2018**, *51*, 649–655.
- (12) Roychowdhury, S.; Ghosh, T.; Arora, R.; Waghmare, U. V.; Biswas, K. *Angew. Chem. Int. Ed.* **2018**, *57*, 15167–15171.
- (13) Samanta, M.; Ghosh, T.; Arora, R.; Waghmare, U. V.; Biswas, K. *J. Am. Chem. Soc.* **2019**, *141*, 19505–19512.

- (14) Banik, A.; Shenoy, U. S.; Saha, S.; Waghmare, U. V.; Biswas, K. *J. Am. Chem. Soc.* **2016**, *138*, 13068–13075.
- (15) Sarkar, D.; Ghosh, T.; Banik, A.; Roychowdhury, S.; Sanyal, D.; Biswas, K. *Angew. Chem. Int. Ed.* **2020**, *59*, 11115–11122.
- (16) Perumal, S.; Roychowdhury, S.; Negi, D. S.; Datta, R.; Biswas, K. *Chem. Mater.* **2015**, *27*, 7171–7178.
- (17) Kresse, G.; Joubert, D. *Phys. Rev. B* **1999**, *59*, 1758–1775.
- (18) Hua, X.; Chen, X.; Goddard, W. A. *Phys. Rev. B* **1997**, *55*, 16103–16109.
- (19) Perdew, J. P.; Burke, K.; Ernzerhof, M. *Phys. Rev. Lett.* **1996**, *77*, 3865–3868.
- (20) Dal Corso, A. *Comput. Mater. Sci.* **2014**, *95*, 337–350.
- (21) van de Walle, A.; Tiwary, P.; de Jong, M.; Olmsted, D. L.; Asta, M.; Dick, A.; Shin, D.; Wang, Y.; Chen, L.-Q.; Liu, Z.-K. *Calphad* **2013**, *42*, 13–18.
- (22) Gresch, D.; Autès, G.; Yazyev, O. V.; Troyer, M.; Vanderbilt, D.; Bernevig, B. A.; Soluyanov, A. A. *Phys. Rev. B* **2017**, *95*, 075146.
- (23) Soluyanov, A. A.; Vanderbilt, D. *Phys. Rev. B* **2011**, *83*, 235401.
- (24) Bhattacharjee, J.; Waghmare, U. V. *Phys. Rev. B* **2005**, *71*, 045106.
- (25) Sarkar, D.; Ghosh, T.; Roychowdhury, S.; Arora, R.; Sajan, S.; Sheet, G.; Waghmare, U. V.; Biswas, K. *J. Am. Chem. Soc.* **2020**, *142*, 12237–12244.
- (26) Sarkar, D.; Roychowdhury, S.; Arora, R.; Ghosh, T.; Vasdev, A.; Joseph, B.; Sheet, G.; Waghmare, U. V.; Biswas, K. *Angew. Chem. Int. Ed.* **2021**, *60*, 10350–10358.
- (27) Teo, J. C. Y.; Fu, L.; Kane, C. L. *Phys. Rev. B* **2008**, *78*, 045426.
- (28) Fu, L. *Phys. Rev. Lett.* **2011**, *106*, 106802.
- (29) Chandra, S.; Biswas, K. *J. Am. Chem. Soc.* **2019**, *141*, 6141–6145.
- (30) Chandra, S.; Dutta, P.; Biswas, K. *ACS Appl. Energy Mater.* **2020**, *3*, 9051–9057.

PART 5

Low Thermal Conductivity in Charged & van der Waals Layered GdTe_3



Low Thermal Conductivity in Charged & van der Waals Layered GdTe₃[†]

Summary

Understanding the mechanism that correlates phonon transport with chemical bonding and solid-state structure is the key to develop materials with low thermal conductivity, which are essential for useful thermoelectric applications and thermal barrier coatings. In this context, strongly correlated electronic systems always remain in the forefront of materials science research due to their fascinating chemical and physical properties. Herein, we have reported low lattice thermal conductivity in GdTe₃, a charge density wave (CDW) material. At ambient conditions, GdTe₃ possess a quasi-2D layered structure where one corrugated GdTe slab is sandwiched between two Te square net sheets. Charge transfer takes place from the GdTe slab to the adjacent Te sheets and there is a presence of van der Waals (vdW) gap between the two neighbouring Te-sheets which makes GdTe₃ a natural heterostructure of charged and vdW layers. The undistorted phase of GdTe₃ is metallic in nature, with a strongly nested Fermi Surface leading to instability and Kohn anomalies in phonon dispersion. The unstable phonon modes involve displacements of Te atoms in bilayers constituting the origin of CDW in GdTe₃. We establish a strong anharmonicity in terms of high Grüneisen parameters of the CDW-related phonon modes along Γ -S direction, which is responsible for suppressing acoustic phonons in transporting heat. Raman spectroscopy reveals the existence of strong electron phonon coupling and low energy optical phonon modes which effectively enhances the phonon scattering in the system and causes low κ_{lat} of $0.7 \text{ W m}^{-1} \text{ K}^{-1}$ at 673 K in polycrystalline GdTe₃ when measured along parallel to SPS pressing direction.

[†]S. Chandra, P. Dutta, K. Debnath, I. Maria, D. Rawat, A. Soni, U. V. Waghmare, and K. Biswas, [2022](#). (Manuscript under preparation)

5.1. Introduction

Materials having extreme thermal conductivity are always important for efficient thermal management.¹ Solids with high thermal conductivity are useful in microelectronic devices due to their efficient heat dissipation, whereas low thermal conductive materials are widely used in thermoelectrics^{2–5} and thermal barrier coatings.⁶ In a nonmagnetic material, the thermal conductivity (κ) is composed of two parts, namely (i) electronic thermal conductivity (κ_{ele}) which is determined by the electrical conductivity (σ) of the material via the Wiedemann–Franz law, $\kappa_{ele} = L\sigma T$ (L = Lorenz number, and T = absolute temperature), and (ii) lattice thermal conductivity (κ_{lat}) which is primarily controlled by phonon (quantum of lattice vibration) transport. To determine the efficiency of a thermoelectric material, κ_{lat} plays a pivotal role because it is a relatively independent parameter and can be tuned easily. After years of effort, researchers have developed several extrinsic and intrinsic strategies to minimize the κ_{lat} by enhancing phonon scattering. Extrinsic approaches like incorporation of point defects and nano/meso structures into a thermoelectric matrix are found to be effective in lowering down the κ_{lat} .^{7–12} However, these extrinsic strategies may hamper the carrier mobility to some extent which in turn can decrease the efficiency of a thermoelectric material. So, to design new materials with intrinsically low κ_{lat} is an important task in thermoelectric research. Several inherent properties associated with crystal structure and chemical bonding such as presence of lattice anharmonicity in two dimensional (2D) layered structure,^{13–16} stereochemically active lone pairs,^{17,18} complex crystal structures,^{19,20} bonding heterogeneity,^{21,22} and resonant bonding²³ are found to be effective for achieving intrinsically low κ_{lat} . In addition to this, materials having ferroelectric instability,^{24,25} rattler atoms^{26–28} and liquid-like cationic motion^{29,30} are found to show intrinsically low κ_{lat} value.

When the charge carrier concentration of a material is not high, the phonon-phonon interaction (PPI) by three-phonon and/or four-phonon process is the most dominant phonon scattering mechanism to determine the κ_{lat} at high temperature.³¹ However, recent studies indicate that the electron-phonon interaction (EPI) starts to play a crucial role in determining the κ_{lat} when the carrier concentration is above 10^{19} cm⁻³.³² Theoretical calculations performed by Liao *et al.* have shown that EPI can reduce the κ_{lat} of *p*-type

silicon up to 45% at room temperature by decreasing the phonon lifetime, when the carrier concentration is at around 10^{21} cm^{-3} .³³ So, materials having strong EPI may show intrinsically low κ_{lat} . In this context, charge density wave (CDW) materials hosting the strong electron phonon coupling may be a good candidate for low lattice thermal conductivity. CDW materials in general have layered structure where strong EPI breaks the translation symmetry of the lattice and induces lattice distortion into the system.³⁴ Recently, Chiritescu *et al.* have obtained an ultralow κ_{lat} of around $0.05 \text{ W m}^{-1}\text{K}^{-1}$ at room temperature in disordered thin films of 2D layered CDW material WSe_2 .³⁵ Realizing this idea of layered and disordered crystal structure, one can expect a low κ_{lat} value in CDW materials.

Among several CDW materials, rare earth tellurides with general formula RTe_3 (R = rare earth element and Te = tellurium) have gained enormous attention in the field of chemistry and condensed matter physics due to their structural diversity,³⁶ exotic magnetic properties³⁷ and pressure induced superconductivity.³⁸ Depending upon the rare earth element present in RTe_3 , the CDW transition temperature (T_{CDW}) can vary from 244 K (TmTe_3)³⁹ to 500 K (LaTe_3)⁴⁰. Application of external pressure can also tune this transition temperature significantly.^{38,41} It is worth to mention here that the heavy rare earth element (Tb-Tm) based RTe_3 system also undergoes a second CDW transition at lower temperature.⁴⁰ Though several physical properties of RTe_3 system have already been studied, the thermoelectric properties remain unexplored. Recently, GdTe_3 , a member of RTe_3 family has drawn huge attraction due to its large carrier mobility ($39000 \text{ cm}^2 \text{ V}^{-1} \text{ s}^{-1}$)⁴² and hence it may be a good candidate for thermoelectric research.

In this chapter, I have synthesized a simple binary CDW material GdTe_3 which shows intrinsically low lattice thermal conductivity of $0.7 \text{ W m}^{-1} \text{ K}^{-1}$ at 673 K along parallel to the SPS pressing direction. Interestingly, we have observed large anisotropy both in the electrical and thermal conductivity data of GdTe_3 when measured along parallel and perpendicular to the SPS pressing, which is quite unusual in polycrystalline materials. To comprehend the origin of such low κ_{lat} and its relationship with the CDW transition, we have performed temperature dependent Raman spectroscopy and augmented our observations with density functional theoretical (DFT) calculations. GdTe_3 exhibits fascinating hierarchical bonding environments where one corrugated GdTe slab is

sandwiched between two Te sheets. From, DFT calculations, it is verified that charge transfer take place from the GdTe slab to the adjacent Te sheets and there is a presence of van der Waals (vdW) gap between the two neighbouring Te-sheets. Thus, the structure can be considered as a natural heterostructure of charged and vdW layers which gives rise to large degree of anharmonicity in the crystal lattice of GdTe₃ that provide significant phonon damping. The presence of unstable phonon modes arising from the displacements of Te-bilayers, strong electron-phonon coupling, and Fermi surface nesting constitute the origin of CDW transition ($T_{CDW} \sim 380$ K) in GdTe₃ as corroborated from the DFT studies. Raman spectroscopy reveals the existence of low-lying optical phonon modes which hinder the acoustic phonon transport and significantly reduce the κ_{lat} . Thus, the inherent strong anharmonicity due to the layered structure, manifestation of quantum effects in transport properties and discretized electronic density of states makes these CDW materials an interesting candidate in the field of thermoelectric research.

5.2. Methods

Reagents. The high purity elements utilized for the synthesis of GdTe₃ sample are gadolinium chips (Gd, Sigma Aldrich 99.99%), and tellurium lumps (Te, Alfa Aesar 99.999+ %).

Synthesis. Desired polycrystalline sample with nominal composition GdTe₃ was prepared by melting the stoichiometric amount of Gd and Te in a vacuum sealed (10^{-5} Torr) quartz ampoule. The ampoule was kept vertically in a box furnace and heated to 950 °C in 10 h and kept at this temperature for 3 days. Then it was cooled down to 550 °C in 3 h and kept for 3 days and finally cooled down to room temperature in 5 h. The resulted ingots were crushed into fine powder by using a mortar and pestle.

Spark plasma sintering (SPS) was done using a SPS211-LX (Dr. Sinter Lab) instrument. The finely powdered samples were sintered to prepare a cylinder (10 mm × 8 mm) using graphite dies at 50 MPa pressure and 450 °C temperature for 15 minutes. The samples were cut and polished in different directions to measure the anisotropic electrical and thermal transport properties. Density of the sample is found to be 6.64 g cm⁻³ which is around 95% of the theoretical density.

Powder X-ray diffraction (PXRD) patterns of the sample were recorded using Cu K α ($\lambda = 1.5406 \text{ \AA}$) radiation in a Rigaku Smartlab (9 kW, rotating anode) x-ray diffractometer. Rietveld refinement of the PXRD pattern was performed using FULLPROF software.⁴³

Thermal gravimetric analysis (TGA) was performed by using a PerkinElmer TGA8000 instrument. Samples were heated at a rate of $5 \text{ }^\circ\text{C min}^{-1}$ in N $_2$ atmosphere (40 mL min^{-1}) throughout a temperature range of 30–625 $^\circ\text{C}$.

Differential scanning calorimetry (DSC). Finely ground powder samples were used for DSC measurements, in which the data were collected in a wide temperature range from 30–500 $^\circ\text{C}$ by using a METTLER TOLEDO DSC 822e at fixed heating/cooling rate of $1 \text{ }^\circ\text{C min}^{-1}$.

Electrical transport properties. Electrical conductivity and Seebeck coefficient were measured simultaneously under helium atmosphere from room temperature to 673 K in a ULVAC-RIKO ZEM-3 instrument system. The SPS processed sample were cut and polished to prepare a rectangular parallelepiped with the dimensions of $\sim 2 \times 2 \times 8 \text{ mm}^3$ to carry out the measurements. Electrical and thermal transport were measured in same direction.

Hall measurement. For determining the carrier concentrations, Hall measurements were carried out on the same rectangular specimens used for electrical transport measurement in four-contact geometry up to a magnetic field of 1 T at room temperature using custom-built equipment developed by Excel Instruments.

Thermal transport properties. Temperature dependent thermal diffusivity (D) was measured using a laser flash diffusivity technique in a Netzsch LFA-457 instrument. The total thermal conductivity (κ) was calculated using the formula, $\kappa = DC_p\rho$, where ρ is density of the sample and the experimentally determined density was found to be $\sim 95\%$ of the theoretical density. We have used the Dulong-Petit law to calculate the heat capacity (C_p) ($0.185 \text{ Jg}^{-1}\text{K}^{-1}$) for the estimation of thermal conductivity. Further, the electrical thermal conductivity, κ_{ele} was derived using Wiedemann-Franz Law, $\kappa_{ele} = L\sigma T$, where L denotes the Lorenz number which was estimated by fitting the temperature dependent Seebeck data.^{44–46}

Magnetic measurements. The dc-magnetization (M) was measured as a function of temperature (T) and magnetic field (H) by using a Quantum Design SQUID magnetometer (MPMS-XL).

Heat capacity measurement. Low-temperature heat capacity was measured in a DynaCool Physical Property Measurement System (PPMS, Quantum Design) in the temperature range of 2-20 K by using the relaxation technique.

Sound velocity measurement. The longitudinal (v_l) and transverse (v_t) sound velocities were measured using disc-shaped and square-shaped samples, respectively, with an Epoch 650 Ultrasonic Flaw Detector (Olympus) instrument with the transducer frequency of 5 MHz. The minimum lattice thermal conductivity (κ_{min}) was then calculated using the Cahill's Model⁴⁷:

$$\kappa_{min} = 1.21n^{2/3}k_B \frac{1}{3}(v_l + 2v_t)$$

where k_B is the Boltzmann constant and n is the number density of atoms.

Poisson ratio (ν_p) and the Grüneisen parameter (γ) were calculated using equations⁴⁸ below (see Table 5.1):

$$\nu_p = \frac{1-2(v_t/v_l)^2}{2-2(v_t/v_l)^2}$$

$$\gamma = \frac{3(1+\nu_p)}{2(2-3\nu_p)}$$

Raman spectroscopy. Raman scattering measurements was performed using Horriba Jobin Vyon LabRAM HR Evolution Raman spectrometer equipped with Czerny-turner grating (1800 gr/mm), 633 nm laser excitation, and Peltier cooled CCD detector. Temperature-dependent Raman measurements were done using a Montana cryostat and Linkam stage in the temperature range of 4-300 K and 300-400 K respectively. An ultra-low frequency filter was used to access the low-frequency Raman modes. All the spectra have been fitted by the Lorentzian function to evaluate the phonon frequency and full width at half maximum (FWHM) of the Raman modes.

The Raman spectroscopy measurements are done in collaboration with Prof. Ajay Soni, IIT Mandi, India.

Computational details. Our first-principles calculations are based on density functional theory as implemented in QUANTUM ESPRESSO,⁴⁹ and ultrasoft pseudopotentials to

model interactions between electrons and the ionic cores. We used a generalized-gradient approximation (GGA)⁵⁰ of the exchange-correlation energy with functional parameterized by Perdew, Burke and Ernzerhof (PBE)⁵¹. We include van der Waals (vdW) interaction with the parametrization given in Grimme scheme.⁵² Electronic wave functions and charge density expansions in plane wave basis sets were truncated at cut-off energies of 50 Ry and 400 Ry respectively. Brillouin Zone (BZ) integrations were sampled on a uniform $12 \times 12 \times 4$ mesh of k-points. We used conventional unit cell of GdTe₃ with 16 atoms as the periodic unit for our theoretical analysis. Our optimized lattice parameters (without considering CDW modulation), a , b and c are 4.32 Å, 4.35 Å and 25.6 Å respectively, within 1% of the respective experimental values.⁴² Electronic spectrum was determined at Bloch wave vectors along high symmetry lines (Γ - S - X - Y - Γ - Z - R - U - T - Z) in the Brillouin Zone with and without inclusion of spin-orbit coupling (SOC) in our calculations. Lattice-dynamical properties were determined within the framework of self-consistent density functional perturbation theory (DFPT) as implemented within the QE code.⁵³ We corroborated these using a $4 \times 4 \times 1$ supercell of GdTe₃ in calculations with PHONOPY⁵⁴ and Vienna Ab-initio Simulation Package (VASP)^{55,56}. We determined the mode Grüneisen parameters using finite difference method and phonon dispersion calculated at two different volumes, $0.98V_0$ and $1.02V_0$ (where V_0 is the equilibrium volume of the ground state structure), employing the formula $\gamma = -\frac{d \ln \omega_{qv}}{d \ln V}$, where γ , V and ω_{qv} denote Grüneisen parameter, unit cell volume, and frequency of a phonon mode at wavevector q for branch ν , respectively.

Theoretical calculations were performed in collaboration with Prof. U. V. Waghmare, JNCASR, India.

5.3. Results and Discussions

In the undistorted state, GdTe₃ adopts a quasi-2D layered structure with orthorhombic symmetry (space group $Cmcm$) where double corrugated GdTe slabs are sandwiched between two “square” planer nets of Te. The layers are stacked along the crystallographic c -direction while the Te sheets are arranged in the ab plane and rotated by an angle of 45° with respect to the GdTe slabs and there exists a vdW gap between the two neighbouring

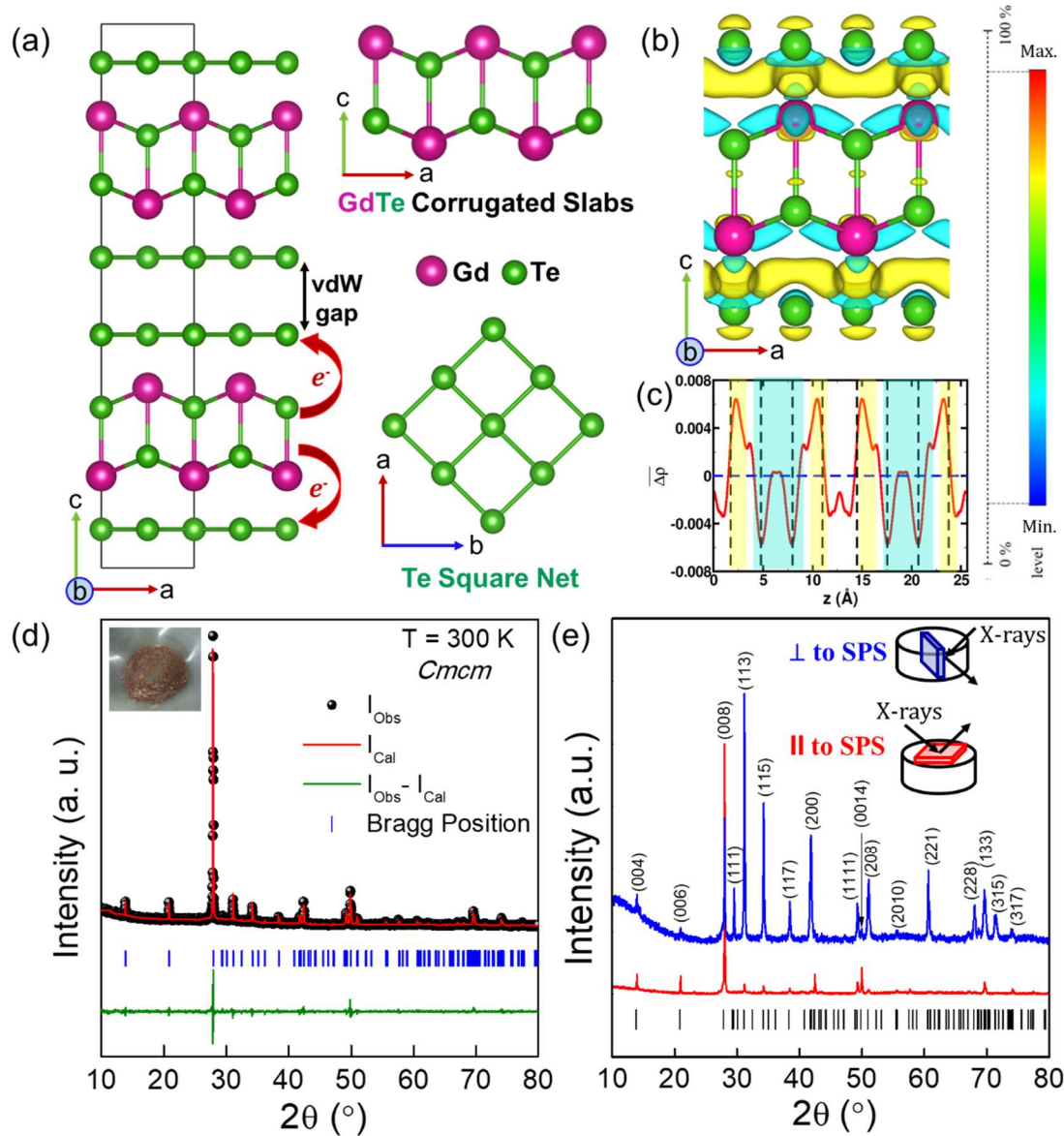


Figure 5.1. (a) The layered, undistorted structure of GdTe₃ where GdTe corrugated slabs and Te sheets are stacked along c-axis and held together by weak van der Waals interaction. The Te sheets are rotated at an angle of 45° with respect to GdTe slabs. Ionic [Gd³⁺Te²⁻]⁺ layers are sandwiched between double layers of Te sheets. (b) Difference in charge densities of GdTe₃ crystal and its building blocks of GdTe slab and Te sheets, and its (c) macroscopic average. The yellow regions (positive values in c) show regions of electronic charge accumulation and cyan regions (negative values in c) indicate charge depletion, showing an overall charge transfer from GdTe slab to the Te sheets. (d) Rietveld refinement of room-temperature PXR data of orthorhombic Cmc_m phase of GdTe₃. The metallic lustre of the powdered GdTe₃ sample is shown in inset of (d). (e) PXR patterns of SPS processed GdTe₃ along the parallel (||) and perpendicular (⊥) directions revealing the anisotropic nature of the sample. The direction of X-ray diffraction has been denoted by the schematic diagrams in inset.

Te-sheets (Figure 5.1a).^{42,57} The Gd-Te bonds of the corrugated slabs are covalent in nature while, the bonding environment of the Te-atoms in the square net is purely metallic. In the GdTe slab, the oxidation state of Gd is +3 and that of Te is -2 whereas, the average charge per Te atom in the square net is -0.5 which leads to the formation of charged domains of $[\text{GdTe}]^+[\text{Te}^{-0.5}]_2$ in crystal lattice of GdTe_3 . However, to achieve the charge neutrality of the system, one electron from the Gd atom of the GdTe slab is transferred to the Te square net sheets, *i.e.*, more precisely one electron is being shared equally by two Te atoms of the two adjacent square nets respectively. To derive insight into the charge transfer in GdTe_3 , we have obtained the difference in charge density between GdTe_3 crystal and its 2D building blocks by electron localization function (ELF) analysis:

$$\Delta\rho = \rho(\text{GdTe}_3) - [\rho(\text{GdTe}) + \rho(\text{Te})]$$

where $\rho(\text{GdTe}_3)$, $\rho(\text{GdTe})$ and $\rho(\text{Te})$ are the charge densities of GdTe_3 , GdTe slab and Te sheets respectively. Accumulation of electronic charge (marked by yellow) in Te sheets and charge depletion in GdTe slab (denoted by cyan region) show electrons transfer (Figure 5.1b). Macroscopic average of $\Delta\rho$ (Figure 5.1c) confirms the electronic charge transfer from Gd atoms in GdTe slab to the Te square net sheets which results in the GdTe slabs being insulating and the Te square-net sheets being conductive in nature. Due to these interesting structural features, GdTe_3 can be considered as a natural heterostructure of charged and vdW layers which can give rise to large degree of anharmonicity in the crystal lattice.

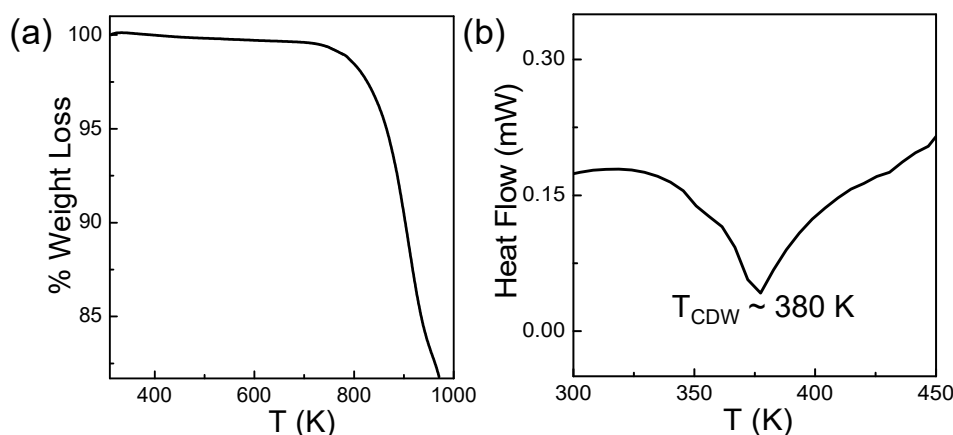


Figure 5.2. (a) Thermal gravimetric analysis (TGA) and (b) Differential scanning calorimetry (DSC) curves of GdTe_3 as a function of temperature.

Figure 5.1d shows the room temperature PXRD pattern of GdTe₃ along with the Rietveld refinement. The PXRD pattern can be indexed to the *Cmcm* orthorhombic phase of GdTe₃. The lattice parameters obtained from the fitting are $a = 4.3174 \text{ \AA}$, $b = 4.3240 \text{ \AA}$ and $c = 25.5635 \text{ \AA}$ which are in good agreement with previously reported data.⁴² Powdered polycrystalline GdTe₃ appears as golden brown in colour with metallic lustre (see the inset of Figure 5.1d). To check the thermal stability of GdTe₃, we have performed thermogravimetric analysis and the result indicates that the sample is stable up to 700 K (Figure 5.2a). We have also verified the CDW transition temperature in GdTe₃ ($T_{CDW} \sim 380 \text{ K}$) from differential scanning calorimetry measurements (Figure 5.2b).

Further to check the purity of the bulk polycrystals and confirm the magnetic behaviour of gadolinium, we have studied the magnetic properties of GdTe₃. Figure 5.3a shows the dc magnetization (M) as a function of temperature in presence of 1 kOe magnetic field (H). The $M(T)$ data indicates that during cooling the sample undergoes a paramagnetic (PM) to antiferromagnetic (AFM) transition at around 12.5 K and this transition temperature matches well with the previously reported single crystals data.^{42,57} A close inspection of $M(T)$ data reveals that there is an anomaly at around 7 K which may be attributed as a second AFM transition as suggested by previous report.⁴² Temperature-dependent heat capacity data recorded at zero magnetic field also confirms the presence of two type of transitions denoted by T_N (Néel temperature) and T_I as shown in Figure 5.3b. Above these transition temperatures, we have fitted the susceptibility ($\chi = M/H$) data by using Curie-Weiss law: $\chi = C/(T-\theta)$, where C and θ are Curie constant and Curie temperature respectively (Figure 5.3c). The θ is found to be negative with an absolute value of 14 K which indicates the presence of predominantly AFM interactions in the system. The obtained effective paramagnetic moment of $7.87 \mu_B/\text{Gd}$ agrees well with the theoretically calculated value of $7.94 \mu_B$ for free Gd³⁺ which indicates that the magnetic moments of $4f$ electrons are strongly localized below the Fermi level. It is important to mention here that we did not observe any anomalous nature in the $M(T)$ data near the CDW transition. This also indicates that $4f$ electrons of Gd³⁺ does not have any significant influence on the CDW ordering.⁵⁸ To shed more light on the magnetic state of the present sample, we have recorded $M(H)$ data at some selective temperatures (Figure 5.3d). Linear behaviour of $M(H)$ data at 50 and 300 K indicate the paramagnetic nature of the sample,

whereas the $M(H)$ curve measured at 2 K shows a change in slope at around 22.4 kOe which may be attributed as spin-flop transition.⁵⁹

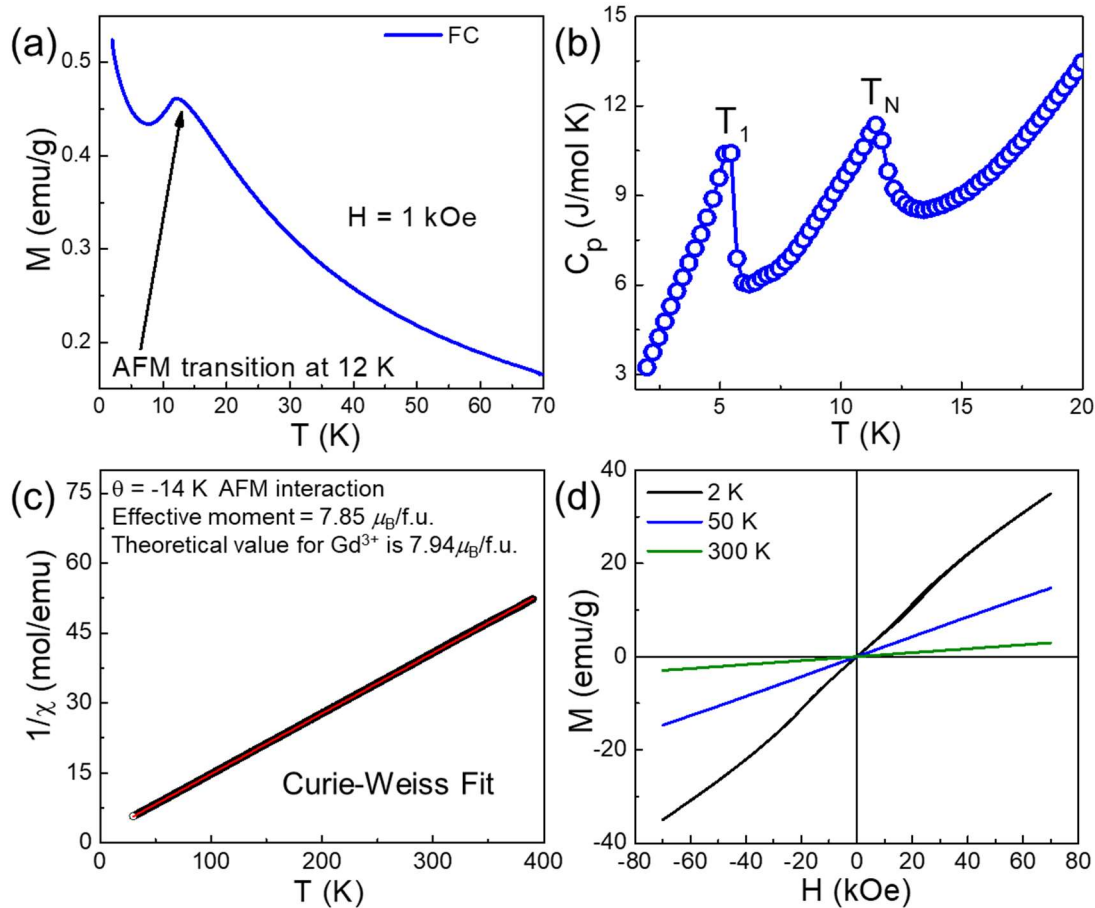


Figure 5.3. (a) The dc magnetization (M) curve as a function of temperature in the presence of 1 kOe magnetic field (H) measured in field cooling (FC) condition. (b) Temperature-dependent heat capacity of GdTe₃. T_N and T_1 correspond to the presence of two different antiferromagnetic transitions in GdTe₃. (c) Curie-Weiss fitting of the susceptibility ($\chi = M/H$) data confirming the presence of AFM interactions in the system. (d) M vs H curves at few selective temperatures.

In order to measure the thermoelectric properties of GdTe₃, we have performed SPS on the powdered polycrystals. Since GdTe₃ possesses a layered crystal structure, we have measured all the thermoelectric properties along two different directions, namely (i) parallel to the SPS pressing direction (\parallel), and (ii) perpendicular to the SPS pressing direction (\perp). To understand the anisotropic behaviour, we have recorded the room temperature PXRD patterns of GdTe₃ along parallel and perpendicular to the SPS

pressing direction (Figure 5.1e). Significant difference in the peak intensities of (008) and (113) planes are clearly observed from the PXRD patterns which suggests the presence of strong anisotropy even in the polycrystalline sample. Figure 5.4a shows the temperature dependence of electrical conductivity (σ) measured along both the directions in the temperature range 300 K to 673 K.

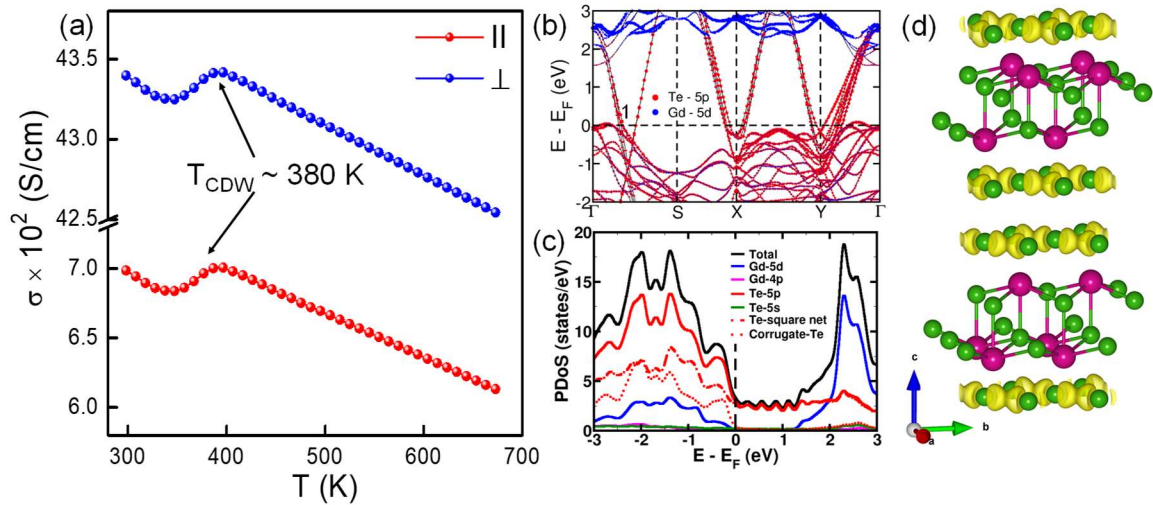


Figure 5.4. (a) Temperature dependent electrical conductivity of $GdTe_3$ measured along parallel and perpendicular to SPS pressing direction. The charge density wave transition temperature is marked by the black arrows. (b) Atom projected electronic structure of $GdTe_3$ calculated without the inclusion of SOC shows that it is a metal with linearly dispersive bands crossing E_F . (c) Projected density of states (PDOS) (without SOC) confirming that the states near E_F have the major contributions from 5p orbitals of Te atoms. (d) Visualization of wave functions of states along Γ -S with energy = E_F (marked as 1 in b) show significant contributions from p-orbitals of Te atoms of square nets.

The sample shows metallic behaviour with a characteristic feature of CDW transition at around 380 K. σ is found to be much higher in perpendicular direction compared to the parallel one. The strong anisotropy ($\sigma_{\perp}/\sigma_{\parallel} = 6.5$ at room temperature) is quite unusual in polycrystalline samples as crystallites generally get oriented randomly in a polycrystalline material. One important observation is that even in the CDW state $GdTe_3$ remains metallic in nature which is in sharp contrast to the other quasi-1D CDW materials like $(TaSe_4)_2I$ where the CDW state shows semiconducting/insulating behaviour.⁶⁰ Most of the cases, the formation of CDW state is governed by Fermi surface (FS) nesting phenomena (different sections of FS are matched by a wave vector \mathbf{q}), which helps to lower down the

electronic energy of the system by opening an energy gap in FS. In general, for quasi-1D CDW systems, the perfect nesting effect is observed which opens the gap at all parts of the FS, resulting in semiconducting/insulating state, whereas, for quasi-2D CDW materials like GdTe_3 , partial nesting condition is achieved which opens gap only at the nested regions keeping other parts gapless and as a result the CDW state tries to remain metallic in nature.⁵⁸

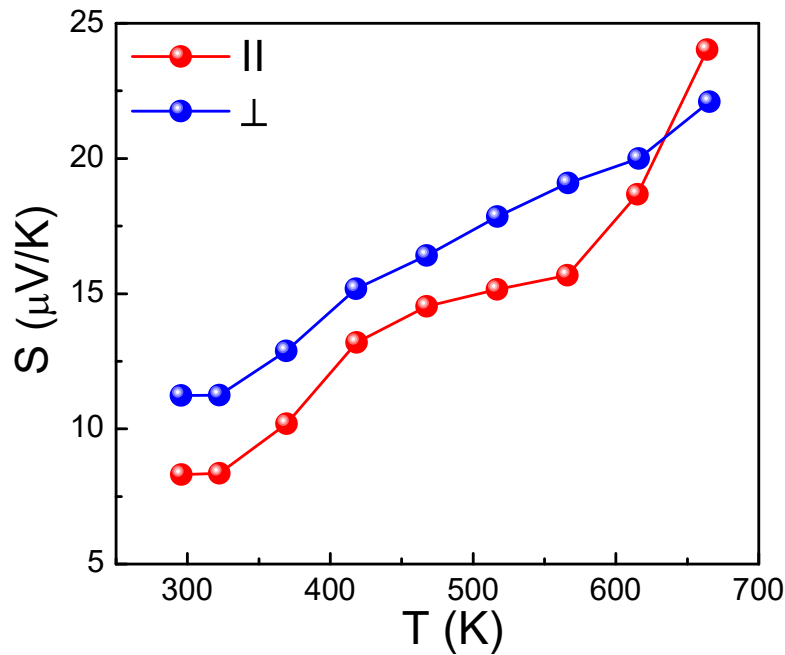


Figure 5.5. Temperature dependent Seebeck coefficient of GdTe_3 measured along parallel and perpendicular to SPS pressing direction.

To obtain deeper insights about the metallic behaviour of GdTe_3 , we have computed the electronic structure from the DFT calculations analysing the effects of spin-orbit coupling (SOC) through the use of relativistic pseudopotentials (Figure 5.4b). Undistorted GdTe_3 is metallic with linearly dispersed steep bands crossing Fermi energy (E_F). The linear bands describe electrons with large group velocity and small effective mass (m^*) giving rise to a high mobility. Inclusion of SOC leads to splitting of bands, but these effects are more pronounced on the states deeper in energy, away from E_F . Since changes in the behaviour of bands near E_F due to inclusion of SOC are small, we have not included SOC in further calculations. From projected density of states of GdTe_3 (calculated without SOC), it is evident that the valence bands (VB) have contributions primarily from Te $5p$

with weak component of Gd $4d$ states whereas the states in conduction bands (CB) comprise largely of d -orbitals of Gd (Figure 5.4c). Visualization of wave functions of the linear bands crossing E_F along Γ - S show significant contributions from p -orbitals of Te atoms belonging to layered Te planar sheets (Figure 5.4d).

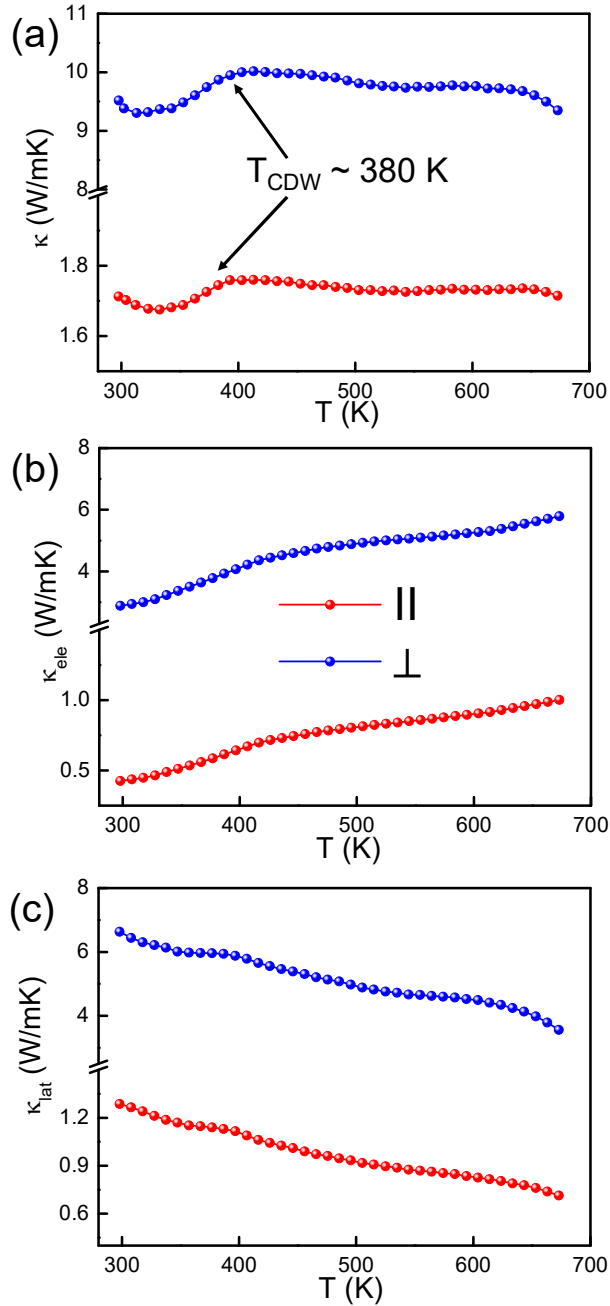


Figure 5.6. Temperature dependent (a) κ , (b) κ_{ele} , and (c) κ_{lat} of $GdTe_3$ measured along parallel and perpendicular to SPS pressing direction. The charge density wave transition temperature is marked by the black arrows in (a).

Since the Seebeck coefficient (S) is an important probe to understand the Fermi surface topology related phenomena like structural distortions and CDW ordering,^{61–64} we have measured S as function of T for GdTe₃ (Figure 5.5). Positive value of S indicates that hole is the majority carrier in the present system. The value of S is quite low (~ 7 $\mu\text{V/K}$ along parallel to the SPS pressing direction at room temperature) and it is found to increase with the increase of temperature suggesting the metallic nature of the sample. CDW transition is not so much clear in the $S(T)$ data as compared to the $\sigma(T)$. But a clear slope change is observed at around ~ 370 K which reflects the CDW transition. Unlike $\sigma(T)$ the anisotropic behaviour of $S(T)$ is quite weak.

Figure 5.6a depicts the temperature dependent thermal conductivity (κ) measured along both parallel and perpendicular to the SPS pressing directions. Clear anomaly observed at around 380 K matches well with the CDW transition temperature of GdTe₃. We have noticed a strongly anisotropic behaviour ($\kappa_{\perp}/\kappa_{\parallel} = 5.6$ at 300 K) in the thermal conductivity data which is very much unusual for polycrystalline materials. Even in single crystalline rare earth based CDW material, like LaPt₂Si₂ shows an anisotropy of around 3 at 300 K when κ is measured along [110] and [001] axis.⁶⁵ Though the present sample is metallic in nature, the thermal conductivity along parallel direction is found to be quite low (1.72 W m⁻¹ K⁻¹ at 300 K). To get further insights, we have calculated the individual contributions of electronic and lattice thermal conductivity of GdTe₃. κ_{ele} shows a significant drop at around CDW transition and this feature is quite identical with the total thermal conductivity (Figure 5.6b). Similar type of behaviour is also observed in other CDW materials like CuTe.⁶⁶ On the other hand, κ_{lat} along both the directions are found to decrease with the increase of temperature (Figure 5.6c). Lattice thermal conductivity along the parallel direction is significantly lower compared to the perpendicular direction due to the presence of vdW gap. At room temperature the κ_{lat} along parallel direction is 1.3 W m⁻¹ K⁻¹ which decreases to 0.7 W m⁻¹ K⁻¹ at 673 K. To understand the origin of such low κ_{lat} and its anisotropic behaviour, we have measured sound velocity along both the directions. Sound velocity plays an important role to determine the lattice thermal conductivity of a material. In general, lower the sound velocity lower would be the value of κ_{lat} . Both longitudinal and transverse sound velocities along parallel direction are significantly lower compared to the perpendicular direction (Table 5.1). The average

sound velocity is found to be 1130 m s^{-1} and 1688 m s^{-1} along parallel and perpendicular directions respectively.

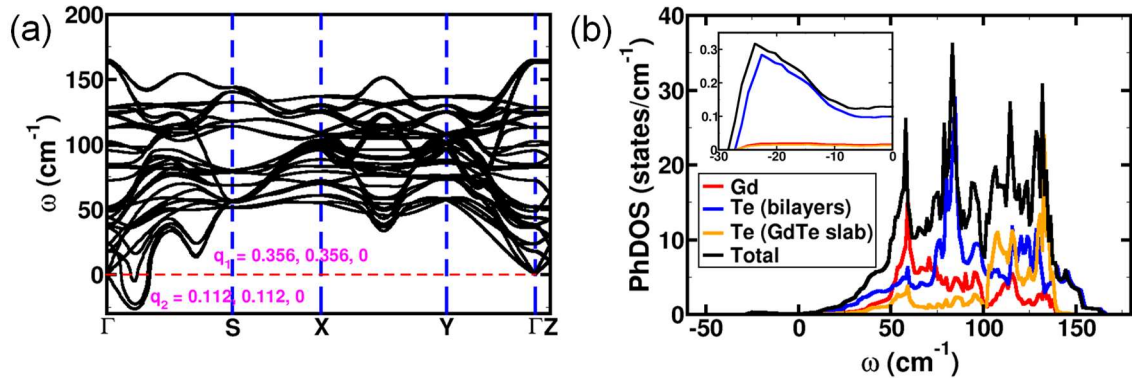


Figure 5.7. (a) Phonon dispersion of GdTe_3 along high symmetry points in BZ shows instability at wavevectors (\mathbf{q}_1 and \mathbf{q}_2) only along Γ - S direction. (b) Atom projected phonon density of states reveal that the unstable and low-frequency optical modes involve the vibrations of Te atoms from the square nets.

To comprehend the origin of such low lattice thermal conductivity, we have calculated the vibrational spectrum in GdTe_3 from DFT analysis. Our calculated phonon dispersion exhibits modes with imaginary frequencies ($\omega^2 < 0$) along Γ - S direction of the Brillouin zone and stable modes along all the other directions (Figure 5.7a). An interesting thing to note in the phonon spectrum is the softening of a phonon branch or Kohn anomaly again along Γ - S and renormalization of the acoustic phonon branch which is a characteristic of CDW or Peierls instability.³⁴ To get insight into the atomic contributions to phonons, we examine the atom-projected phonon density of states (PhDOS) (Figure 5.7b), which shows dominant contributions of Te bilayer to the modes with imaginary frequencies. It is clearly seen from PhDOS that there exist several low-frequency optical phonon branches below 50 cm^{-1} which have major contributions from the Te bilayers. The origin of this lattice instability can be traced to the Fermi surface which is quasi two-dimensional due to the existence of two different layered structural motifs (GdTe slab and Te square nets). Linearly dispersed bands crossing E_F , are principally constituted of Te p -orbitals of Te sheets resulting in a diamond-shaped FS (Figure 5.8a). The strong nesting and perturbation modulated with nesting wave vectors destabilize the structure driving it to lower energy, similar to Peierls instability, in GdTe_3 . The nesting wave vectors \mathbf{q}_1 and \mathbf{q}_2

along Γ - S direction correspond to the instability and Kohn anomaly, respectively in the phonon spectrum (Figure 5.7a). The nesting vector \mathbf{q}_2 can also be visualized in the band structure of GdTe₃ revealing the coupling between linearly dispersed bands (Figure 5.8b).

Table 5.1. Experimental sound velocities, minimum thermal conductivity (κ_{min}), Poisson ratio (ν_p) and Grüneisen parameters (γ) of GdTe₃.

Orientation	Longitudinal sound velocity (m s ⁻¹)	Transverse sound velocity (m s ⁻¹)	Average sound velocity (m s ⁻¹)	κ_{min} (Wm ⁻¹ K ⁻¹)	ν_p	γ
() to SPS pressing	2285	1000	1130	0.23	0.38	2.42
(⊥) to SPS pressing	2755	1514	1688	0.30	0.28	1.68

The unstable modes and Kohn anomaly involve the displacements of Te atoms arranged in square-net sheets (Figure 5.8c) constitutes the origin of CDW in GdTe₃. Thus, the lattice instability involving the Te bilayers is of ‘sliding nature’ and plays a significant role to reduce the lattice thermal conductivity of the sample. Distortion of the structure by freezing of eigen-displacements of unstable modes would lead to structure with lower energy, opening up a gap in band structure. However, with periodicity of $2\pi/q$, the structure will involve a supercell of $8 \times 8 \times 1$ making its simulation computationally expensive and hence it remains beyond the scope of the present study.

On the other hand, it is well-known that sound velocity (v) is directly related to the lattice thermal conductivity of a material by the relation: $\kappa_{lat} = \frac{1}{3} C_v v l$, where C_v is the heat capacity at constant volume and l is the phonon mean-free path.⁶⁷ Phonon dispersion of GdTe₃ also exhibits notably soft acoustic phonon modes with cut-off frequencies below $\sim 50 \text{ cm}^{-1}$ (Figure 5.7a) in all directions of the BZ, responsible for low speeds of sound. The average sound velocities determined from the slope of the linear region of acoustic phonon branches along in-plane (Γ - S) and out-of-plane (Γ - Z) are 2135

m s^{-1} and 1643 m s^{-1} respectively, consistent with experimental findings that κ_{lat} is lower along the parallel to the SPS pressing direction. Thermal conductivity of a solid is also affected by anharmonic interactions between phonons.⁶⁷ In GdTe_3 , interactions between the low-energy optical phonons and acoustic phonons are significant, causing strong scattering of heat carrier acoustic modes resulting in low κ_{lat} . To quantify the strength of this anharmonicity, we have determined the Grüneisen parameters (γ) from the changes

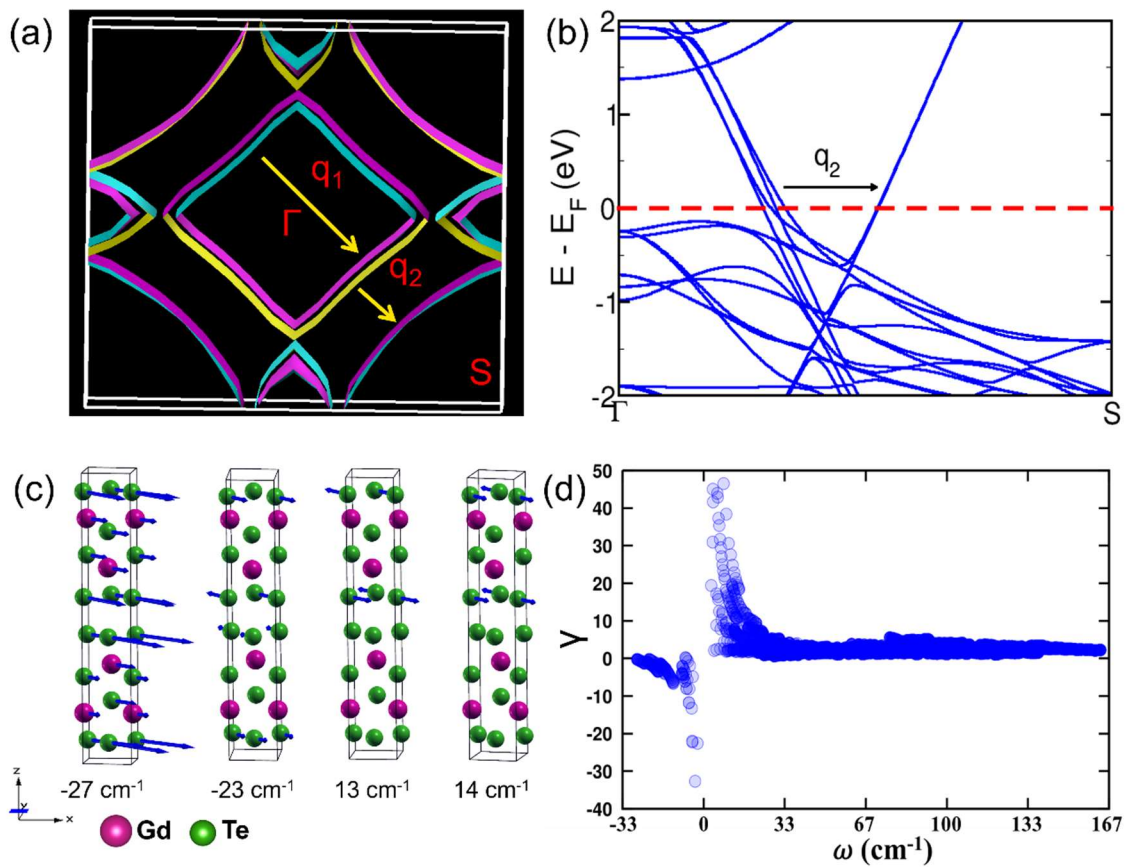


Figure 5.8. (a) The diamond-shaped Fermi surface (FS) exhibits nesting by wave vectors (\mathbf{q}_1 and \mathbf{q}_2) along Γ - S direction leading to Peierls-like instability in GdTe_3 . (b) The nesting vector \mathbf{q}_2 marked in band structure reveals the coupling between linearly dispersed bands. (c) Atomic displacements of unstable modes at \mathbf{q}_2 corresponding to (1) $27i \text{ cm}^{-1}$ and (2) $23i \text{ cm}^{-1}$ and Kohn anomaly at \mathbf{q}_1 with frequencies at (3) 13 cm^{-1} and (4) 14 cm^{-1} involve displacements of Te atoms in the planar sheets of Te. (d) Grüneisen parameters of phonons at \mathbf{q} vectors on a uniform mesh of k -points in reciprocal space as a function of frequency clearly show strong coupling between acoustic and low-frequency optical phonon modes. Anomalously high γ indicates strong lattice anharmonicity induced by lattice distortion in Te bilayer.

of phonon frequencies with strain, for the phonon branches along Γ - S direction which is associated with CDW instability and Kohn anomaly arising from modes localized in Te bilayers (Figure 5.8d). Acoustic phonons and low-energy optical phonons exhibit anomalously high γ ($\gg 1$) indicating strong phonon-phonon coupling in GdTe₃ which also corroborates with the estimated high average Grüneisen parameter from experimental sound velocities ($\gamma = 2.42$ along parallel to SPS pressing direction, Table 5.1). The phonon scattering rate is inversely proportional to phonon lifetime and increases with inverse square of γ , indicating that large contributors to low κ_{lat} in GdTe₃ are the anomalous CDW-related modes along Γ - S direction.

The occurrence of low-lying optical phonon modes is further verified by temperature dependent Raman spectroscopic analysis. Figure 5.9a represents the temperature dependent (3-340 K) Raman spectra of GdTe₃ in the range of 20-200 cm⁻¹, where ten Raman active modes were observed when irradiated with 633 nm laser. The positions and symmetry of all the Raman modes are provided in Table 5.2. Here, the ultra-low frequency Raman modes at ~ 58 cm⁻¹, and ~ 74 cm⁻¹ involve mainly the vibration of the Gd atoms (Figure 5.9c) and can be attributed to the collective amplitude mode (AMP) of the CDW state as they show strong temperature dependence.^{68,69} Whereas high intensity modes at ~ 88 cm⁻¹, and ~ 96 cm⁻¹ involve the vibration of the Te square net sheets and can be regarded as zone-folded (ZF) modes.^{68,69} In general, the amplitude mode corresponds to a soft-phonon coupled to the electronic density at the CDW wavevector q and dressed by the amplitude fluctuations of the CDW order parameter. The ZF mode corresponds to normal phonons folded to the zone centre of the Brillouin zone due to the establishment of the CDW state.⁷⁰ As the temperature increases, intensity of the modes ~ 58 cm⁻¹ and 74 cm⁻¹ vary in a reverse manner with each other. At 240 K both modes share the same spectral width and after 240 K a crossover was observed and then they merged into a broad mode ~ 38 cm⁻¹ at ~ 340 K which is quite comparable with the earlier literature.⁶⁹ Apart from the variation in intensity, there is significant softening and broadening of modes have also been observed. Variation of the phonon frequency with the temperature extracted from Lorentzian fit for the four low-frequency modes (AMP-1, AMP-2, ZF-1, and ZF-2) represented in Figure 5.9b.

Anomalous responses of the modes ~ 58 cm⁻¹ and 74 cm⁻¹ have been observed as T_{CDW}

~ 380 K is approaching that indicates the substantial electron-phonon coupling associated with the CDW.⁷¹ We have fitted the ω vs T data corresponding to the AMP-1 mode by using a modified mean-field model⁷⁰:

$$\omega(T) = \omega_{amp} \left[1 - \frac{x^4}{3} \right] (1 - x^4)^\beta$$

where, $x = \frac{T}{T_{CDW}}$, ω_{amp} is the CDW amplitude mode Raman shift at a low temperature limit, and β is a critical exponent. Considering T_{CDW} as 380 K, the fitting (indicated by red solid curve in Figure 5.9b) yields $\omega_{amp} = 58.7 \text{ cm}^{-1}$, and $\beta = 0.27$ that is well consistent with previous reports.⁶⁹

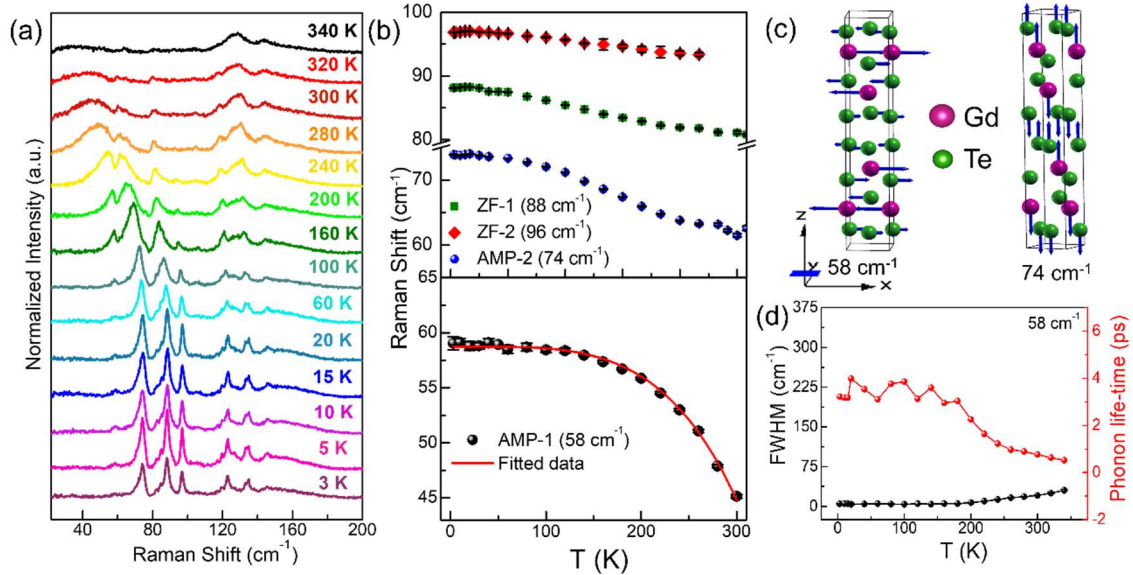


Figure 5.9. Temperature-dependence of (a) Raman spectra and (b) phonon frequencies of GdTe_3 . Here the amplitude modes (AMP-1, and AMP-2), and zone-folded modes (ZF-1, and ZF-2) correspond to the phonon frequencies of 58 cm^{-1} , 74 cm^{-1} , 88 cm^{-1} , and 96 cm^{-1} respectively. (c) Atomic displacements of optically active phonon modes at 58 cm^{-1} , and 74 cm^{-1} . (d) Temperature dependent FWHM and phonon lifetime of the AMP-1 at 58 cm^{-1} .

We have also calculated the electron-phonon coupling constant $\lambda = \frac{\omega_{amp}^2}{\omega_{2kF}^2}$, where ω_{2kF} ($= -27 \text{ cm}^{-1}$) was estimated from the phonon spectrum. The value of λ is estimated to be 4.7 which is higher than those reported in many other CDW systems⁷⁰ verifying the presence of strong electron-phonon coupling in of GdTe_3 .

Table 5.2. Comparison of the theoretically predicted and experimentally observed Raman modes at 3 K.

Raman modes (cm ⁻¹) (DFT calculations)	Symmetry	Raman modes (cm ⁻¹) (Experiment)
35.94	A _g	36
52.03	A _g	58
72.12	A _g	74
82.99	A _g	88
98.96	A _g	96
102.04	A _g	105
124.79	A _g	125
128.37	A _g	134
162.49	B _g	145
164.78	A _g	156

We have also estimated the temperature dependent phonon lifetime $\tau = 1/(2\pi \times FWHM)$ of the AMP-1 mode.²² Figure 5.9d represents the variation of *FWHM* and τ of the AMP-1 mode at 58 cm⁻¹ which has a direct correlation with lattice thermal conductivity. As T_{CDW} is approaching there is a significant decrement in the calculated value of τ . The value of τ at room temperature is found to be ~ 3 pico-seconds, which is quite less indicating the presence strong phonon scattering in GdTe₃. Thus, the presence of strong electron-phonon coupling, large anharmonicity, unstable acoustic and low-lying optical phonon modes and natural heterostructure of charged and vdW layers can be attributed to the experimentally observed low lattice thermal conductivity of GdTe₃ along parallel to the SPS pressing direction.

5.4. Conclusion

In conclusion, we have investigated the origin of low lattice thermal conductivity in GdTe₃, a charge density wave material. GdTe₃ possesses a quasi-2D layered structure where one corrugated GdTe slab is sandwiched between two Te square net sheets. From, first-principles theoretical calculations, it was verified that charge transfer take place from the GdTe slab to the adjacent Te sheets and there is a presence of van der Waals gap between the two neighbouring Te-sheets. Thus, the structure can be considered as a

natural heterostructure of charged and vdW layers. Interestingly, we have observed large anisotropy both in the electrical and thermal conductivity data of GdTe₃ when measured along parallel and perpendicular to the SPS pressing, which is quite unusual in polycrystalline materials. The undistorted phase of GdTe₃ is metallic in nature, with a strongly nested Fermi surface leading to instability and Kohn anomalies in phonon dispersion. The unstable phonon modes involve displacements of Te atoms in bilayers constituting the origin of CDW in GdTe₃. We establish a strong anharmonicity in terms of high Grüneisen parameters of the CDW-related phonon modes along Γ - S direction, which is responsible for suppressing acoustic phonons in transporting heat and causing low κ_{lat} of 0.7 W m⁻¹ K⁻¹ at 673 K in GdTe₃ when measured along parallel to SPS pressing direction. Further Raman spectroscopy reveals the existence of low-lying optical phonon modes which also effectively enhance the phonon scattering in the system. Thus, the presence of strong electron-phonon coupling, large anharmonic phonon modes and natural heterostructure of charged and vdW layers of GdTe₃ establish a rich chemistry between the bonding hierarchy and lattice dynamics which could be beneficial for several thermoelectric applications.

5.5. References

- (1) Ball, P. *Nature* **2012**, *492*, 174–176.
- (2) Tan, G.; Zhao, L.-D.; Kanatzidis, M. G. *Chem. Rev.* **2016**, *116*, 12123–12149.
- (3) Xiao, Y.; Zhao, L. D. *Science* **2020**, *367*, 1196–1197.
- (4) Roychowdhury, S.; Ghosh, T.; Arora, R.; Samanta, M.; Xie, L.; Singh, N. K.; Soni, A.; He, J.; Waghmare, U. V.; Biswas, K. *Science* **2021**, *371*, 722–727.
- (5) Zhao, L.-D.; Dravid, V. P.; Kanatzidis, M. G. *Energy Environ. Sci.* **2014**, *7*, 251–268.
- (6) Padture, N. P.; Gell, M.; Jordan, E. H. *Science* **2002**, *296*, 280–284.
- (7) Biswas, K.; He, J.; Blum, I. D.; Wu, C.-I.; Hogan, T. P.; Seidman, D. N.; Dravid, V. P.; Kanatzidis, M. G. *Nature* **2012**, *489*, 414–418.
- (8) Fu, L.; Yin, M.; Wu, D.; Li, W.; Feng, D.; Huang, L.; He, J. *Energy Environ. Sci.* **2017**, *10*, 2030–2040.
- (9) Poudel, B.; Hao, Q.; Ma, Y.; Lan, Y.; Minnich, A.; Yu, B.; Yan, X.; Wang, D.; Muto, A.; Vashaee, D.; Chen, X.; Liu, J.; Dresselhaus, M. S.; Chen, G.; Ren, Z. *Science* **2008**, *320*, 634–638.
- (10) Ma, J.; Delaire, O.; May, A. F.; Carlton, C. E.; McGuire, M. A.; VanBebber, L. H.; Abernathy, D. L.; Ehlers, G.; Hong, T.; Huq, A.; Tian, W.; Keppens, V. M.; Shao-Horn, Y.; Sales, B. C. *Nat. Nanotechnol.* **2013**, *8*, 445–451.
- (11) Chandra, S.; Biswas, K. *J. Am. Chem. Soc.* **2019**, *141*, 6141–6145.
- (12) Chandra, S.; Dutta, P.; Biswas, K. *ACS Nano* **2022**, *16*, 7–14.
- (13) Samanta, M.; Ghosh, T.; Chandra, S.; Biswas, K. *J. Mater. Chem. A* **2020**, *8*, 12226–12261.
- (14) Zhao, L.-D.; Lo, S.-H.; Zhang, Y.; Sun, H.; Tan, G.; Uher, C.; Wolverton, C.; Dravid, V. P.; Kanatzidis, M. G. *Nature* **2014**, *508*, 373–377.
- (15) Chang, C.; Wu, M.; He, D.; Pei, Y.; Wu, C.-F.; Wu, X.; Yu, H.; Zhu, F.; Wang, K.; Chen, Y.; Huang, L.; Li, J.-F.; He, J.; Zhao, L.-D. *Science* **2018**, *360*, 778–783.
- (16) Zhou, C.; Lee, Y. K.; Yu, Y.; Byun, S.; Luo, Z.; Lee, H.; Ge, B.; Lee, Y.-L.; Chen, X.; Lee, J. Y.; Cojocaru-Mirédin, O.; Chang, H.; Im, J.; Cho, S.; Wuttig, M.; Dravid, V. P.; Kanatzidis, M. G.; Chung, I. *Nat. Mater.* **2021**, *20*, 1378–1384.
- (17) Skoug, E. J.; Morelli, D. T. *Phys. Rev. Lett.* **2011**, *107*, 235901.

- (18) Nielsen, M. D.; Ozolins, V.; Heremans, J. P. *Energy Environ. Sci.* **2013**, *6*, 570–578.
- (19) Snyder, G. J.; Toberer, E. S. *Nat. Mater.* **2008**, *7*, 105–114.
- (20) Li, X.; Liu, P.-F.; Zhao, E.; Zhang, Z.; Guidi, T.; Le, M. D.; Avdeev, M.; Ikeda, K.; Otomo, T.; Kofu, M.; Nakajima, K.; Chen, J.; He, L.; Ren, Y.; Wang, X.-L.; Wang, B.-T.; Ren, Z.; Zhao, H.; Wang, F. *Nat. Commun.* **2020**, *11*, 942.
- (21) Dutta, M.; Pal, K.; Waghmare, U. V.; Biswas, K. *Chem. Sci.* **2019**, *10*, 4905–4913.
- (22) Acharyya, P.; Ghosh, T.; Pal, K.; Kundu, K.; Singh Rana, K.; Pandey, J.; Soni, A.; Waghmare, U. V.; Biswas, K. *J. Am. Chem. Soc.* **2020**, *142*, 15595–15603.
- (23) Lee, S.; Esfarjani, K.; Luo, T.; Zhou, J.; Tian, Z.; Chen, G. *Nat. Commun.* **2014**, *5*, 3525.
- (24) Sarkar, D.; Ghosh, T.; Roychowdhury, S.; Arora, R.; Sajan, S.; Sheet, G.; Waghmare, U. V.; Biswas, K. *J. Am. Chem. Soc.* **2020**, *142*, 12237–12244.
- (25) Banik, A.; Ghosh, T.; Arora, R.; Dutta, M.; Pandey, J.; Acharya, S.; Soni, A.; Waghmare, U. V.; Biswas, K. *Energy Environ. Sci.* **2019**, *12*, 589–595.
- (26) Dutta, M.; Samanta, M.; Ghosh, T.; Voneshen, D. J.; Biswas, K. *Angew. Chem. Int. Ed.* **2021**, *60*, 4259–4265.
- (27) Voneshen, D. J.; Refson, K.; Borissenko, E.; Krisch, M.; Bosak, A.; Piovano, A.; Cemal, E.; Enderle, M.; Gutmann, M. J.; Hoesch, M.; Roger, M.; Gannon, L.; Boothroyd, A. T.; Uthayakumar, S.; Porter, D. G.; Goff, J. P. *Nat. Mater.* **2013**, *12*, 1028–1032.
- (28) Jana, M. K.; Pal, K.; Warankar, A.; Mandal, P.; Waghmare, U. V.; Biswas, K. *J. Am. Chem. Soc.* **2017**, *139*, 4350–4353.
- (29) Liu, H.; Shi, X.; Xu, F.; Zhang, L.; Zhang, W.; Chen, L.; Li, Q.; Uher, C.; Day, T.; Snyder, G. J. *Nat. Mater.* **2012**, *11*, 422–425.
- (30) Li, B.; Wang, H.; Kawakita, Y.; Zhang, Q.; Feygenson, M.; Yu, H. L.; Wu, D.; Ohara, K.; Kikuchi, T.; Shibata, K.; Yamada, T.; Ning, X. K.; Chen, Y.; He, J. Q.; Vaknin, D.; Wu, R. Q.; Nakajima, K.; Kanatzidis, M. G. *Nat. Mater.* **2018**, *17*, 226–230.
- (31) Xu, Q.; Zhou, J.; Liu, T.-H.; Chen, G. *Appl. Phys. Lett.* **2019**, *115*, 023903.
- (32) Shi, X.; Pei, Y.; Snyder, G. J.; Chen, L. *Energy Environ. Sci.* **2011**, *4*, 4086.

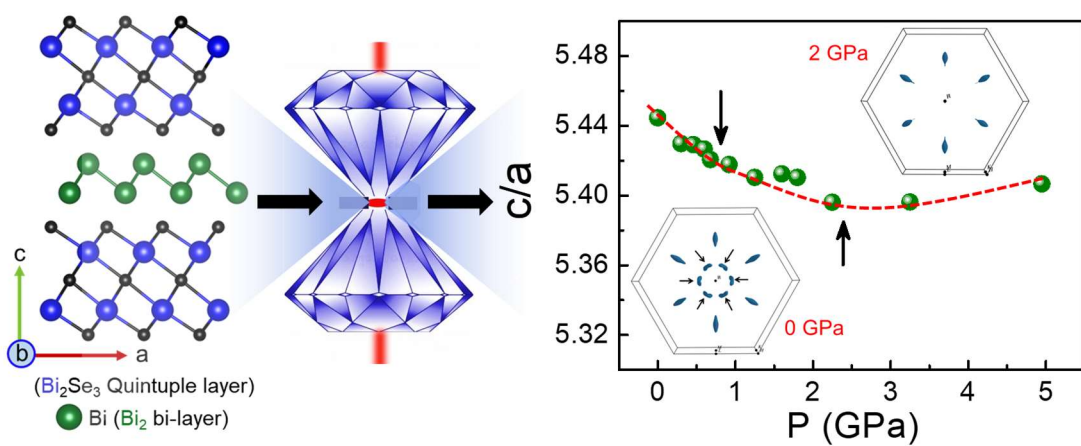
-
- (33) Liao, B.; Qiu, B.; Zhou, J.; Huberman, S.; Esfarjani, K.; Chen, G. *Phys. Rev. Lett.* **2015**, *114*, 115901.
- (34) Grüner, G. *Density Waves in Solids*; CRC Press, 1994.
- (35) Costescu, R. M.; Cahill, D. G.; Fabreguette, F. H.; Sechrist, Z. A.; George, S. M. *Science* **2004**, *303*, 989–990.
- (36) Malliakas, C.; Billinge, S. J. L.; Kim, H. J.; Kanatzidis, M. G. *J. Am. Chem. Soc.* **2005**, *127*, 6510–6511.
- (37) Ru, N.; Chu, J.-H.; Fisher, I. R. *Phys. Rev. B* **2008**, *78*, 012410.
- (38) Zocco, D. A.; Hamlin, J. J.; Grube, K.; Chu, J.-H.; Kuo, H.-H.; Fisher, I. R.; Maple, M. B. *Phys. Rev. B* **2015**, *91*, 205114.
- (39) Ru, N.; Condrón, C. L.; Margulis, G. Y.; Shin, K. Y.; Laverock, J.; Dugdale, S. B.; Toney, M. F.; Fisher, I. R. *Phys. Rev. B* **2008**, *77*, 035114.
- (40) Kogar, A.; Zong, A.; Dolgirev, P. E.; Shen, X.; Straquadine, J.; Bie, Y. Q.; Wang, X.; Rohwer, T.; Tung, I. C.; Yang, Y.; Li, R.; Yang, J.; Weathersby, S.; Park, S.; Kozina, M. E.; Sie, E. J.; Wen, H.; Jarillo-Herrero, P.; Fisher, I. R.; Wang, X.; Gedik, N. *Nat. Phys.* **2020**, *16*, 159–163.
- (41) Sacchetti, A.; Condrón, C. L.; Gvasaliya, S. N.; Pfuner, F.; Lavagnini, M.; Baldini, M.; Toney, M. F.; Merlini, M.; Hanfland, M.; Mesot, J.; Chu, J.-H.; Fisher, I. R.; Postorino, P.; Degiorgi, L. *Phys. Rev. B* **2009**, *79*, 201101.
- (42) Lei, S.; Lin, J.; Jia, Y.; Gray, M.; Topp, A.; Farahi, G.; Klemenz, S.; Gao, T.; Rodolakis, F.; McChesney, J. L.; Ast, C. R.; Yazdani, A.; Burch, K. S.; Wu, S.; Ong, N. P.; Schoop, L. M. *Sci. Adv.* **2020**, *6*, eaay6407.
- (43) Rodríguez-Carvajal, J. *Phys. B Condens. Matter* **1993**, *192*, 55–69.
- (44) Banik, A.; Shenoy, U. S.; Saha, S.; Waghmare, U. V.; Biswas, K. *J. Am. Chem. Soc.* **2016**, *138*, 13068–13075.
- (45) Sarkar, D.; Ghosh, T.; Banik, A.; Roychowdhury, S.; Sanyal, D.; Biswas, K. *Angew. Chem. Int. Ed.* **2020**, *59*, 11115–11122.
- (46) Perumal, S.; Roychowdhury, S.; Negi, D. S.; Datta, R.; Biswas, K. *Chem. Mater.* **2015**, *27*, 7171–7178.
- (47) Cahill, D. G.; Watson, S. K.; Pohl, R. O. *Phys. Rev. B* **1992**, *46*, 6131–6140.
- (48) Zhao, L.-D.; He, J.; Berardan, D.; Lin, Y.; Li, J.-F.; Nan, C.-W.; Dragoe, N. *Energy*

- Environ. Sci.* **2014**, *7*, 2900–2924.
- (49) Quantum-ESPRESSO is a community project for high-quality quantum-simulation software, based on density-functional theory, and coordinated by P. Giannozzi. See <https://www.quantum-espresso.org> and <http://www.pwscf.org>.
- (50) Hua, X.; Chen, X.; Goddard, W. A. *Phys. Rev. B* **1997**, *55*, 16103–16109.
- (51) Perdew, J. P.; Burke, K.; Ernzerhof, M. *Phys. Rev. Lett.* **1996**, *77*, 3865–3868.
- (52) Grimme, S. *J. Comput. Chem.* **2004**, *25*, 1463–1473.
- (53) Karsch, F.; Patkós, A.; Petreczky, P. *Rev. Mod. Phys.* **1997**, *401*, 69–73.
- (54) Togo, A.; Oba, F.; Tanaka, I. *Phys. Rev. B* **2008**, *78*, 134106.
- (55) Kresse, G.; Furthmüller, J. *Phys. Rev. B* **1996**, *54*, 11169–11186.
- (56) Kresse, G.; Furthmüller, J. *Comput. Mater. Sci.* **1996**, *6*, 15–50.
- (57) Liu, J. S.; Huan, S. C.; Liu, Z. H.; Liu, W. L.; Liu, Z. T.; Lu, X. L.; Huang, Z.; Jiang, Z. C.; Wang, X.; Yu, N.; Zou, Z. Q.; Guo, Y. F.; Shen, D. W. *Phys. Rev. Mater.* **2020**, *4*, 114005.
- (58) Wu, D.; Liu, Q. M.; Chen, S. L.; Zhong, G. Y.; Su, J.; Shi, L. Y.; Tong, L.; Xu, G.; Gao, P.; Wang, N. L. *Phys. Rev. Mater.* **2019**, *3*, 024002.
- (59) Iyeiri, Y.; Okumura, T.; Michioka, C.; Suzuki, K. *Phys. Rev. B* **2003**, *67*, 1444171–1444177.
- (60) Gooth, J.; Bradlyn, B.; Honnali, S.; Schindler, C.; Kumar, N.; Noky, J.; Qi, Y.; Shekhar, C.; Sun, Y.; Wang, Z.; Bernevig, B. A.; Felser, C. *Nature* **2019**, *575*, 315–319.
- (61) Kuo, C. N.; Hsu, C. J.; Tseng, C. W.; Chen, W. T.; Lin, S. Y.; Liu, W. Z.; Kuo, Y. K.; Lue, C. S. *Phys. Rev. B* **2020**, *101*, 155140.
- (62) Kim, J. H.; Rhyee, J.-S.; Kwon, Y. S. *Phys. Rev. B* **2012**, *86*, 235101.
- (63) Lue, C. S.; Kuo, Y.-K.; Hsu, F. H.; Li, H. H.; Yang, H. D.; Fodor, P. S.; Wenger, L. E. *Phys. Rev. B* **2002**, *66*, 033101.
- (64) Liu, Y.; Lei, H.; Wang, K.; Abeykoon, M.; Warren, J. B.; Bozin, E.; Petrovic, C. *Phys. Rev. B* **2018**, *98*, 094519.
- (65) Falkowski, M.; Doležal, P.; Andreev, A. V.; Duverger-Nédellec, E.; Havela, L. *Phys. Rev. B* **2019**, *100*, 064103.
- (66) Kuo, C. N.; Huang, R. Y.; Kuo, Y. K.; Lue, C. S. *Phys. Rev. B* **2020**, *102*, 155137.

-
- (67) Morelli, D. T.; Jovovic, V.; Heremans, J. P. *Phys. Rev. Lett.* **2008**, *101*, 035901.
- (68) Lavagnini, M.; Eiter, H.-M.; Tassini, L.; Muschler, B.; Hackl, R.; Monnier, R.; Chu, J.-H.; Fisher, I. R.; Degiorgi, L. *Phys. Rev. B* **2010**, *81*, 081101.
- (69) Chen, Y.; Wang, P.; Wu, M.; Ma, J.; Wen, S.; Wu, X.; Li, G.; Zhao, Y.; Wang, K.; Zhang, L.; Huang, L.; Li, W.; Huang, M. *Appl. Phys. Lett.* **2019**, *115*, 151905.
- (70) Wang, S.; Chen, X.; An, C.; Zhou, Y.; Zhang, M.; Zhou, Y.; Han, Y.; Yang, Z. *Appl. Phys. Lett.* **2022**, *120*, 151902.
- (71) Singh, N. K.; Rawat, D.; Dey, D.; Elsukova, A.; Persson, P. O. Å.; Eklund, P.; Taraphder, A.; Soni, A. *Phys. Rev. B* **2022**, *105*, 045134.

PART 6

Evidence of Pressure-induced Multiple Electronic Topological Transitions in Thermoelectric BiSe



Evidence of Pressure-induced Multiple Electronic Topological Transitions in Thermoelectric BiSe[†]

Summary

BiSe, an exciting member of homologous family $(\text{Bi}_2)_m(\text{Bi}_2\text{Se}_3)_n$ has recently gained enormous attention in thermoelectric research due to its intrinsically ultralow lattice thermal conductivity and promising n-type thermoelectric performance near room temperature. It is experimentally observed to be a weak topological insulator and possesses a fascinating crystal structure where Bi-bilayer is sandwiched between two Bi_2Se_3 quintuple layers and thus BiSe can be considered as a natural van der Waals heterostructure of Bi_2Se_3 - Bi_2 - Bi_2Se_3 . Herein, we have studied the pressure (P) induced electronic topological transition in BiSe through high pressure synchrotron X-ray diffraction, Raman spectroscopy and first-principles density functional theory calculations. We have observed clear anomalies at ~ 1 and ~ 2.2 GPa in the pressure dependent lattice parameters (a, c, and c/a ratio), cell volume, Raman mode shift and Raman mode linewidth data suggesting the onset of two electronic topological transitions (ETTs) in this system which is further verified by DFT calculations of electronic structure under pressure. The origin of these ETTs is associated with the two different vibrational modes arising from of Bi_2 bilayer and Bi_2Se_3 quintuple layers of BiSe. Detailed electronic band structure calculations also indicate that the emergence of multiple band extrema both in the valence and conduction bands near the vicinity of ETT can improve the thermopower and thermoelectric performance of BiSe.

[†]S. Chandra, P. Dutta, J. Sunil, K. Pal, M. Samanta, B. Joseph, C. Narayana, and K. Biswas, [2022](#). (Manuscript Under Preparation)

6.1. Introduction

Pressure (P), a fundamental thermodynamic variable, has been identified as a powerful tool to modify the crystal, electronic and magnetic structure of a material without introducing any impurities. For example pressure can induce insulator to metal transition,^{1,2} structural phase transition,³⁻⁵ superconductivity,⁶⁻⁸ and exchange bias effect⁹ in a system by tuning the chemical and physical properties. Recently, pressure-induced electronic topological transition (ETT) and topological quantum phase transition (TQPT) have gained enormous attention in thermoelectric research as it can lead to a significant enhancement in the power factor of a material.¹⁰⁻¹⁴

ETT, also known as Lifshitz transition is a second order isostructural phase transition where a drastic change in the topology of the Fermi surface (in the form of void formation or destruction, or/and disruption of Fermi surface neck) is observed when subjected to external perturbations such as hydrostatic pressure or chemical doping.¹⁵ During ETT band extremum in the electronic density of states (DOS) *i.e.*, van Hove singularity, crosses the Fermi level (E_F) resulting a strong redistribution of the density of states near E_F . This redistribution of the Fermi surface gives rise to anomaly in the electrical, mechanical, and vibrational properties of a material.¹⁶⁻²⁰ On the other hand, in TQPT, non-adiabatic band inversion happens at the time reversal invariant momenta points of the Brillouin zone and the topological invariant (Z_2) changes from 0 (conventional insulator) to 1 (topological insulator) at the transition points. TQPT can be obtained by tuning the spin-orbit coupling of a material via chemical doping or hydrostatic pressure.²¹⁻²³ For example, several inorganic materials such as TlBiS_2 ,²⁴ Sb_2Se_3 ,²⁵ BiTeI ,²³ and BiTeBr ²⁶ are found to exhibit hydrostatic pressure induced TQPT.

Since ETT is accompanied by redistribution of the DOS, it is expected to affect the transport properties of a material significantly.^{27,28} Among different transport phenomena, thermopower (S) is the most sensitive to the variation of Fermi surface, as according to the semiclassical Boltzmann theory, S is directly proportional to the energy derivative of the DOS near the Fermi energy.²⁹ Thus, it is obvious that the ETT can greatly influence the thermoelectric performance of a material. Few reports indicate that the pressure induced ETT has significantly enhanced the thermoelectric performance of some of the low dimensional systems where the competition between intra-layers covalent bonds and

inter-layers van der Waals forces plays a pivotal role.^{14,27,30–32} Recently, Nishimura *et al.* have studied the pressure dependent thermoelectric properties of a low dimensional compound SnSe where they have observed a pressure induced Lifshitz transition which leads to huge (>100%) enhancement in the thermoelectric power factor.¹³ Thus, it is pertinent to study the pressure induced ETT in exciting low-dimensional thermoelectric materials.

Among several low-dimensional systems, metal chalcogenides with general formula A_2B_3 ($A = \text{Bi, Sb}$ and $B = \text{Te, Se, S}$) are the most studied one due to their exceptional near-room temperature thermoelectric performance and various technological applications.^{33–37} Three narrow band gap (E_g) semiconductors with nominal composition Bi_2Te_3 ($E_g = 0.12$ eV), Bi_2Se_3 ($E_g = 0.30$ eV), and Sb_2Te_3 ($E_g = 0.28$ eV) of the A_2B_3 family are found to be three dimensional (3D) topological insulators which show insulating behaviour in the bulk but conducting nature at their surface.^{38–43} High-pressure studies on these above-mentioned semiconductors have increased tremendously in the last few years after the discovery of 3D topological insulators. At ambient conditions, these compounds exhibit layered tetradymite crystal structure (space group: $R\bar{3}m$) and with the application of pressure they undergo a series of structural phase transitions from rhombohedral to monoclinic to body-centered cubic.^{20,44,45} Some of them exhibit ETT and superconductivity under applied pressure.²⁷ Recently, Bai *et al.* have shown that the pressure induced ETT in $\text{Bi}_{0.5}\text{Sb}_{1.5}\text{Te}_3$ has enhanced the thermoelectric figure of merit (zT) up to 1.6 at room temperature under the application of 1.8 GPa pressure.⁴⁶ Motivated by these facts, we have purposefully chosen BiSe, an excellent n -type thermoelectric material with ultra-low lattice thermal conductivity⁴⁷ for the pressure dependent studies. At ambient conditions, BiSe, an exciting member of $(\text{Bi}_2\text{Se}_3)_m(\text{Bi}_2)_n$ homologous series, exhibits a two-dimensional trigonal crystal structure ($P\bar{3}m1$), where Bi-bilayer is sandwiched between two Bi_2Se_3 quintuple layers and it can be considered as a natural van der Waals heterostructure of Bi_2Se_3 -Bi₂- Bi_2Se_3 (Figure 6.1a).⁴⁷ Interestingly, BiSe has emerged as a weak topological insulator, whereas Bi_2Se_3 , a popular member of $(\text{Bi}_2\text{Se}_3)_m(\text{Bi}_2)_n$ series, is a well-established strong topological insulator.⁴⁸ Till date, several pressure dependent studies have been performed on Bi_2Se_3 and it has been proven to show ETT at ~ 5 GPa.^{20,49} However, we thought it would worthy to investigate pressure

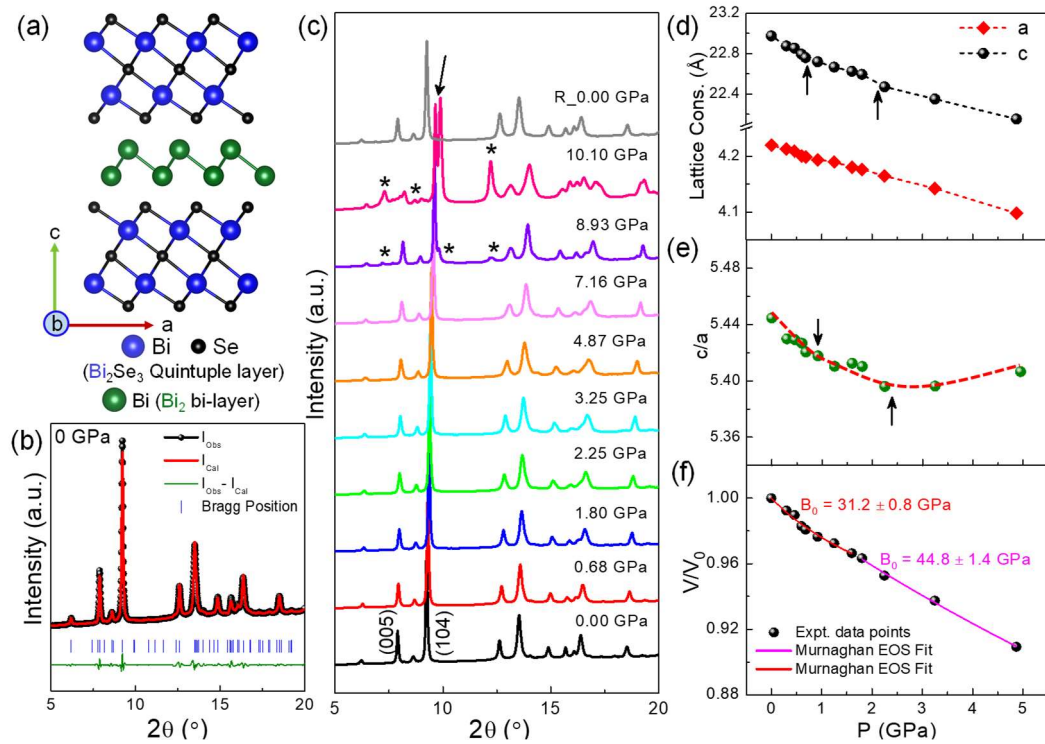


Figure 6.1. (a) Layered structure of BiSe viewed along b -axis. (b) Rietveld refinement of synchrotron PXR pattern of BiSe recorded at 0 GPa inside the diamond anvil cell. (c) Pressure dependence of the synchrotron XRD patterns ($\lambda = 0.4957 \text{ \AA}$) of BiSe at selected pressure values. The appearance of new Bragg's peaks is marked by asterisk (*) in the diffraction patterns of 8.93 and 10.10 GPa. "R" denotes released pressure. The arrow in the diffraction pattern of 10.10 GPa indicates the splitting of the (104) peak suggesting the onset of structural phase transition in BiSe. Pressure dependent (d) lattice constants, (e) c/a ratio, and (f) reduced volume ($\frac{V}{V_0}$). The dotted lines in (d) and (e) are guide to the eyes and black arrows denote the position of anomalies. The solid lines in (f) represents the Murnaghan EOS fit.

dependent studies on BiSe due to its unique crystal and electronic structure.

In this chapter, I have performed a detailed pressure (0 - 10 GPa) dependent studies on BiSe by *in-situ* synchrotron powder X-ray diffraction (PXR) and Raman spectroscopy. Ambient phase of BiSe (trigonal, $P\bar{3}m1$) is stable up to ~ 7 GPa. However, we have noticed anomalies in the pressure dependent crystal lattice parameter, volume, Raman mode shift and Raman mode line widths, which suggest the onset of multiple ETTs in BiSe. We have corroborated emergence of multiple Lifshitz transition from the pressure-induced change of Fermi surface topology near the vicinity of the ETT by the first-principles density functional theory (DFT). Additionally, electronic structure

calculation by DFT have demonstrated that BiSe undergoes a semiconductor to semimetal transition at ~ 6 GPa. We have also noticed that the emergence of multiple band extrema in the valence and conduction bands as a function of pressure which may tailor the thermopower and thermoelectric performance of BiSe.

6.2. Methods

Reagents. The high purity elements utilized for the synthesis are bismuth (Bi, SRL chemicals, 99.99%), and selenium (Se, Alfa Aesar 99.9999%).

Synthesis. Desired polycrystalline sample with nominal composition BiSe was prepared by mixing stoichiometric amounts of high purity Bi, and Se in a quartz ampule. The ampule was sealed under vacuum (10^{-5} Torr) and were slowly heated to 723 K and then to 1123 K over a time of 12 and 5 h, respectively. Then it was soaked for 6 h at 1123 K and cooled slowly to 893 K and was annealed for 6 h. Finally, it was cooled down to room temperature over 8 h. The obtained ingot was crushed into fine powder and used for high-pressure XRD and Raman experiments.

Pressure dependent synchrotron XRD. The *in-situ* high-pressure XRD measurements were performed at Xpress beamline of the Elettra synchrotron radiation facility, Trieste, Italy. The wavelength (λ) of the synchrotron radiation was ~ 0.4957 Å and the beam diameter was 40 μm . The MAR-345 imaging plate detector is used for the present experiment. Initially, the sample to detector distance was calibrated with a CeO₂ sample and found to be ~ 273.41 mm. Pressure was applied *in-situ* using a membrane diamond anvil cell (DAC) with diamonds having a culet size of 500 μm . The sample chamber for the pressure studies were prepared by pre-indenting a 200 μm thick steel gasket to about 80 μm and preparing a hole of diameter 160 μm in the middle. Pressed pellets of the sample occupied roughly 20 percent of the sample chamber volume, the rest being silicone oil as the pressure transmitting medium. One or more Ruby chips of diameter in the range of 5-20 μm were also included in the sample chamber for *in-situ* pressure monitoring using fluorescence measurements. Pressure was applied using an automatic membrane pressure drive. Pressure stability during diffraction measurements was ensured by several successive Ruby fluorescence measurements before the actual data collection

at various pressure points in addition to a fixed waiting time between the pressure points. Typical accumulation time for each collected synchrotron XRD pattern is 10 minutes. The collected two-dimensional (2D) diffraction image patterns were converted to one-dimensional (1D) patterns (intensity versus 2θ) using the fit2D software.⁵⁰ The Le Bail method fitting of the powder XRD patterns was performed using the FULLPROF software.^{51,52}

High pressure XRD experiments were performed in collaboration with Dr. Bobby Joseph, Elettra Sincrotrone, Trieste, Italy.

High-pressure Raman spectroscopy. Horiba, LabRAM HR Evolution spectrometer linked to the Labspec6 software was used for Raman measurements and data collection. In order to avoid surface oxidation and local heating of the material, we used the 785 nm solid state laser (with high penetration depth) with an optimized the power of at 6 mW on the sample. The spectra were gathered in back-scattering geometry (180°), with an accumulation time of around 300 s for each spectrum. With a grating of 1800 grooves per mm and an entry slit width of 200 μm , the spectral resolution is around 1 cm^{-1} . The *in-situ* high-pressure Raman scattering measurements were performed using a Mao–Bell type DAC with a culet size of 400 μm . Starting with a thickness of 250 μm , a completely hardened stainless steel (T301) gasket was pre-intended to a thickness of 100 μm . A 150 μm diameter hole was made in the center of the pre-intended region using a tungsten carbide drill bit to act as the sample chamber. The sample chamber was filled with a 4:1 combination of methanol and ethanol as the pressure transmitting medium (PTM). This liquid PTM holds the hydrostatic limit up to 10.5 GPa.⁵³ Along with the sample and the PTM, 5 to 10 μm Ruby spheres were loaded within the sample chamber. The Ruby fluorescence technique was used for *in-situ* pressure calibration.⁵⁴

Pressure dependent Raman experiments were performed in collaboration with Prof. Chandrabhas Narayana, JNCASR, India.

Computational details. All density functional theory (DFT) simulations are performed using the Vienna Ab-initio Simulation Package (VASP)^{55,56} utilizing the projector augmented-wave (PAW)^{57,58} potentials for Bi ($5d^{10} 6s^2 6p^3$), and Se ($4s^2 4p^4$). We used the PBEsol^{59,60} exchange-correlation functional in our calculations, which reproduces ($a = 4.196\text{ \AA}$, $c = 22.654\text{ \AA}$) the experimental lattice constants ($a = 4.179\text{ \AA}$, $c = 23.080\text{ \AA}$)

well at ambient conditions. The kinetic energy cut-off was set to 350 eV and a k-point mesh of $16 \times 16 \times 2$ was used for the full relaxation of the unit cell parameters at different hydrostatic pressures with a tight threshold for energy (10^{-8} eV) and force (10^{-3} eV/Å) convergence. The electronic structure and Fermi surfaces of BiSe were calculated at each pressure taking the optimized unit cells and with the inclusion of the spin-orbit coupling (SOC).⁶¹ For the calculations of Fermi surfaces, a relatively dense grid of k-points ($16 \times 16 \times 4$) was used spanning the entire Brillouin zone. We visualized the Fermi surfaces using the IFermi tool.⁶² We estimated the topological invariants of BiSe at each pressure using the topological quantum chemistry approach.⁶³ The phonon frequencies of BiSe were calculated at each pressure using Phonopy⁶⁴ code which uses a finite-displacement method to calculate the second-order harmonic interatomic force constants (IFCs). We used $2 \times 2 \times 1$ supercells (48 atoms) of the relaxed primitive unit cells containing 12 atoms for generating the displaced configurations and calculated the forces on the atoms using $4 \times 4 \times 4$ k-points. The SOC was not included in the phonon calculations.

Theoretical calculations were performed in collaboration with Dr. Koushik Pal, Northwestern University, United States.

6.3. Results and Discussions

At ambient condition, BiSe crystallizes in a layered trigonal structure with space group $P\bar{3}m1$. The Rietveld refinement of the powder XRD pattern of BiSe recorded at 0 GPa (when loaded in the DAC) has shown in Figure 6.1b. The obtained lattice parameters from the refinement ($a = 4.2198$ Å, $c = 22.9751$ Å, and $V = 354.30$ Å³) are in good agreement with the previous literature.^{47,48} Figure 6.1c represents the typical pressure dependent diffraction patterns of BiSe up to ~ 10 GPa (at few selected P points) which indicates that the trigonal phase of BiSe is stable up to ~ 7 GPa. However, upon further increasing the pressure, we have observed appearance of new Bragg's peak in the diffraction pattern (marked with asterisks in Figure 6.1c) suggesting the onset of structural phase transition in BiSe. At 10.10 GPa, we have noticed the splitting of the (104) peak which signifies the emergence of another structure at higher pressure regime. The pressure induced phase transition is fully reversible as after releasing the pressure (denoted by R_0 GPa), BiSe retains its initial structure (see the top diffraction pattern of

Figure 1c). Here, we have restricted our detailed investigation up to ~ 7 GPa to study the possible electronic topological transition in the trigonal ($P\bar{3}m1$) phase of BiSe.

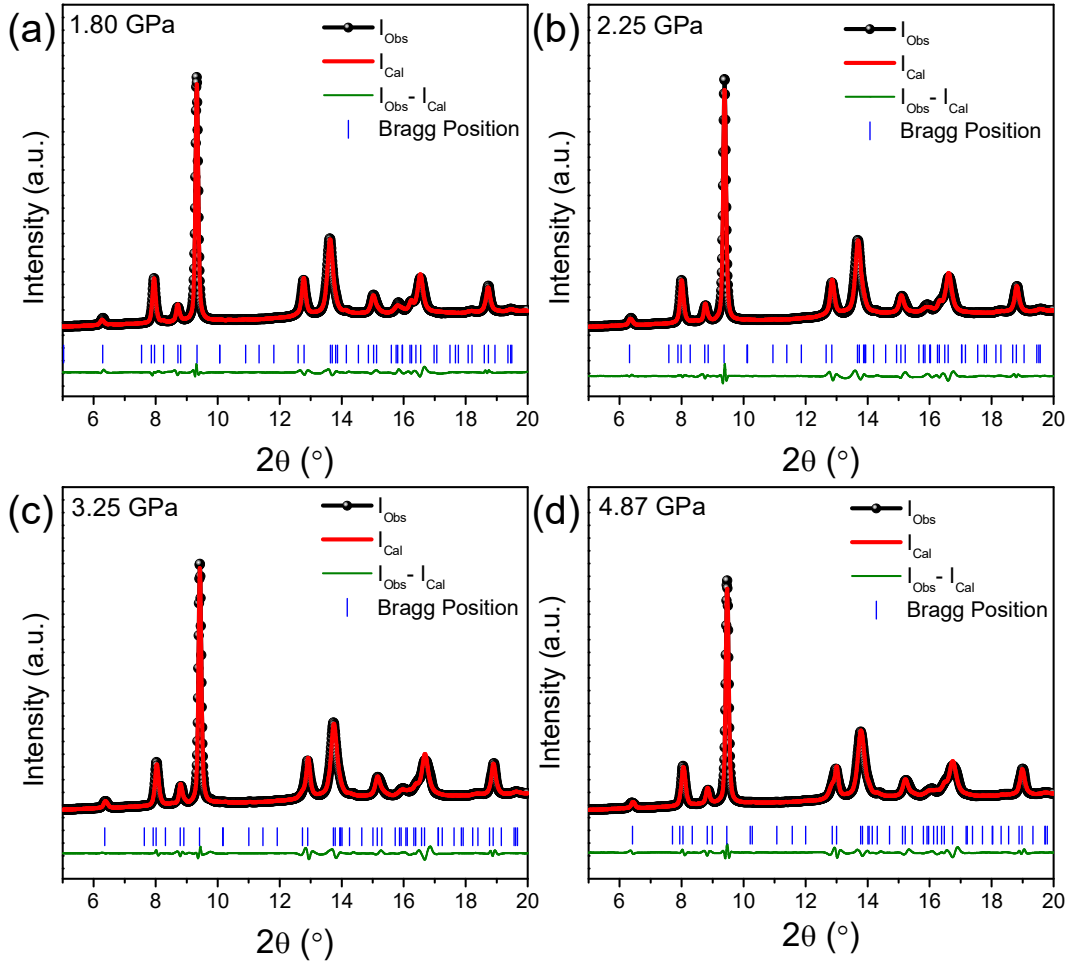


Figure 6.2. Le Bail fit to the synchrotron XRD patterns ($\lambda = 0.4957 \text{ \AA}$) of BiSe at (a) 1.80 GPa, (b) 2.25 GPa, (c) 3.25 GPa, and (d) 4.87 GPa.

Since pressure strongly affects the texture of the sample inside a DAC, we were unable to perform the complete Rietveld refinement of the measured XRD data accurately. Similar limitation has also been identified in several reports previously.^{24,65} Thus, we have only used the Le Bail method⁵² to fit the synchrotron XRD data collected up to 4.87 GPa and extracted the lattice constants and volume from the fitted data. The patterns were fitted with the trigonal crystal symmetry $P\bar{3}m1$ of BiSe. The refinements at few selected pressure points are shown in Figure 6.2. The change in lattice parameters (a & c) as a function of pressure is represented in Figure 6.1d. The pressure dependent trend of c -axis

is quite different from the a -axis. We have noticed two anomalies in the pressure dependent c parameter near ~ 0.9 and ~ 2.2 GPa (marked by black arrows in Figure 6.1d). At $P = 4.87$ GPa, the obtained lattice parameters are $a = 4.0976$ Å and $c = 22.1545$ Å which are shorter by $\sim 2.9\%$ and 3.6% respectively from the $P = 0$ GPa values indicating that c -axis is more compressible than a -axis. The pressure dependent c/a ratio is plotted in Figure 6.1e. The high value of the c/a ratio (5.4) at ambient pressure suggests the presence of strong anisotropy in the system as observed earlier in the electrical and thermal transport measurements.⁴⁷ Interestingly we have observed a parabolic behavior of the c/a vs. pressure graph with a minima at ~ 2.2 GPa. This anomaly in the c/a ratio indicates the existence of isostructural electronic transition in BiSe. Similar type of parabolic nature is also observed previously in Bi_2Se_3 and Bi_2Te_3 .^{49,66} This behavior is further supported by the DFT calculated pressure dependent lattice parameters (Figure 6.3).

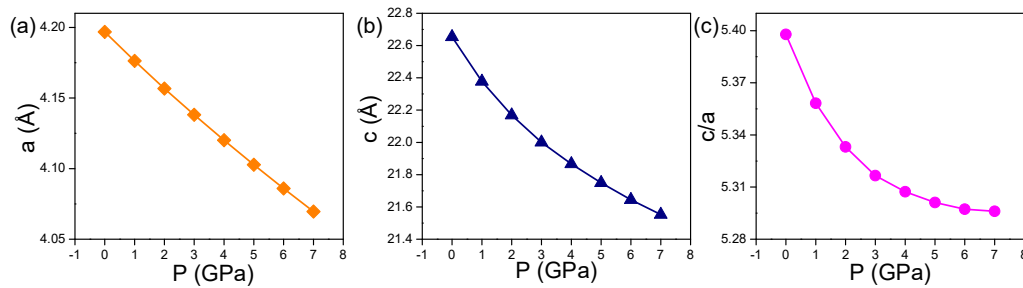


Figure 6.3. DFT calculated (a) a -axis length, (b) c -axis length, and (c) c/a ratio as a function of pressure.

To get further insights, we have plotted the unit cell volume (V) of BiSe as a function of pressure (Figure 6.4). We have not observed any significant discontinuity in the pressure dependent volume plot which confirms the absence of any first order structural transition up to 5 GPa. However, at higher pressure of 4.87 GPa, the unit cell volume compresses to $\sim 9\%$ as compared to its atmospheric value (at 0 GPa). We have used the following Murnaghan equation of state (EOS)⁶⁷ to fit the pressure dependent unit cell volume data:

$$\frac{V}{V_0} = \left[1 + \left(\frac{B'_0}{B_0} \right) P \right]^{-\frac{1}{B'_0}} \quad (1)$$

where V_0 , B_0 , and B'_0 are volume at 0 GPa, isothermal bulk modulus at ambient conditions

and first-order derivative of bulk modulus, respectively. First, we have fitted the reduced volume ($\frac{V}{V_0}$) in the pressure region 0 - 1.60 GPa by using equation (1) and obtained $B_0 = 31.2 \pm 0.8$ GPa and $B'_0 = 20.3 \pm 0.5$ GPa (Figure 6.1f). The fit in the pressure range 1.80 - 4.87 GPa yields B_0 , and B'_0 values of 44.8 ± 1.4 GPa and 2.8 ± 0.2 GPa. The fact that the pressure dependent change in the reduced volume ($\frac{V}{V_0}$) could not be fitted with a single Murnaghan EOS suggests the presence of an anomaly or isostructural transition ~ 2 GPa in BiSe. It also infers that the decrease of interatomic distances on the application of high pressure has significant impact on the electronic interactions between the adjacent atoms.¹²

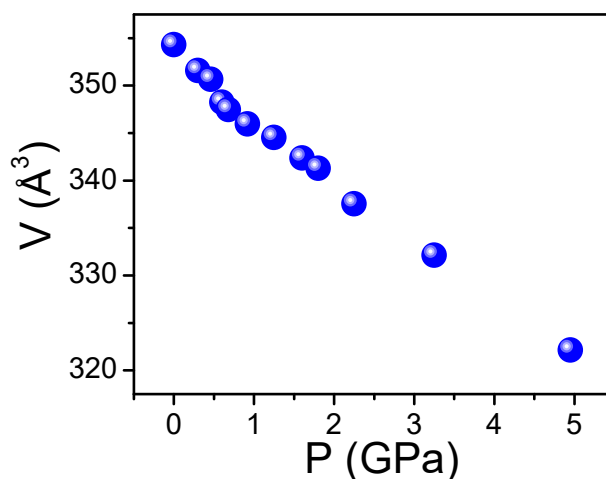


Figure 6.4. Pressure dependent change in volume as obtained from the refinement of the synchrotron PXRD patterns.

Moreover, the obtained value of the average bulk modulus ($B_0 = 38.2$ GPa) indicates that BiSe is relatively softer than the other tetradymite semiconductors like Bi_2Se_3 ($B_0 = 53$ GPa),⁴⁹ Bi_2Te_3 ($B_0 = 39.7$ GPa)⁶⁸, and Sb_2Te_3 ($B_0 = 54.7$ GPa).⁴⁵ Recent reports on Bi_2Se_3 ⁴⁹ and Bi_2Te_3 ^{27,66} suggests that the change in compressibility or bulk modulus without any discontinuity in volume and a pronounced slope change in c/a ratio experimentally verifies the presence of ETT in these systems. Our present results also show a slope change in c/a ratio and a significant change in the bulk modulus at ~ 2 GPa indicating the onset of ETT in BiSe. Relatively weak change of slope in c versus P data at around 0.9 GPa may suggest the presence of an additional ETT in the system.

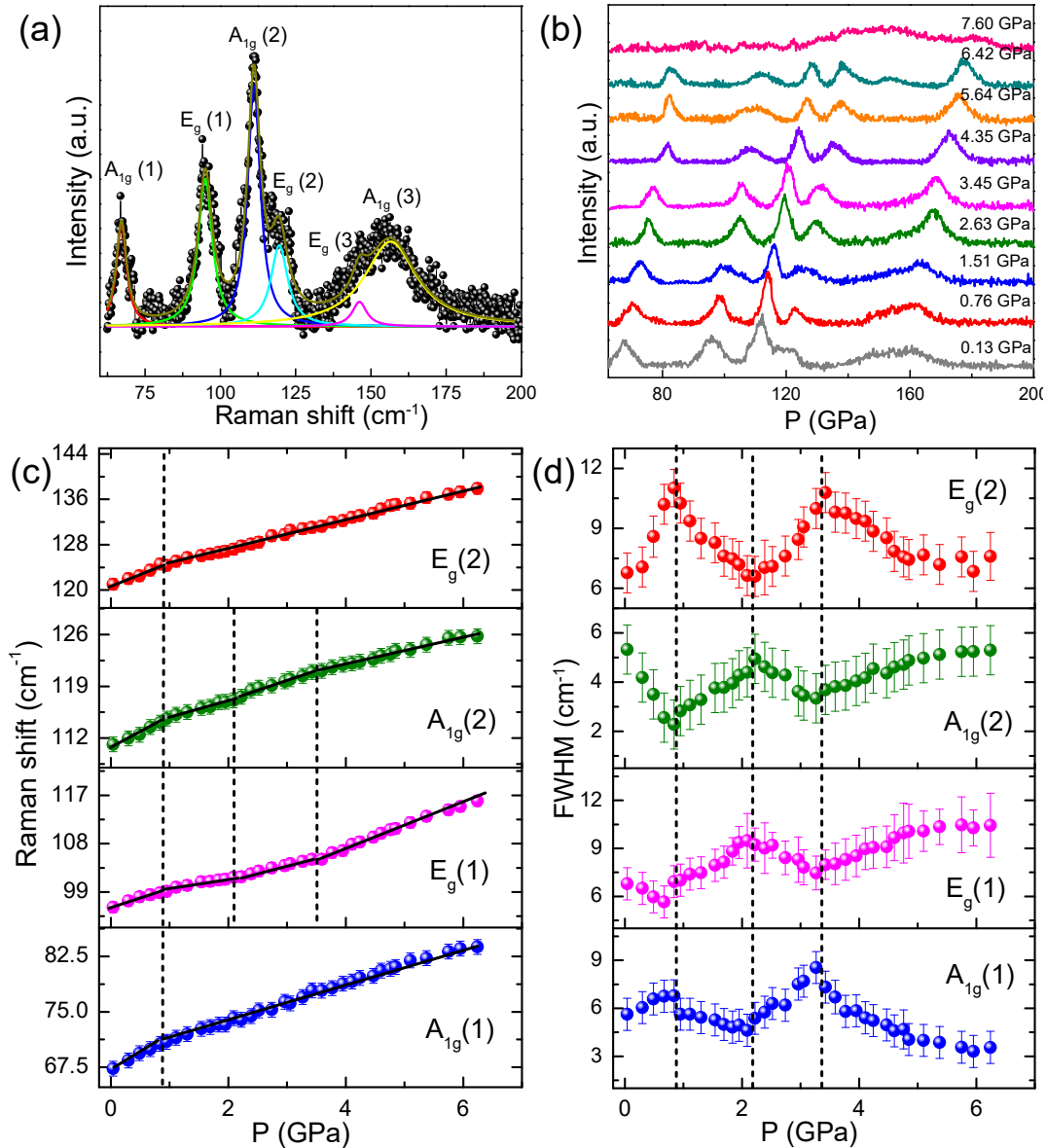


Figure 6.5. (a) Ambient Raman spectra of BiSe. (b) High-pressure evolution of Raman spectra of BiSe at selected pressure points. Pressure dependent (c) frequencies and (d) FWHM of various Raman modes. The black solid lines in (c) represent the linear fits to the observed frequencies. The black vertical lines indicate the isostructural transition pressures.

To address the above-mentioned anomalies in the pressure dependent XRD data, we have performed the high-pressure Raman scattering experiments up to 7.6 GPa. Raman spectroscopy is a sensitive method that can shed light on the structural, electronic, and topological changes in a system. At ambient conditions, the Raman spectrum of BiSe shows 6 Raman modes between 60 cm^{-1} and 200 cm^{-1} , as shown in Figure 6.5a. Factor

group analysis reveals the presence of twelve Raman active modes at the Γ point, including six A_{1g} modes and six E_g modes. Since, the experimental detection is limited by the signal-to-noise ratio of the used spectrometer, we could not be able to detect the other Raman active modes having lower scattering cross sections.⁶⁹ The observed Raman modes are assigned based on the DFT calculated phonon modes and tabulated Table 6.1.

Table 6.1. Comparison between the experimentally observed and theoretically calculated Raman frequencies. The origin of the corresponding Raman modes is also tabulated.

Raman mode	Calculated Peak Position (cm ⁻¹)	Experimental Peak Position (cm ⁻¹)	Origin of the Raman Mode
$A_{1g}(1)$	69.5	67.5	Bi ₂ Se ₃ layer out-of-plane vibration
$E_g(1)$	99.6	94.5	Bi ₂ -Se in-plane vibration
$A_{1g}(2)$	121.3	110	Bi ₂ layer out-of-plane vibration
$E_g(2)$	128.6	119.5	Se-Bi ₂ -Se in-plane vibration
$E_g(3)$	137.8	146	Se-Se in-plane vibration
$A_{1g}(3)$	150.3	155	Se-Se out-of-plane vibration

The corresponding Eigen mode visualizations are also provided in Figure 6.6. Figure 6.5b shows the pressure evolution of Raman spectrum till 7.6 GPa. With the initial increase in pressure, the intensity of most of the Raman modes shows a gradual reduction, except the $E_g(2)$ and $A_{1g}(3)$ modes. At around 7.6 GPa, we have observed a broad weak hump in the range of 130 – 170 cm⁻¹ which may suggest the onset of a structural transition in the material, further supported by the high-pressure synchrotron XRD studies.

To get more information about the lattice dynamics of the system under pressure, we have studied the Raman shift of various modes as a function of pressure. Due to the difficulty in precisely deconvoluting the broad peaks, the Raman shift and FWHM of the $A_{1g}(3)$ and $E_g(3)$ modes are not plotted. The Raman shift of the $A_{1g}(1)$, $A_{1g}(2)$, $E_g(1)$ and $E_g(2)$ modes plotted against pressure up to ~ 6.4 GPa is shown in Figure 6.5c. After 6.4 GPa, the peaks show very low intensity and hence it is difficult to deconvolute from the background. Generally, under hydrostatic compression, a systematic increase in Raman

frequency (hardening) is expected for a phonon mode. Here, all the plots show a gradual hardening of the modes, with a clear slope change around 0.8 GPa. However, $A_{1g}(2)$ mode and $E_g(1)$ mode corresponding to the out-of-plane and in-plane vibrations of the Bi_2 bilayer, respectively show two additional changes of slope ~ 2.2 GPa and ~ 3.5 GPa. The regions 0 - 0.8 GPa, 0.8 - 6.4 GPa are linearly fitted separately for $A_{1g}(1)$ and $E_g(2)$ modes to obtain the pressure coefficients, while for $A_{1g}(2)$ and $E_g(1)$ modes the linear fitting is further divided to four regions, 0 - 0.8 GPa, 0.8 - 2.2 GPa, 2.2 - 3.5 GPa, and 3.5 - 6.4 GPa. The pressure coefficients are listed in Table 6.2.

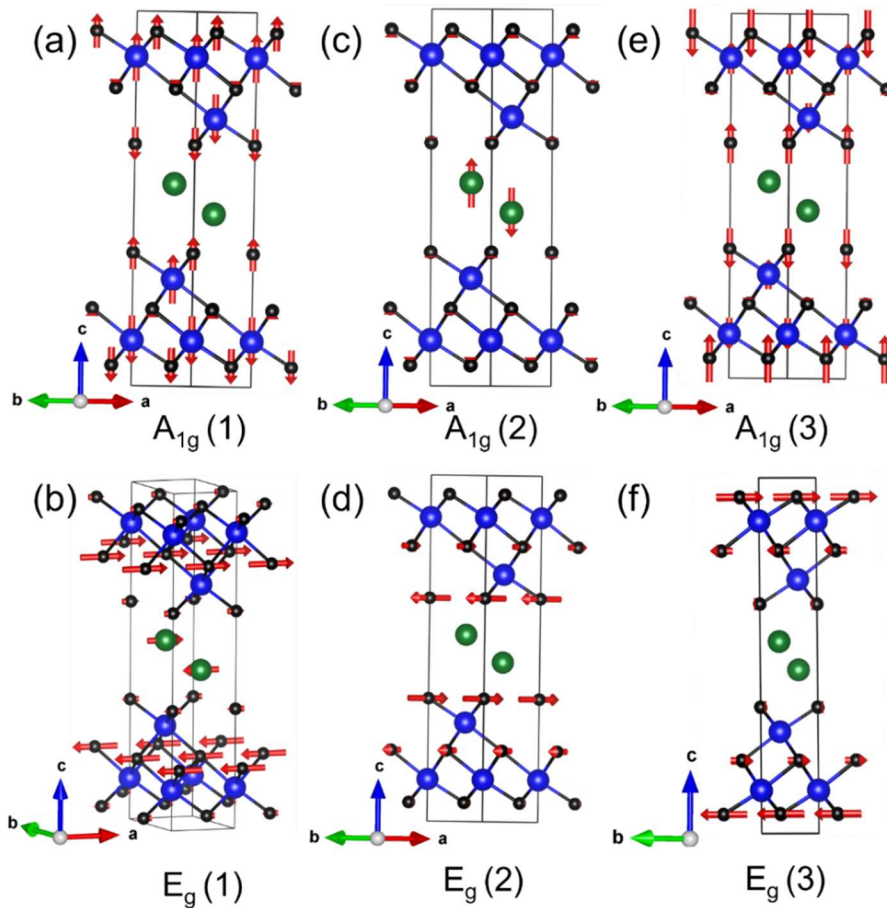


Figure 6.6. Eigenvector visualizations of Raman active modes at Γ point for $BiSe$. Green, blue, and black colors represent Bi of Bi_2 layer, Bi of Bi_2Se_3 layer, and Se atoms, respectively.

In general, for crystalline materials, Raman linewidth is inversely proportional to phonon lifetime. Thus, the linewidth of the Raman active phonon modes can reveal

essential information about the system's excitation-phonon interactions such as electron-phonon and spin-phonon coupling, in addition to phonon-phonon interactions.^{69,70} Here, to acquire a better understanding of the changes occurring in the system, the FWHM of various A_{1g} and E_g modes are plotted against pressure as shown in Figure 6.5d. According to the anharmonic approximation, a linear increase in FWHM with pressure is expected.⁷¹

Table 6.2. Pressure coefficients (a_1) of various Raman modes of BiSe. To obtain the pressure coefficients, the Raman shifts were fitted in various pressure ranges using the equation⁴⁹: $\omega(P) = \omega(P_0) + a_1(P - P_0)$, where $a_1 = \left(\frac{\partial\omega}{\partial P}\right)$.

Mode	Pressure Region	ω (P_0) (cm^{-1})	a_1 ($\text{cm}^{-1} \text{ GPa}^{-1}$)
A_{1g} (1)	0.0 - 0.8 GPa	67.18	4.20
A_{1g} (1)	0.8 - 6.4 GPa	68.57	2.563
E_g (1)	0.0 - 0.8 GPa	96.21	3.37
E_g (1)	0.8 - 2.2 GPa	97.53	2.01
E_g (1)	2.2 - 3.5 GPa	96.11	2.64
E_g (1)	3.5 - 6.4 GPa	91.04	4.09
A_{1g} (2)	0.0 - 0.8 GPa	110.89	3.71
A_{1g} (2)	0.8 - 2.2 GPa	112.64	2.19
A_{1g} (2)	2.2 - 3.5 GPa	112.44	2.44
A_{1g} (2)	3.5 - 6.4 GPa	114.06	1.96
E_g (2)	0.0 - 0.8 GPa	120.79	4.31
E_g (2)	0.8 - 6.4 GPa	122.04	2.61

However, FWHM for all the modes are showing deviation from this expected behavior with 3 anomalies, ~ 0.8 GPa, ~ 2.2 GPa and ~ 3.5 GPa. From Figure 6.5d, the $A_{1g}(1)$ mode shows the expected linear increase in FWHM from ambient pressure to 0.8 GPa. But after 0.8 GPa, the FWHM show a linear decrease between 0.8 to 2.2 GPa and linear increase between 2.2 GPa and 3.5 GPa. From 3.5 GPa, a non-linear decrease in FWHM is observed. The FWHM of $E_g(2)$ mode corresponding to the in-plane vibrations of the Bi_2Se_3 quintuple layers, also shows a similar behavior. On the other hand, the FWHM of

both $A_{1g}(2)$ and $E_g(1)$ modes associated with the Bi_2 bilayer show the opposite trends compared to Bi_2Se_3 layers between 0 GPa and 3.5 GPa. Contrary to normal behavior, FWHM starts to decrease with pressure up to 0.8 GPa. After 0.8 GPa, there is a linear increase in the FWHM up to 2.2 GPa followed by a linear decrease till 3.5 GPa. Above 3.5 GPa, the modes show a non-linear increase in FWHM with pressure. It is interesting to note that the modes originating from the vibrations in Bi_2 layer and the modes that are originated from the Bi_2Se_3 quintuple layer shows opposite behavior in their FWHM with respect to the pressure.

Munoz-Sanjose *et al.*, have studied the pressure induced ETT in topological insulators like Bi_2Se_3 , Bi_2Te_3 , and Sb_2Te_3 ,²⁰ where they observed the decrease in FWHM of the A_{1g} and E_g modes with pressure, however the Raman mode shifts exhibited linear hardening with little to no slope change around the transition pressure points. In the case of weak topological insulator $BiSe$, the decrease in the FWHM of modes associated with Bi_2 bilayers is observed from 0 to 0.8 GPa, whereas for Bi_2Se_3 quintuple layers the same behavior is noticed from 0.8 to 2.2 GPa. Thus, we can infer that the two anomalies at ~ 0.8 GPa and ~ 2.2 GPa indicates two ETTs in the system, mediated by Bi_2 layers and Bi_2Se_3 layers, respectively.

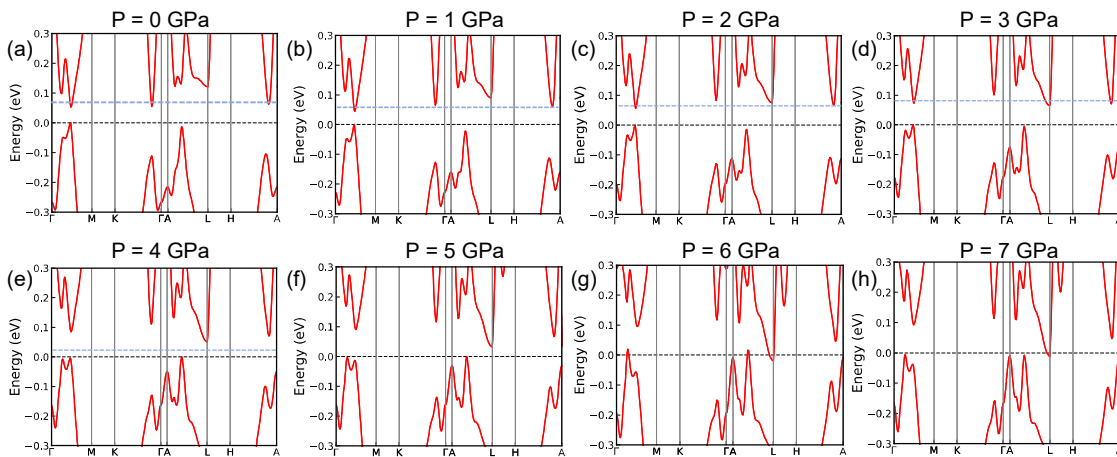


Figure 6.7. Spin-orbit coupled electronic structures of $BiSe$ at different pressures (0 - 7 GPa). The dashed lines at 0 eV denotes the Fermi level for the undoped system. The blue dashed line corresponds to the energy level 0.017 eV above the conduction band minimum (CBM) in each electronic structure. The Fermi surface has been visualized at this energy for the conduction band in Figure 6.8 in 0 - 4 GPa range.

To understand the origin of pressure dependent anomalies observed in the synchrotron XRD and Raman data, we have studied the electronic structures and band topology of BiSe as a function of hydrostatic pressure using the DFT calculations. The spin-orbit coupled electronic structures of BiSe are shown in Figure 6.7, which reveals intriguing changes as a function of pressure. At 0 GPa (*i.e.*, ambient conditions), BiSe is a semiconductor which has a band gap of 53 meV. The black dashed line which is set at the top of valence band maximum (VBM) appearing along the Γ -M line in Figure 6.7a denotes the Fermi level for the undoped compound. It is seen that a second maximum in the valence band appears along the A-L line just a few meV below the VBM in BiSe.

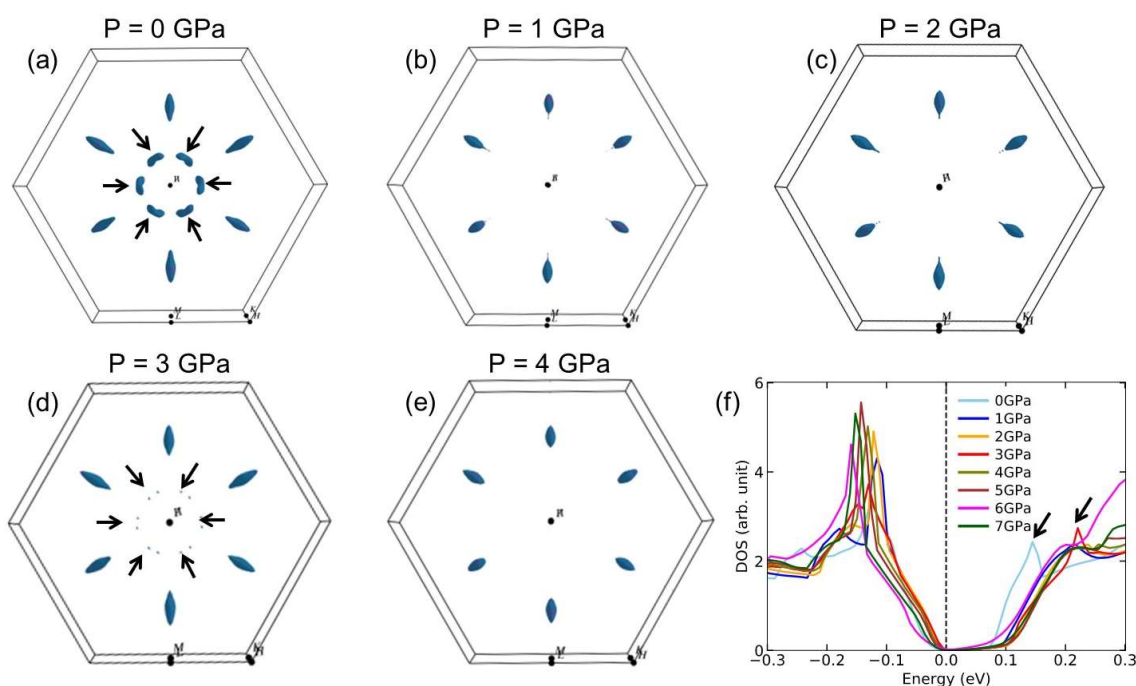


Figure 6.8. (a-e) Visualization of Fermi surfaces in the 0 - 4 GPa range. The Fermi surface has been visualized at 0.017 eV (blue dashed line in Figure 6.7) above the CBM in the conduction band. The arrows in (a) and (d) indicates the Fermi surface pockets that disappears from 0 to 1 GPa and reappears at 3 GPa again before disappearing at 4 GPa. (f) The total electronic density of states (DOS) of BiSe under pressure, which shows sharp peak appears at 1 GPa and 3 GPa, signifying the appearance of van Hove singularities (indicated by black arrows).

However, as the compound is intrinsically doped with electrons, the Fermi level rises and crosses the conduction bands, shown by the blue dashed line. The *n*-type carrier

concentration in BiSe sample is experimentally measured to be $3.2 \times 10^{19} \text{ cm}^{-3}$ at 0 GPa. Our DFT analysis suggests that this change in carriers in an undoped BiSe lead to a change in a Fermi level by 0.017 eV into the conduction band. Hence, we mark the Fermi level at 0.017 eV above the CBM in each pressure by a blue dashed line in Figure 6.7, assuming that the carrier concentration does not change significantly as a function of pressure. At this position of the Fermi level, three bands cross the Fermi level along Γ -M, K- Γ , and H-A directions in the Brillouin zone at 0 GPa. The conduction band minimum (CBM) appears along the Γ -M direction and the other two band extrema appearing along K- Γ , and H-A directions are nearly degenerate in energy with the CBM. These three degenerate bands signify the presence of band convergence in BiSe. The visualization of Fermi surfaces at this position of the Fermi level reveals the presence of electron pockets along Γ -M, K- Γ , and H-A directions in the hexagonal BZ shown in a top-down view in Figure 6.8a.

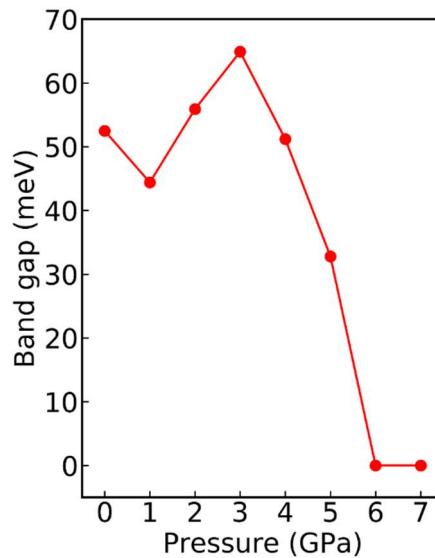


Figure 6.9. The band gap (with spin-orbit coupling) of BiSe as a function of hydrostatic pressure.

As we increase the hydrostatic pressure to 1 GPa, the band gap decreases to 44 meV with the CBM staying along the Γ -M direction. However, the two other peaks in the lowest conduction bands along the K- Γ and H-A directions go up in energy with respect to the CBM. Therefore, the Fermi level only crosses the CBM along the Γ -M direction.

As a result, the Fermi surface electron pockets that appeared along K- Γ , and H-A directions in the BZ at 0 GPa (marked with arrows in Figure 6.8a) disappears at 1 GPa (Figure 6.8b). The disappearance of the electron pockets marks the onset of first electronic topological transition or Lifshitz transition in BiSe. At 2 GPa, the band gap increases to 56 meV with no significant changes in the electronic structure and the CBM stays along the Γ -M direction. Consequently, the Fermi surface at 2 GPa remains qualitatively unchanged (Figure 6.8c). However, with further increase in pressure, the band gap increases to 65 meV up to 3 GPa, where the CBM changes its position and appears at L point. At this pressure, a new electron pocket appears (larger electron clouds in Figure 6.8d) at the L point that extends towards the Γ -L direction in the BZ. The smaller electron packets (indicated by arrows in Figure 6.8d) correspond to the crossing of the lowest conduction bands along the H-A direction. Thus, comparing Figure 6.8c and Figure 6.8d, it can be said that BiSe exhibits second ETT at 3 GPa. At 4 GPa, the CBM at L points further lowers its energy, reducing the band gap of BiSe to 51 meV. At the same time the Fermi level (blue dashed line) no longer crosses the lowest conduction band along the H-A direction, resulting in disappearance of the smaller electron pockets in Figure 6.8d. Thus, the appearance and disappearance of electron pockets at 1 and 3 GPa signifies the presence of multiple ETTs in BiSe which is affirmed by the sharp peaks (*i.e.*, van Hove singularities that are marked by black arrows in Figure 6.8f) in electronic density of states at those pressures. From Figure 6.7, it is also seen that pressure induces band convergence in the valence bands as well as in the conduction bands as we increase the pressure. The valence band extrema at A point increases its energy as a function of pressure and become nearly degenerate (within a few meV) with the band extrema appearing along Γ -M and A-L direction in the BZ, signifying band convergence that is concomitant with the emergence of ETTs in BiSe. Therefore, it is expected that the thermopower hence the thermoelectric performance can be further improved with the application of pressure for both the *n* and *p*-type dopants in BiSe.

The variation of the theoretically calculated band gap as a function of pressure shows that after 3 GPa the band gap starts to decrease drastically and eventually it becomes zero at 6 GPa, *i.e.*, BiSe becomes a semimetal at this pressure (Figure 6.9). In the Raman studies, we have observed a sharp drop in the intensity of all the Raman modes after 6.4

GPa (Figure 6.5b) which can be correlated with metallic state of BiSe. It is important to note that the drop of intensity of Raman modes owing to the decreased penetration depth during metallization is a well-known phenomenon. Metallization would increase the number of conduction electrons and screen the incident radiation, which would in turn reduce the scattering cross section.⁶⁵ Similar anomalies during semiconductor to metal transitions have been observed previously in the Raman studies of InTe,⁶⁵ and AgBiSe₂.⁷² The slight discrepancy of applied pressure between the experimental Raman studies and the theoretical calculations regarding the semiconductor to semimetal transition may arise from several aspects like temperature, the typical error in calculated lattice parameters and band gaps (depends on the pseudo-potential and exchange correlation functional), *etc.* Plenty of previous studies have also reported this type of mismatch between the experimentally obtained critical pressure values with the DFT studies which may primarily originate from different approximations considered during the theoretical calculations.^{23,72–75}

Table 6.3. Pressure dependent topological indices of BiSe.

P (GPa)	Topological Indices ($Z_{2w,3}$)
0	1
1	1
2	1
3	1
4	1
5	1
6	1
7	1

DFT calculations have also revealed the absence of band gap closing and re-opening as a function of hydrostatic pressure which excludes the band inversion phenomena in BiSe. This indicates that there is no pressure induced TQPT present in this system. To confirm this, we have calculated the topological invariants of BiSe using the ideas of topological quantum chemistry,⁶³ which reveals that between 0 and 7 GPa, the topological

indices remain unchanged to $Z_{2w,3} = 1$ (Table 6.3), which signifies its weak topological insulating phase.

6.4. Conclusion

In summary, the *in-situ* high pressure synchrotron XRD and Raman studies reveal that the trigonal ($P\bar{3}m1$) phase of BiSe is stable up to ~ 7 GPa. The anomalies at ~ 1 and ~ 2.2 GPa in the pressure dependent lattice parameters (a , c , and c/a ratio), cell volume, Raman shift and Raman linewidth data suggest the onset of multiple electronic topological transitions in this system which was further verified by first-principles DFT calculations of electronic structure under pressure. We have also observed a change in the Fermi surface topology and appearance of van Hove singularities near the vicinity of ETTs in BiSe. Our DFT calculations have also predicted that BiSe undergoes a semiconductor to semimetal transition at ~ 6 GPa. Moreover, we observe emergence of multiple band extrema both in the valence and conduction bands at high pressure condition which may enhance the thermopower and hence improve the thermoelectric performance of BiSe under pressure. The two ETT's in BiSe have different origins; the first transition is associated with the Bi_2 bilayer, whereas the second ETT is due to the presence of Bi_2Se_3 quintuple layers. Hence, the structural heterogeneity with natural van der Waals like heterostructure of BiSe plays a crucial role behind such novel observation. Our present study suggests that other heterostructure compounds (with different m and n values) of the homologous family $(\text{Bi}_2)_m(\text{Bi}_2\text{E}_3)_n$ [$\text{E} = \text{Se/Te}$] can also be explored in the context of pressure induced Lifshitz transition in near future, which have significant new scope.

6.5. References

- (1) Cai, W.; He, J.; Li, H.; Zhang, R.; Zhang, D.; Chung, D. Y.; Bhowmick, T.; Wolverton, C.; Kanatzidis, M. G.; Deemyad, S. *Nat. Commun.* **2021**, *12* 1509.
- (2) Devidas, T. R.; Chandra Shekar, N. V.; Sundar, C. S.; Chithaiah, P.; Sorb, Y. A.; Bhadram, V. S.; Chandrabhas, N.; Pal, K.; Waghmare, U. V.; Rao, C. N. R. *J. Phys. Condens. Matter* **2014**, *26*, 275502.
- (3) Biswas, K.; Muthu, D. V. S.; Sood, A. K.; Kruger, M. B.; Chen, B.; Rao, C. N. R. *J. Phys. Condens. Matter* **2007**, *19*, 436214.
- (4) Sarkar, D.; Roychowdhury, S.; Arora, R.; Ghosh, T.; Vasdev, A.; Joseph, B.; Sheet, G.; Waghmare, U. V.; Biswas, K. *Angew. Chem. Int. Ed.* **2021**, *60*, 10350–10358.
- (5) Liang, A.; Turnbull, R.; Popescu, C.; Manjón, F. J.; Bandiello, E.; Rodriguez-Hernandez, P.; Muñoz, A.; Yousef, I.; Hebboul, Z.; Errandonea, D. *Phys. Rev. B* **2022**, *105*, 054105.
- (6) Cai, W.; Lin, W.; Li, L.-H.; Malliakas, C. D.; Zhang, R.; Groesbeck, M.; Bao, J.-K.; Zhang, D.; Sterer, E.; Kanatzidis, M. G.; Deemyad, S. *J. Am. Chem. Soc.* **2019**, *141*, 15174–15182.
- (7) Cai, W.; Lin, W.; Yan, Y.; Hilleke, K. P.; Coles, J.; Bao, J. K.; Xu, J.; Zhang, D.; Chung, D. Y.; Kanatzidis, M. G.; Zurek, E.; Deemyad, S. *Chem. Mater.* **2020**, *32*, 6237–6246.
- (8) Hung, T. L.; Huang, C. H.; Deng, L. Z.; Ou, M. N.; Chen, Y. Y.; Wu, M. K.; Huyan, S. Y.; Chu, C. W.; Chen, P. J.; Lee, T. K. *Nat. Commun.* **2021**, *12*, 5436.
- (9) Dutta, P.; Pramanick, S.; Das, D.; Chatterjee, S. *J. Phys. D. Appl. Phys.* **2016**, *49*, 385001.
- (10) Chen, L. C.; Chen, P. Q.; Li, W. J.; Zhang, Q.; Struzhkin, V. V.; Goncharov, A. F.; Ren, Z.; Chen, X. J. *Nat. Mater.* **2019**, *18*, 1321–1326.
- (11) Shchennikov, V. V.; Ovsyannikov, S. V.; Derevskov, A. Y. *Phys. Solid State* **2002**, *44*, 1845–1849.
- (12) Yu, H.; Chen, L. C.; Pang, H. J.; Qin, X. Y.; Qiu, P. F.; Shi, X.; Chen, L. D.; Chen, X. J. *Mater. Today Phys.* **2018**, *5*, 1–6.
- (13) Nishimura, T.; Sakai, H.; Mori, H.; Akiba, K.; Usui, H.; Ochi, M.; Kuroki, K.;

- Miyake, A.; Tokunaga, M.; Uwatoko, Y.; Katayama, K.; Murakawa, H.; Hanasaki, N. *Phys. Rev. Lett.* **2019**, *122*, 226601.
- (14) Polvani, D. A.; Meng, J. F.; Chandra Shekar, N. V.; Sharp, J.; Badding, J. V. *Chem. Mater.* **2001**, *13*, 2068–2071.
- (15) Lifshitz, I. M. *Sov. Phys. JETP.* **1960**, *11*, 1130–1135.
- (16) Gupta, S. N.; Singh, A.; Pal, K.; Muthu, D. V. S.; Shekhar, C.; Elghazali, M. A.; Naumov, P. G.; Medvedev, S. A.; Felser, C.; Waghmare, U. V.; Sood, A. K. *J. Phys. Condens. Matter* **2018**, *30*, 185401.
- (17) Gupta, S. N.; Singh, A.; Pal, K.; Chakraborti, B.; Muthu, D. V. S.; Waghmare, U. V.; Sood, A. K. *Phys. Rev. B* **2017**, *96*, 094104.
- (18) Bera, A.; Pal, K.; Muthu, D. V. S.; Waghmare, U. V.; Sood, A. K. *J. Phys. Condens. Matter* **2016**, *28*, 105401.
- (19) Sorb, Y. A.; Rajaji, V.; Malavi, P. S.; Subbarao, U.; Halappa, P.; Peter, S. C.; Karmakar, S.; Narayana, C. *J. Phys. Condens. Matter* **2016**, *28*, 015602.
- (20) Manjón, F. J.; Vilaplana, R.; Gomis, O.; Pérez-González, E.; Santamaría-Pérez, D.; Marín-Borrás, V.; Segura, A.; González, J.; Rodríguez-Hernández, P.; Muñoz, A.; Drasar, C.; Kucek, V.; Muñoz-Sanjosé, V. *Phys. Status Solidi B* **2013**, *250*, 669–676.
- (21) Xu, S.-Y.; Xia, Y.; Wray, L. A.; Jia, S.; Meier, F.; Dil, J. H.; Osterwalder, J.; Slomski, B.; Bansil, A.; Lin, H.; Cava, R. J.; Hasan, M. Z. *Science* **2011**, *332*, 560–564.
- (22) Yan, C.; Liu, J.; Zang, Y.; Wang, J.; Wang, Z.; Wang, P.; Zhang, Z.-D.; Wang, L.; Ma, X.; Ji, S.; He, K.; Fu, L.; Duan, W.; Xue, Q.-K.; Chen, X. *Phys. Rev. Lett.* **2014**, *112*, 186801.
- (23) Xi, X.; Ma, C.; Liu, Z.; Chen, Z.; Ku, W.; Berger, H.; Martin, C.; Tanner, D. B.; Carr, G. L. *Phys. Rev. Lett.* **2013**, *111*, 155701.
- (24) Rajaji, V.; Arora, R.; Sarma, S. C.; Joseph, B.; Peter, S. C.; Waghmare, U. V.; Narayana, C. *Phys. Rev. B* **2019**, *99*, 184109.
- (25) Li, W.; Wei, X. Y.; Zhu, J. X.; Ting, C. S.; Chen, Y. *Phys. Rev. B* **2014**, *89*, 035101.
- (26) Ohmura, A.; Higuchi, Y.; Ochiai, T.; Kanou, M.; Ishikawa, F.; Nakano, S.; Nakayama, A.; Yamada, Y.; Sasagawa, T. *Phys. Rev. B* **2017**, *95*, 125203.

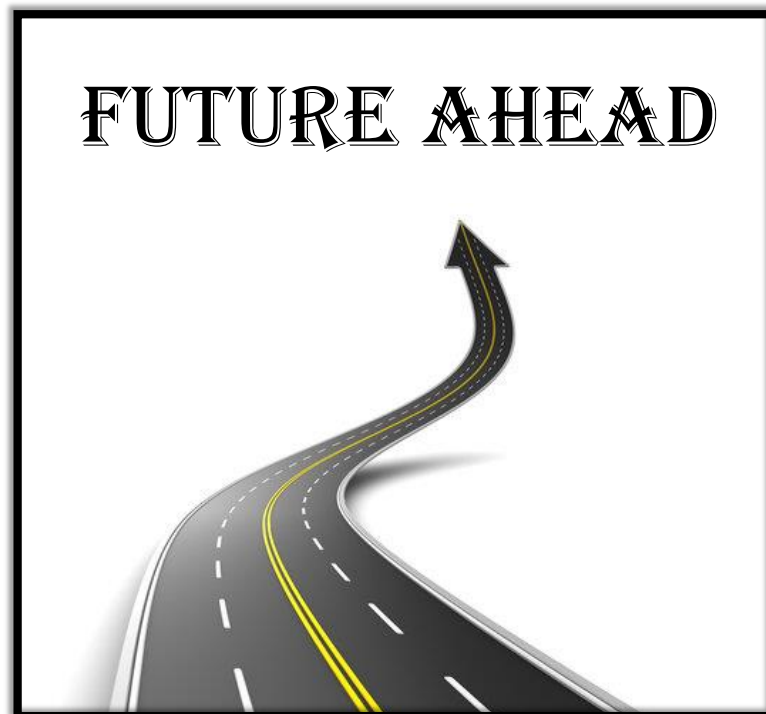
- (27) Polian, A.; Gauthier, M.; Souza, S. M.; Trichês, D. M.; Cardoso de Lima, J.; Grandi, T. A. *Phys. Rev. B* **2011**, *83*, 113106.
- (28) Barber, M. E.; Gibbs, A. S.; Maeno, Y.; Mackenzie, A. P.; Hicks, C. W. *Phys. Rev. Lett.* **2018**, *120*, 076602.
- (29) Barnard, R. D. *Thermoelectricity in Metals and Alloys*; Taylor & Francis, 1972.
- (30) Ovsyannikov, S. V.; Morozova, N. V.; Korobeinikov, I. V.; Lukyanova, L. N.; Manakov, A. Y.; Likhacheva, A. Y.; Ancharov, A. I.; Vokhmyanin, A. P.; Berger, I. F.; Usov, O. A.; Kutasov, V. A.; Kulbachinskii, V. A.; Okada, T.; Shchennikov, V. V. *Appl. Phys. Lett.* **2015**, *106*, 143901.
- (31) Ovsyannikov, S. V.; Shchennikov, V. V.; Vorontsov, G. V.; Manakov, A. Y.; Likhacheva, A. Y.; Kulbachinskii, V. A. *J. Appl. Phys.* **2008**, *104*, 053713.
- (32) Ovsyannikov, S. V.; Shchennikov, V. V. *Chem. Mater.* **2010**, *22*, 635–647.
- (33) Poudel, B.; Hao, Q.; Ma, Y.; Lan, Y.; Minnich, A.; Yu, B.; Yan, X.; Wang, D.; Muto, A.; Vashaee, D.; Chen, X.; Liu, J.; Dresselhaus, M. S.; Chen, G.; Ren, Z. *Science* **2008**, *320*, 634–638.
- (34) Kim, S. I.; Lee, K. H.; Mun, H. A.; Kim, H. S.; Hwang, S. W.; Roh, J. W.; Yang, D. J.; Shin, W. H.; Li, X. S.; Lee, Y. H.; Snyder, G. J.; Kim, S. W. *Science* **2015**, *348*, 109–114.
- (35) Hor, Y. S.; Richardella, A.; Roushan, P.; Xia, Y.; Checkelsky, J. G.; Yazdani, A.; Hasan, M. Z.; Ong, N. P.; Cava, R. J. *Phys. Rev. B* **2009**, *79*, 195208.
- (36) Biswas, K.; Zhao, L.-D.; Kanatzidis, M. G. *Adv. Energy Mater.* **2012**, *2*, 634–638.
- (37) Zheng, G.; Su, X.; Li, X.; Liang, T.; Xie, H.; She, X.; Yan, Y.; Uher, C.; Kanatzidis, M. G.; Tang, X. *Adv. Energy Mater.* **2016**, *6*, 1600595.
- (38) Hasan, M. Z.; Kane, C. L. *Rev. Mod. Phys.* **2010**, *82*, 3045–3067.
- (39) Zhang, H.; Liu, C.-X.; Qi, X.-L.; Dai, X.; Fang, Z.; Zhang, S.-C. *Nat. Phys.* **2009**, *5*, 438–442.
- (40) Xia, Y.; Qian, D.; Hsieh, D.; Wray, L.; Pal, A.; Lin, H.; Bansil, A.; Grauer, D.; Hor, Y. S.; Cava, R. J.; Hasan, M. Z. *Nat. Phys.* **2009**, *5*, 398–402.
- (41) Hsieh, D.; Xia, Y.; Qian, D.; Wray, L.; Meier, F.; Dil, J. H.; Osterwalder, J.; Patthey, L.; Fedorov, A. V.; Lin, H.; Bansil, A.; Grauer, D.; Hor, Y. S.; Cava, R. J.; Hasan, M. Z. *Phys. Rev. Lett.* **2009**, *103*, 146401.

-
- (42) Roychowdhury, S.; Samanta, M.; Banik, A.; Biswas, K. *J. Solid State Chem.* **2019**, *275*, 103–123.
- (43) Heremans, J. P.; Cava, R. J.; Samarth, N. *Nat. Rev. Mater.* **2017**, *2*, 17049.
- (44) Zhu, L.; Wang, H.; Wang, Y.; Lv, J.; Ma, Y.; Cui, Q.; Ma, Y.; Zou, G. *Phys. Rev. Lett.* **2011**, *106*, 145501
- (45) Ma, Y.; Liu, G.; Zhu, P.; Wang, H.; Wang, X.; Cui, Q.; Liu, J.; Ma, Y. *J. Phys. Condens. Matter* **2012**, *24*, 475403.
- (46) Bai, F.; Yu, H.; Peng, Y.; Li, S.; Yin, L.; Huang, G.; Chen, L.; Goncharov, A. F.; Sui, J.; Cao, F.; Mao, J.; Zhang, Q.; Chen, X. *Adv. Sci.* **2022**, *9*, 2105709.
- (47) Samanta, M.; Pal, K.; Pal, P.; Waghmare, U. V.; Biswas, K. *J. Am. Chem. Soc.* **2018**, *140*, 5866–5872.
- (48) Majhi, K.; Pal, K.; Lohani, H.; Banerjee, A.; Mishra, P.; Yadav, A. K.; Ganesan, R.; Sekhar, B. R.; Waghmare, U. V.; Anil Kumar, P. S. *Appl. Phys. Lett.* **2017**, *110*, 162102.
- (49) Vilaplana, R.; Santamaría-Pérez, D.; Gomis, O.; Manjón, F. J.; González, J.; Segura, A.; Muñoz, A.; Rodríguez-Hernández, P.; Pérez-González, E.; Marín-Borrás, V.; Muñoz-Sanjose, V.; Drasar, C.; Kucek, V. *Phys. Rev. B* **2011**, *84*, 184110.
- (50) Hammersley, A. P.; Svensson, S. O.; Hanfland, M.; Fitch, A. N.; Hausermann, D. *High Press. Res.* **1996**, *14*, 235–248.
- (51) Rodríguez-Carvajal, J. *Phys. B Condens. Matter* **1993**, *192*, 55–69.
- (52) Le Bail, A.; Duroy, H.; Fourquet, J. L. *Mater. Res. Bull.* **1988**, *23*, 447–452.
- (53) Klotz, S.; Chervin, J.-C.; Munsch, P.; Le Marchand, G. *J. Phys. D: Appl. Phys.* **2009**, *42*, 075413.
- (54) Chervin, J. C.; Canny, B.; Mancinelli, M. *High Press. Res.* **2001**, *21*, 305–314.
- (55) Kresse, G.; Furthmüller, J. *Comput. Mater. Sci.* **1996**, *6*, 15–50.
- (56) Kresse, G.; Furthmüller, J. *Phys. Rev. B* **1996**, *54*, 11169–11186.
- (57) Blöchl, P. E. *Phys. Rev. B* **1994**, *50*, 17953–17979.
- (58) Kresse, G.; Joubert, D. *Phys. Rev. B* **1999**, *59*, 1758–1775.
- (59) Perdew, J. P.; Burke, K.; Ernzerhof, M. *Phys. Rev. Lett.* **1996**, *77*, 3865–3868.
- (60) Perdew, J. P.; Ruzsinszky, A.; Csonka, G. I.; Vydrov, O. A.; Scuseria, G. E.;

- Constantin, L. A.; Zhou, X.; Burke, K. *Phys. Rev. Lett.* **2008**, *100*, 136406.
- (61) Setyawan, W.; Curtarolo, S. *Comput. Mater. Sci.* **2010**, *49*, 299–312.
- (62) Ganose, A.; Searle, A.; Jain, A.; Griffin, S. *J. Open Source Softw.* **2021**, *6*, 3089.
- (63) Bradlyn, B.; Elcoro, L.; Cano, J.; Vergniory, M. G.; Wang, Z.; Felser, C.; Aroyo, M. I.; Bernevig, B. A. *Nature* **2017**, *547*, 298–305.
- (64) Togo, A.; Tanaka, I. *Scr. Mater.* **2015**, *108*, 1–5.
- (65) Rajaji, V.; Pal, K.; Sarma, S. C.; Joseph, B.; Peter, S. C.; Waghmare, U. V.; Narayana, C. *Phys. Rev. B* **2018**, *97*, 155158.
- (66) Nakayama, A.; Einaga, M.; Tanabe, Y.; Nakano, S.; Ishikawa, F.; Yamada, Y. *High Press. Res.* **2009**, *29*, 245–249.
- (67) Murnaghan, F. D. *Proc. Natl. Acad. Sci.* **1944**, *30*, 244–247.
- (68) Koc, H.; Mamedov, A. M.; Ozbay, E. *Joint IEEE International Symposium on Applications of Ferroelectric and Workshop on Piezoresponse Force Microscopy* **2013**, 41–44.
- (69) Cardona, M. *High Press. Res.* **2004**, *24*, 17–23.
- (70) Bera, A.; Pal, K.; Muthu, D. V. S.; Sen, S.; Guptasarma, P.; Waghmare, U. V.; Sood, A. K. *Phys. Rev. Lett.* **2013**, *110*, 107401.
- (71) Menéndez, J.; Cardona, M. *Phys. Rev. B* **1984**, *29*, 2051–2059.
- (72) Rajaji, V.; Malavi, P. S.; Yamijala, S. S. R. K. C.; Sorb, Y. A.; Dutta, U.; Guin, S. N.; Joseph, B.; Pati, S. K.; Karmakar, S.; Biswas, K.; Narayana, C. *Appl. Phys. Lett.* **2016**, *109*, 171903.
- (73) Bahramy, M. S.; Yang, B. J.; Arita, R.; Nagaosa, N. *Nat. Commun.* **2012**, *3*, 679.
- (74) Rajaji, V.; Dutta, U.; Sreeparvathy, P. C.; Sarma, S. C.; Sorb, Y. A.; Joseph, B.; Sahoo, S.; Peter, S. C.; Kanchana, V.; Narayana, C. *Phys. Rev. B* **2018**, *97*, 085107.
- (75) Rajaji, V.; Janaky, S.; Sarma, S. C.; Peter, S. C.; Narayana, C. *J. Phys. Condens. Matter* **2019**, *31*, 165401.

PART 7

Summary and Future Outlook



Summary and Future Outlook[†]

7.1. Summary

Recently, two dimensional (2D) layered materials have gained enormous attention among researchers due to their outstanding physical and chemical properties. Unique optical, electronic, and thermal transport properties make this class of compounds as potential candidates for energy conversion. Very recently, metal-based chalcogenides with 2D layered structure are found to show superior thermoelectric performance. In my Ph.D. work, I have synthesized and investigated detailed structure-property relationships of a few novel 2D layered metal chalcogenides and studied their fundamental physical properties and applicability in thermoelectric research. The thesis is divided into seven parts.

In part 1, I have given a brief introduction to the 2D layered metal chalcogenides and their importance in the field of thermoelectrics. Then, I have discussed about the intriguing crystal structure, lattice dynamics, and electronic structure of tin selenide and addressed the key challenges in the way of optimizing the thermoelectric performance of SnSe. I have also discussed about the favourable electronic and phonon transport of a charge density wave (CDW) material, gadolinium tri-telluride (GdTe₃) and why CDW materials are potential candidates for thermoelectrics. Further, I have discussed about the effect of pressure on the electronic transition in topological quantum materials and provided a brief introduction about the crystal and electronic structure of bismuth selenide (BiSe), a weak topological insulator. Lastly, I have described the experimental details including various synthesis, characterizations, and measurement techniques.

In Part 2, I have optimized the thermoelectric properties of solution grown SnSe nanocrystals by adopting various doping strategies. It is divided into 3 chapters. Chapter 1 deals with the high thermoelectric figure of merit ($zT = 2.1$) in two dimensional (2D)

[†]A part of this chapter is published in M. Samanta, T. Ghosh, S. Chandra, and K. Biswas, *J. Mater. Chemistry A*, 2020, 8, 12226-12261 (Invited Review); S. Chandra, P. Dutta, and K. Biswas, *ACS Nano*, 2022, 16, 7-14 (Invited Perspective).

nanoplates of Ge doped SnSe synthesized by a simple hydrothermal route followed by spark plasma sintering (SPS). Ge-doping in SnSe nanoplates significantly enhances the *p*-type carrier concentration which results in high electrical conductivity and power factor. In addition to nanoscale grain boundary and high lattice anharmonicity in SnSe nanoplates, phonon scattering due to Ge precipitates in the SnSe matrix gives rise to an ultralow lattice thermal conductivity (κ_{lat}) of ~ 0.18 W/mK at 873 K in 3 mol% Ge doped SnSe nanoplates. In Chapter 2, I have obtained significant enhancement in thermoelectric performance in 2D SnSe nanoplates by introducing magnetic Gd dopants. The *p*-type carrier concentration increases significantly upon 3 mol% Gd addition in SnSe nanoplates due to phase separation of Gd₂Se₃ nanoprecipitates (2-5 nm) and subsequent Sn²⁺ vacancy formation. The presence of magnetic fluctuations induced by small nano-precipitates of Gd₂Se₃ provides additional scattering of the phonons in SnSe, which reduces the κ_{lat} significantly in Sn_{0.97}Gd_{0.03}Se. Chapter 3 deals with the solution phase synthesis and thermoelectric transport properties of ultrathin (1.2-3 nm thick) few layered *n*-type Bi doped SnSe nanosheets. Bi-doped nanosheets exhibit ultralow κ_{lat} (~ 0.3 W/mK) throughout the temperature range of 300-720 K which can be ascribed to the effective phonon scattering by interface of SnSe layers, nanoscale grain boundaries and point defects.

Part 3 is divided into 2 chapters. In Chapter 1, I have reported record high *zT* of 2.0 in *n*-type polycrystalline SnSe_{0.92} + 1 mol% MoCl₅ resulting from the simultaneous optimization of *n*-type carrier concentration and enhanced phonon scattering due to the formation of modular of layered intergrowth [(SnSe)_{1.05}]_m(MoSe₂)_n like compounds within the SnSe matrix. These 2D layered modular intergrowth compound resembles the natural nano-heterostructures and their periodicity of 1.2 - 2.6 nm matches the phonon mean free path of SnSe. Thus, the heat carrying phonons were blocked effectively and an ultra-low low κ_{lat} and ultra-high thermoelectric performance were obtained in *n*-type polycrystalline SnSe. Chapter 2 deals with the high thermoelectric performance of *n*-type SnSe_{0.92} upon WCl₆ doping. The successful creation of Se vacancy and substitution of W⁶⁺ at Sn²⁺ and Cl⁻ ions at Se²⁻ sites effectively enhance the total *n*-type carrier concentration, thus improving its electrical conductivity. The occurrence of WSe₂ precipitates in the SnSe matrix drastically reduces the lattice thermal conductivity which

gives rise to high zT in $\text{SnSe}_{0.92} + 2 \text{ mol\% WCl}_6$ sample.

In part 4, I have reported the successful stabilization of the high-pressure cubic rock-salt phase of SnSe at ambient conditions by introducing chemical pressure into the lattice upon alloying with 30 mol% AgBiSe_2 . The band gap of the pristine orthorhombic SnSe is 0.90 eV, whereas, when SnSe is alloyed with AgBiSe_2 , band gap closes rapidly near to zero at $x = 0.30$ due to increase in chemical pressure originating from a sharp decrease in unit cell volume. We confirm the stabilization of the cubic structure and its associated changes in electronic structure using first-principles theoretical calculations. Pristine cubic SnSe exhibits topological crystalline insulator (TCI) quantum phase, but the cubic $(\text{SnSe})_{1-x}(\text{AgBiSe}_2)_x$ ($x = 0.33$) possesses semi-metallic electronic structure with overlapping conduction and valence bands. Cubic polycrystalline $(\text{SnSe})_{0.70}(\text{AgBiSe}_2)_{0.30}$ sample shows n -type conduction at room temperature while the orthorhombic $(\text{SnSe})_{1-x}(\text{AgBiSe}_2)_x$ ($0.00 \leq x < 0.28$) samples retain its p -type character. Thus, by optimizing the electronic structure and the thermoelectric properties of polycrystalline SnSe, a high zT of 1.3 at 823 K has been achieved in $(\text{SnSe})_{0.78}(\text{AgBiSe}_2)_{0.22}$.

In part 5, I have investigated the origin of low lattice thermal conductivity in GdTe_3 , a charge density wave (CDW) material. GdTe_3 possess a quasi-2D layered structure where one corrugated GdTe slab is sandwiched between two Te sheets. From, first-principles theoretical calculations, it was verified that charge transfer take place from the GdTe slab to the adjacent Te sheets and there is a presence of van der Waals gap between the two neighbouring Te-sheets. Thus, the structure can be considered as a natural heterostructure of charge and vdW layers. Strong electron-phonon coupling, and Fermi surface nesting play the crucial role behind the CDW transition ($T_{CDW} \sim 380 \text{ K}$) in GdTe_3 . Large anisotropic behaviour was observed both in the electrical and thermal conductivity data of GdTe_3 when measured along parallel and perpendicular to the SPS pressing, which is quite unusual in polycrystalline materials. From the theoretical calculations and Raman spectroscopic analysis, we have confirmed the existence of low-lying optical phonon modes in GdTe_3 which couples with the heat carrying acoustic phonon branches. Thus, the presence of strong electron-phonon coupling and natural heterostructure of charge and vdW layers effectively scatter the phonons which gives rise to low lattice thermal conductivity in GdTe_3 .

In part 6, I have studied the impact of hydrostatic pressure on the weak topological insulator BiSe, a promising thermoelectric material. We have performed detailed pressure dependent powder X-ray diffraction and Raman spectroscopic analysis of BiSe and inferred that the room temperature trigonal ($P\bar{3}m1$) phase is stable up to ~ 7 GPa. Interestingly, we have observed clear anomalies at ~ 1 and ~ 2.2 GPa in the pressure dependent lattice parameters (a , c , and c/a ratio), cell volume, Raman mode shift and Raman mode linewidth data suggesting the onset of two electronic topological transitions (ETTs) in this system which is further verified by DFT calculations of electronic structure under pressure. The origin of these ETTs is associated with the two different vibrational modes arising from Bi_2 bilayer and Bi_2Se_3 quintuple layers of BiSe. Detailed electronic band structure calculations also indicate that the emergence of multiple band extrema both in the valence and conduction bands near the vicinity of ETT can improve the thermopower and thermoelectric performance of BiSe.

To summarize, the initial part of the thesis involves the synthesis and enhancement of the thermoelectric performance of p -type nanocrystals and n -type polycrystals of SnSe (Part 2 and 3). Then, I have studied the structural attributes of SnSe where I could be able to successfully stabilize the metastable cubic rock-salt phase of SnSe at ambient conditions with the aid of chemical pressure (Part 4). I have also performed an in-depth study to understand the origins of low thermal conductivity in a charge density wave material, GdTe_3 (Part 4). Finally, I have studied the pressure dependent electronic topological transitions in a weak topological insulator BiSe (Part 6).

7.2. Future Outlook

The thermoelectric research in the layered materials has truly thrived in recent years. The overwhelming interest stems from the complex electronic structure and phonon transport of these materials.¹

For example, single crystals of SnSe have recently created sensation in thermoelectrics. Despite being its simple chemical formula, the electronic and phonon transport of SnSe is truly unique which garnered attention of researchers among various fields of chemistry and materials science. However, synthesis of SnSe single crystals is time consuming and expensive; and the single crystals exhibits poor mechanical strength.

Thus, there is enormous room to improve the thermoelectric performance of nanocrystalline and polycrystalline SnSe. But the performance of the polycrystalline SnSe degrades as it has the thermal conducting SnO₂ coating on the surface. Over recent years, the zT of nano/polycrystalline SnSe has been improved from 0.6 to 2.2 with various synthetic modulations.² However, new strategies like H₂ treatment to remove the surface oxidation in p -type polycrystalline SnSe,³ or surface coating of SnSe nanoparticles with CdSe molecular complexes⁴ are in the nascent stages and several problems are yet to be tackled such as: (i) The highly anisotropic thermoelectric properties of SnSe single crystals, SPS or hot pressed polycrystals and nanocrystals required careful transport measurements with special care in same direction measurement of electrical and thermal transport. (ii) In some of the previous reports, it has been debated that the single crystals of SnSe suffer from a uniform density distribution which may limit their reproducibility and reversibility thermoelectric properties.⁵ Similar problem has been also observed in some of the polycrystalline and nanocrystalline samples which needed to be resolved by tailoring the synthesis procedure. (iii) To estimate the total thermal conductivity of SnSe systems, the experimentally measured heat capacity (C_p) values either obtained from the indirectly during measurement of thermal diffusivity or directly obtained by differential scanning calorimetry (DSC) should be used. C_p values of SnSe should be greater than its Dulong-Petit's limit above the room temperature as the Debye temperature (205 K)⁶ of SnSe is much lower than the room temperature. (iv) Most of the SnSe nanocrystals and polycrystals possess high zT value at elevated temperatures whereas, the zT_{avg} still remains low for these systems which results in low thermoelectric power conversion efficiency.⁷ This problem could be overcome by tuning the synthesis procedure or by doping-control by innovative strategies. (v) Both the p and n -type doping in nanocrystalline SnSe during solution growth is extremely challenging, which need to be addressed. (vi) Two-dimensional heterostructures with SnSe nanostructure along with other 2D materials should be studied for exploratory thermoelectric property investigations. Had these problems been addressed properly, nano/polycrystalline SnSe will serve as a steppingstone towards the research of high performance thermoelectrics based on 2D layered materials.

Layered interfaces are known to strongly scatter acoustic phonons resulting in low

lattice thermal conductivity. van der Waals layered heterostructure with vertical stacking of two different materials can have ultralow thermal conductivity. So, this class of compounds are found to exhibit low lattice thermal conductivity due to the presence of bonding heterogeneity and strong lattice anharmonicity. Recently, it has been shown that the strong electron-phonon coupling (EPC) can effectively reduce the lattice thermal conductivity of a material when the carrier concentration is above 10^{19} cm^{-3} .⁸ Realizing the idea of layered disordered crystal structure, as well as strong electron phonon coupling, charge density wave (CDW) materials can be a good candidate for low lattice thermal conductivity as they have layered structure where strong EPC breaks the translation symmetry of the lattice and induces lattice distortion into the system. However, thermoelectric properties of charge density wave systems have not been studied yet and there remains a plenty of room to improve its thermoelectric performance.

Recently, topological quantum materials with corrugated layered structure such as Bi_2Te_3 ,^{9,10} Bi_2Se_3 ,¹¹ BiSe ,¹² and BiTe ¹³ have been demonstrated to have promising thermoelectric performance with low thermal conductivity while retaining the high carrier mobility (μ). Very recently, pressure-induced electronic topological transition (ETT) and topological quantum phase transition (TQPT) have gained enormous attention in thermoelectric research as it can lead to a significant enhancement in the power factor of these materials.^{14,15} However, the field is still unexplored with detailed understanding of the correlation between electronic topological transition and pressure dependent thermoelectric properties. Thus, the exciting chemistry which have strong influence on the electron and phonon transports in these materials needs to be better understood to further improve the thermoelectric performance of these materials.

Although there are large number of layered materials, high thermoelectric performance has been achieved only in a handful of them. Therefore, there is a continuous search for new materials with promising thermoelectric performance. In this context, the recent discovery of 2.5D materials could unlock new breakthroughs in the research of materials science.¹⁶ Moreover, with the advancement of nanotechnology and nano-electronic devices, there is an ever-increasing attention to develop and integrate nanoscale thermoelectric devices. The development of atomically thin materials, since the discovery of graphene, further fuelled this surge in general. The inherent strong anisotropy in

thermal properties due to layered structure, manifestation of quantum effects in transport properties and discretized electronic density of states makes these layered materials an attractive playground for thermoelectrics.^{17,18}

7.3. References

- (1) Samanta, M.; Ghosh, T.; Chandra, S.; Biswas, K. *J. Mater. Chem. A* **2020**, *8*, 12226–12261.
- (2) Chandra, S.; Dutta, P.; Biswas, K. *ACS Nano* **2022**, *16*, 7–14.
- (3) Zhou, C.; Lee, Y. K.; Yu, Y.; Byun, S.; Luo, Z.; Lee, H.; Ge, B.; Lee, Y.-L.; Chen, X.; Lee, J. Y.; Cojocaru-Mirédin, O.; Chang, H.; Im, J.; Cho, S.; Wuttig, M.; Dravid, V. P.; Kanatzidis, M. G.; Chung, I. *Nat. Mater.* **2021**, *20*, 1378–1384.
- (4) Liu, Y.; Calcabrini, M.; Yu, Y.; Lee, S.; Chang, C.; David, J.; Ghosh, T.; Spadaro, M. C.; Xie, C.; Cojocaru-Mirédin, O.; Arbiol, J.; Ibáñez, M. *ACS Nano* **2021**, *16*, 78–88.
- (5) Wei, P.-C.; Bhattacharya, S.; He, J.; Neeleshwar, S.; Podila, R.; Chen, Y. Y.; Rao, A. M. *Nature* **2016**, *539*, E1–E2.
- (6) Karunarathne, A.; Gladden, J. R.; Priyadarshan, G.; Wei, P.-C.; Hung, T.-L.; Parajuli, P.; Bhattacharya, S.; Chen, Y.-Y.; Rao, A. M. *ACS Appl. Energy Mater.* **2018**, *1*, 6123–6128.
- (7) Shi, X.; Wu, A.; Liu, W.; Moshwan, R.; Wang, Y.; Chen, Z.-G.; Zou, J. *ACS Nano* **2018**, *12*, 11417–11425.
- (8) Shi, X.; Pei, Y.; Snyder, G. J.; Chen, L. *Energy Environ. Sci.* **2011**, *4*, 4086–4095.
- (9) Poudel, B.; Hao, Q.; Ma, Y.; Lan, Y.; Minnich, A.; Yu, B.; Yan, X.; Wang, D.; Muto, A.; Vashaee, D.; Chen, X.; Liu, J.; Dresselhaus, M. S.; Chen, G.; Ren, Z. *Science* **2008**, *320*, 634–638.
- (10) Kim, S. Il; Lee, K. H.; Mun, H. A.; Kim, H. S.; Hwang, S. W.; Roh, J. W.; Yang, D. J.; Shin, W. H.; Li, X. S.; Lee, Y. H.; Snyder, G. J.; Kim, S. W. *Science* **2015**, *348*, 109–114.
- (11) Hor, Y. S.; Richardella, A.; Roushan, P.; Xia, Y.; Checkelsky, J. G.; Yazdani, A.; Hasan, M. Z.; Ong, N. P.; Cava, R. J. *Phys. Rev. B* **2009**, *79*, 195208.
- (12) Samanta, M.; Pal, K.; Pal, P.; Waghmare, U. V.; Biswas, K. *J. Am. Chem. Soc.* **2018**, *140*, 5866–5872.
- (13) Samanta, M.; Pal, K.; Waghmare, U. V.; Biswas, K. *Angew. Chem. Int. Ed.* **2020**, *59*, 4822–4829.
- (14) Bai, F.; Yu, H.; Peng, Y.; Li, S.; Yin, L.; Huang, G.; Chen, L.; Goncharov, A. F.;

-
- Sui, J.; Cao, F.; Mao, J.; Zhang, Q.; Chen, X. *Adv. Sci.* **2022**, *9*, 2105709.
- (15) Polvani, D. A.; Meng, J. F.; Chandra Shekar, N. V.; Sharp, J.; Badding, J. V. *Chem. Mater.* **2001**, *13*, 2068–2071.
- (16) Ago, H.; Okada, S.; Miyata, Y.; Matsuda, K.; Koshino, M.; Ueno, K.; Nagashio, K. *Sci. Technol. Adv. Mater.* **2022**, *23*, 275–299.
- (17) Dresselhaus, M. S.; Hicks, L. *Phys. Rev. B* **1993**, *47*, 727–731.
- (18) Dresselhaus, M. S.; Chen, G.; Tang, M. Y.; Yang, R.; Lee, H.; Wang, D.; Ren, Z.; Fleurial, J. P.; Gogna, P. *Adv. Mater.* **2007**, *19*, 1043–1053.

List of Publications

- **Included in thesis**

Articles

1. **Sushmita Chandra**, Prabir Dutta, and Kanishka Biswas, High-Performance Thermoelectrics Based on Solution-Grown SnSe Nanostructures, *ACS Nano*, 2021, *16*, 7-14. (Invited Perspective)
2. **Sushmita Chandra**, Raagya Arora, Umesh V Waghmare, and Kanishka Biswas, Modulation of the Electronic Structure and Thermoelectric Properties of Orthorhombic and Cubic SnSe by AgBiSe₂ Alloying, *Chem. Sci.*, **2021**, *12*, 13074-13082.
3. **Sushmita Chandra**, Prabir Dutta, and Kanishka Biswas, Enhancement of the Thermoelectric Performance of 2D SnSe Nanoplates through Incorporation of Magnetic Nanoprecipitates, *ACS Appl. Energy Mater.*, **2020**, *3*, 9051-9057.
4. **Sushmita Chandra**, and Kanishka Biswas, Realization of High Thermoelectric Figure of Merit in Solution Synthesized 2D SnSe Nanoplates via Ge Alloying, *J. Am. Chem. Soc.*, **2019**, *141*, 6141-6145.
5. **Sushmita Chandra**, Ananya Banik, and Kanishka Biswas, *n*-Type Ultrathin Few-layer Nanosheets of Bi Doped SnSe: Synthesis and Thermoelectric Properties, *ACS Energy Lett.*, **2018**, *3*, 1153-1158.
6. **Sushmita Chandra**, Usha Bhat, Prabir Dutta, Aditya Bhardwaj, Ranjan Datta, and Kanishka Biswas, Modular Nanostructures Facilitate Low Thermal Conductivity and Ultra-High Thermoelectric Performance in *n*-type SnSe, **2022**. (Manuscript under review)
7. **Sushmita Chandra**, Prabir Dutta, Janaky Sunil, Koushik Pal, Manisha Samanta, Boby Joseph, Chandrabhas Narayana, and Kanishka Biswas, Evidence of Pressure-induced Multiple Electronic Topological Transitions in Thermoelectric BiSe, **2022**. (Manuscript under preparation)
8. **Sushmita Chandra**,[#] Prabir Dutta,[#] Koyendrila Debnath, Ivy Maria, Divya Rawat, Umesh V Waghmare, Ajay Soni, and Kanishka Biswas, Low Thermal Conductivity in Charged & van der Waals Layered GdTe₃, **2022**. ([#]contributed equally, Manuscript under preparation)
9. **Sushmita Chandra**, Prabir Dutta, Usha Bhat, Aditya Bhardwaj, Ranjan Datta, and Kanishka Biswas, Realization of Excellent Thermoelectric Performance in *n*-type SnSe via WCl₆ Doping, **2022**. (Manuscript under preparation)

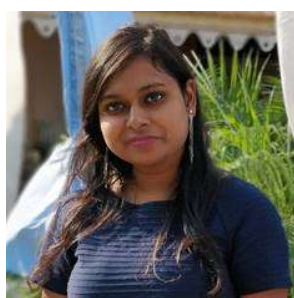
Book Chapter

10. **Sushmita Chandra**, Manisha Samanta, and Kanishka Biswas, High-performance Thermoelectric Energy Conversion Based on Lead-free Group IV–VI Metal Chalcogenides. In *Inorganic Thermoelectric Materials: From Fundamental Concepts to Materials Design*; A. V. Powell, Eds.; [Royal Society of Chemistry, 2021](#); pp 157–215.

• Not included in thesis

1. Manisha Samanta, Tanmoy Ghosh, **Sushmita Chandra**, and Kanishka Biswas, Layered Materials with 2D Connectivity for Thermoelectric Energy Conversion, *J. Mater. Chem. A*, **2020**, 8, 12226-12261. (Invited Review)
2. Prabir Dutta, **Sushmita Chandra**, and Kanishka Biswas, Low Temperature Thermal Conductivity Studies of BiSe and Bi₂Se₃. (Manuscript under preparation)
3. Prabir Dutta, **Sushmita Chandra**, and Kanishka Biswas, Understanding Low Temperature Transport Properties of MnTe. (Manuscript under preparation)
4. Vaishali Taneja, **Sushmita Chandra**, Prabir Dutta and Kanishka Biswas, Realization of High Thermoelectric Figure of Merit in Solution Processed SnSe Doped with WCl₆. (Manuscript under preparation)

Biography



Sushmita Chandra was born on February 16, 1995, in Kolkata, West Bengal (India). She did her B.Sc. Hons. Chemistry (2016) from Lady Brabourne College, University of Calcutta. She joined as an Int. PhD student (Chemical Sciences) at New Chemistry Unit of Jawaharlal Nehru Centre for Advanced Scientific Research (JNCASR), Bangalore, India in August 2016. Currently, she is working with Prof. Kanishka Biswas as a Ph. D. student from August 2019. Her research work is focused on thermoelectric properties of layered metal chalcogenides.